

UNIVERSITY OF BIRMINGHAM

Synthesis and Characterisation of S = 1/2 Kagome Magnets in Metal-Organic Frameworks

by

Tristan Niles Dolling

A thesis submitted to the University of Birmingham for the degree of

DOCTOR OF PHILOSOPHY

The Clark Group

School of Chemistry

College of Chemistry

University of Birmingham

April 2024

UNIVERSITY OF
BIRMINGHAM

University of Birmingham Research Archive

e-theses repository

This unpublished thesis/dissertation is copyright of the author and/or third parties. The intellectual property rights of the author or third parties in respect of this work are as defined by The Copyright Designs and Patents Act 1988 or as modified by any successor legislation.

Any use made of information contained in this thesis/dissertation must be in accordance with that legislation and must be properly acknowledged. Further distribution or reproduction in any format is prohibited without the permission of the copyright holder.

© Copyright by Tristan Niles Dolling, 2024

All Rights Reserved

Abstract

Magnetic frustration is a phenomenon that may occur in materials when the arrangement of magnetic atoms in a structure results in competing magnetic exchange interactions. One example of this is the kagome arrangement, featuring corner sharing triangles of magnetic atoms, this motif is expected to generate magnetic frustration in cases where antiferromagnetic order is present. In this thesis, several magnetic kagome containing metal-organic frameworks were investigated. This diverse class of materials, comprised of magnetic metal nodes and organic ligands, provides the opportunity to examine the bulk magnetic behaviours that arise due to the use of distinct geometries, such as the kagome, which is anticipated to host interesting magnetic characteristics at low temperatures. In our initial investigation, we focus on a single member of the $Cu_3(CO_3)_2(x)_3{\cdot}2ClO_4$ family of metal-organic frameworks, where x represents a ditopic ligand such as bis(3-pyridyl)acetylene. This metal-organic framework features Cu^{2+}, $CO_3{}^{2-}$ kagome layers which are coordinated by the ditopic ligands to form a three-dimensional network. Using X-ray and neutron diffraction techniques, along with magnetic susceptibility measurements, we were able to definitively characterise the crystal structure and magnetic properties of this MOF. The magnetic properties we describe were consistent with those observed in other compounds belonging to the same $Cu_3(CO_3)_2(x)_3{\cdot}2ClO_4$ family, where ferromagnetic and antiferromagnetic order coexist.

In our second investigation, we study the impact of eliminating covalent bonding between the kagome layers. To do this, we explore two additional systems with the formula

$Cu_3(CO_3)_2(x)_6{\cdot}2ClO_4$, where x represents a monodentate ligand such as methylpyridine or 2,4-bipyridine. These monodentate ligands give rise to a non-covalent, stacked arrangement of Cu^{2+}, $CO_3{}^{2-}$ kagome layers, which were expected to suppress or eliminate magnetic exchange interactions between nearest neighbour kagome layers, forming a magnetic quasi-two-dimensional kagome structure. Using X-ray/neutron diffraction, heat capacity, and magnetic susceptibility measurements, we were able to confirm the existence of ferromagnetic exchange interactions within the kagome layers, with no evidence for antiferromagnetic exchange interactions between layers. Furthermore, we extend our investigation by exfoliating these three-dimensional materials to the monolayer limit, tracking success using atomic force microscopy. Our observations reveal compelling evidence for the successful exfoliation to a monolayer; however, further examination is required for the confirmation of crystallinity and magnetic activity.

In our final investigation, we explore the impact of altering intra-plane exchange pathways on magnetic exchange interactions within a kagome lattice by synthesising a two-dimensional MOF with the formula $Cu_3(C_6O_6)_2$. This material features no inter-plane coordination and employs a distinct superexchange pathway anticipated to accommodate antiferromagnetic exchange interactions. By conducting high-resolution X-ray powder diffraction measurements, we were able to dispel contradictory findings from the literature, with our data suggesting a $C2/m$ space group assignment. Furthermore, by examining heat capacity, magnetic susceptibility, and muon spin relaxation data, we observe no sign of a well-defined long-range ordered ground state. This suggested that this system may host an exotic magnetic ground state at low temperature, one such as the elusive quantum spin liquid state.

The overall conclusion of this research is that metal-organic framework chemistry provides an excellent experimental route to characterising physical examples of theoretically significant magnetic models.

Declaration

I declare that the work presented in this thesis was carried out by myself unless otherwise stated in the text or acknowledgements. This thesis has not been submitted to any other institution for the award of this degree.

Tristan N. Dolling

April 2024

Acknowledgements

First and foremost I thank my supervisor, Dr. Lucy Clark, for providing me with the opportunity to pursue the research interests contained within this thesis. Without your support and commitment to improving my academic writing over the course of my PhD I would not have been able to produce a thesis of this quality. Finally, thank you for leading by example on many of the skills required to work as a professional in academia, I see a significant improvement in myself and my ability to act appropriately in situations requiring professionalism. I also thank Dr. Samuel Ivko for his support, providing me with strong foundations upon which to build independently in all aspects of my project. I also thank Dr. Jem Pitcairn, better late than never, not only a talented researcher but an inspirational voice in the later stages of my PhD, it's impossible to say what the final months would have been like without you. I thank the University of Birmingham for funding my Ph.D. studentship and the UKRI Science and Technology Facilities Council for funding many of the beamtime experiments performed throughout my research.

Of course, much of the research contained within this thesis would not have been possible without the help of talented and helpful external academics and beamline scientists. As such, I thank Dr. Peter Baker for an exceptionally enjoyable experience on MuSR. I also thank Dr. Pascal Manuel for countless hours of help and support on WISH, our late night table tennis matches at NMSUM will not be easily forgotten. I also thank Dr. Angel Arevalo-Lopez, because without his support with our heat capacity measurements, I would not have been able to tackle the complex fitting and data processing on my own.

Furthermore, all the tutors at the Durham Crystallography training school were fantastic; however, a special thanks for Dr. Jeremiah Tidey is warranted, I doubt anyone could make intense crystallography discussions as enjoyable as he does while providing hands-on help.

A special thanks to members of the Clark group old and new, Dr. Jennifer Graham, I would not have been able to refine structures in GSAS2 and Fulprof without your help, you were an inspirational member of the group, and you have a bright future ahead of you. Dr. Aly Abdeldaim, I would need an entire new section to thank you to the extent you deserve, not only an incredible source of knowledge and assistance during my PhD but a true lifelong friend. Thank you Amie Troath for your support and kindness, I wish you the absolute best with the *twists* and *turns* of your PhD, even if things feel like they just go *round* in *circles*, I am sure you can find the sweeter side of that *doughnut*... or *mug*. Thank you Elizabeth Evans, there were few times your humour did not brighten the room, I wish you the best of luck with the AFM, I'm sure your chances of success are not too *slim*. Jem I already thanked you, don't be greedy.

Finally, I thank my family, Ben and Claire, and I owe them both a lot for their kindness in allowing me to live with you when I needed. Mum, thanks for always being there, for providing me with a supportive and constructive ear, to encourage me and of course for all those science kits I had growing up. Jen, from joining the MC seminar Zoom meeting early to endless good times, I couldn't ask for a better "Doom dozor" in what is a very mid deck. Thank you for being there for me during the stress and of course the entire thesislynn era, you're the best, that's about it, see ya.

Contents

Abstract i

Acknowledgements v

Contents vii

List of Figures xiii

List of Tables xxxv

1 Introduction 1

1.1 Materials, Magnetism and Magnetic Frustration 3

1.1.1 Metal-Organic Frameworks 3

1.1.2 The Origin of Atomic Magnetism 4

1.1.3 Properties of the Magnetic Moment 6

1.1.4 Crystal Field Splitting and Jahn-Teller Distortion 8

1.1.5 Magnetic Order in Transition Metal Systems 10

1.1.6 Magnetic Frustration 13

1.1.7 The Quantum Spin Liquid and the Resonating Valence Bond Model 14

1.1.8 Ferromagnetic Kagome Containing Magnets and Approaching the Two Dimensional Limit 15

1.2 Magnetic materials of interest 17

1.2.1 Inorganic Realisations of Kagome Magnets 18

1.2.2 Kagome Containing Metal-Organic Magnets 21
1.2.3 3D Copper Carbonate Kagome Containing Metal-Organic Magnets 25
1.2.4 Quasi-2D Copper Carbonate Kagome Containing Metal-Organic Magnets 31
1.2.5 2D Antiferromagnetic Copper Kagome Containing Metal-Organic Magnets 32

2 Experimental Methods 33

2.1 Synthetic methods 34
2.1.1 Solvay-Based MOF Synthesis 35
2.1.2 Solution Based MOF Synthesis 35
2.1.3 Mechanical exfoliation 36
2.2 Organic Elemental Analysis 36
2.3 Fourier-Transform Infrared Spectroscopy 37
2.4 Scanning Electron Microscopy 37
2.5 Nanosheet Characterisation 38
2.5.1 Atomic Force Microscopy 39
2.6 Diffraction Methods 40
2.6.1 Powder X-ray Diffraction 42
2.6.2 Single Crystal X-ray Diffraction 46
2.6.3 Neutron Powder Diffraction 47
2.6.4 Magnetic Neutron Scattering 50
2.7 Magnetic Susceptibility 51
2.8 Heat Capacity 56
2.9 Muon Spectroscopy 59
2.9.1 Fitting μSR data 63

3 Crystal and Magnetic Structure Determination of Kagome Containing Metal-Organic Frameworks 65

3.1 Introduction . . . 65
3.2 Experimental Methods . . . 70
3.2.1 Single-Crystal Synthesis . . . 70
3.2.2 Powder X-ray Diffraction . . . 72
3.2.3 Single-Crystal X-ray Diffraction . . . 72
3.2.4 Magnetic Susceptibility . . . 73
3.2.5 Neutron Powder Diffraction . . . 73
3.3 Results and Discussion . . . 74
3.3.1 Crystal Growth . . . 74
3.3.2 Single-Crystal Structural Determination . . . 75
3.3.3 Laboratory Powder X-Ray Structure Confirmation . . . 78
3.3.4 High-Resolution Powder X-Ray Structure Determination . . . 80
3.3.5 Comparisons of Magnetic Susceptibility Data . . . 83
3.3.6 Determination of the Magnetic Structure of MOF-*bpa* by Neutron Powder Diffraction . . . 86
3.4 Conclusions . . . 92

4 Approaching the Two-Dimensional Limit of the $S = \frac{1}{2}$ Kagome Ferromagnet Within Two Metal-Organic Frameworks 95

4.1 Introduction . . . 95
4.2 Experimental Methods . . . 100
4.2.1 Single-Crystal Synthesis . . . 100
4.2.2 Exfoliation Method . . . 101
4.2.3 Powder X-ray Diffraction . . . 102
4.2.4 Single-Crystal X-ray Diffraction . . . 102
4.2.5 Magnetic Susceptibility . . . 103
4.2.6 Heat Capacity . . . 103
4.2.7 Neutron Powder Diffraction . . . 104
4.2.8 Atomic Force Microscopy . . . 104

4.3 Results and Discussion . . . 104
4.3.1 Crystal Growth . . . 104
4.3.2 Structural Determination by Single Crystal X-ray Diffraction . . . 106
4.3.3 Powder X-ray Diffraction Analysis of MOF-*mp* . . . 115
4.3.4 Structural Confirmation by Neutron Powder Diffraction . . . 118
4.3.5 Bulk Magnetic Characterisation by Magnetic Susceptibility . . . 121
4.3.6 Differences in Magnetic Heat Capacity Data . . . 124
4.3.7 Magnetic characterisation by Neutron Powder Diffraction . . . 130
4.3.8 Nanosheet characterisation by Atomic Force Microscopy . . . 137
4.4 Conclusions . . . 140

5 Realising the $S = \frac{1}{2}$ Kagome Antiferromagnet in a Metal-Organic-Framework 143
5.1 Introduction . . . 143
5.2 Experimental Methods . . . 147
5.2.1 Powder X-ray Diffraction . . . 148
5.2.2 Magnetic Susceptibility . . . 149
5.2.3 Heat Capacity . . . 149
5.2.4 Scanning Electron Microscopy . . . 149
5.2.5 Neutron Powder Diffraction . . . 150
5.2.6 Muon Spin Relaxation . . . 150
5.3 Results and Discussion . . . 150
5.3.1 Optimisation of Synthesis . . . 150
5.3.2 Water Content Analysis by Fourier Transform Infrared Spectroscopy and Thermogravimetric Analysis . . . 152
5.3.3 Structure Determination by High-Resolution X-ray Diffraction . . . 154
5.3.4 Magnetic Characterisation by Magnetic Susceptibility . . . 157
5.3.5 Missing Entropy in Magnetic Heat Capacity . . . 161
5.3.6 Indications of a Lack of Long-Range Order by Neutron Powder Diffraction . . . 164

5.3.7 Muon Spin Relaxation Spectroscopy for the Confirmation of Spin Dynamics down to 98 mK 172
5.3.8 Conclusions 176

6 Chapter Summaries and Outlook **179**
6.1 Chapter Summaries 179
6.2 Outlook 183

References **187**

A Appendix **213**

List of Figures

1.1 Examples of organic ligands, monodentate ligands have one metal binding site, bidentate have two and multidentate may have three or more. These ligands were used throughout this thesis in the synthesis of magnetic MOFs. 4

1.2 The S shell is a three-dimensional sphere equidistant in all axes containing two electrons, the p shells are spit into three, specifically propagating the x, y and z axis, each containing two electrons. Finally the d shells occupy five discrete conformations containing two electrons each, image edited from Libre texts [33]. 9

1.3 The six d-orbitals of d^9, Cu^{2+}, in the presence of an octahedral crystal field these six degenerate energy levels are split into the t_{2g} and e_g, where the higher e_g energy levels align with octahedral bonding geometries. These may be split further by Jahn-Teller distortion, where elongated bonds in one axis create an energy gap splitting the e_g level further, into its d_{z^2} and $d_{x^2-y^2}$ components. In extreme cases, the axial bond may elongate beyond bonding range, leading to an effective square planar geometry, in these cases the orbitals containing a z component decrease in energy. . . . 9

1.4 Typical ferromagnetic and antiferromagnetic superexchange pathways. a) Here 180° superexchange leads to antiferromagnetic exchange coupling between neighbouring magnetic metal sites. b) Here 90° superexchange leads to ferromagnetic exchange coupling between neighbouring magnetic metal sites. 12

1.5 Representations of the arrangements of magnetic moments in the paramagnetic, ferromagnetic and antiferromagnetic state. 13

1.6 An illustration of the resonating valence bond model upon a kagome lattice, featuring nearest neighbour exchange coupling only, here we see how resonating antiferromagnetic dimers would stabilise a dynamic non-magnetic ground state. Blue circles represent a metal atom, orange lines are bonds and green highlights indicate antiferromagnetic dimer couples. 14

1.7 Crystal structure of CrI_3 where two-dimesnisonal magnetic layers are weakly layered shown by the black arrow, with no covalent interactions between, CrI_3 was discovered to host ferromagetic exchange coupling in two-dimensions only. 16

1.8 Reported structural models of herbertsmithite by Khuntia *et al* [50]. a) Here we observe the copper (blue) kagome bridged by oxygen (red) and zinc (yellow) presenting magnetically isolated kagome layers. b) Here we see a single layers of the kagome, showing the ideal positions of oxygen to facilitate the nearest neighbour exchange interactions likley to induce a QSL like state. 18

1.9 Reported structural models of barlowite by Ranjith *et al* [63]. (left) Here we see a single kagome layer supported by copper hydroxide bonding, with disordered copper and bromine occupying the interplane sites. (right) Here we see how the disordered copper and bromine bridge the gap between kagome layers. 20

1.10 Muon spin relaxation data collected for two zinc substituted barlowite species reported by Tustain *et al* and herbertsmithite reported by Mendels *et al* [67, 60]. We see here that in all cases, a plateau persists below 1 K down to 50 mK, this plateau would not emerge in cases where a long-range ordered state exists. 21

1.11 Reported structural models of Cu(1,3-*bdc*) showing how benzenedicarboxylate simultaneously forms the kagome layers and bridges the gap between them shown alongside [76]. 23

1.12 A section of MOF-*bpe* showing the Jahn-Teller distorted Cu-O bond shown as a dashed line, this distortion results in a "breathing" kagome lattice featuring inequivalent kagome triangles. 26

1.13 The reported crystal structure of $[Cu_3(CO_3)_2(bpe)_3]\cdot 2ClO_4$ by Kanoo *et al*. a) This octahedrally coordinated system features a copper carbonate kagome lattice with Jahn-Teller distorted Cu-O bond meaning that the Cu-O bonds are equatorial-axial in nature. b) The copper carbonate kagome layers are then coordinated by long, ditopic 1,2-bis(4-pyridyl)ethane ligands to afford a three-dimensional structure [85]. C) shows some ligands which are able to interchelate copper carbonate kagome layers (left to right) *bpe*, *bpy*, *azpy* and *bpa* discussed throughout. 27

1.14 The proposed magnetic phase diagram for MOF-*bpe* by Jain *et al*, here we see that below a critical field of 125 Oe the system adopts a short range canted antiferromagnetic state [84]. 29

1.15 Illustration of the Cu−O···O−Cu superexchange angles present between nearest neighbour copper ions in the copper carbonate kagome network, according to DFT calculations the ϕ_1 = 82.6(3)° and ϕ_2 = 217.4(3)° would result in ferromagnetic exchange coupling [12, 83, 90]. 30

1.16 Comparison of (a) MOF-*bpa* and (b) MOF-*bipy*, MOF-*bpa* features covalenty linkage between kagome layers while MOF-*bipy* is non-covalently stacked through weak interactions. 32

2.1 A layered material may be exfoliated to nanosheets through ultrasonication. Here, sonic waves impart enough energy to liberate layers bound by weak intermolecular forces, most commonly observed in graphene [106]. After exfoliation a mixture of exfoliated, partially exfoliated and unexfoliated material exist in suspension, these can be separated through centrifugation methods, isolating the fully exfoliated material in suspension. 36

2.2 Atomic force microscopy data collected for aluminum tetra-(4-carboxyphenyl) porphyrin framework (Al-MOF). (left) The AFM image showing a height profile of 1.9 nm. (right) The proposed crystal structure of a single Al-MOF nanosheet. 40

2.3 An illustration of a PXRD set up. A collimated X-ray beam is directed at the sample; in a Debye-Scherrer set-up the sample holder rotates. The incident X-rays are then diffracted by the atoms lying along the crystallographic planes within. Bragg intensity is only observed when parallel X-rays are diffracted by planes separated by integars, n, of the wavelength of the incident beam, λ. In these cases the X-rays interact constructively producing a signal at the detector. Diffracted planes yield "diffraction cones", generated by these constructively interacting X-rays, where the cone radii in 2θ corresponds to the Bragg position of a crystallographic plane. A one-dimensional slice of these data reveals a diffraction pattern, where intensity is plot against 2θ. The peak shape, intensity and positions observed are a direct result of factors such as atomic radii, position, thermal parameters, strain, size, preferred orientation, diffraction angle, unit cell parameters and more. 44

2.4 An illustration of a SCXRD set-up. Here, an X-ray beam is diffracted by a single crystal, generating a two-dimensional diffraction pattern of Bragg spots. These arise in SCXRD when an incident wavevector, k, satisfies Bragg's law by intersecting a reciprocal lattice vector, g, on the surface of a theoretical construct known as the Ewald's sphere. The diffraction patterns are then collected at all angles in a spherical rotation before collation, resulting in a three-dimensional pattern of Bragg spots in reciprocal space. Here, symmetry elements can be applied to the observed pattern provided the observed Bragg reflections are mostly consistent with a single space-group assignment. Due to the direct relationship between X-ray scattering and electron density, the Bragg intensity is consistent with the atomic radii of elements present within these diffraction planes. Provided agreement between the observed spots and space group assignment, the Fourier transform of the data yields an electron density map constrained by the applied symmetry. This electron density map exists in real-space and can therefore be used to generate crystallographic models using software packages such as OLEX2 [120]. 47

2.5 An illustration showing the principle interactions of neutrons and X-rays, here we see that neutrons may be scattered through the strong nuclear and dipole-dipole interactions, while X-rays are scattered by electromagnetic interactions with electron density [121]. 48

2.6 An illustration of the MPMS 3 SQUID sample area. A sample is secured in a straw sample holder before being inserted into the SQUID. Here the specialised pick-up coils act as super-sensitive detectors for magnetic flux about the sample. In this arrangement, external field and temperature can be manually adjusted while the sample is moved through these pick-up coils. The magnetic flux generated by the movement of a magnetic sample through these coils is then collected and converted to more useful data relating to the magnetic susceptibility of the sample for further analysis. . 53

2.7 Some theoretical examples of magnetometry data. a) A paramagnetic material will produce a smooth upturn in magnetic susceptibility data without spontaneous deviation. In the case of a ferromagnetically ordered material a spontaneous increase in susceptibility at T_{Curie} is expected, while a reduction in susceptibility at T_{Neel} is expected for an antiferromagnetic material. b) In an ordered ferromagnetic material, hysteresis is observed in magnetisation vs. field data. This is observed as saturated moments aligning with the field in one direction require a significant applied field in the opposing direction to reverse their orientation, no hysteresis would be observed in a paramagnetic/antiferromagnetic material. c) In zero field cooled and field cooled data, a bifurcation between the two datasets indicates no field-induced spin freezing [25]. 55

2.8 Some literature magnetic susceptibility data. a) Magnetic susceptibility vs. temperature data showing a shift in T_{max} between the two samples, suggesting differing ordering temperatures. b) Magnetisation vs. field data combined with c) ZFC vs. FC data showing a bifurcation these combined data indicate the onset of ferromagnetic order [134]. 56

2.9 An illustration of how a μSR set-up works. **a)** Antimuons are generated at a spallation source, either continuously or by pulsing. The produced antimuons must be spin-polarised for use in the experiment as the perturbation of their spin indirectly provides us with magnetic information. **b)** Once these spin-polarised, antimuons are implanted within a sample, the presence of internal or applied magnetic fields cause a precession of their spin. **c)** Antimuons have a range of lifetimes, averaging 2.2 μs, and once decayed, produce a positron which can be detected at either a forward or backward detector. With a full spectrum of antimuon lifetimes generating positrons at many time points, we begin to observe an asymmetry between the forward and backward detectors due to continuous precession and decay. The decay lifetime and spin precession allow us to plot the detector asymmetry ratio vs. time, in which the changes in antimuon asymmetry with lifetime provide information on the magnetic fields that perturbed the implanted antimuon spin. **d)** Experimentally, a transverse field may be applied to the sample, the oscillations observed in these data of frequency, f, are directly proportional to the applied field strength felt by the antimuon, allowing for the calibration of the set-up for later observation of internal fields in a material. The peaks and troughs of this oscillation can be ascribed to a muon decaying at a time where it is directly facing one detector over the other. 61

2.10 Some literature MuSR data for a QSL candidate system, $H_3LiIr_2O_6$. (left) muon asymmetry vs. time showing the fast relaxation of implanted muons across a range of temperatures. (right) Relaxation rate vs. time plot showing a low temperature plateau at $\sim$ 1 K indicative of spin dynamics [144]. 62

3.1 A section of a copper carbonate kagome lattice, the proposed exchange pathway and the associated angles are given by black lines, with this model outlined by Mulrooney et al. [83] 67

3.2 The structure of $Cu_3(CO_3)_2(bpa)_3{\cdot}2ClO_4$, illustrated from refined crystallographic information, the system is made up of Cu^{2+} carbonate kagome layers (a), covalently linked by the organic ligand 4,4-bipyridyl acetylene (b). Dashed lines represent Jahn-Teller distorted bonds while the perchlorate is shown to be heavily disordered removed from (b) for clarity. 70

3.3 A comparison of each MOF system, MOF-*bpe*, *bpy* and *azpy* are in the *P*3 while MOF-*bpa* is in the higher symmetry *P*6/*m* space group. The pink atoms and bonds represent disorder about their respective sites, while we see that MOF-*bpa* contains disorder only in the perchlorate counterions. . 77

3.4 Le Bail fits using; the *P*3 model for MOF-*bpe*, *bpy* and *azpy*, alongside the *P*6/m model for MOF-*bpa*, against laboratory collected PXRD data Cu*Kα*. 79

3.5 Rietveld refinement of MOF-*bpa* against the *P*6/m model obtained from SCXRD analysis with a weighted R value, R_{WP} = 8.793 % 81

3.6 Temperature dependent magnetic susceptibility measured in an applied field of 0.1 T. Curie-Weiss fits (black) of the inverse susceptibility (red) were performed across temperature ranges above 100 K using Equation 2.5. The insets show the low-temperature behaviour in each case. Note: an instrumental error led to a loss of data in MOF-*bpy* and MOF-*bpa* between 13 – 14 K. 84

3.7 Derivative plots of temperature dependent magnetic susceptibility measured in an applied field of 0.1 T for MOF-*bpe*, *bpy*, *azpy* and *bpa*. These plots indicate the presence of inflection points corresponding to spontaneous change in the magnetic susceptibility of internal moments. 85

3.8 Rietveld refinement of the *P*6/m model of MOF-*bpa* against 25 K data collected on the WISH diffractometer. Refined lattice parameters are a = 9.1552(5) and c = 13.6104(3) with a global R_{WP} = 3.20 % 89

3.9 Magnetic Rietveld refinement of the *P*1 structure against subtracted NPD data from 1.4 and 25 K collections. A gap in the fit around 8 Å was applied due to a thermal contraction feature. Here, the red line is the fit, blue is the difference between fit and data and points are data. 90

3.10 The proposed magnetic structure of MOF-*bpa*, in which we see ferromagnetically coupled kagome planes, antiferromagnetically coupled, giving us a c-axis length of 27.24 Å in the assigned magnetic unit cell. 91

4.1 Structural models of MOF-*bipy* and MOF-*bpa*. a) Here we see the copper carbonate kagome lattice, shared by both MOF-*bipy* and MOF-*bpa*, where disordered perchlorate occupies the hexagonal channels of the framework. b) Here, we see how the copper carbonate kagome layers are stacked by monodentate *bipy* ligands, which leads to a structure featuring no covalent inter-plane linkage at a separation distance of 21.270 Å between kagome layers. c) Here we see MOF-*bpa*, previously studied in Chapter 3, the copper kagome layers present are covalently bound resulting in antiferromagnetic exchange coupling studied by neutron powder diffraction methods, the inter-layer distance here is 13.579 Å. 97

4.2 Crystallographic models of MOF-*mp* generated from SCXRD data. a) One layer of MOF-*mp* confirming the presence of the copper carbonate kagome lattice. b) One unit cell of MOF-*mp* showing that kagome layers stack through weak inter-layer interactions where layers do not stack directly on top of each other, instead an *abab* pattern where layers are related, rotated through 60°. 99

4.3 Two SEM images taken on crystals of (a) MOF-*bipy* at a magnification of 20x and (b) MOF-*mp* at a magnification of 30x. These images show the size of crystals formed by our optimised synthetic methods, as well as the ability to observe discrete crystal domains confirmed by polarised optical microscopy. 105

4.4 Crystallographic models for MOF-*bipy* generated from data taken on the I19 beamline at Diamond Light Source at 30 and 300 K. In 30 K data we observe a kagome arrangement of corner sharing triangles made up of Cu^{2+} ions chelated by CO_3^{2-} ligands, here, 2,4'-bipyridine, (*bipy*) bridges the gap between kagome layers, stacking them via weak intermolecular forces. These ligands are rotationally disordered about the ring containing the 4' position nitrogen in a refined ratio of 65:35. In the 300 K data, corner sharing triangles are maintained, however, they are larger due to the distortion to the kagome. This leads to a change in Cu-Cu distances (4.574 Å at 30 K and 4.801 Å at 300 K). The *bipy* ligands at 300 K are also rotationally disordered in a fixed ratio of 50:50. 108

4.5 Some sections of copper carbonate chains taken from the literature and from generated models of MOF-*bipy* SCXRD data. a) Two similar chain motifs commonly adopted by copper carbonate [172], analogous to b) a section of the copper carbonate kagome lattice modelled for MOF-*bipy* from 30 K data. c) Another possible copper carbonate chain motif [173], this time analogous to a section of d) a section of MOF-*bipy* modelled from 300 K data. 109

4.6 Crystallographic models of MOF-*mp* generated from SCXRD data collected at 100 K. Here, a and b are taken from data processed without the inclusion of disorder, while c and d are modelled inclusive of disorder. a) MOF-*mp* viewed along the *c*-axis, showing the copper carbonate kagome lattice, perchlorate omitted for clarity. b) A single unit cell of MOF-*mp*, this shows the stacking of kagome layers by weak intermolecular forces, hydrogen omitted for clarity. c) Here, we observe the effects of including disorder to our model, leading to the emergence of two overlain distorted kagome lattices. d) Here, we observe a section of the disordered MOF-*mp* model, from which we observe that disorder is facilitated by the rotation of the carbonate ligand through 22.46(2)° 111

4.7 Two stacked kagome layers with all other atoms removed for clarity. a) Here we see MOF-*bipy*, where we are unable to see the second layer due to a parallel stacking motif characterised by the pattern, *aa*. b) Here we see MOF-*mp*, where two layers are observed to stack in a motif characterised by the pattern, *abab*, we also observe here that the layers are linked by a symmetry operation, a 60° rotation about the centre of the circled carbonate ligand. 113

4.8 Laboratory PXRD data for MOF-*mp* collected at 300 K. Here we see almost no intensity besides the (0 0 2*l*) reflections, (0 0 *l*) reflections are forbidden here due to the symmetry of the *P*6/*m* space group. 116

4.9 Laboratory PXRD data collected for MOF-*mp* at 300 K refined using the Le Bail method, extracted lattice parameters were $a = b = 9.5861(2)$ Å and $c = 31.2699(9)$ Å with an $R_{WP} = 12.75$ 116

4.10 High-resolution PXRD data collected on the I11 beamline at Diamond Light Source at 300 K fit to the $P6_3/m$ space group using the Le Bail method. We are able to fit all peaks to the 100 K model of MOF-*mp* with lattice parameters $a = b = 9.2998(2)$ Å and $c = 31.5186(6)$ Å, $R_{WP} = 38.04$ %. Here, the peak intensities of all (0 0 2l) are under-fit by the model, with peak shoulders present in the (0 0 2) and (0 0 4) reflections leading to a peak shift which likely affects our extracted lattice parameters. We also observe in the rightermost inset that (h k 0) reflections are severely broadened which may originate from ligand disorder in the (h k 0) plane. . 117

4.11 Rietveld and Le Bail refinement of the $P6_3/m$ structure of MOF-*mp* against data collected on the WISH diffractometer at 15 K. Here Bank 1 is fit using the Rietveld method and Banks 2 – 5 were fit simultaneously using the Le Bail method, with refined lattice parameters $a = b = 9.5281(1)$ Å and $c = 31.119(2)$ Å and the scale factor = 4.3347(2), $R_{\mathrm{WP}} = 3.680$ % 119

4.12 Rietveld refinement of the $P\bar{3}$ structure of MOF-*bipy* against data collected on the WISH diffractometer at 14 K. Here we simultaneously refine all five banks to give lattice parameters $a = b = 15.8848(4)$ Å and $c = 21.2240(3)$ Å and the scale factor = 4.9478(7), $R_{\mathrm{WP}} = 2.855$ % 120

4.13 Temperature-dependent magnetic susceptibility data for MOF-*bipy* and MOF-*mp* at 0.1 T. Here we plot the magnetic and inverse magnetic susceptibility for both systems, upon fitting the data to the Curie-Weiss equation we obtain values for the Curie-Weiss temperatures (θ_{CW}) which were 22.05(6) and 24.25(7) K for MOF-*bipy* and MOF-*mp* respectively. These values suggest dominant ferromagnetic exchange interactions within both MOFs [12, 6]. We also extract values for the effective moment (μ_{eff}) which, in both cases, are consistent with the expected 1.72 μ_B for a $S = \frac{1}{2}$ system. 122

4.14 Derivative plots of temperature dependant magnetic susceptibility data collected in an applied field of 0.1 T for both MOF-*bipy* and MOF-*mp*. From these data we are able to extract an estimate for T_C from the point of inflection in each case. Ordering temperatures extracted were $T_C = 8.529(2)$ and 4.798(6) K for MOF-*bipy* and MOF-*mp* respectively. 123

4.15 Magnetisation vs. field data for both MOF-*bipy* and MOF-*mp* overlain. Here we see no significant signs of magnetic hysteresis and a 1 T applied field appears to fully saturate both systems. Both systems near saturation at 1 T, with MOF-*bipy* approaching full saturation at lower field to MOF-*mp*. 124

4.16 Heat capacity data for MOF-*bipy* collected in zero-applied field between 1.8 and 300 K. (a) A plot of zero field heat capacity vs. temperature data fit to three Debye functions across a temperature range of $25 - 300$ K, this approximates the phonon contribution to total heat capacity given by the simulated curve. (b) A log plot of temperature-dependent heat capacity vs. temperature, with the subtraction of the simulated curve from obtained data giving (c) the magnetic temperature-dependent heat capacity. Here, a broad feature is observed below 12 K with a peak at ~7 K. (d) The total magnetic entropy release can be calculated by taking the integral of the temperature-dependent magnetic heat capacity indicating an entropy release of 33.05 % of the expected entropy release of a single, ($S = \frac{1}{2}$), Cu^{2+} ion. 126

4.17 Magnetic heat capacity data for MOF-*bipy* fit to the Schottky anomoly, providing an extracted energy gap of 1.38(17) meV for a two-level $S = \frac{1}{2}$ system. 127

4.18 Heat capacity data for MOF-*mp* collected in zero-applied field between 1.8 and 300 K. (a) A plot of zero field heat capacity vs. temperature data fit to three Debye functions across a temperature range of 25 – 300 K, this approximates the phonon contribution to total heat capacity given by the simulated curve. (b) A log plot of temperature-dependent heat vs. temperature, with the subtraction of the simulated curve from obtained data giving (c) the magnetic temperature-dependent heat capacity. Here, a broad feature appears to be dominated by a rise in magnetic heat capacity below ~8 K which rises until the lowest collected temperature of 1.8 K. (d) The total magnetic entropy release can be calculated by taking the integral of the temperature-dependent magnetic heat capacity indicating an entropy release of 31.59 % of the expected entropy release of a single, ($S = \frac{1}{2}$), Cu^{2+} ion. 128

4.19 The magnetic refinement of subtracted MOF-*bipy* WISH neutron powder diffraction data to the constrained $P1$ model. The refinement was performed by constraining the moment orientation of 11 copper sites to the *ab*-plane, fixing cell parameters to $a = b = 15.8760(4)$ Å and $c = 21.2175(8)$ Å with a scale factor of 4.9478(7). A thermal contraction can be observed between 7.8 and 8.2 Å. 132

4.20 In the proposed magnetic structure of MOF-*bipy* ferromagnetically coupled Cu^{2+} atoms within the *ab*-plane lie within kagome planes, with no sign of antiferromagnetic coupling between kagome layers. This model may suggest the presence of isolated magnetic kagome layers, however ferromagnetic coupling between these layers cannot be ruled out. 133

4.21 Magnetic fits to temperature subtracted neutron powder diffraction data, with a thermal contraction removed between 15.05−16.61 Å. a) For this fit, one layer containing three copper atoms was allowed to refine constrained to the *a*-axis producing an ordered moment of 0.76(8) μ_B. b) In this fit the complete unit cell containing six copper atoms was allowed to refine with each layer constrained to be equal but opposite in the *a*-axis producing an ordered moment for the layers of 0.38(8) and -0.38(8) μ_B. c) In this fit, the complete unit cell containing six copper atoms was allowed to refine, with each layer pointing in a different crystallographic plane with ordered moments of 0.428 μ_B in the *a*-axis and 0.42(8) μ_B in the *b*-axis. 134

4.22 Proposed magnetic structures for MOF-*mp* based upon the magnetic fits performed. a) In this model three magnetic moments per cell are coupled ferromagnetically pointing in the *a*-axis; b) In these models we observe layers of ferromagnetically coupled moments, the nearest-neighbour layers may be modelled pointing in any direction in the *ab*-plane, as the fit only provides information on two layers separated by one unit cell. The numbers denote equivalent layers. 135

4.23 Atomic force microscope images and respective height profile maps for specified points for (top) MOF-*bipy* where we see height profiles ~2 nm with a lateral scale of 500 nm, and (bottom) MOF-*mp* where we see height profiles ~3 nm with a lateral scales up to 3 μm. 138

5.1 The proposed resonant forms of the C_6O_6 ligand. For the charge of the Cu-HHB to be balanced, an average charge of 3- must be upheld, this was confirmed through electron diffraction (ED) and X-ray photoemission spectroscopy (XPS) studies by Meng *et al* [98]. 145

5.2 A crystallographic model of Cu-HHB viewed along (a) the *c*-axis, here we observe the kagome lattice, generated by the affixation of the HHB liagnds to copper. In (b), the *b*-axis, we observe no covalent bonds bridging the kagome layers separated by ~ 3 Å, we would instead expect pancake bonds to occupy this space, water is omitted here for clarity. 146

5.3 An image of unwashed Cu-HHB, the large square morphology is a THQ crystal upon which Cu-HHB nucleates, covering the entire crystal. The white spheres can be attributed to a soluble amorphous copper ammonium species formed during the reaction, which is not present in the washed samples. Copper was confirmed to be on the surface by energy-dispersive X-ray (EDX) analysis (Figure A.4) of this sample. The lack of crystals of this scale and morphology in all washed samples further confirm that this is a THQ crystal. 151

5.4 Two fixed scale SEM and powder XRD plots for two samples with the *C*2/*m* structure of Cu-HHB (left) 14 mg per 15 cm^3, featuring sharper peaks along a comparable *x* and *y* axis to (right) a 7 mg per 15 cm^3 sample. In both cases we confirmed the presence and purity of Cu-HHB by Le Bail refinement. 152

5.5 FTIR spectra for THQ (red) and Cu-HHB (blue), here we observe a clear signal due to water in Cu-HHB along, a significant reduction in C=O stretching observed at 1650 cm^{-1} and the loss of O-H stretching in our Cu-HHB sample indicating the complete removal of THQ from our sample. 153

5.6 Two TGA datasets collected from a sample of Cu-HHB, indicating a mass loss due to water of 0.338 mg (Left) and 0.534 mg (Right). These data suggest a loss of 4.4 and 3.7 molecules of water per formula unit of Cu-HHB respectively. 154

5.7 The Rietveld refinement of Cu-HHB against the $C2/m$ model, weighted R factor, R_{WP} = 4.395 %, where refined lattice paramters are a = 22.3016(7), b = 13.1465(1) and c = 6.2218(6) Å. In this refinement, four molecules of water with their hydrogen atoms removed were included, their atomic coordinates were allowed to refine freely providing us with a significantly better fit than in models where these water positions were not refined. . . . 155

5.8 Evidence for the assignment of the $C2/m$ model in the Le Bail refinement of Cu-HHB. We see here that Bragg intensity is not observed at many of the low 2θ Bragg reflections expected for the $P2/m$ space group for Cu-HHB. The Bragg reflections corresponding to the $P2/m$ model of Cu-HHB were generated using ISODISTORT [186]. 157

5.9 Field cooled and zero field cooled data taken at 0.1 T for a sample of Cu-HHB Here we see no bifurcation of the two datasets, suggesting no field-induced spin freezing or transition to an ordered state. 158

5.10 Temperature dependant magnetic susceptibility data for Cu-HHB in a 0.01 T applied field between 0.4 – 300 K, inverse susceptibility data were fit to the Curie-Weiss equation providing a θ_{CW} = −35.0(1), alongside a Curie constant of 0.384(1) corresponding to a μ_{eff} = 1.66(5) μ_B. We see no clear evidence for a long-range ordered transition in these magnetic susceptibility data, characterised by a deviation from the smooth curve. 159

5.11 Field dependance of the magnetic moment collected at 5, 2 and 0.4 K. These data show a reduced saturation of moments to the applied field at lower temperatures, suggesting the onset of short-range antiferromagnetic correlations, further supported by the sharper increase in saturation at lower field in 0.4 K data. 160

5.12 Heat capacity data for Cu-HHB collected between 1.8 and 301 K. (a) Temperature dependence of zero field specific heat capacity data fit to three Debye functions to approximate the phonon contribution given by the simulated curve. (b) A log plot of temperature-divided specific heat, with the subtraction of simulated from experimental data providing the magnetic contribution to specific heat. (c) Subtracted data reveals a broad feature below 5 K. (d) Calculated magnetic entropy release indicates that only 22.57 % of magnetic entropy is taken into account when compared to the calculated magnetic entropy of a single ($S = \frac{1}{2}$), Cu^{2+} ion. We cannot rule out the fact that some additional magnetic entropy would be gained from a lower temperature dataset however the amount of entropy would not recover the missing 73 %. 162

5.13 Magnetic heat capacity data obtained from the phonon subtraction method outlined above. We fit this data using a Schottky function (Equation 2.13) between 2.5 and 10 K, yielding a good fit to the data and a calculated energy gap of 0.71(5) meV. 163

5.14 In these Bank 4 data, we observe sharp copper peaks at Bragg positions denoted in black, these peaks dominate the powder pattern up to around 2.1 Å. Very few peaks beyond 2.1 Å d-spacing, the refinement against the $C2/m$ Cu-HHB model is unlikely to provide more information on Cu-HHB than our high-resolution powder X-ray diffraction data. 164

5.15 Le Bail refinement of the $C2/m$ structure of Cu-HHB against data collected on the WISH diffractometer at 40 K. For this, the lattice parameters were refined across 5 banks to a = 22.0753(2), b = 13.1799(7) and c = 6.2258(7) Å. We were unable to fit regions dominated by copper Bragg reflections and so limits were set on these data to ensure the inclusion of Bragg reflections solely originated from Cu-HHB. 165

5.16 Neutron powder diffraction data collected for Cu-HHB (1) at 40 and 68 mK, here we observe a significant shift between the two datasets which we initally proposed came from the switching between cryostat and dilution fridge sample holder. 166

5.17 Neutron powder diffraction data collected for Cu-HHB (2) across five temperature points, taken between 40 and 68 mK (Base). Here we observe the anomolous increase in background intensity with increasing temperature, the consistency of this background throughout nuclear and non-nuclear positions of the pattern make it unlikley to be an effect of atomic thermal motion (Debye-Waller) [191]. 167

5.18 Plot of intensity against temperature point at 3.999 Å d-spacing, fit to a simple exponential function (χ^2 = 12.3435). This plot suggests that the increase in background intensity due to temperature becomes less pronounced as temperatures increase beyond 40 K. 168

5.19 NPD patterns for Bank 2 WISH data. a) Two simulated diffraction patterns using the $C2/m$ model for Cu-HHB, with all water molecules present, and with them all removed, we notice here that the ratio between the peaks ~6 – 6.7 Å are unique to the presence of water. b) We see here that for sample (1) the peak ratio more closely matches the simulated pattern where water is present. c) We see here that for sample (2) the peak ratio follows the simulated pattern without water more closely. 169

5.20 The Rietveld refinement of one feature in Bank 1, Cu-HHB data to the $C2/m$ model, collected on the WISH diffractometer. R_{wp} = 2.368%, scale factor = 2.4476(5). We are unable to fit multiple peaks to the model here while simultaneously obtaining a consistent scale factor, therefore we select the most intense Bragg peak for refinement. 170

5.21 Temperature subtracted data from Bank 1, fit to the $P1$ structure providing an extracted moment of 7.71(47) μ_b which is significantly greater than the expected moment of 1.73 μ_b for Cu^{2+}. 171

5.22 MuSR data collected at 120 K in an applied transverse field of 20 G for Cu-HHB, these data are fit to an oscillatory function combined with a Lorentzian relaxation function providing a good fit to the data. From this fit we can extract the frequency corresponding directly to the applied field which then allows us to calculate the detector calibration constant $\alpha = 1.4400$. 172

5.23 MuSR data collected at 0.098 K in a) zero field, fit to Kubo-Toyabe and Gaussian relaxation functions, providing a relaxation rate of 0.2009(23) cm^{-1} and a static field of -6.33(3) mT. b) Several longitudinal fields were applied across the sample to ascertain the field required to fully decouble the nuclear moments of the system, we find that 111 G is ample for the full decoupling of nuclear moments, characterised by a flattening of the zero-field signal. 174

5.24 Two plots of MuSR temperature dependent relaxation rate data. a) In Cu-HHB, we see a sharp increase in relaxation rate from ~ 8 K corresponding to a slowing of muon precession, followed by a plateau from 1.9 – 0.098 K indicating spin dynamics [60, 142, 192]. b) Here we see temperature-dependent normalised muon spin relaxation rate data for substituted Zn-barlowite where x = 0.99(1) and 0.66(1), alongside overlain, published data for herbertsmithite (X_{Herb} = 1) [60]. We observe in all cases a sharp rise in muon relaxation rate beginning at ~3 K, rising to a plateau ~0.6 K indicative of spin dynamics [67]. 175

A.1 Two SEM images collected for MOF-*bipy* and MOF-*mp* at the same magnification. We can see here the difference in layering of these materials, with MOF-*mp* heavily intergrown and layered, these images are representative across several synthetic batches of these MOFs. 215

A.2 Zero field and field cooled measurements for MOF-*bipy* and MOF-*mp* showing no bifurcation in either case ruling out spin-freezing. In both cases there appears to be an indication of a transition, with $T_C \approx 5.5$ K for MOF-*mp* and ≈ 11 K for MOF-*bipy* 216

A.3 MuSR data collected at 10 K in zero applied field showing that a small variation in the initial asymmetry is present between the two sample holders. 216

A.4 Scanning electron microscopy images analysed using energy dispersive X-ray capabilities. Here we see that the material surface contains copper, suggesting supporting our conclusions that Cu-HHB nucleates on the surface of THQ crystals. 217

A.5 MuSR data collected at three temperatures in 111 G applied LF, fit to a single Lorentzian function describing the relaxation observed. The calculated relaxation rates for 0.1, 2 and 50 K data were 0.2009(23), 0.1935(20) and 0.1190(11) cm^{-1}respectively showing a small decrease in relaxation rate between 0.1 and 2 K but a large decrease in relaxation rate upon increasing to higher temperature. 218

List of Tables

3.1 Summarised crystallographic data for MOF-*bpe*, -*bpy*, -*azpy* and -*bpa* from the refinement of data collected on the I19 beamline at Diamond Light Source at 298 K. 76

3.2 Summary of refined lattice parameters collected on a Panalytical Empyrean at 300 K. 80

3.3 Refined structure parameters for the $P6/m$ model of MOF-*bpa* fit to XRD data collected on I11, Diamond, at 300 K. Final refined lattice parameters were a = 9.2503(4) Å and c = 13.5812(5) Å, R_{WP} = 8.637 % and reduced χ^2 = 1.56. 82

3.4 Comparisons of key data from magnetic susceptibility and Fisher specific heat measurements. 86

3.5 Refined structure parameters for the $P6/m$ model of MOF-*bpa* fit to NPD data collected on WISH, ISIS, at 25 K. Final refined lattice parameters were a = 9.1552(5)Å and c = 13.6104(3) Å, global R_{WP} = 3.20 % and reduced χ^2 = 170.82. 87

3.6 Summary of magnetic moment size refined from subtracted NPD data, data collected for MOF-*bpe*, *bpy* and *azpy* refined by Katherine Tustain*. [12] . 91

4.1 Summarised SCXRD data for MOF-*bipy* collected at 30 and 300 K on the I19 beamline at Diamond Light Source and 100 K modelled by Mulrooney *et al* [83]. We observe a change in cell parameters between 30 and 300 K data due to a distortion of the kagome lattice through carbonate rotation. 107

4.2 Summarised SCXRD data for MOF-*mp* collected at 100 K. We observe that the collected data can be modelled in different ways. 112

5.1 Refined structural parameters for the $C2/m$ model of Cu-HHB fit to XRD data collected on I11, Diamond, at 298 K. Rigid bodies were defined for two HHB ligand halves (1) and (2); with refined origins of [0.2554(6), 0.0665(6), 0.2310(9)] and [0.2604(3), 0.4009(7), 0.2964(6)]. Thermal parameters for these rigid bodies could not be refined stably. The final refined lattice parameters were a = 22.3016(7), b = 13.1465(1) and c = 6.2218(6) Å, R_{WP} = 4.439 % and reduced χ^2 = 489.35. 155

A.1 Summarised relaxation rates extracted from Lorentzian fits of μSR data collected at several temperature points. 213

A.2 Refined structure parameters for the $P\bar{3}$ model of MOF-*bipy* fit to all 5 banks, NPD data collected on WISH, at 15 K. Final refined lattice parameters were a = 15.8848(4)Å and c = 21.2240(3) Å, R_{WP} = 2.855 % and reduced χ^2 = 828.8. 213

Chapter 1

Introduction

Solid-state chemistry has long facilitated the discovery of materials with a range of functional properties [1]. As our understanding of the underlying chemistry develops, our ability to intelligently design systems likely to host desirable properties improves. These improvements have allowed us to synthesise and characterise novel materials capable of improving energy storage [2, 3], data storage [4], memory [5], and many, many more such avenues. In this thesis, we target magnetic solid-state materials, where their magnetic properties are derived from the presence of unpaired electrons, which give rise to the magnetic moment [6]. Similarly to how lodestone was once used to make compasses [7], modern magnetic materials have become more complex than ever before, with some materials theorised to host magnetic states that were never previously observed in a material setting [8]. Such states highlight the new quantum age of materials research, with some researchers striving towards the synthesis of materials which may facilitate our jump into the quantum computational world. In many cases, these "quantum" materials, where classical mechanics fails to describe their electronic/magnetic properties, hinge upon the presence of exotic magnetic phenomena brought about through many intriguing routes discussed in this thesis. Some of these exotic phenomena may be described by topological magnon bands, superconductivity, Dirac band splitting and the key topic of interest within this thesis, the quantum spin liquid.

In the materials we are interested in, magnetism arises due to magnetic atoms containing unpaired electrons, while unpaired electrons have qualities which allow them to behave analogously to a magnetic dipole, or moment [6]. In a material, magnetic moments exist throughout a structure in a periodic array, in these cases, magnetic moments may interact with each other, giving rise to collective effects like ferromagnetism, which is a state of magnetic order, giving rise to the permanent field observed on a bar magnet for example [6, 7]. Ferromagnetism describes the long-range order adopted by neighbouring magnetic moments aligning in parallel; this may lead to permanent magnetisation and is what made the original magnet lodestone magnetic, as the aligned moments produce a cumulative moment about the bulk material similar to Figure 1.5. In the opposite case, moments may align antiparallel, known as antiferromagnetic ordering, where the net moment of the material becomes zero. In some cases, these long-range ordered ground states may be suppressed by the presence of competing exchange interactions, generating exotic magnetic states [6]. One of these exotic states is the quantum spin liquid, this state is characterised by magnetic moments eluding long-range magnetic order, instead remaining dynamic down to the thermal limit [8, 9]. These exotic magnetic states are expected to assist us in moving into the future of quantum technologies as these spin dynamic states may be utilised in the generation of qubits or as electronically spin-switchable spintronics [8, 10, 11].

The research and discovery of these quantum materials is non-trivial, and our abilities to unambiguously characterise such complex magnetic states of matter remains an obstacle to discovering materials suitable for applications in quantum technologies [8]. In Chapter 3, we introduce the copper carbonate kagome-containing metal-organic framework (MOF) family, these systems host similar exchange pathways to A-type antiferromagnetic perovskites where both ferromagnetic and antiferromagnetic exchange coupling propagates two different exchange pathways simultaneously, due to inequivalent exchange pathways.

This gives us an indication that MOF systems hosting this exchange may be studied for magnetism approaching the two-dimensional limit as exchange can be weakened or removed entirely in one axis [12]. In Chapter 4, through alterations to the MOF structures studied in Chapter 3, we aimed to eliminate the antiferromagnetic exchange pathway, thus isolating quasi-two-dimensional ferromagnetic layers within a three-dimensional material, as the ferromagnetic kagome poses an interesting model for study. In Chapter 5 we study a material hosting an unconventional magnetic ground state, where competing exchange interactions prevent the adoption of long-range magnetic order. We therefore aim to study this system as a promising quantum spin liquid candidate, examining whether the low-temperature magnetism matches the behaviours expected for such a system. A rigorous study of these materials by X-ray and neutron diffraction techniques allowed for our unambiguous structural determination, while magnetic susceptibility, heat capacity, neutron diffraction and muon spin relaxation spectroscopy allow us to begin characterising the unconventional magnetic ground states therein.

1.1 Materials, Magnetism and Magnetic Frustration

1.1.1 Metal-Organic Frameworks

In recent decades, MOFs have been gaining increasing attention for the study of tailored properties and varied functionalities [13]. MOFs are the result of binding metal nodes to organic ligands to form extended networks with with some of the ligands used in this thesis illustrated in Figure 1.1. Synthesis may be approached by microwave [14], electrochemical [15], solvothermal [16], mechanochemical [17] and more, all of which have benefits and drawbacks for MOF formation, it is therefore important to select the right method for the material, the levels of crystallinity and purity desired [18]. The broad range of synthetic methods and reagents has led to the exploration of MOFs across a range of fields including but not limited to; catalysis [19, 20], sensing [21, 22], drug delivery [23], electronics [24] and key to this thesis the study of magnetism [25]. The modularity of MOFs, where

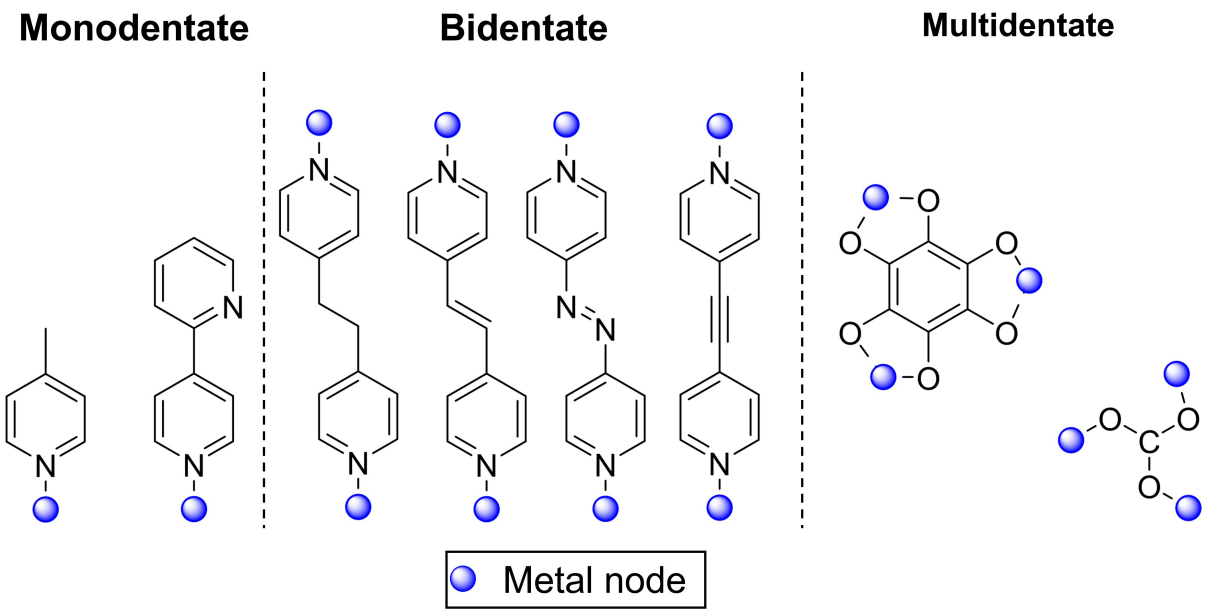


Figure 1.1: Examples of organic ligands, monodentate ligands have one metal binding site, bidentate have two and multidentate may have three or more. These ligands were used throughout this thesis in the synthesis of magnetic MOFs.

ligands and metals can be viewed as building blocks in larger-scale structures, allowing for substitutions of these components for those more fit for purpose. For example, MOFs designed for catalysis can be optimised toward maximum effective surface area by varying the ligands present, while simultaneously ensuring that the correct functional groups and pore sizes are maintained [26]. Due to this freedom, MOFs have become one of the dominant classes of materials in studying the functional properties of materials in recent years [18]. As mentioned, this thesis focusses on the use of MOFs for the study of magnetism, where we can synthesise several related MOFs sharing a magnetic network as a result of their modular nature and the ability to substitute ligands with similar binding modes, which allows us to study the effects of the nonmagnetic components on the magnetic behaviour of the material.

1.1.2 The Origin of Atomic Magnetism

In classical physics when an electrical charge is in motion, a magnetic field is generated. This phenomenon is best described in the study of electromagnetism, where the movement

of electrons, or current, through a wire generates an electromagnetic field. Electrons are negatively charged fundamental particles which have an associated magnetic moment generated by "spin" and orbital angular momentum. The classical model of electrons, although useful, does not paint the full picture; instead, in modern physics, we understand electrons using both classical and quantum mechanical approaches, as classical mechanics fails to fully describe the reality of the subatomic landscape. With the orbitals of atoms better described as areas in which an electron is statistically likely to exist at all times, uncertainty over its precise position is present. In fact, because of the wave-particle duality of matter, these electron orbitals may be described as standing waves, surrounding the nucleus as a discrete energy level. In the case of the electron, spin is not literal; instead, it describes the intrinsic spin angular momentum which we observe through experiments such as the Stern-Gerlach experiment. In this experiment, vaporised silver, possessing one unpaired 5s orbital electron, is fired through an inhomogeneous field. Randomly orientated unpaired electrons entering the applied field then align parallel or antiparallel to the field direction, depending upon which is energetically favourable dependent upon the original orientation of said unpaired electron. This results in the observation of two discrete positions at the detector corresponding to the assigned spin quantum numbers $s = \frac{1}{2}$ and $-\frac{1}{2}$ [27]. Experiments to discover the quantum mechanical properties of electrons involve a more rigorous mathematical approach. Specifically, three quantum numbers describing the electron are derived from the Schrodinger equation, which describes the behaviour of quantum particles in a given quantum system. The solution for this equation is given by Equation 1.1,

$$H\psi(\mathbf{r}) = E\psi(\mathbf{r}). \tag{1.1}$$

Where H represents the total energy of the system, $\psi(\mathbf{r})$ is the wave function and E is the energy eigenvalue associated with the given wave function. In solving this equation for a given quantum particle we obtain three quantum numbers; n, the principal quantum number; l, the azimuthal quantum number; m_l, the magnetic quantum number, with the spin quantum number m_s emerging as a consequence of the other quantum numbers. The

extraction of these quantum numbers allow us to understand the quantum mechanical view of energy level occupation by electrons, which has long been understood through classical means such as the orbital shells proposed by Niels Bohr [28].

From a materials perspective, atoms within a system may possess unpaired electrons and therefore magnetic moments, materials made up of these atoms then host a range of magnetic behaviours depending on the local environment and exchange interactions. In the case of silver, used in the Stern-Gerlach experiment, an unpaired electron resides within the 5s orbital, the moment of which is free to interact with an external field much like how a bar magnet would interact with an external field. Silver, [Kr] $4d^{10}$ $5s^1$, is a paramagnetic material, meaning that the unpaired electrons in its structure are attracted to an applied field, but maintain no permanent magnetisation when this field is removed as the s shells are not within range to interact with nearest neighbours. Zinc, [Ar] $3d^{10}$ $4s^2$, is a diamagnetic material, meaning that all electrons are paired and the net moment is zero. Here the response to an external magnetic field is resisted by an induced current in the material, leading to a magnetic response suggesting repulsion of the applied field direction. In transition metal species things become more complex. Before we discuss the role of electrons in the crystal field we must first address the important ways in which we quantify electrons, as these provide us with the tools to quantify collective electron properties such as magnetic order.

1.1.3 Properties of the Magnetic Moment

As we have touched upon, electrons can be considered magnetic moments, with total spin S, and total orbital angular momentum, L giving rise to the total moment. The motion of electrons within an atom may be described using L, which is related to the intrinsic spin angular momentum (μ) through the proportional relationship to a gyromagnetic ratio γ given by Equation 1.2:

$$\mu = \gamma L. \tag{1.2}$$

For a specific case such as an electron about a hydrogen nucleus, μ may be described by Equation 1.3:

$$\mu = -\frac{e\hbar}{2m_e} = -\mu_{\mathrm{B}}. \tag{1.3}$$

Here, e is the charge of an electron, $\hbar$ is the reduced Plancks constant, m_e is the mass of the electron and μ_{B} is the Bohr magneton with a value of $9.274{\times}10^{-24}$ J T^{-1}. Throughout this thesis μ_{B} is a unit used for the spin orbital angular momentum, with the expected value of a $S = \frac{1}{2}$ system being 1.73 μ_{B}. The spin and orbital angular momentum values s and l for a single electron can be described by Equations 1.4 and 1.5:

$$s = \sqrt{s(s+1)}\hbar \tag{1.4}$$

and

$$l = \sqrt{l(l+1)}\hbar. \tag{1.5}$$

Here s and l correspond to the respective quantum numbers. We are aware that spin may take two values, either $s = \frac{1}{2}$ or $s = -\frac{1}{2}$, while l may possess an integer value corresponding to the electronic orbital it describes. The sum of both orbital angular momentum and spin angular momentum provide us with the total angular momentum, J, the total moment then, is dictated by the proportions imparted by both S and L. The value for the effective moment (μ_{eff}) can then be understood in terms of J:

$$\mu_{\mathrm{eff}} = g_J\sqrt{J(J+1)}\mu_B. \tag{1.6}$$

Where g_j is the Lande g-factor defining an electron with spin and orbital angular momenta. Through these mathematical relationships between quantum numbers and electronic properties, we are able to consider the Pauli exclusion principle. This states that two or more particles sharing a half integer spin cannot occupy the same quantum state, which is where m_s is derived. For electrons, this means that no two electrons may share all four associated quantum numbers, explaining why electrons pair in their respective

orbitals with equal and opposite spin, which we will cover later [29].

1.1.4 Crystal Field Splitting and Jahn-Teller Distortion

In 1909, we considered electrons as separate entities to atoms, expecting them to exist near a positively charged nucleus to balance charge, the plum pudding model [30]. Since then, our understanding of the electron has improved, from the saturnian orbital model posed by Hantaro Nagaoka [31], to Niels Bohr's semi-classical model [28], and the modern quantum mechanical view of electron shells and standing waves. These shells are capable of holding a varying numbers of electrons defined by the Pauli exclusion principle. It is this exclusion principle that explains why electrons possessing equal and opposite spin are able to pair in the same energy levels. These energy levels are described by orbitals, the physical limits about a nucleus in which an electron may exist at any time [32]. Here, a range of orbital shells may host electrons providing the Pauli exclusion principle is satisfied and therefore we observe discrete orbital shells. For example, the s, p, and d shells possessed by the first row transition metals, s orbitals may contain two electrons, p orbitals six and d orbitals ten split equally between the orbital projections illustrated in Figure 1.2. In the transition metals, outer orbital electrons reside within the d-orbitals, these orbitals are long reaching and capable of interacting with their surroundings [1]. If one considers a single ion of Cu^{2+} possessing 9 d-electrons, the energy levels of the occupied d-shells are equivalent in energy. When this free ion is bound by coordinating ligands in an octahedral structure, the degenerate energy levels of the d-orbitals are split by the octahedral crystal field as in this case the bonding orbitals (d_{z^2} and $d_{x^2-y^2}$) become higher energy due to the repulsion of the ligand field and electron density along the axes. The t_{2g} level hosts the d_{xy}, d_{xz} and d_{yz} orbitals, while the higher energy e_g level contains the d_{z^2} and $d_{x^2-y^2}$ orbitals. Crystal field splitting is further complicated in d^9, Cu^{2+}, which may experience Jahn-Teller distortion (Figure 1.3).

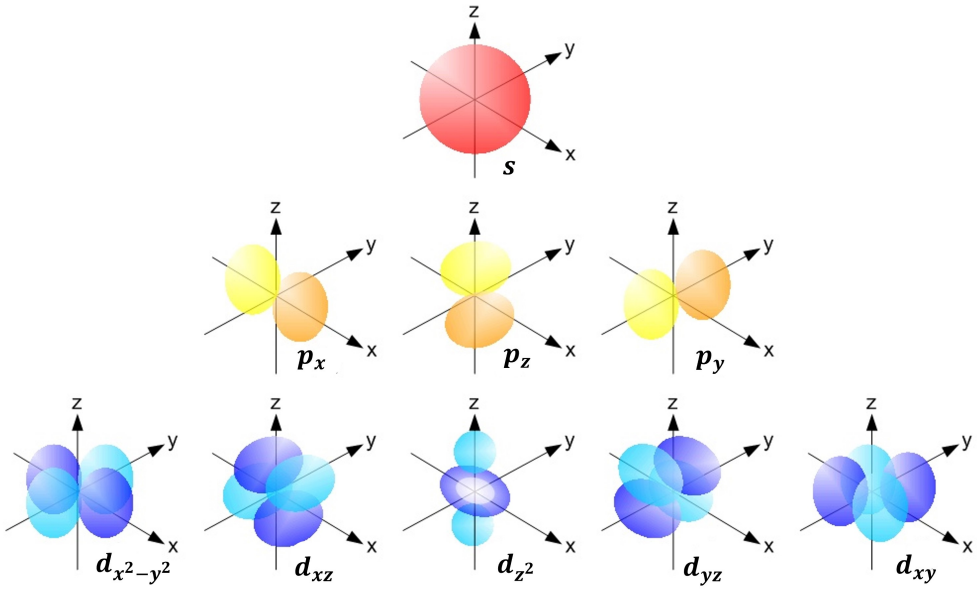


Figure 1.2: The S shell is a three-dimensional sphere equidistant in all axes containing two electrons, the p shells are spit into three, specifically propagating the x, y and z axis, each containing two electrons. Finally the d shells occupy five discrete conformations containing two electrons each, image edited from Libre texts [33].

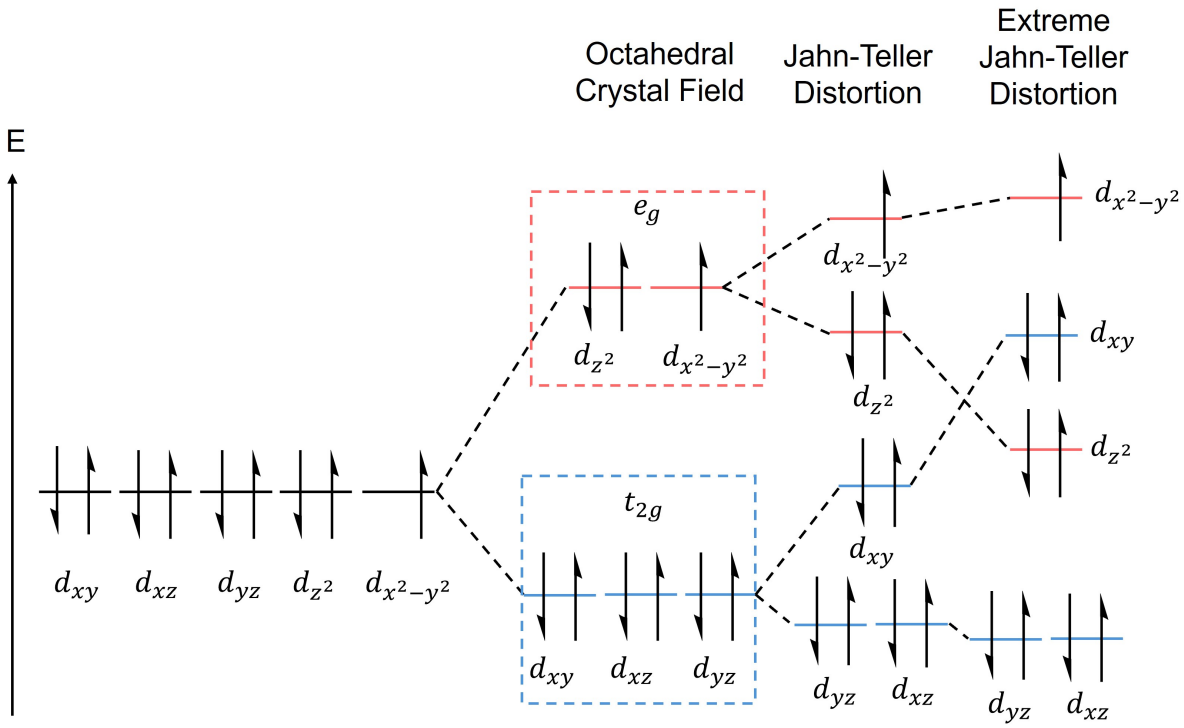


Figure 1.3: The six d-orbitals of d^9, Cu^{2+}, in the presence of an octahedral crystal field these six degenerate energy levels are split into the t_{2g} and e_g, where the higher e_g energy levels align with octahedral bonding geometries. These may be split further by Jahn-Teller distortion, where elongated bonds in one axis create an energy gap splitting the e_g level further, into its d_{z^2} and $d_{x^2-y^2}$ components. In extreme cases, the axial bond may elongate beyond bonding range, leading to an effective square planar geometry, in these cases the orbitals containing a z component decrease in energy.

This effect arises in d^9 copper because a single unpaired electron in the e_g level may lie directly in line with equatorial bonds, therefore bond elongation directly affects the electron density and thus the energy gap, splitting e_g. To approach stability, orbitals with z character reduce in energy in line with elongation, while those with x/y character increase in energy as they overlap more with the shorter bonding orbitals. The Jahn-Teller effect dictates the crystal field environment in cases such as in Cu^{2+} where a single unpaired electron occupies the e_g orbitals. Additionally, in some extreme cases axial bonds may elongate so much that the ligands are no longer in bonding range, resulting in the effective geometry of the system becoming square planar. In these cases, the higher equatorial electron density will cause the $d_{x^2-y^2}$ energy level to increase while the d_{z^2} may drop lower in energy than even the d_{yz}. In Chapters 3 and 4 we see extended solids featuring cooperative Jahn-Teller distortion, where the direction of distortion is ordered throughout the material. In Chapter 5 we see a MOF in an effective square planar geometry which may be stabilised by extreme Jahn-Teller distortion.

1.1.5 Magnetic Order in Transition Metal Systems

Now that we have considered how electrons order in an octahedral crystal field we may begin to discuss the magnetic properties of transition metal materials. The thing that distinguishes a magnetically ordered material from a para or diamagnetic material is the ability for it to undergo spontaneous magnetisation. This is made possible by the interactions of neighbouring magnetic moments throughout a material. Transition metals are exceptionally good at facilitating interactions between neighbouring magnetic moments as the unpaired electrons reside within the outermost d-orbitals. We see this in the iron oxide material lodestone, where the magnetic moments within interact and order permanently, magnetising the material. The mechanism for exchange in lodestone is double exchange, which is mediated by exchanging metal centres with varying oxidation states. The mechanism of magnetic exchange between two magnetic atoms may also be through superexchange, illustrated in Figure 1.4. Here, antiferromagnetic exchange cou-

pling occurs when the virtual electron transfer is between half-filled overlapping orbitals, i.e $M-L-M$ where all orbitals are half filled (180°). Interactions are ferromagnetic when virtual electron transfer occurs between a half-filled and empty shell, i.e $M-L_1-L_2-M$ where $L_1/2$ represent two p-orbitals of the ligand which are filled or half-filled (90°). Magnetic superexchange is one mechanism which may facilitate the permanent magnetisation of some materials. In cases where a material is magnetised by an external field, moments align with that field. The superexchange interactions between neighbouring moments then stabilise the ordered state much like two bar magnets in parallel stick to each other in alignment. In other cases, materials may become spontaneously magnetised at a critical temperature, as moments adopt an energy saving ordered state [6]. Importantly, spontaneous magnetisation occurs due to the nature and strength of exchange interactions present. In the specific example of iron oxide it behaves as a ferromagnetic material, meaning the internal magnetic moments align in parallel. As discussed, ferromagnetically ordered materials are magnetised, with the bulk magnetic property of the ordered material dictated by the orientation of the locally ordered moments, hence an iron oxide bar magnet has a permanent north and south pole. Another type of magnetic order we may observe is antiferromagnetic order, in this case magnetic moments align anti-parallel to their exchange partner, leading to a net cancellation of the magnetic moment of the material, as paired electrons do not possess an effective magnetic moment. The magnetically ordered states: ferromagnetic, antiferromagnetic and paramagnetic can be defined by the motifs illustrated in Figure 1.5. As stated, magnetically ordered materials hosting magnetic superexchange may undergo a spontaneous transition to magnetic order at a critical temperature. For ferromagnetic materials this is the Curie temperature (T_C) and for antiferromagnetic materials this is the Néel temperature (T_N). These come from the Curie-Weiss law, which describes the relationship between the magnetic susceptibility, χ, of a magnet as a function of the temperature. At high temperatures, the thermal energy is larger than the energy scale of the interactions between the moments, so they are randomly oriented. At a critical temperature, the interactions become stronger than the

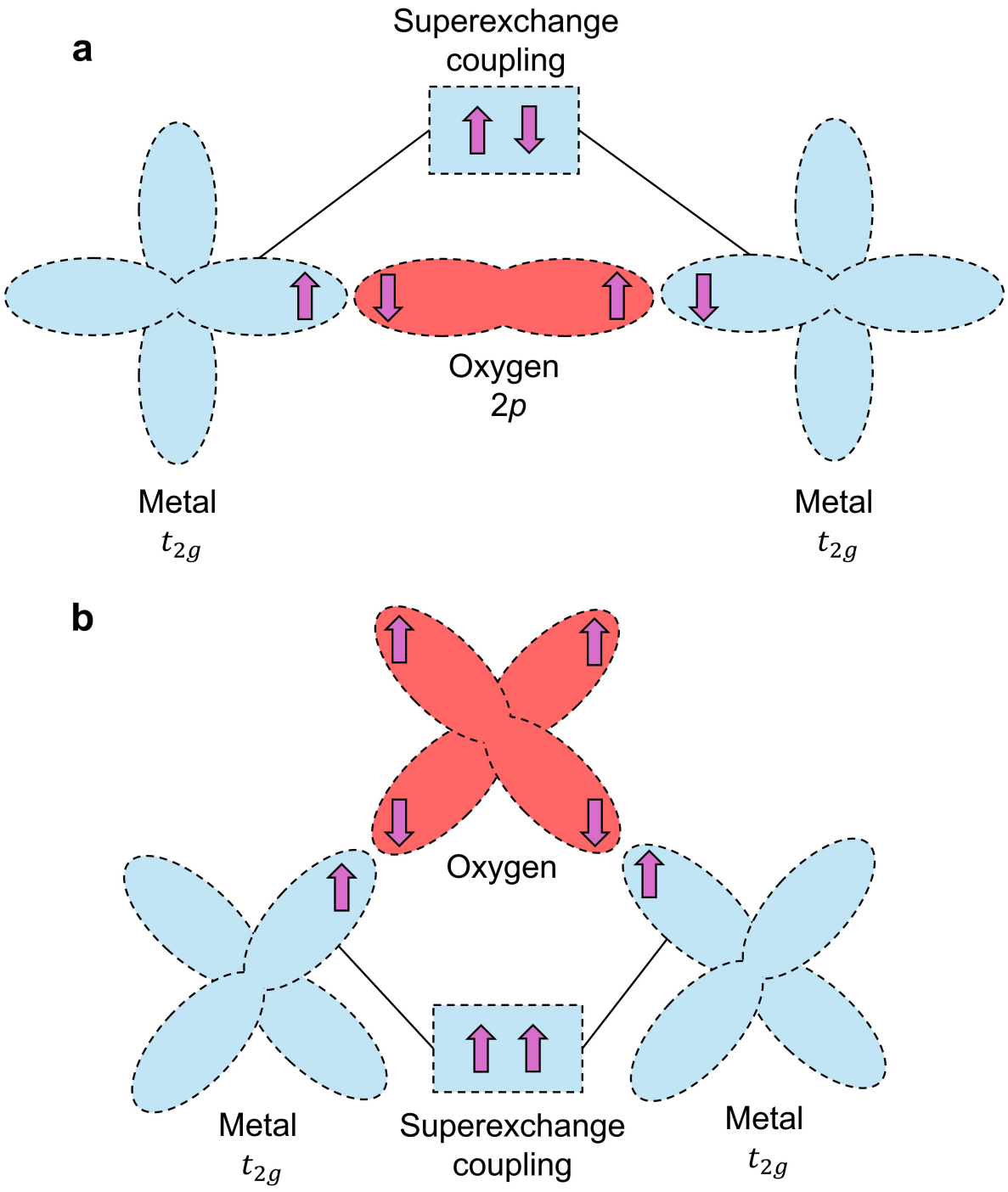


Figure 1.4: Typical ferromagnetic and antiferromagnetic superexchange pathways. a) Here 180° superexchange leads to antiferromagnetic exchange coupling between neighbouring magnetic metal sites. b) Here 90° superexchange leads to ferromagnetic exchange coupling between neighbouring magnetic metal sites.

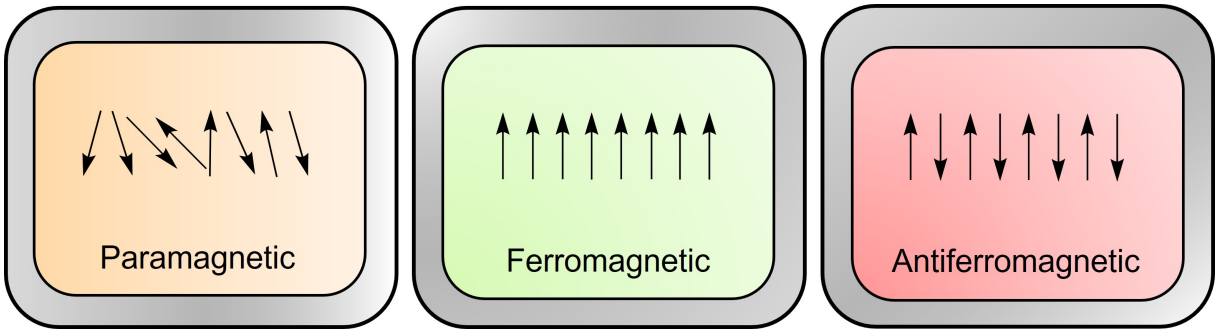


Figure 1.5: Representations of the arrangements of magnetic moments in the paramagnetic, ferromagnetic and antiferromagnetic state.

kinetic energy and so the system may spontaneously adopt a long range ordered state. But what happens in cases where this spontaneous transition to a magnetically ordered ground state is prevented by the geometric arrangement of the magnetic moments held within?

1.1.6 Magnetic Frustration

Magnetic frustration arises in systems where competing exchange interactions exist. In such cases, exotic magnetic ground states may emerge, hosting interesting magnetic properties some examples of which are discussed later. To generate magnetic frustration one simply has to introduce competing exchange pathways. A common method of doing this is through geometric frustration, where magnetic moments are positioned in such a way that long-range order may not exist alongside such competing interactions. Examples of this include the triangular lattice where antiferromagnetically couple magnetic moments exist upon the vertices of a triangle. Here, long-range magnetic order is prevented as each magnetic moment cannot simultaneously satisfy both neighbouring moments. Another example is a square lattice where nearest and next nearest neighbour exchange interactions compete if their exchange strengths are of similar in magnitude. The geometry we focus on in this Thesis is the kagome arrangement, featuring corner-sharing triangles, geometric magnetic frustration is expected to lead to a suppression of long-range antiferromagnetic order.

1.1.7 The Quantum Spin Liquid and the Resonating Valence Bond Model

In cases where frustrated geometries and antiferromagnetic exchange coupling are present order may be suppressed, leading to some unconventional magnetic ground states, examples of these are spin glass [34], spin ice [35] and the quantum spin liquid. Of these magnetic states, the quantum spin liquid remains an elusive synthetic target, with theory suggesting that this state may emerge in the kagome antiferromagnet model [36]. The quantum spin liquid is thought to be a non-magnetic state characterised by a lack of long-range magnetic order down to 0 K. One way to visualise such a ground state is through the gapped resonating valence bond (RVB) model, where nearest neighbour antiferromagnetically coupled spin dimers resonate within a structure, this is illustrated on a kagome lattice in Figure 1.6. For us to begin the process of chemically designing a system likely

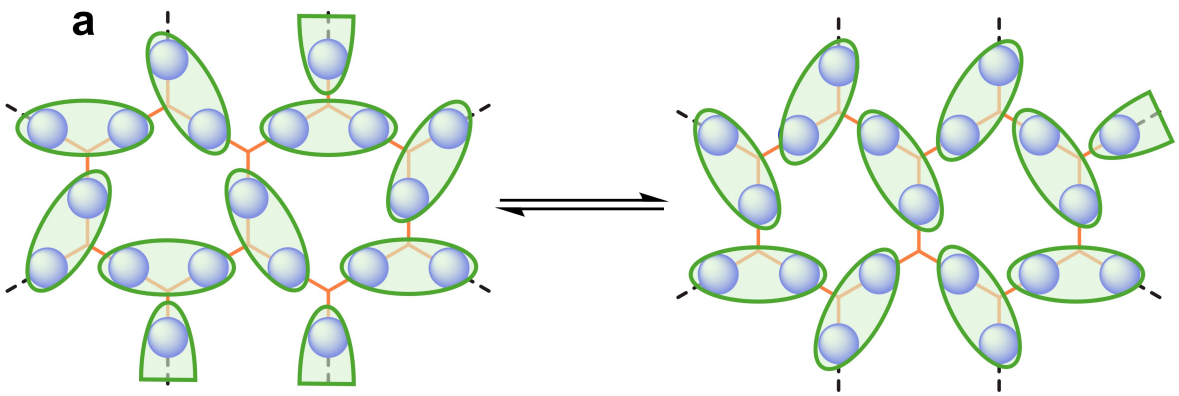


Figure 1.6: An illustration of the resonating valence bond model upon a kagome lattice, featuring nearest neighbour exchange coupling only, here we see how resonating antiferromagnetic dimers would stabilise a dynamic non-magnetic ground state. Blue circles represent a metal atom, orange lines are bonds and green highlights indicate antiferromagnetic dimer couples.

to exhibit such behaviours we must first consider the properties expected to induce such a state. We have covered geometric frustration, but additionally to this it is important to use low-spin ($S = \frac{1}{2}$) systems as these host strong quantum effects, which are believed to eliminate the energy barrier which prevents magnetic moments from fluctuating even down to 0 K [37, 38]. Another property expected to increase frustration and lead to the

emergence of a RVB-like state is to reduce dimensionality. A reduction in dimensionality increases the impact of quantum fluctuations, which suppress long-range order, while also reducing the number of potential magnetic exchange pathways. With this, we begin to understand the synthetic targets chosen for study in this Thesis. In all three chapters, we use $S = \frac{1}{2}$, Cu^{2+} as our magnetic ion in a kagome arrangement, bound by varying organic ligands in the hopes of realising systems hosting magnetic ground states of interest.

1.1.8 Ferromagnetic Kagome Containing Magnets and Approaching the Two Dimensional Limit

The kagome is not simply a geometry suitable for hosting frustration in the presence of antiferromagnetic exchange coupling, in fact, magnetic moments arranged in a kagome are also interesting for the study of phenomena arising in ferromagnetic systems. The physics currently studied within ferromagnetic kagome-containing systems ranges; however, an important consideration is that many of the interesting phenomena arise in systems where the kagome is magnetically isolated approaching two-dimensionality [39, 40, 41, 42].

Quasi-two dimensional, describes three-dimensional magnets where the magnetic exchange interactions within are inequivalent in three-dimensions. For instance a layered material where the magnetic exchange interactions between layers are negligible, and so experimentally, the material will have properties synonymous with two-dimensional magnetism. In such systems, the magnetic order observed is not necessarily the key finding, two-dimensional magnets are expected to expand on our potential to experimentally realise novel phases of matter such as the quantum spin liquid [43], unconventional superconductivity and more [44]. The material realisations of two-dimensional magnets are part of an emerging field, with CrI_3 (Figure 1.7) discovered to host ferromagnetism in 2018 [45], van der waals materials are becoming widely studied [46, 47]. Often, the interesting properties originating from ferromagnetic kagome contaning materials are from electronic properties, one such property is the Hall effect characterised by the generation



Figure 1.7: Crystal structure of CrI_3 where two-dimesnisonal magnetic layers are weakly layered shown by the black arrow, with no covalent interactions between, CrI_3 was discovered to host ferromagetic exchange coupling in two-dimensions only.

of an electric field perpendicular to an applied field. The anomalous Hall effect remains incompletely understood, and therefore the study of this phenomenon in a material setting aids in the full understanding of the phenomenon. This characteristic is particularly observable in the kagome arrangement as the magnetisation has been found to vary significantly between fields applied in the ab-plane and the c-plane approaching the Curie temperature. This means that the anomolaous hall effect can be directly observed as a function of applied field application. This characteristic of the kagome make it an interesting material for study as the observation of the anomalous Hall effect may be observed toward the kagome's crystallographic easy axis meaning that the onset of this effect can be directly controlled aiding in its understanding [39]. Another interesting observation in the ferromagnetic kagome is spin wave transport, hoped to advance the transmission of information, spins may be compared to binary information which, when flipped create a ripple or spin wave which travels throughout the material [40]. This is an effect which is studied in the ferromagnetic kagome again, due to the prominent easy axis magnetisation facilitated by asymmetric exchange strengths in three dimensions. It is clear from these examples that the kagome arrangement hosts interesting electronic phenomena due to the two dimensional layers and so the production of more ferromagnetic kagome containing systems like those studied in both Chapters 3 and 4 allow for these systems to be reproduced by groups specialising in the electronic characterisation of phenomena hoped to advance some highly novel technologies susch as quantum computing.

Ultimately, ferromagnetic kagome containing materials are highly exciting as they provide access to the study of characteristics previously unexplored in a materials setting; two-dimensional phase transitions [48], electronic excitations discussed above [39, 40], field and temperature dependent magnetic phenomena and a broad range of potential applications make up the bulk of interest in this class of materials and this is before we consider the two-dimensional kagome [49]. A further reason the ferromagnetic kagome is such an exciting model for two-dimensional magnetic study is that the arrangement of atoms also naturally support Dirac points, flat bands and Van Hove singularities, as such many topological, correlated phases may be realised in two-dimensional kagome magnets [39]. Within Chapter 4 we explore kagome-containing MOFs expected to host quasi-two dimensional magnetism and explore the magnetic properties of the systems as a foundation for groups who may wish to study the in-depth electronic characteristics of such kagome containing ferromagnets.

1.2 Magnetic materials of interest

Having outlined much of the relevant theory behind magnetism and the generation of magnetic frustration in materials, we focus our attention to some examples in the literature, many of which formed key foundations for the ideas and experiments within this Thesis. As discussed, the kagome lattice is a geometry sought after in solid-state physics research for the study of complex magnetic ground states such as the QSL, as corner-sharing triangles are expected to generate magnetic frustration when antiferromagnetic exchange interactions are present [8]. The purpose of the following section is to explore the literature on magnetic kagome-containing materials, outlining their relevance to the synthetic targets, characterisation techniques and general aims of this Thesis. While also focussing on the limitations of our characterisation techniques when it comes to the study of states such as the quantum spin liquid.

1.2.1 Inorganic Realisations of Kagome Magnets

Some of the first discovered materials hosting a kagome arrangement of magnetically active atoms were minerals. A few minerals we will cover here are; herbertsmithite ($Cu_3Zn(OH)_6Cl_2$), volborthite ($Cu_3V_2O_7(OH)_2{\cdot}2H_2O$) and barlowite ($Cu(OH)_6FBr$) all of which possess a kagome arrangement with the magnetism studied in each case. First, herbertsmithite (Figure 1.8) hosts copper hydroxide based kagome layers bridged by inter-plane zinc atoms. Multiple reports find the dominant exchange interactions in herbert-

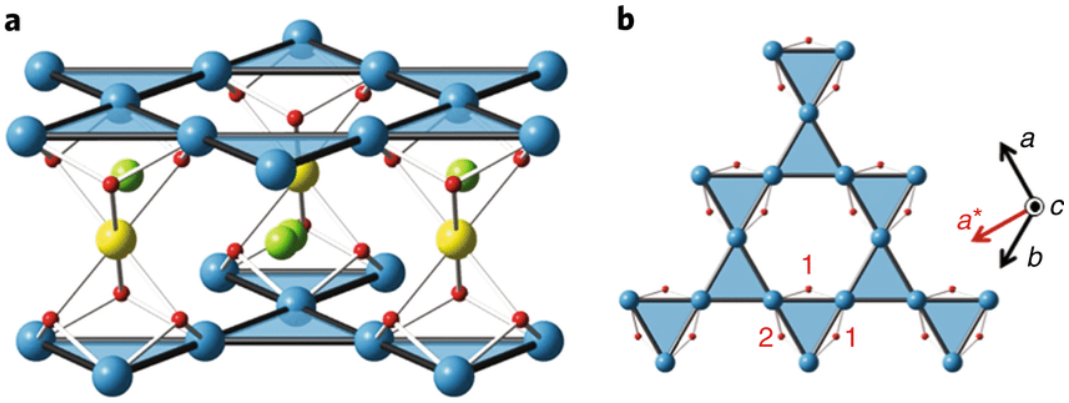


Figure 1.8: Reported structural models of herbertsmithite by Khuntia *et al* [50]. a) Here we observe the copper (blue) kagome bridged by oxygen (red) and zinc (yellow) presenting magnetically isolated kagome layers. b) Here we see a single layers of the kagome, showing the ideal positions of oxygen to facilitate the nearest neighbour exchange interactions likley to induce a QSL like state.

smithite are antiferromagnetic in nature [51, 52, 53]. The onset of long-range magnetic order is also found to be suppressed below their measurements taken at 50 mK in multiple magnetic susceptibility, heat capacity, and neutron diffraction studies, which made herbertsmithite a material of interest in elucidating the QSL state [52, 53, 54]. Although in 2007, the relative strength and pathways of antiferromagnetic exchange interactions could not be derived from the data, the observation of a QSL hallmark was made through the use of spin-polarized inelastic neutron spectrometry, fractional $S = \frac{1}{2}$, excitations [53]. The fractionalisation of exications is a hallmark of unconventional magnetism, however these are challenging to probe [55], initially these were studied by Helton *et al* using models for triangular lattices, and so the conclusions drawn were based on assumptions

that these fractionalised excitations would also exist for a QSL ground state of a kagome antiferromagnet [53]. As shown in Figure 1.7, the ideal structure of herbertsmithite possesses magnetically isolated kagome layers, bound by non-magnetic zinc resulting in the perfect antiferromagnetically coupled moments within a frustrated geometry expected to host the QSL state [9]. However, in practice, it was discovered that magnetic site disorder characterised by partial substitution of non-magnetic zinc positions with magnetic copper (II) resulted in the breakdown of this ideal magnetically frustrated motif [56]. This magnetic site disorder presents a challenge as the introduction of magnetic exchange pathways between kagome layers reduces the magnetic frustration of the kagome lattice through the emergence of alternate exchange pathways, which then dominate the observed low-temperature magnetic regime [50, 57, 58, 59]. Taking into account the formula of herbertsmithite hosting magnetic site disorder, $Cu_{4-x}Zn_x(OH)_6Cl_2$, it has been shown that for values of $x \approx 1$, indications of a QSL-like state can be observed [60]. Even recently, in 2020, studies of herbertsmithite have shown the detrimental effects of magnetic site disorder in terms of measured length scales for exchange interactions [61]. At this point, we may consider magnetic site disorder to be one of the main barriers to examining QSL states in materials using inorganic systems. A second kagome-containing species previously studied is volborthite, featuring a copper (II) kagome lattice coordinated by pillaring V_2O_7. Volborthite showed promise experimentally, with strong dominant antiferromagnetic exchange interactions reported [62]. Unfortunately, volborthite suffered from a different barrier to accessing the antiferromagnetic kagome model, a structural transition. It was discovered that volborthite undergoes a structural transition below 155 K, transforming from the kagome-containing $C2/c$ or $C2/m$ space groups to a square lattice containing $I2/a$ or $P21/a$ space groups [54]. Although competing interactions on a square lattice may prove interesting in general, the study of the low-temperature magnetism of a kagome lattice was clearly not possible in volborthite [54]. Another compound of interest was barlowite, which also contained a copper kagome lattice this time separated by halides Br^- and F^- (Figure 1.9). Similarly to herbertsmithite however, barlowite

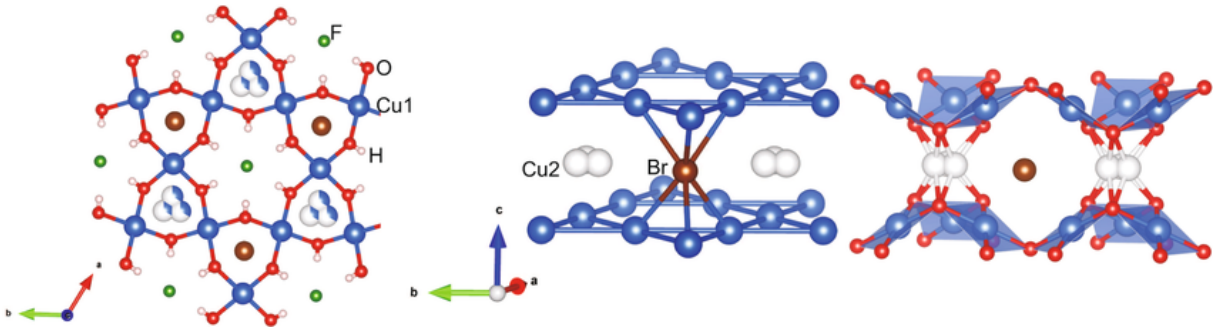


Figure 1.9: Reported structural models of barlowite by Ranjith *et al* [63]. (left) Here we see a single kagome layer supported by copper hydroxide bonding, with disordered copper and bromine occupying the interplane sites. (right) Here we see how the disordered copper and bromine bridge the gap between kagome layers.

also suffers from magnetic site disorder of the interlayer atomic positions, with disordered copper atoms occupying all inter-plane sites. Initial studies on the magnetic properties of barlowite found an ordering transition temperature T_N = 15 K [64], and dominant antiferromagnetic exchange coupling [65]. At this stage, it was becoming clear that if a QSL state was to be observed in an inorganic system, the obstacle of magnetic site disorder would need to be overcome. It was suggested through DFT calculations [66], that the disordered magnetic copper sites in barlowite may be filled instead with non-magnetic zinc ions, thus isolating magnetic copper kagome layers in a zinc doped barlowite species. A comprehensive muon study of Zn-barlowite for Zn substitutions of 0 - 0.99(1) %, marked a cornerstone in the realisation of a system hosting the kagome antiferromagnet model at low temperatures [67]. In this study, zinc composition was varied through the use of stoichiometric ratios of reagents, tracked via refinements of neutron powder diffraction data, which allowed the occupancies of these inter-plane positions to be modelled [67]. Similarly to the work carried out in Chapter 5, a temperature-dependent muon spin relaxation study confirmed that the relaxation rate as a function of time was not consistent with the onset of long-range magnetic order or a spin glass, and was instead consistent with the results reported for herbertsmithite in cases where inter-plane sites were largely occupied by non-magnetic atoms (Figure 1.10) [67]. Instead, a long plateau is observed in the muon spin relaxation rate, consistent with a system which is not in a long-range

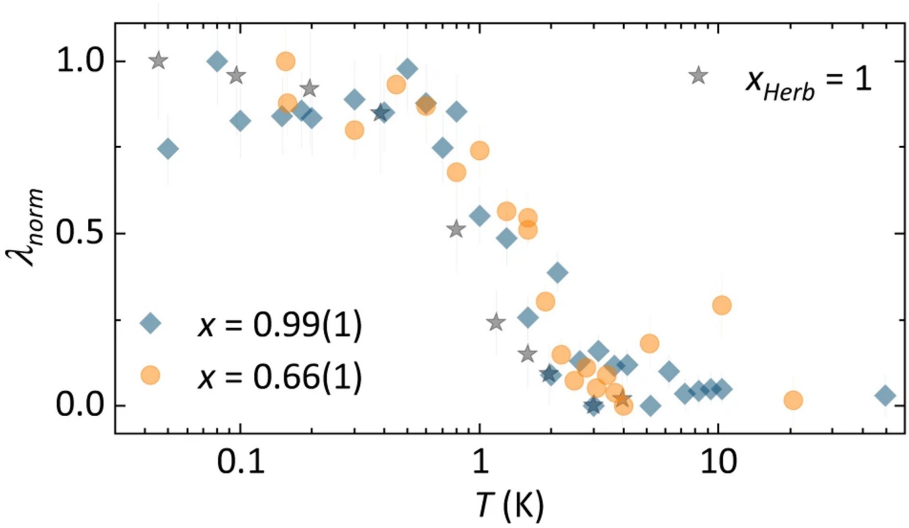


Figure 1.10: Muon spin relaxation data collected for two zinc substituted barlowite species reported by Tustain *et al* and herbertsmithite reported by Mendels *et al* [67, 60]. We see here that in all cases, a plateau persists below 1 K down to 50 mK, this plateau would not emerge in cases where a long-range ordered state exists.

ordered state in Zn-barlowite samples with $>$ 60 % zinc occupation of inter-plane sites. It was discussed here that these results may characterise the role of hydroxide and halides or the role of interlayer Cu^{2+} moments present in the structure [67]. Ultimately, this study indicated that the substitution of magnetically disordered sites with non-magnetic atoms was a promising route to bypass the barriers to QSL discovery posed by these disordered inorganic materials [67]. Although disorder remains a significant issue [68]. This study also marked the optimisation of years of study towards realising inorganic materials capable of consistently hosting such exotic magnetic ground states. This wealth of study naturally posed the question, can such exotic magnetic states be observed within other branches of chemistry, and if so, might these systems mitigate the chemical barriers associated with previously studied inorganic systems?

1.2.2 Kagome Containing Metal-Organic Magnets

With the foundations for the examination of complex magnetic ground states established through the extensive study of inorganic kagome-containing materials, the opportunity to seek such exotic states within other synthetic realisations presented itself. As discussed

MOFs are made up of metal nodes and organic ligands, with these forming extended networks, with functional properties spanning most fields of chemistry [18]. The incorporation of magnetic metal nodes in MOFs to form magnetic MOFs, or metal-organic magnets (MOMs), presents a wide landscape for the study of magnetic phenomena for several reasons. First, MOFs may be synthesised using a far wider range of organic ligands than the atomic coordinations observed in inorganic systems [69]. Second, MOFs containing the same magnetic atoms may be synthesised using different organic ligands, assuming similar coordination, ligand selection may alter the lattice parameters and unit cell while preserving the magnetic topology [70]. This is considered "tuning" of the framework, or synthetically optimising the structure towards desired magnetic phenomena, a practise used throughout this Thesis, and in the literature [71]. These attributes allow us to synthesise broad families of MOMs with related magnetic properties. Additionally, MOMs allow us to easily explore novel systems likely to share key structural and magnetic properties through the denticity of the ligand or the selection of the magnetic atom. Another key property of MOMs is the relatively weak magnetic superexchange, which often propagates longer organic ligands [25]. In some cases ligand selection may be used to suppress long-range order by reducing the effective magnetic dimensionality of the system [72, 73], also increasing the effect of quantum fluctuations [74], which are key theoretical routes to inducing a QSL state.

With these features in mind, we begin to see how effective MOMs may be in the synthetic design of new and exciting magnetic topologies such as the antiferromagnetic kagome. One of the first reported magnetic kagome-containing MOFs was Cu_2(pyrazine)$_2$(benzenedicarboxylate)$_2$)$_3$ in 2002, with magnetic analysis suggesting the presence of weak ferromagnetic exchange interactions [75]. In 2008, a similar kagome-containing MOF, Cu(1,3-*bdc*), was studied [76]. After the crystal structure was described by modelling single-crystal XRD data (Figure 1.11). Through the magnetic characterisation of Cu(1,3-*bdc*), it was discovered to host both dominant antiferromagnetic exchange interactions while showing signs

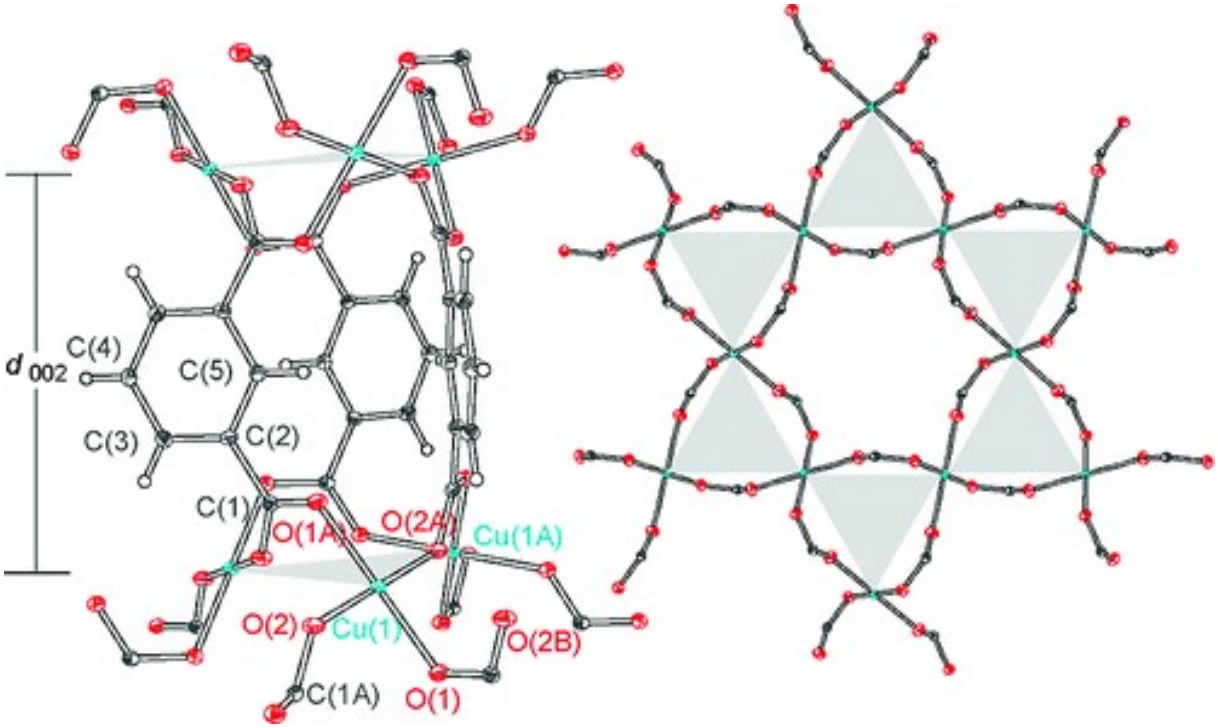


Figure 1.11: Reported structural models of Cu(1,3-*bdc*) showing how benzenedicarboxylate simultaneously forms the kagome layers and bridges the gap between them shown alongside [76].

of being a soft ferromagnet. [76]. To explain these seemingly conflicting data, Nytko *et al* proposed that antiferromagnetic exchange propagates within the kagome plane while ferromagnetic exchange interactions propagate between the kagome layers [76]. These assertions were supported by reports of Cu_2(*bdc*) dimers hosting ferromagnetic exchange coupling through a seven-atom pathway [77, 78]. This was later refuted in 2015, through the analysis of neutron scattering data, suggesting that exchange interactions were, in fact, ferromagnetic within the kagome plane and antiferromagnetic through the inter-plane seven-atom pathway [79]. From the example of Cu(1,3-*bdc*), two common themes emerge which repeat amongst other kagome-containing MOMs; first, the observation of two co-existent magnetic exchange pathways in and out of the kagome plane, and second, the mis-assignment of anti and ferromagnetic exchange components when neutron diffraction data is not available. The latter here highlights the strength of neutron diffraction methods we will discuss later, as these probe the magnetic exchange interactions throughout a magnetic crystalline network such as a kagome-containing MOM. One consequence

of the discussion of the ferromagnetic kagome layers in Cu(1,3-*bdc*) is that we can no longer expect to study the system as an antiferromagnetic kagome system likely to host a QSL state. However, this combination of features remains an exciting research avenue as topological magnon bands were found to arise in such systems [79]. Topological magnon bands are supported by the kagome as it hosts symmetry-protected band crossings, which retain their degeneracy in the presence of exchange interactions [80]. This highlights that kagome-containing MOMs, in general, are exciting systems for magnetic study, whether the kagome planes feature ferromagnetic or antiferromagnetic coupling.

In 2005, another interesting MOM was reported containing kagome layers of Co^{2+}, chelated by imidazole 4,5-dicarboxylic acid in the equatorial plane and 4,4'-bipyridine in the axial plane to afford a three-dimensional kagome-containing network [81]. This MOM of formula, $[Co_3$(imidazole 4,5-dicarboxylic acid$)_2$(4,4'-bipyridine$)_3]\cdot 6H_2O\cdot$DMF, (Co-*bipy*) features a near perfect kagome lattice with equatorial bond lengths of Co-O of 2.129 and 2.061 Å with Co-N bonds 2.130 Å [81], suggesting Jahn-Teller distortion of the $d_{x^2-y^2}$ orbital, which will also be a recurring theme in Jahn-Teller active kagome MOMs containing an octahedral binding motif [12, 82, 83, 84, 85, 86]. In addition to structural analysis, magnetic characterisation of Co-*bipy* was performed which suggested that the dominant exchange interactions between cobalt sites were antiferromagnetic in nature. These bulk magnetic results were also replicated in 2015 for the same system, finding similarly that dominant antiferromagnetic exchange coupling was present [87], however no further magnetic characterisation was undertaken. Interestingly, this system may provide an interesting avenue for study by neutron diffraction techniques to fully elucidate the magnetic exchange interactions present, similarly to Cu(1,3-*bdc*). More importantly, their findings suggest that the synthesis of a copper analogue may be a good candidate for the study of a $S = \frac{1}{2}$ antiferromagnetically coupled kagome network and, of course, the potential for this to host a QSL state [8, 25].

Another kagome-containing MOM reported in 2010 featured manganese oxide kagome layers, linked by benzene tricarboxylate to give the formula $[Mn_3(C_6H_3(COO)_3)_2]$, (Mn-*btc*). Magnetic analysis was performed for Mn-*btc*, where it was discovered to host dominant antiferromagnetic exchange interactions; however, no further evidence is provided for the exchange pathways these exchange interactions propagate [88]. It is highly unlikely that the antiferromagnetic exchange interactions suggested by the analysis of both Co-*bipy* and Mn-*btc* originate from one nearest-neighbour exchange pathway when considering the three-dimensional nature of the materials. Although many of these kagome-containing systems are unlikely to host a QSL state due to $S > \frac{1}{2}$ metals used, they highlight the diversity and depth for study into a class of material as specific as the kagome-containing MOM. These reports also highlight the benefits of utilising characterisation techniques such as neutron diffraction in the study of magnetic materials.

1.2.3 3D Copper Carbonate Kagome Containing Metal-Organic Magnets

At this stage, we have seen that three-dimensional kagome-containing MOMs are highly likely to host multiple routes for exchange coupling, and as such, the complexity of outlining their magnetic ground states increases. Here, we may ask the question, can three-dimensional magnetic exchange in a kagome-containing MOM be suppressed by the use of inter-plane ligands which are so long that they no longer host magnetic superexchange? Well, in 2009, a report on a Cu^{2+}, CO_3^{2-} kagome lattice layered upon relatively long, 1,2-bis(4-pyridyl)ethane, (*bpe*) ligands was published [85]. This marked the beginning of many research papers covering systems with the general formula $Cu_3(CO_3)_2(x)_3{\cdot}2ClO_4$, where x was a long ditopic ligand such as *bpe*, we will call this MOF-*bpe* (Figure 1.13). In this first report of MOF-*bpe*, the copper atoms within are in an octahedral geometry and as such, the bond lengths of Cu-O were found to be 1.949(4) and 2.763(5) Å, and Cu-N bonds, 1.987 Å, suggesting an extreme case of Jahn-Teller distortion, so extreme it appears as a tranformation of octahedral geometry to an effective square planar geometry

(Figure 1.12).

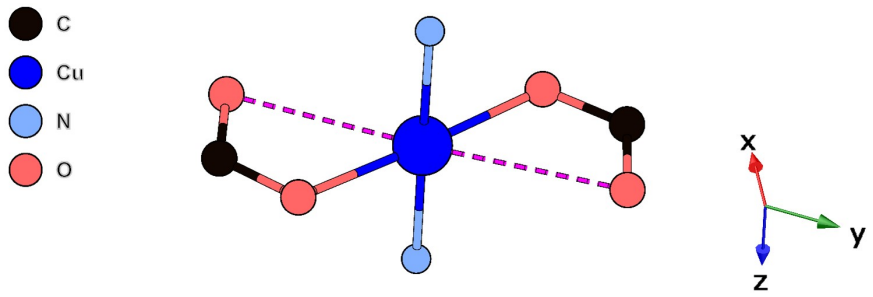


Figure 1.12: A section of MOF-*bpe* showing the Jahn-Teller distorted Cu-O bond shown as a dashed line, this distortion results in a "breathing" kagome lattice featuring inequivalent kagome triangles.

The magnetic study suggested weak antiferromagnetic exchange interactions were dominant but suggested that there may be competing ferro- and antiferromagnetic exchange interactions [85]. From these data, comparisons are made with the previously discussed system Cu(1,3-*bdc*) where antiferromagnetic exchange was thought to propagate the kagome planes and ferromagnetic exchange propagates between them [76, 85]. Their conclusions for MOF-*bpe* were that magnetic exchange occurs predominantly through the equatorial-axial Cu-O bonds, with one heavily Jahn-Teller distorted d_{z^2} orbital likely to facilitate far weaker exchange interactions potentially causing competition. The final conclusions of this research were that $Cu_3(CO_3)_2(bpe)_3{\cdot}2ClO_4$ hosted antiferromagnetically coupled kagome layers that were weakly ferromagnetically coupled through the coordinated ditopic *bpe* ligands. In 2014, a report of a related system of formula $Cu_3(CO_3)_2(bipyridylacetylene)_3{\cdot}2ClO_4$, MOF-*bpa* was made, the acetylene ligand is linear and rigid, unlike *bpe*, which was confirmed to eliminate the rotational disorder observed in the crystal structures reported for MOF-*bpe* [85, 86]. For MOF-*bpa* magnetic analysis suggested dominant in-plane ferromagnetic exchange interactions with their magnetic model opposing the prior literature. For MOF-*bpa*, it has been suggested that ferromagnetic kagome layers coupled antiferromagnetically to adjacent layers characterised the magnetic ground state. This was one of the first indications in the literature that the

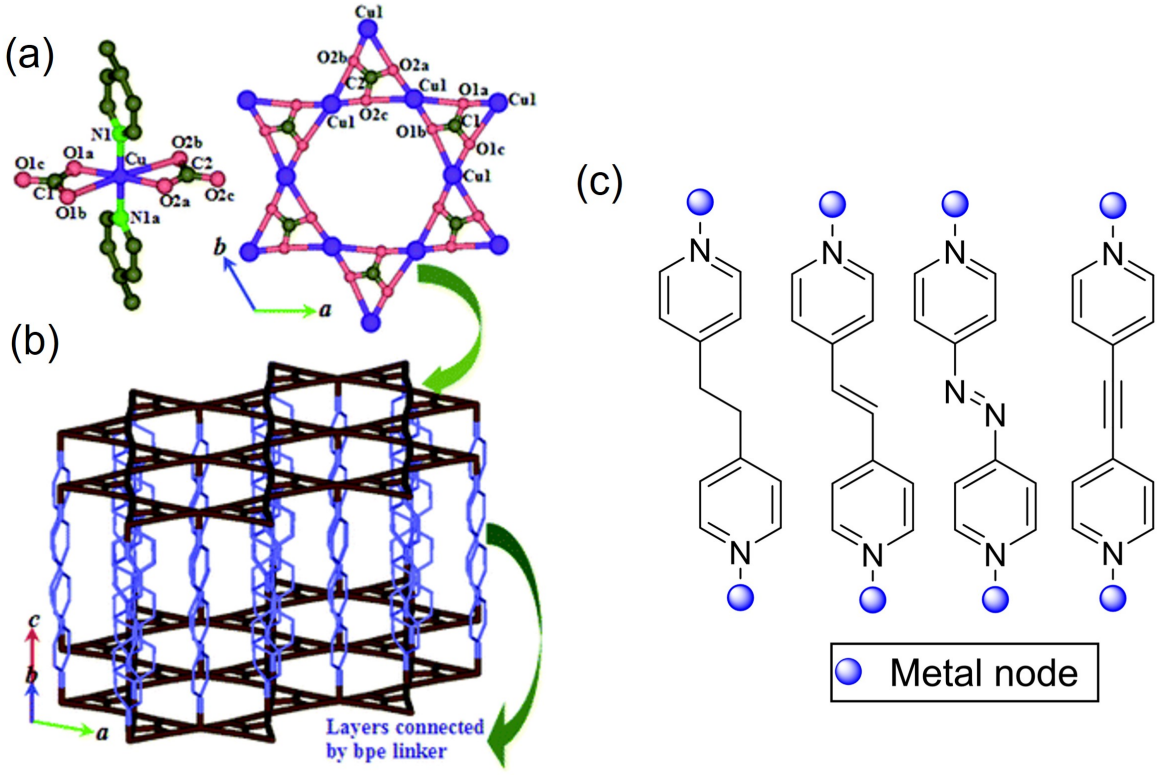


Figure 1.13: The reported crystal structure of $[Cu_3(CO_3)_2(bpe)_3]\cdot 2ClO_4$ by Kanoo *et al.* a) This octahedrally coordinated system features a copper carbonate kagome lattice with Jahn-Teller distorted Cu-O bond meaning that the Cu-O bonds are equatorial-axial in nature. b) The copper carbonate kagome layers are then coordinated by long, ditopic 1,2-bis(4-pyridyl)ethane ligands to afford a three-dimensional structure [85]. C) shows some ligands which are able to interchelate copper carbonate kagome layers (left to right) *bpe*, *bpy*, *azpy* and *bpa* discussed throughout.

selection of organic ligands in this family of MOMs may effect the magnetic ground state significantly and, as such, the in-depth study of MOF-*bpa* is the topic of discussion in Chapter 3.

In 2015, the experimental promise of antiferromagnetic copper carbonate kagome layers indicated by Kanoo *et al* had sparked interest in the further study of MOF-*bpe* by Ajeesh *et al* [82]. Here, a comparative study in which the pillaring ditopic *bpe* ligand was substituted for 1,2-bis(4-pyridyl)ethene (*bpy*) giving a formula, $Cu_3(CO_3)_2(bpy)_3{\cdot}2ClO_4$, (MOF-*bpy*). The synthesis of this similar system allowed them to explore the effects of this chemical change on the magnetic response, reiterating a key benefit of MOF chemistry [25]. For both MOF-*bpe* and MOF-*bpy*, magnetic measurements indicated the presence of dominant ferromagnetic exchange interactions, contrary to the findings of Kanoo *et al* [82, 85]. Despite similar data for MOF-*bpa* said to indicate the presence of ferromagnetic kagome layers a year prior, they instead claimed that ferromagnetic exchange interactions must be mediated by the *bpe* and *bpy* ligands as the 180° bonding geometries within kagome planes would favour antiferromagnetic exchange according to the Goodenough-Kanamori rule [89], which was again a reasonable conclusion at the time. Ultimately, the picture of antiferromagnetic kagome layers coordinated by ferromagnetically exchanging ditopic organic ligands remained the most up-to-date description of the magnetism within MOF-*bpe* and MOF-*bpy* while the opposite was believed to be the case for MOF-*bpa* highlighting the conflicts within the literature for this closely related family of MOMs. In 2020, the study of MOF-*bpe* was taken further, with specific heat capacity and neutron powder diffraction analysis of the system reported [84]. Once again, magnetic measurements were taken with findings consistent with Ajeesh *et al* [82, 84]. However, this study was the first to utilise neutron powder diffraction on a sample of MOF-*bpe*, from which they came to the conclusion that there was no evidence for long-range magnetic order down to 1.5 K, something that would be clearly indicated from these data. Instead, a magnetic phase diagram is constructed, asserting that at a critical field a short-range

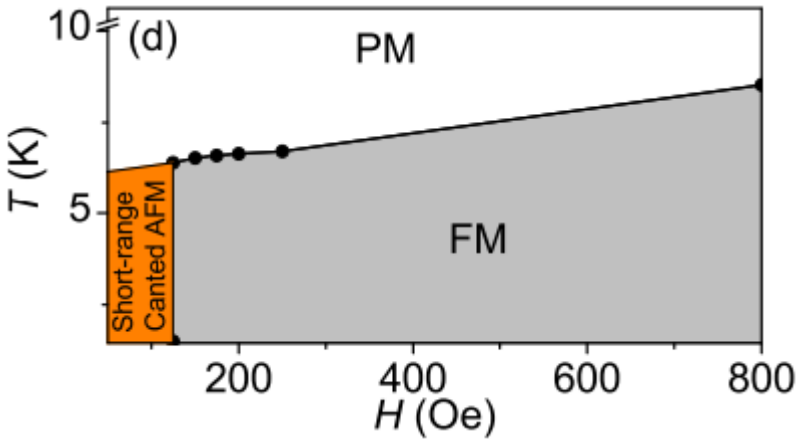


Figure 1.14: The proposed magnetic phase diagram for MOF-*bpe* by Jain *et al*, here we see that below a critical field of 125 Oe the system adopts a short range canted antiferromagnetic state [84].

canted antiferomagnetically ordered state is adopted in MOF-*bpe* [84], above which, ferromagnetic interactions consistent with the applied field are observed. This led to their conclusion that MOF-*bpe* had a "fragile" magnetic ground state (Figure 1.14), which was also the first report to fully assign a magnetic ground state. That is to say, the previous reports of this system made claims about the type and pathway of magnetic exchange interactions based on theory, not experimental evidence.

It is thus clear that despite over 10 years of study, the underlying magnetic phenomena within this family of $Cu_3(CO_3)_2(x)_3{\cdot}2ClO_4$ kagome-containing MOMs was yet to be truly elucidated. This led us to report our own publication in 2022, considering previous reports of these systems and collecting our own data for the structural and magnetic characterisation of three members of this $Cu_3(CO_3)_2(x)_3{\cdot}2ClO_4$ family, where x was, 1,2-bis(4-pyridyl)ethane (*bpe*), 1,2-bis(4-pyridyl)ethene, (*bpy*) and 4,4'-azopyridine, (*azpy*) [12]. First, the growth of single-crystals allowed us to fully characterise the structures of these MOMs in a chemically sensible way, at which point we discovered that the previously outlined space group assignments for MOF-*bpe* were not chemically reasonable, leading to C-C bond distances and angles which were unlikely to exist in a stable conformation.

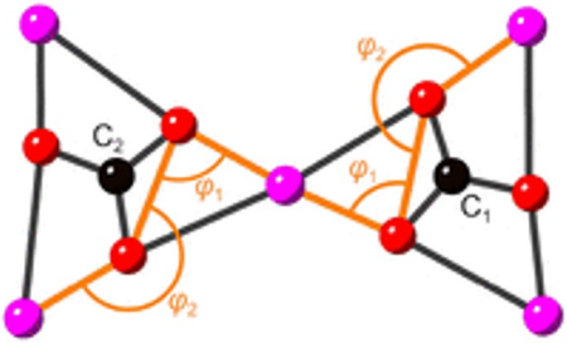


Figure 1.15: Illustration of the Cu−O···O−Cu superexchange angles present between nearest neighbour copper ions in the copper carbonate kagome network, according to DFT calculations the ϕ_1 = 82.6(3)° and ϕ_2 = 217.4(3)° would result in ferromagnetic exchange coupling [12, 83, 90].

Instead, we modelled the data in a different space group, allowing for a model of MOF-*bpe* in a chemically sensible geometry which MOF-*bpy* and MOF-*azpy* also share. Our magnetic characterisation suggested dominant ferromagnetic exchange coupling in all three cases [12]. We were then able to generate magnetic structural models for each system using neutron diffraction techniques, models which suggested that ferromagnetic interactions exist within kagome planes and antiferromagnetic interactions between them. Our results suggested that the assignment of antiferromagnetic kagome layers based upon the Goodenough-Kanamori rule were not consistent with the evidence we obtained. Therefore, it was likely that the magnetic intra-layer exchange pathways present are not simply propagating a ~180° route for antiferromagnetic coupling as previously assumed [82], but instead a route proposed from DFT calculations outlined by Mateus *et al*, Figure 1.15 [90]. From here, we were content with the evidence supporting our claims that intra-layer ferromagnetic and inter-layer antiferromagnetic exchange characterised the kagome-containing $Cu_3(CO_3)_2(x)_3{\cdot}2ClO_4$, MOM family and so we turned our attention to further extending this family to include the discussed, disorder free bipyridyl acetylene ligand (*bpa*). As discussed, the inter- and intra-layer exchange coupling assignments for MOF-*bpa* was reported to be consistent with our reports for MOF-*bpe*, *bpy* and *azpy*, however much room was left in this report to further elucidate the magnetic ground state of MOF-*bpa*.

In Chapter 3, we explore, by comparison to MOF-*bpe*, *bpy* and *azpy*, the effects, if any, on the magnetic behaviour of MOF-*bpa*. The main goal of this chapter is to explore the magnetic structure of MOF-*bpa* and understand whether linear, disorder-free ligands significantly affect the low-temperature magnetic characteristics.

1.2.4 Quasi-2D Copper Carbonate Kagome Containing Metal-Organic Magnets

As mentioned, one of the original expectations of synthesising kagome-containing MOMs featuring long inter-plane ligands was that these ligands may be long enough to suppress magnetic exchange interactions between kagome layers. This was expected to manifest as quasi-2D magnetic layers within a three-dimensional structure, however this has since been proven incorrect and that instead, magnetic exchange interactions still propagate these long ditopic ligands [12]. The direction of Chapter 4 is removing the covalent coordination present between kagome layers through ligand selection to afford magnetically isolated, stacked kagome layers within a MOM. From our previous study, we would expect these copper carbonate kagome layers to host ferromagnetic exchange interactions. As such, the focus of this chapter is on the elucidation of the magnetic ground state of non-covalently bound kagome-containing MOMs, acting as an extension to the $Cu_3(CO_3)_2(x)_3{\cdot}2ClO_4$ family previously outlined (Figure 1.16). One system fitting this description was reported in 2018, featuring copper carbonate kagome layers bridged by noncovalent 2,4'-bipyridine ligands with formula $Cu_3(CO_3)_2(2,4' - bipyridine)_6{\cdot}2ClO_4$, MOF-*bipy*. As expected, the magnetic characterisation reported suggests the presence of ferromagnetic exchange coupling [83]. However, this is the only result reported for MOF-*bipy*. With the low temperature magnetic ground state of this system still unknown, the basis of Chapter 4 presents itself, elucidating the magnetic ground state of MOF-*bipy* alongside the magnetic ground state of a material previously unreported in the literature of formula $Cu_3(CO_3)_2(methylpyridine)_3{\cdot}2ClO_4$, MOF-*mp*.

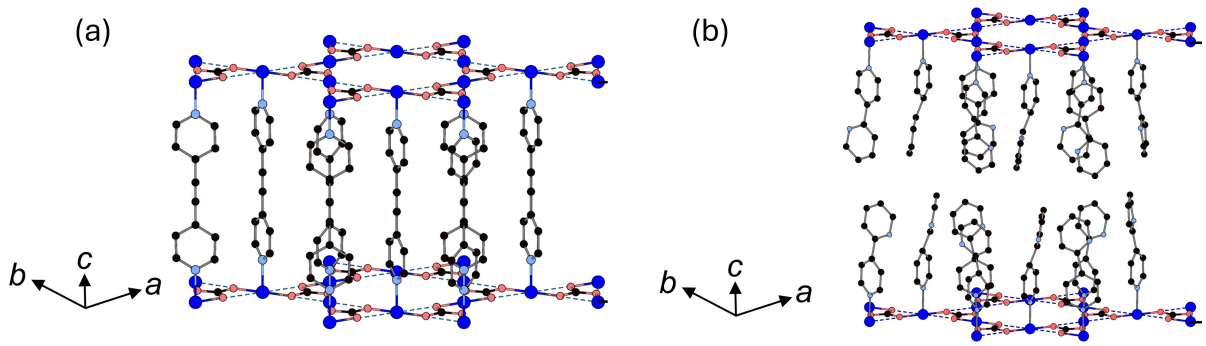


Figure 1.16: Comparison of (a) MOF-*bpa* and (b) MOF-*bipy*, MOF-*bpa* features covalenty linkage between kagome layers while MOF-*bipy* is non-covalently stacked through weak interactions.

1.2.5 2D Antiferromagnetic Copper Kagome Containing Metal-Organic Magnets

In Chapter 5, we begin to explore both changes to intra-plane ligands and the elimination of interplane coordination. This leads to these MOMs often being referred to as two-dimensional. With many of these kagome-containing MOMs falling into the general formula M_3L_2, where M is a metal and L is the coordinating ligand within the kagome plane. Regarding the magnetism observed in such MOMs the literature is broad and not limited to, spintronic materials proposed for many transition metal species [91, 92], high temperature (~200 K) ferromagnetic ordering temperatures in $Mn_3(C_6S_6)$ monolayers [93], and antiferromagnetic kagome-containing materials with the potential to host the long sought after QSL state [94, 95]. The multifunctionality of these 2D materials is also exemplified by systems such as $Cu_3(HHTP)_2$ where HHTP is hexahydroxytriphenylene, where magnetic order appears to be suppressed down to 38 mK alongside its potential for use as a semiconductor [96]. In Chapter 5 we focus on the $Cu_3(C_6O_6)_2$ system (Cu-HHB), with reports in the literature suggesting dominant antiferromagnetic exchange coupling and a lack of long-range order as shown by magnetic susceptibility and heat capacity measurements [97, 98], this system is an excellent target for study utilising neutron and muon techniques to probe the low-temperature magnetic characteristics.

Chapter 2

Experimental Methods

The characterisation of exotic magnetic states of matter is an ongoing challenge in condensed matter and solid-state physics and chemistry [99]. Observing or defining these quantum states through single, direct measurement is currently impossible, and so it is necessary to employ multiple complementary techniques to truly elucidate the magnetic ground state. A lack of long-range magnetic order down to 0 K is thought to be a key characteristic of a quantum spin liquid (QSL), a "holy grail" of quantum materials discovery. However, a lack of order down to 0 K is not indicative solely of a QSL, since suppression of long-range magnetic order can be observed due to lower-dimensionality [100], "hidden" order [101], and short-range spin correlations [102]. To confirm the presence of a complex magnetic state, we use complementary techniques such as; magnetic susceptibility, elastic and inelastic neutron scattering, muon spin relaxation spectroscopy (μSR), and heat capacity measurements, these are used alongside X-ray diffraction (XRD) methods for full characterisation. These listed methods have been employed herein for the elucidation of the complex magnetic ground states of several kagome-containing metal-organic framework materials.

As discussed, suppression of magnetic order can be induced by geometric frustration of antiferromagnetically interacting magnetic moments [9]. The competing exchange in-

teractions generated provide ideal conditions for the observation of a QSL state [82]. In finding suitable QSL candidates however, it is important to highlight synthetic targets that possess features hypothesised to host such complex magnetic phenomena; it is also common to find materials along the way that host their own unconventional magnetic properties, as discussed in Chapters 3 and 4. Throughout this Thesis, two things remain constant; the use of $S{=}\frac{1}{2}$, Cu^{2+} and the use of copper within MOFs. Both of these factors allow us to generate the ideal conditions for which non-trivial magnetic phenomena are expected to arise, specifically, when $S{=}\frac{1}{2}$, Cu^{2+} ions are positioned in a frustrated geometry such as the kagome [8, 60].

MOFs are not without flaw; they can be challenging to structurally characterise because they commonly host large unit cells containing many atoms which hinders facile structural characterisation by diffraction methods [12]. Despite this added challenge, the synthesis and structural determination of target materials via single-crystal X-ray diffraction neutron powder diffraction and powder X-ray diffraction (SCXRD, NPD, and PXRD, respectively) provide the foundation for further study of the magnetic characteristics of these systems. Crystallographic techniques are highly complementary to magnetic techniques because they provide us with the structural context in which magnetic phenomena emerge [25]. This foundation is crucial in understanding nearest-neighbour exchange, and often outlines why, and through which pathways, long-range magnetic order prevails. The following chapter aims to summarise and outline all the techniques and their importance in the synthesis, modification, and characterisation of the materials investigated within this Thesis.

2.1 Synthetic methods

All reagents and solvents used for the syntheses within this Thesis, unless otherwise specified, were acquired from Sigma-Aldrich, or Fluorochem at purities of 98+%.

2.1.1 Solvay-Based MOF Synthesis

The synthesis of the MOFs outlined in Chapters 3 and 4 were achieved through a modified Solvay process [86, 103]. An industrial technique where ammonia (NH_3) in brine is used to fix CO_2 as hydrogencarbonate (HCO_3) in large-scale production of sodium carbonate ($NaCO_3$). This process was modified to fix carbonates to metal ions under basic conditions, with hydrogencarbonate solubility increasing in solution due to the presence of aqueous ammonia. As ammonia is gaseous at room temperature, it slowly evaporates from the solution, allowing carbonate anions to chelate metal ions. This modified Solvay process provides a facile and environmentally friendly way of producing MOF crystals at room temperature while removing CO_2 from the atmosphere. The carbonate anion is a robust ligand with the potential to chelate in a mono-, bi-, tri-, and tetra-dentate manner, making for an ideal anion in the formation of many metal-organic systems with varied compositions, topologies, and characteristics [25]. With respect to Chapter 4, the quasi-two-dimensional kagome layers therein are derived from the tridentate coordination of CO_3^- anions with Cu^{2+} ions.

2.1.2 Solution Based MOF Synthesis

Synthesis of the MOF described in Chapter 5 was achieved through a reaction between the sparingly soluble organic linker (tetrahydroxyquinone) and the metal salt (copper nitrate hemipentahydrate) in degassed water, along with a buffer (ammonium acetate), leading to slow formation of MOF polycrystals. These polycrystals form on the surface of gradually dissolving tetrahydroxyquinone crystals, which ultimately leads to the need for a long washing stage, separating the insoluble MOF from the partially soluble ligand [80, 97, 98]. The detailed description of this synthesis is given in Chapter 5.

2.1.3 Mechanical exfoliation

The exfoliation of materials may be approached through a "top-down" approach where a bulk crystal is delaminated to the monolayer [104]. We approach nanosheet synthesis by a "top-down" approach, in sonicating layered samples hosting weak interlayer forces we expect these to be overcome by the energy imparted by the sonicator affording nanosheets. The post-exfoliated sample can then be qualitatively assessed by shining laser light through the suspension. Reflected laser light indicates that nanoparticulates are present, this effect is called Tyndall scattering [105]. We can then centrifuge and decant to size separate our nanosheets, with this technique summarised in Figure 2.1.

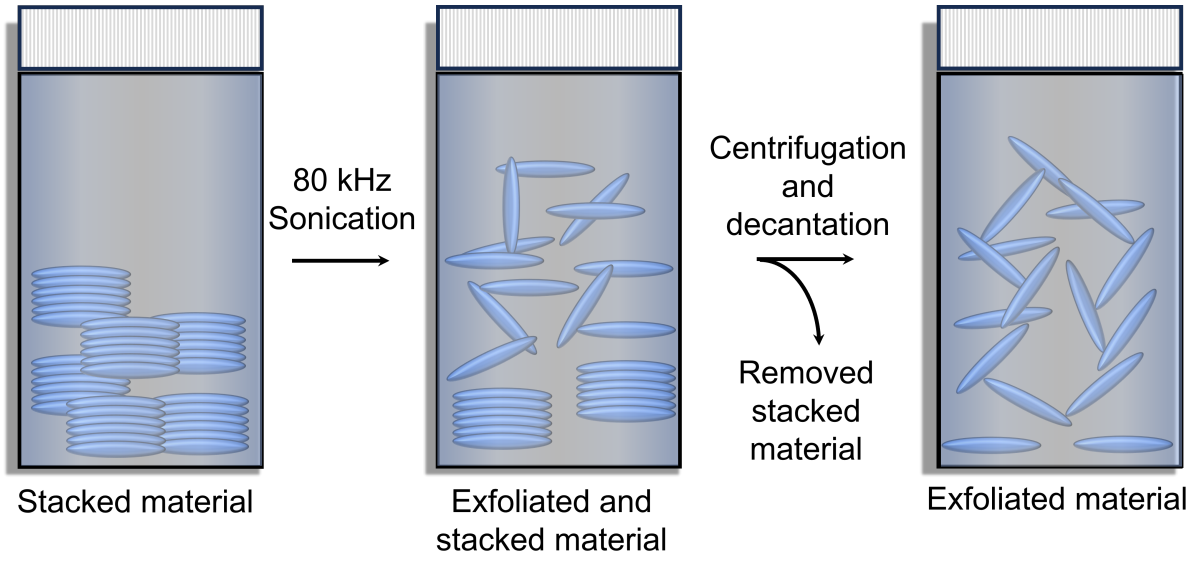


Figure 2.1: A layered material may be exfoliated to nanosheets through ultrasonication. Here, sonic waves impart enough energy to liberate layers bound by weak intermolecular forces, most commonly observed in graphene [106]. After exfoliation a mixture of exfoliated, partially exfoliated and unexfoliated material exist in suspension, these can be separated through centrifugation methods, isolating the fully exfoliated material in suspension.

2.2 Organic Elemental Analysis

In some instances growing large single crystals for comprehensive structural determination of MOFs can be challenging. Organic elemental analysers (OES) can be an invaluable

technique in the initial confirmation of phase purity, providing elemental ratios of carbon, hydrogen and nitrogen found match the expected ratio for a given system [107]. This can provide an indication of phase purity in cases where highly crystalline material is not available for diffraction methods. For the data reported herein, samples were sent to the London Metropolitan analysis service where they were weighed on a Mettler Toledo high-precision scale and analysed using a ThermoFlash 2000. This technique works by full combustion of the sample in the presence of oxygen, forming combustion products of carbon, nitrogen and hydrogen which are then separated by a gas chromatography column before passing through a thermal conductivity detector providing a gas chromatogram from which quantitative data are extracted [107].

2.3 Fourier-Transform Infrared Spectroscopy

Fourier-Transform Infrared Spectroscopy (FTIR) is an extremely sensitive technique for the analysis of vibrational, stretching and bending modes of chemical bonds [108]. Unlike dispersive infrared spectroscopy, FTIR uses a non-monochromated infrared source, allowing for the simultaneous collection of data arising from all incident wavelengths, these data are then converted by Fourier transform to a spectral pattern. Radiation absorbed by bonds corresponding to their bond excitations yield characteristic peaks in the data, for instance, a C-C stretching mode in an alkane falls between $800 - 1000$ cm^{-1} [109]. Another use for FTIR spectroscopy is in the observation of water, characterised by a broad feature at high wavenumber [110]. This facile method of confirming the presence of water was employed in Chapter 5.

2.4 Scanning Electron Microscopy

Sometimes, the synthesis of large, high-quality crystals is challenging, so synthetic optimisation may require the use of qualitative characterisation techniques, allowing us to directly observe the effects of reaction conditions on the resulting product. In cases

such as these, microscopy techniques can be used to observe the size and morphology of crystallites, showing us the effects of varying reaction conditions on these features [111]. In scanning electron microscopy (SEM), a focused beam of high-energy electrons raster across small areas interacting with the sample via electromagnetic interactions. Secondary electrons are generated by the collision of this electron beam incident on the surface of the material, exciting orbital electrons, and releasing characteristic X-rays [111]. These X-rays are then detected alongside reflected secondary electrons, generating a current response at the detector, allowing for a topographical map to be generated from the raster scans, hence the name scanning electron microscopy [111]. In Chapter 5, the identification of crystalline materials was made possible by SEM at scales beyond the resolution of the optical microscope. As a qualitative method, the interpretation of the results plays a large role in the data analysis; however, the characteristics of crystalline materials are known. Crystallites with sharp defined edges with corner angles consistent with the crystal system would be excellent indications that a sample is indeed crystalline. This technique was particularly useful in Chapter 5, where a study of growing larger crystallites was undertaken to assist with further characterisation by diffraction methods.

2.5 Nanosheet Characterisation

The study of magnetic materials down to the two-dimensional (2D) limit has become more prevalent over the past several years, with materials such as CrI_3 paving the way for this influx of interest [45]. In cases where interesting magnetic phenomena are anticipated to emerge in two dimensions, such as the frustrated kagome, materials must be synthesised but, equally importantly, characterised. With the intensive study of 2D materials so recent, the range of characterisation techniques remain underdeveloped, recent advances in techniques such as electron diffraction however, push the field of microcrystal structural determination forward [112]. But why are 2D materials difficult to characterise? In short, they are very small, therefore difficult to handle and they are challenging to synthesise

in large quantities [113]. These characteristics mean that methods such as single crystal diffraction, neutron powder diffraction, and even powder XRD are seldom suitable due to crystal quality, size, and quantity. These factors mean that new or specially optimised techniques must be developed to streamline the process of nanosheet characterisation. The difficulty in characterisation is also generally dependent on the methods used to synthesise the nanosheets [114]. For example, nanosheets formed via top-down approaches, are often less challenging to initially characterise, as the 3D crystal structure is known prior to the exfoliation process, allowing for a level of comparison in cases where several structural features are retained in the exfoliated material [115]. In these cases, first steps toward structural determination can be made using techniques such as atomic force microscopy. This technique allows us to search for features that match the expected height profiles of single layers of an exfoliated material.

2.5.1 Atomic Force Microscopy

In the study of 2D materials, their height profiles offer unprecedented insight into the success or failure of the exfoliation process. The atomic force microscope (AFM) can resolve height profiles as small as 1 nm, with a resolution of fractions of nanometres [116]. The AFM works by using a photodiode to detect small changes in laser light reflected off a cantilever incident and sensitive to charge on the surface of a sample [117]. The cantilever is made incident a few nanometers above a small area and a topographic map is generated based entirely on the response of the cantilever to the sample as it rasters across an area. Ideal nanosheets in some cases can be characterised by sharp angular edges with height profiles following a sharp rise, a long plateau, and a sharp fall; a rectangular traced signal observed in some literature data (Figure 2.2) [115]. However, what was often observed in post-exfoliated samples in Chapter 4 were circular features with height profiles ranging between $5 - 100$ nm. These can be ascribed to amorphous or microcrystalline material that clumps together during the exfoliation process outlined previously.

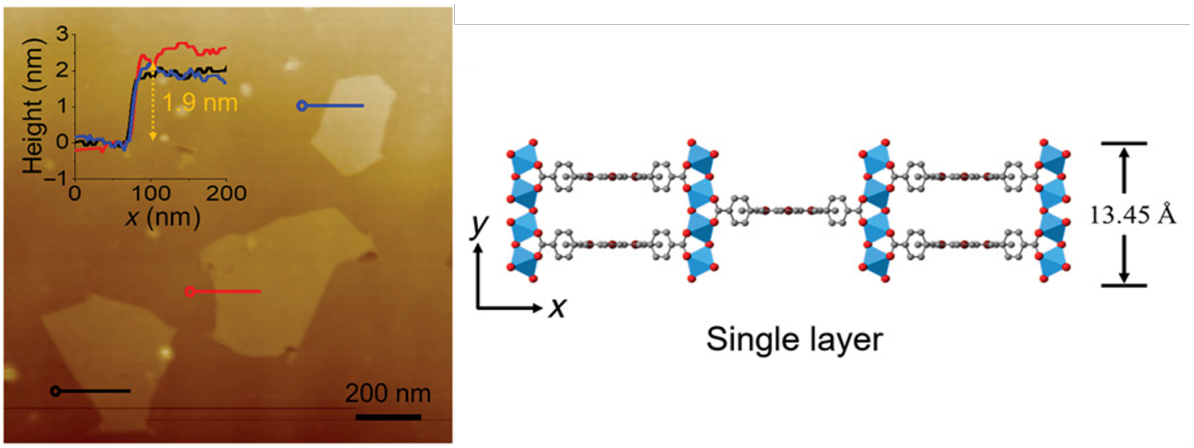


Figure 2.2: Atomic force microscopy data collected for aluminum tetra-(4-carboxyphenyl) porphyrin framework (Al-MOF). (left) The AFM image showing a height profile of 1.9 nm. (right) The proposed crystal structure of a single Al-MOF nanosheet.

2.6 Diffraction Methods

As discussed, rigorously characterising the magnetic properties of a systems requires the foundation of an accurate model of the crystal structure. Diffraction as a characterisation technique spans nearly all solid state chemistry research and is widely used in the MOF field [25, 118]. The technique relies heavily on a few key principles, the first of which is Bragg's law ($2d_{hkl}\sin\theta{=}n\lambda$) which treats crystals as periodic arrangements of atoms laying on specific crystallographic planes related to each other by symmetry. The term d_{hkl} corresponds to the perpendicular distance between adjacent planes (d-spacing) while θ represents the angle of incidence for incoming radiation of wavelength λ. When n has an integer value, Bragg's law is satisfied, which means that waves of radiation incident on parallel planes, separated by nλ, are in phase. These in-phase waves constructively interfere producing a Bragg reflection corresponding to the crystallographic plane which diffraction occurred upon [119]. This technique is widely used because it can resolve crystal structures with excellent atomic precision for most atoms, making it a universal technique in the study of crystalline materials.

For single crystals composed of periodically aligned atoms, the 3D structure can be de-

termined by single-crystal diffraction methods. Here, radiation diffracted by a sample hits a specialised phosphorous membrane detector, yeilding a pattern of Bragg spots in reciprocal space which correspond to the Bragg reflections present at a given angle the single-crystal is rotated through. This facilitates 3D structural determination because reciprocal space is directly related to the Fourier transform of real space, so through calculation, the real space structure can be determined. In a three-dimensional crystalline solid, Bragg peaks associated with individual planes of atoms can be derived from the reciprocal lattice through rotation across all necessary 2θ angles. As the unit cell dimensions, symmetry elements and atomic positions can be generated from the reciprocal space information obtained, structural models can be obtained and refined using software such as Olex II [120].

In situations where single crystals can not be obtained, either due to a lack of suitable synthetic route or a lack of suitable experimental set-up, diffraction can be performed on powder samples. We define a powder here as a sample of polycrystalline material in which crystal domains are randomly orientated in all possible directions. When a beam of radiation at a given angle is incident on the sample, a fraction of the randomly orientated crystal domains will satisfy Bragg's law, leading to the production of a diffraction cone at the detector. As the incident radiation is moved through a range of angles, a diffracted cone of radiation is observed at the detector at every angle satisfying Bragg's law corresponding to a crystallographic plane. These planes are labelled with Miller indices (hkl) where h, k, and l are integers indicating the positions of crystallographic planes [1]. The instrument generates a powder diffraction pattern, taking a one-dimensional slice through the diffracted cones and plotting these as intensity against 2θ which corresponds to the incident angle of radiation. The intensity plot against 2θ or powder diffraction pattern, is highly unique to the material studied as several factors dictate the peak intensity, shape and position [121]. The positions of Bragg peaks in these diffraction patterns provide information on the size and symmetry group associated with the unit cell, while the in-

tensities provide information on the atomic radii and their positions in relation to the allowed Miller planes of the space group symmetry assigned to the unit cell. Factors affecting peak shape can arise from instrumental broadening effects, as well as material effects such as strain, size and stacking faults. The instrumental factors affecting peak shape can often be mitigated through the analysis of a standard where a refinement provides values for the instrumental parameters. Within this Thesis, the X-ray sources CuKα and MoKα provide X-rays of wavelength 1.5406 Å and MoKα 0.7100 Å, respectively, for laboratory XRD experiment. Synchrotron XRD experiments were carried out at Diamond Light Source (DLS), where incident X-ray radiation can be set to any value between 0.5 and 2.1 Å . While at the ISIS Neutron and Muon Source, a tungsten target is radiated by high-energy protons to afford neutrons for neutron diffraction experiments.

Diffraction can be thought of as an elastic scattering of radiation, since the loss of energy has no bearing on the collected diffraction data [121]. However, inelastic scattering can also be used to study energy-dependent electronic excitations in materials. These excitations can include the lattice vibration from phonons, magnons, and even the spinons thought to come from quantum-entangled states such as the QSL [9]. Powder X-ray and neutron diffraction both have benefits and drawbacks when it comes to structural determination, especially when it comes to hydrogen. This often leads to them being used in conjunction to mitigate these drawbacks and allows for the interpretation of more complex data. This section outlines the key benefits of each method for use in the study of magnetically frustrated MOFs.

2.6.1 Powder X-ray Diffraction

As mentioned, PXRD is a powerful technique for the study of microcrystalline materials, the set-up of which is illustrated in Figure 2.3. The X-rays produced by the radiation source are scattered by the electron density of the atomic nuclei via relatively long-range electromagnetic interactions. Due to the direct interaction between electron density and

X-rays, the scattering of the X-ray beam is more intense in atoms with greater electron density [121]. The structure factor (F_{hkl}) links reciprocal space to real space referring to the sum of all wave vectors associated with all atoms of the unit cell described by Equation 2.1.

$$F_{hkl} = \sum_{n} f_n \exp[2\pi i(hx_n + ky_n + lz_n)] \tag{2.1}$$

Herein, x_n, y_n and z_n are the positional coordinates of atom "n", while h, k and l define the lattice points in reciprocal space. The points in reciprocal space are linked to the Miller planes in real space by this structure factor, where the final term f_n, the form factor, describes the scattering power of the radiated atoms. Among the three discussed diffraction types; PXRD, SCXRD and NPD, PXRD is the most accessible, with facilities researching solid-state materials usually possessing one of these instruments. The ability to rapidly collect data on relatively small samples makes PXRD the ideal first measurement in confirming the phase purity. With a wide array of experimental set-ups available, analysing samples with specific requirements, such as inert atmospheres and controlled temperatures is often possible.

This wide accessibility and ease of use make laboratory PXRD a valuable tool in the initial analysis of solid-state materials [122]. In some cases, synchrotron diffractometers are required. These are far less accessible than laboratory diffractometers, but provide exceptionally high resolution, reducing error and allowing for more accurate refinements of the data [123]. For laboratory data, a Le Bail refinement against a known structure may be used to fit data to a known structure. This, refinement method only takes into account cell parameters however, treating the unit cell as an empty box allowing arbitrary peak intensity assignment and the ability to refine instrumental peak shape parameters. This method provides no information on the atoms within the cell, so it is generally used to confirm the space group symmetry and unit cell dimensions of a newly synthesised sample to confirm its phase purity [124]. Synchrotron data however, provide a significant improvement in resolution, allowing for the assignment and refinement of atomic positions,

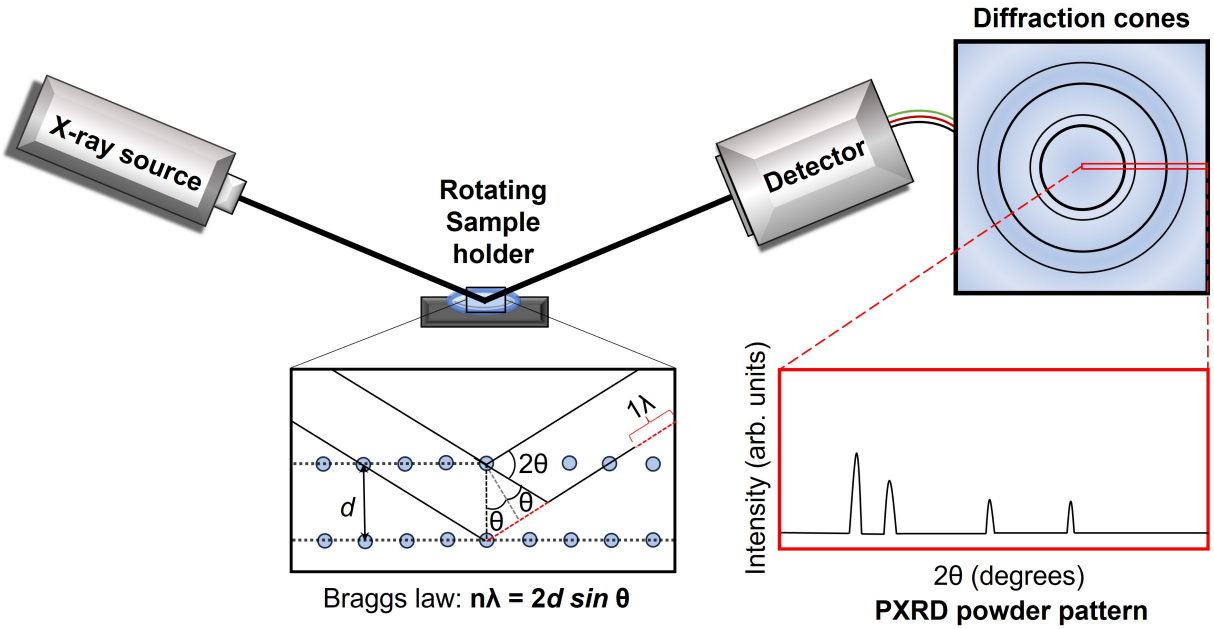


Figure 2.3: An illustration of a PXRD set up. A collimated X-ray beam is directed at the sample; in a Debye-Scherrer set-up the sample holder rotates. The incident X-rays are then diffracted by the atoms lying along the crystallographic planes within. Bragg intensity is only observed when parallel X-rays are diffracted by planes separated by integars, n, of the wavelength of the incident beam, λ. In these cases the X-rays interact constructively producing a signal at the detector. Diffracted planes yield "diffraction cones", generated by these constructively interacting X-rays, where the cone radii in 2θ corresponds to the Bragg position of a crystallographic plane. A one-dimensional slice of these data reveals a diffraction pattern, where intensity is plot against 2θ. The peak shape, intensity and positions observed are a direct result of factors such as atomic radii, position, thermal parameters, strain, size, preferred orientation, diffraction angle, unit cell parameters and more.

thermal parameters and fractional occupancies. This is known as Rietveld refinement, this takes into account all structural factors influencing the powder pattern and optimises the fit against a known structure, fitting the average features of a large sample of crystallites [125]. Since the known structure is often collected from a single crystal, the Rietveld refinement of a powder sample is often used to develop a more accurate average model of the system. Rietveld refinement can also be used to generate structures where atoms are changed but the crystal structure remains largely the same as the atomic positions and thermal parameters can be refined to a model which fits the data. This was performed in the literature with MOF-bpy when no single crystal data was currently reported. In Chapter 4 laboratory data could only be fit by Le Bail methods, while conflicts in the literature in Chapter 5 [98] required our use of high-resolution data to isolate a consistent average model.

Conclusively, PXRD provides the foundation for magnetic structural determination. To properly model atomic positions is to properly model magnetic site positions, their associated symmetry, and respective scale factors, all of which play a major role in the understanding of long-range magnetic order. However, the powder diffraction method is not without flaw; many of the materials outlined in this Thesis have characteristics that increase the complexity of modelling them. These include crystallite size, stacking faults, and preferred orientation, all of which result in increased complexity in producing accurate models. This difficulty comes from the artificial inflation of peak intensities which then require dedicated modelling provided these effects are in fact physical.

Preferred orientation can be thought of as an increased number of specified planes scattering the incident X-rays, often occurring in crystals with preferential growth meaning a greater presence of specific planes are present, this leads to systematic intensity increases. Stacking faults may result in differing peak shapes as atoms are shifted outside of planes leading to scattering which deviates from the ideal Bragg position. To com-

pound these difficulties, the direct relationship of electron density to scattering intensity leads to uncertainty in the assignment of light nuclei such as hydrogen [121]. This can become problematic in magnetic determination when we consider that magnetic superexchange is known to occur through the p-orbitals of lighter atoms such as carbon or oxygen [126]. Thus, uncertainty in the positions of these atoms leads to added uncertainty in the magnetic exchange pathways, which are essential for rigorously characterising long-range magnetic order [6].

2.6.2 Single Crystal X-ray Diffraction

A highly ordered, periodic arrangement of atoms (forming a crystal domain) can be considered to be a single crystal. An illustration of the SCXRD experimental set up is given in Figure 2.4. These domains then act as three-dimensional diffraction gratings to incident radiation, producing a pattern of Bragg spots at the detector collectively known as a reciprocal space pattern. In SCXRD, X-rays are also scattered by the electron density of the nuclei present; however, unlike PXRD, SCXRD produces unique Bragg spots in a three-dimensional space at defined hkl positions, all of which make up a reciprocal lattice. The real lattice is directly related to the reciprocal lattice through the Fourier transform of these hkl positions. This Fourier transformation allows for the generation of an electron density map which can be processed in software packages such as Olex 2 [120] to generate 3D models which fit the obtained data.

It is important to understand at this stage, that the crystallographic models extracted from SCXRD data only provide information on the single crystal being analysed. To understand the underlying average structure it is essential to use SCXRD in conjunction with PXRD highlighting whether bulk effects such as stacking faults or preffered orientation are present in the sample. Once a SCXRD pattern is modelled a crystallographic information file (CIF) can be used in Le Bail or Rietveld refinements of PXRD data [124, 125].

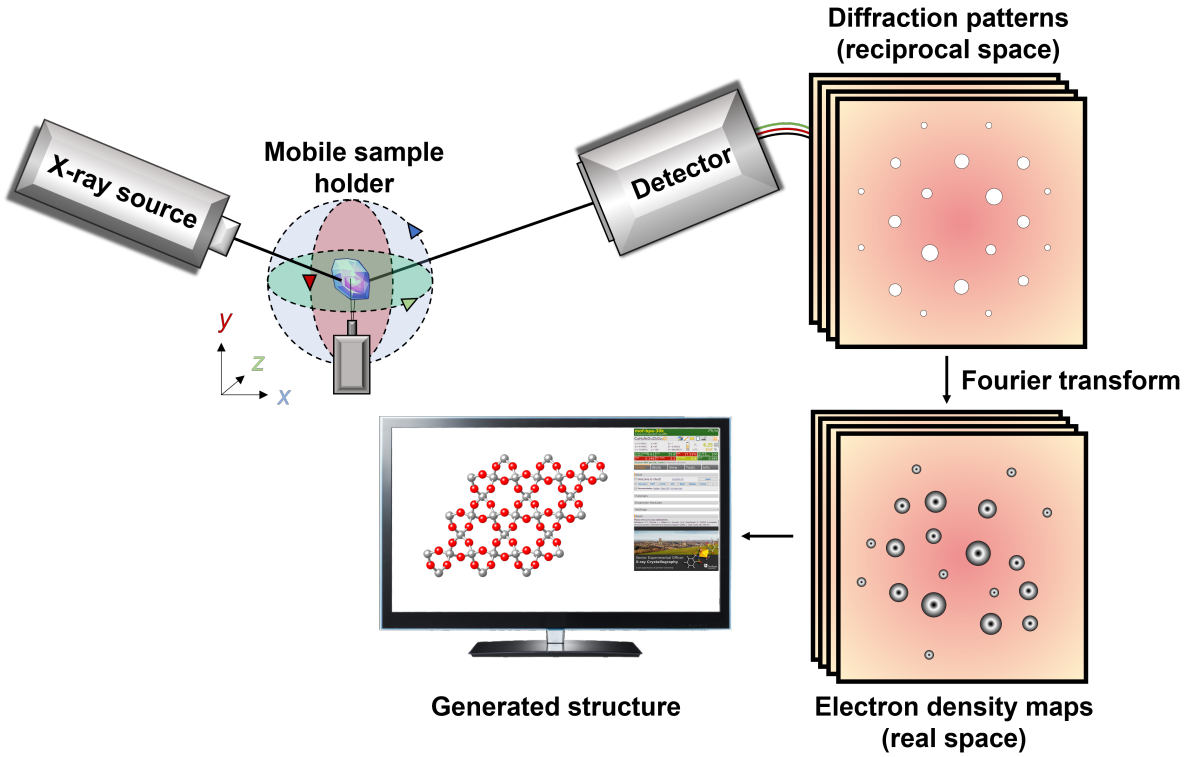


Figure 2.4: An illustration of a SCXRD set-up. Here, an X-ray beam is diffracted by a single crystal, generating a two-dimensional diffraction pattern of Bragg spots. These arise in SCXRD when an incident wavevector, k, satisfies Bragg's law by intersecting a reciprocal lattice vector, g, on the surface of a theoretical construct known as the Ewald's sphere. The diffraction patterns are then collected at all angles in a spherical rotation before collation, resulting in a three-dimensional pattern of Bragg spots in reciprocal space. Here, symmetry elements can be applied to the observed pattern provided the observed Bragg reflections are mostly consistent with a single space-group assignment. Due to the direct relationship between X-ray scattering and electron density, the Bragg intensity is consistent with the atomic radii of elements present within these diffraction planes. Provided agreement between the observed spots and space group assignment, the Fourier transform of the data yields an electron density map constrained by the applied symmetry. This electron density map exists in real-space and can therefore be used to generate crystallographic models using software packages such as OLEX2 [120].

2.6.3 Neutron Powder Diffraction

At its core, the neutron is an uncharged particle made up of three quarks, bound by the strong nuclear force. These three quarks, one up quark and two down quarks, give rise to the overall spin on the neutron ($S = \frac{1}{2}$), which is able to interact with other nuclei via the short-range strong nuclear force, as well as magnetically, through dipole dipole

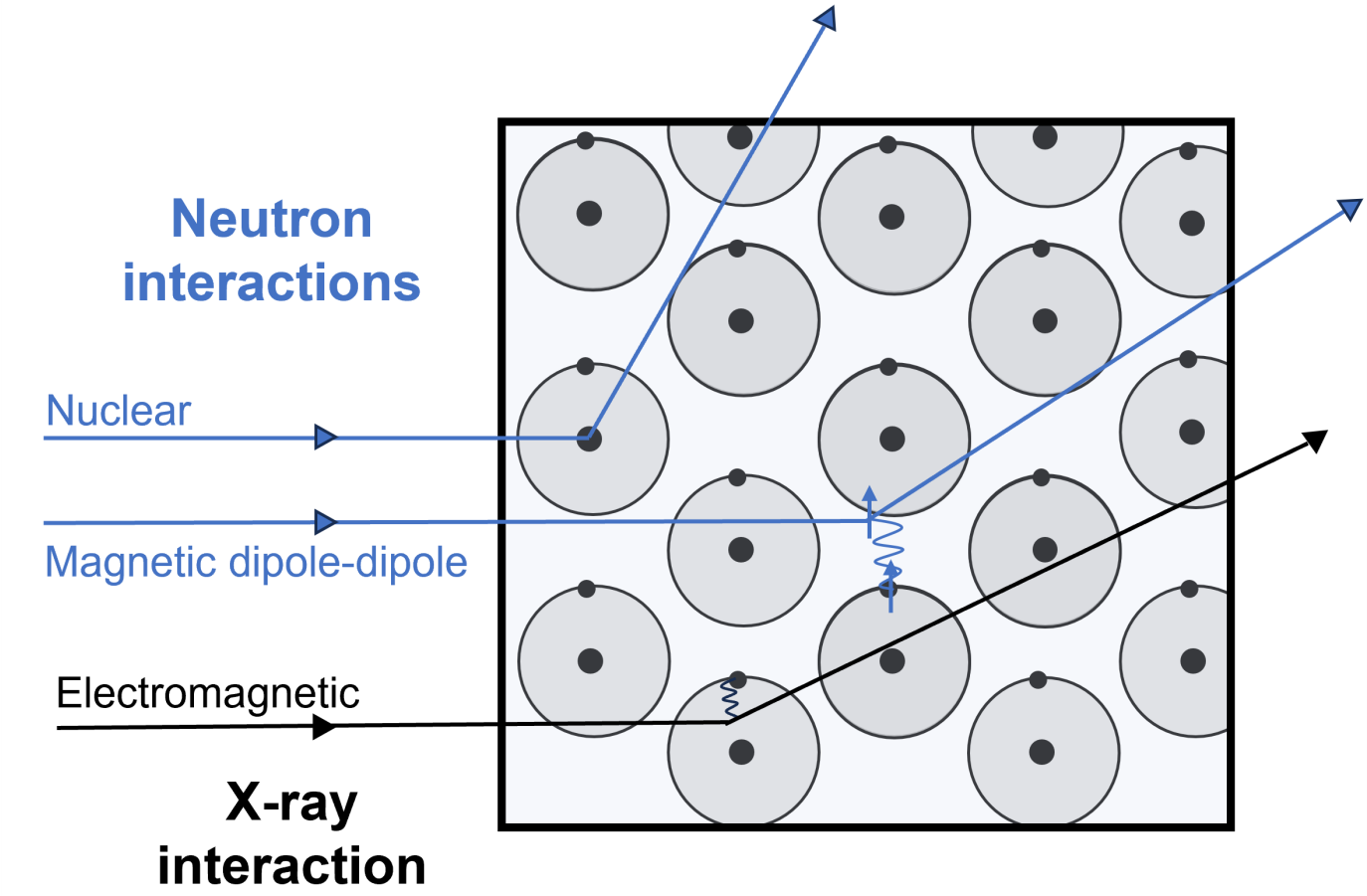


Figure 2.5: An illustration showing the principle interactions of neutrons and X-rays, here we see that neutrons may be scattered through the strong nuclear and dipole-dipole interactions, while X-rays are scattered by electromagnetic interactions with electron density [121].

interactions (Figure 2.5) [121]. As discussed previously, X-rays are more strongly scattered by a greater electron density. Neutrons however, have isotropic scattering power, making the distinction between atoms of similar electron density less challenging. This isotropic scattering power comes from the signal of scattered neutrons originating from the total scattering cross section σ_{tot}. Consisting of coherent and incoherent parts σ_{coh} and σ_{incoh} respectively, the ratio of these, dictate the scattering power of the neutron. This also means that the larger the area of the sample, the more intense the scattering will be, small samples provide insufficient intensity due to the weaker scattering of neutrons due to the fact that neutrons scatter at the nucleus while electrons scatter from electron

density which is relatively larger. Hence, significantly larger quantities of sample are required for neutron scattering compared to X-ray scattering experiments. The interaction of neutrons with matter follows the atomic collision equation, $\sigma_{\text{tot}} = 4\pi b^2$. Here, b is the length of scattering, which depends on the nuclear composition and spin, allowing the neutron as a probe to differentiate nuclei better than X-rays [121]. One limitation of neutron powder diffraction however, comes when dealing with the proton. To understand this, we must reiterate that the total scattering cross section σ_{tot} is made up of two components, σ_{coh} and σ_{incoh}. While coherent scattering provides us with crystallographic information derived from nuclear correlation lengths, the incoherent scattering is due to the differing isotopes and spin states of the nuclei. Since the proton has two spin isotopes, "para" and "ortho", which may or may not align with the neutron spin, we observe a large incoherent scattering response [127]. The incoherent scattering of the proton translates experimentally to a large featureless background signal, which artificially inflates all signal and therefore masks the coherently scattering signal. This incoherent background is the main reason for the preference of deuterated samples in neutron diffraction experiments, a topic discussed in Chapter 5.

Unlike X-rays, the production of neutrons is less simple, with the only sources being a nuclear reactor or spallation source. The neutrons produced at the ISIS Neutron and Muon source are spallation generated, meaning a high-energy proton is forced to collide with a heavy metal target such as tungsten, producing a "pulse" of neutrons in response to the collision. These pulses contain neutrons possessing a range of energies, and so their energies are normalised by the calculation of their time of flight, which is directly related to the incident neutron energy. This is done through time-of-flight analysis, wherein the time taken for a neutron to travel from a moderator, such as solid methane, to a given detector provides the information on its energy. In this analysis, higher-energy neutrons will reach the detectors faster and vice versa. The detectors for these neutrons are also divided into multiple banks, positioned to capture scattered neutrons at multiple specific

scattering angles with a known path length L, allowing for the calculation of neutron wavelength via the de Broglie wavelength given by Equation 2.2.

$$\lambda = \frac{h}{mv} \tag{2.2}$$

Where h is the Planck constant, m is the mass and v is the velocity calculable by dividing L by the time taken to reach the detector, time of flight (TOF). Once an effective wavelength for incident neutrons is calculated, a diffraction experiment can be carried out in a similar way to X-ray experiment. If required, time-of-flight data can be converted to d-space or Q-space, provided that instrumental parameters are known for conversions.

There are, of course, different neutron sources across many central facilities, all featuring specific benefits and drawbacks for characterisation. For the MOF systems outlined throughout this Thesis, the WISH diffractometer at ISIS was used due to the long d-space (~40 Å) range in the Bank 1 detector. This is a crucial feature for the study of MOFs with large unit cells, as the features observed at high d-space would not be observed using other set-ups, discussed in all Chapters of this Thesis. It is no surprise then that NPD, especially on WISH, has been gaining interest in the structural study of MOF materials, alongside their magnetic characterisation, since neutrons can also act as a probe for magnetism [12, 73, 128].

2.6.4 Magnetic Neutron Scattering

Since neutrons possess spin and interact with matter at such short ranges, their diffraction path can also be perturbed by the presence of magnetic moments about the nuclei. These moments come from unpaired electrons within orbital shells of magnetic atoms, which often interact with nearest neighbours via magnetic superexchange to form ordered magnetic domains at low temperatures [6]. If a neutron scatters elastically with magnetic nuclei through a dipole-dipole interaction, the total scattering of neutrons will be

equal to the combined magnetic and nuclear scattering. This links the magnetic Bragg intensity to nuclear Bragg intensity, since the scattering of a single magnetic nuclei provide Bragg intensity for both types of scattering [121]. Thus, nuclear and magnetic unit cells may be refined by this method. However, complexity is added, as the symmetry of an ordered magnetic cell is not always consistent with the nuclear symmetry, leading to the emergence of magnetic Bragg intensity at non-nuclear cell positions [129]. This may occur in systems where the magnetic cell is not described by unit cell symmetry, commonly in systems where antiferromagnetic order is observed, as these equal and opposite moments break the symmetry of the nuclear cell [12]. To refine a magnetic unit cell, data collected above an ordering transition temperature must be subtracted from data collected below this transition. Subtractions of this nature leave only the magnetic contribution to Bragg intensity, allowing for magnetic structure refinement. The ability to collect magnetic structural data makes neutron diffraction a powerful tool in the study of magnetically ordered systems. But more so, it is an essential tool in confirming a lack of long-range order in materials expected to have dynamic magnetic ground states such as the kagome antiferromagnet outlined in Chapter 5. A major consideration for the analysis of magnetic neutron scattering data is that the magnetic scattering intensity is lower at a lower d spacing, meaning that magnetic Bragg reflections may only be observed at long d-spacing. This may lead to false claims of a lack of long-range order in cases where the magnetic Bragg intensity is outside the range of the instrument. This reiterates the importance of using suitable neutron instruments, such as WISH, which features long d-spacing detection banks.

2.7 Magnetic Susceptibility

Magnetic susceptibility measurements are often considered to be the first step towards bulk magnetic characterisation. Measurements can be performed on Superconducting Quantum Interference Devices (SQUIDs) with its set up illustrated in Figure 2.6. These

instruments are able to measure exceptionally small variations in the local magnetic flux of a sample due to the superconducting coil and insulating layers known as Josephson junctions; these allow for the superconductivity of the coil to be quenched and recharged at will, and are exceptionally sensitive to external magnetic fields [130]. To measure a samples magnetisation, a magnetically inactive capsule is used to hold the sample; this is then attached to a sample holding rod and inserted into the SQUID where it is pushed through the superconducting ring by internal motors. At the same time, temperature, field, or frequency (in AC susceptibility) may be varied to probe the magnetic signal of the material. This signal is picked up as magnetic moments within the sample induce a measurable change in current in the surrounding pick-up coils. Since the magnetisation is proportional to the current generated, we can measure the magnetic susceptibility of the sample.

The first and often most enlightening measurement we take is magnetic susceptibility as a function of temperature. In the case of a paramagnet, we would expect this plot to be a smooth exponential approaching zero [6]. While a characteristic change in gradient is indicative of spontaneous order at a critical temperature (Figure 2.7). Additionally, differential plots of temperature multiplied magnetic susceptibility data are a useful tool for determining subtle gradient differences in cases where deviations from a paramagnetic regime are less clear, this is known as Fishers specific heat, calculated using the differential in Equation 2.3, where χ is the magnetic susceptibility and T is temperature [131].

$$\frac{d(y)}{d(x)} = \frac{d(\chi \cdot T)}{d(T)} \tag{2.3}$$

In cases where magnetic order is suppressed completely, such as in an ideal geometrically frustrated kagome antiferromagnet, the expected response would appear to be a smooth curve increasing toward lower temperatures known as Curie-Weiss behaviour [132]. How-

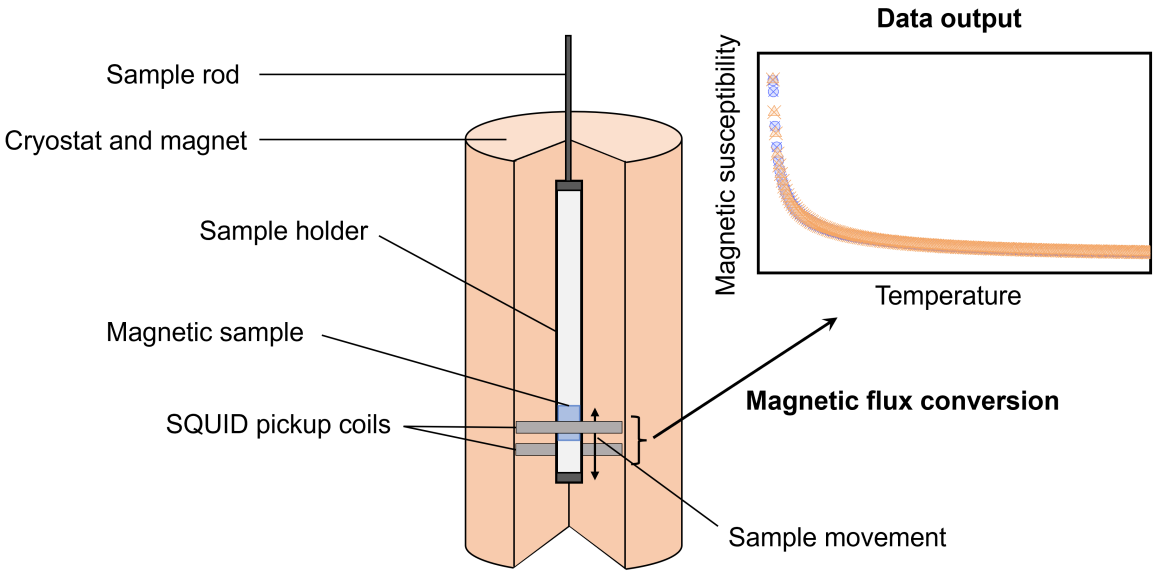


Figure 2.6: An illustration of the MPMS 3 SQUID sample area. A sample is secured in a straw sample holder before being inserted into the SQUID. Here the specialised pick-up coils act as super-sensitive detectors for magnetic flux about the sample. In this arrangement, external field and temperature can be manually adjusted while the sample is moved through these pick-up coils. The magnetic flux generated by the movement of a magnetic sample through these coils is then collected and converted to more useful data relating to the magnetic susceptibility of the sample for further analysis.

ever, more information can be extracted from these data using models such as the Curie-Weiss model, this can provide us with information about the magnitude and nature of magnetic exchange interactions of our material [132]. This works by fitting the inverse susceptibility data within the paramagnetic regime, above the critical temperature, giving a material-specific value for both the Curie constant C and the Curie-Weiss temperature, θ_{CW}. The Curie-Weiss equation is given by Equation 2.4.

$$\chi = \frac{C}{T - \theta_{CW}} \tag{2.4}$$

Where χ is the magnetic susceptibility, T is temperature in Kelvin and θ_{CW} is the material specific Curie-Weiss temperature. Rearranging to fit the reciprocal, linear region, above θ_{CW} gives Equation 2.5.

$$\frac{1}{\chi} = \frac{T - \theta_{CW}}{C} \tag{2.5}$$

Where the gradient is given by the reciprocal of C and the extrapolated x intercept provides the θ_{CW}. In general, θ_{CW} values which are positive indicate dominant ferromagnetic exchange coupling, and values which are negative indicate dominant antiferromagnetic exchange coupling but does not necessarily correspond to a long-range ordered transition [6]. In systems that show no signs of long-range order in magnetic susceptibility measurements, such as QSL candidates, measurements at significant temperatures must be taken. This is to rule out the possibility of the ordering transition simply being suppressed below the ~1.7 K limit of most cryostat-based instruments. This often requires the use of extreme cooling techniques, such as the use of dilution refrigerators. These cooling systems can achieve temperatures below 100 mK by using the dilution and vacuum pumping of a mixture of helium-3 and helium-4. In this process, the removal and recirculation of helium-3 via this pumping process leads to a significant loss of entropy allowing these millikelvin temperatures to be reached [133]. At these extreme temperatures we can begin to consider the materials we are measuring as being consistent with their behaviours at absolute zero. When ruling out the onset of spontaneous order and acquiring values for θ_{CW}

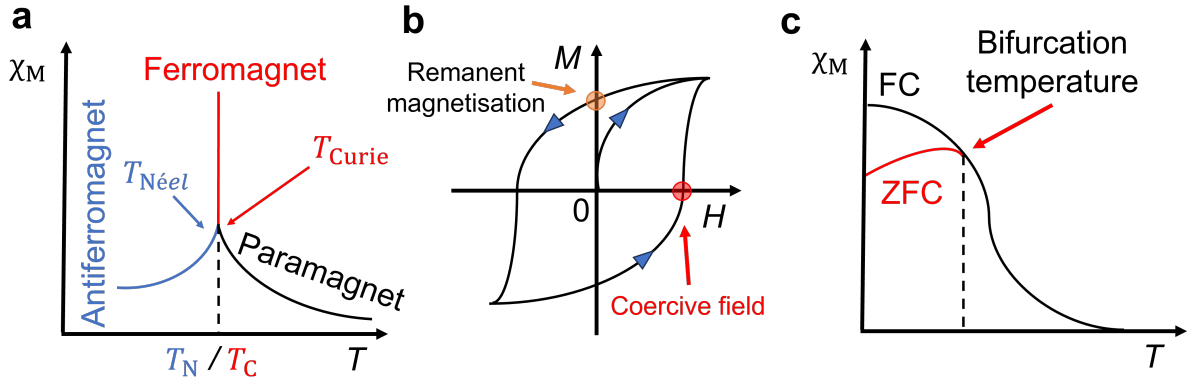


Figure 2.7: Some theoretical examples of magnetometry data. a) A paramagnetic material will produce a smooth upturn in magnetic susceptibility data without spontaneous deviation. In the case of a ferromagnetically ordered material a spontaneous increase in susceptibility at T_{Curie} is expected, while a reduction in susceptibility at T_{Neel} is expected for an antiferromagnetic material. b) In an ordered ferromagnetic material, hysteresis is observed in magnetisation vs. field data. This is observed as saturated moments aligning with the field in one direction require a significant applied field in the opposing direction to reverse their orientation, no hysteresis would be observed in a paramagnetic/antiferromagnetic material. c) In zero field cooled and field cooled data, a bifurcation between the two datasets indicates no field-induced spin freezing [25].

and C, we may also use magnetic susceptibility measurements to rule out the presence of spin glass. A spin glass is visualised as the freezing of randomly orientated magnetic moments at a critical temperature known as the glass transition T_{f}. This is characterised by a bifurcation in zero-field and field-cooled susceptibility vs. temperature data (Figure 2.7c). Here, the divergence between the two datasets below T_{f} is indicative of spin freezing. Some reference examples of data are illustrated in Figure 2.7 with experimental context given by Figure 2.8. Here we see some of the commonly expected features in magnetometry measurements and their meanings. Experimentally, we see added complexity when it comes to unambiguously assigning magnetic phenomena and so multiple complimentary techniques are required for full magnetic chracterisation. Beyond temperature-dependent measurements, field dependence can also be studied. These measurements can provide information on ferromagnetically ordered materials, where magnetic hysteresis is indicative of ferromagnetism [134]. These magnetisation vs. field measurements can also be taken at different temperatures. This can provide insight into the fragility of local moments to

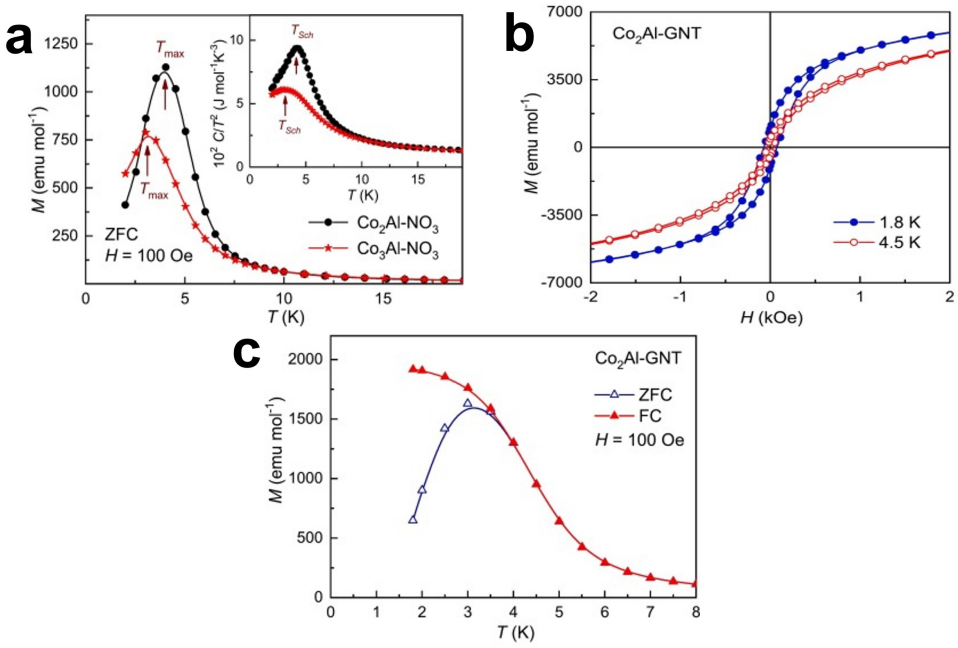


Figure 2.8: Some literature magnetic susceptibility data. a) Magnetic susceptibility vs. temperature data showing a shift in $T_{\max}$ between the two samples, suggesting differing ordering temperatures. b) Magnetisation vs. field data combined with c) ZFC vs. FC data showing a bifurcation these combined data indicate the onset of ferromagnetic order [134].

an external field below and above the critical temperature [12, 134]. When a system is in an ordered state, we would expect the susceptibility to an external field to be lesser, while moments in a disordered state would be more likely perturbed by this field due to the energy barrier of manipulating ordered moments [6]. This can further evidence an ordered state in cases where the magnetic susceptibility vs. temperature does not show a clear magnetic phase transition. In cases where magnetic susceptibility measurements do not indicate a long-range ordered state, samples may be further analysed with the physical property measurement system (PPMS) in heat capacity measurements.

2.8 Heat Capacity

Heat capacity measurements can be carried out using a PPMS in conjunction with a specialised sample puck possessing advanced calorimetry detectors. First, the definition of heat capacity at constant pressure, C_p, is the heat energy, Q, required to increase the

temperature, T, of a given mass by one unit. Measurements are performed under vacuum to ensure this constant pressure and that there is no loss of heat energy to surrounding air particles. This relationship is given by Equation 2.6.

$$C_p = \left(\frac{dQ}{dT}\right)_p \tag{2.6}$$

In heat capacity measurements we are often interested in extracting information useful for understanding the energy dynamics of a system, and so, we implement the use of entropy, S. Entropy is often used in conjunction with the study of electronic excitations [135] and is given by Equations 2.7,

$$dS = \frac{dQ}{T} \tag{2.7}$$

Substitution of Equation 2.6 into Equation 2.7 then gives Equation 2.8,

$$C_p = T\frac{dS}{dT} \tag{2.8}$$

providing information on the change in a systems entropy as a function of changing temperature. What this means for magnetic systems that undergo an ordering transition is that there is a spontaneous change in entropy around the critical temperature [136]. This entropy change is induced by the absorption of heat energy as magnetic moments spontaneously orient themselves to an ordered, minimal-entropy conformation. This spontaneous ordering is characterised by a sharp feature in temperature-dependent heat capacity data, where the magnetic entropy released can be calculated by integration of the magnetic entropy as a function of temperature. In an ideal system without additional sources of electron spin, S, the calculated entropy change ΔS would be equivalent to Equation 2.9.

$$\Delta S = Rln(2S + 1) \tag{2.9}$$

where R is the gas constant. For example, in an $S = \frac{1}{2}$ system,

$$\Delta S = 8.314\, ln\, ((2 * 0.5) + 1) = \underline{5.762}\, JK^{-1}mol^{-1}, \tag{2.10}$$

gives us an indication of the expected entropy release for a given magnetic system, allowing for our collected data to be compared.

A consideration for the magnetic heat capacity analysis is that the total heat capacity is a combination of four components; nuclear, C_{nuc}, electronic, C_{ele}, lattice, C_{lat}, and magnetic, C_{mag}. Each of these contributes to the observed excitations at varying temperature scales. Fortunately, electronic and nuclear contributions are often dominated by magnetic contributions at low temperature, while the lattice contribution arising from phonon excitations dominates at higher temperatures [137]. To effectively extract the magnetic heat capacity alone, a subtraction of the phonon contribution must be performed. Ideally, a non-magnetic analogue ($C_{\text{nuc}} + C_{\text{ele}} + C_{\text{lat}}$) would be measured alongside the magnetic sample ($C_{\text{nuc}} + C_{\text{ele}} + C_{\text{lat}} + C_{\text{mag}}$), allowing C_{mag} to be extracted through the subtraction of both datasets. However, when complex MOF samples are considered, analogues can be difficult to synthesise, so an alternative method must be used. The most commonly used approach is Debye-Einstein modelling, which uses both the Debye,

$$C_{Debye} = 9NR\left(\frac{T}{\theta_{Debye}}\right)^3 \int_0^{\frac{\theta_{Debye}}{T}} \frac{x^4 e^x}{(e^x - 1)^2} dx \tag{2.11}$$

and Einstein equations,

$$C_{Einstein} = 3NR\left(\frac{\theta_{Einstein}}{T}\right)^2 \frac{e^{\frac{\theta_{Einstein}}{T}}}{(e^{\frac{\theta_{Einstein}}{T}} - 1)^2} \tag{2.12}$$

in tandem to fit the phonon heat capacity at high, phonon dominating, temperatures, allowing extrapolation to lower temperatures. In these expressions, N is the number of atoms within the formula unit, R is the ideal gas constant, T is temperature, and θ_{Debye}

$/\theta_{Einstein}$ are the respective Debye/Einstein temperatures measuring the inflexibility of the lattice [138]. This extrapolation then gives an estimation of the phonon contribution at low temperatures, allowing a subtraction to be undertaken in lieu of non-magnetic experimental data. These two equations are used to calculate the acoustic and optical phonons, respectively, providing a comprehensive phononic model [138]. There is however, debate on the accuracy of this combined model, as several assumptions about the spectrum of frequencies of the vibrational modes are made [137]. Although these assumptions create uncertainty, the calculated magnetic entropy changes and missing magnetic entropy may still be exctracted and compared with expected values, allowing for an assessment of their reliability to be made with caution. Overall, Debye-Einstein modelling of phonon contributions to heat capacity is fit for purpose, providing key insight into the magnetic behaviour of frustrated, and unconventionally ordered magnetic states of matter such as the QSL. Furthermore, information on the energy scales of magnetic interactions may be extracted from magnetic heat capacity data through Schottky analysis [139]. Although these analyses should also be treated with caution due to the uncertainty discussed, they can provide estimates for comparison with experimental methods such as inelastic neutron scattering. To extract an energy scale from a two-level system, data may be fit to a Schottky anomaly (Equation 2.13).

$$C_{Schottky} = R(\frac{\Delta}{T})^2 \frac{e^{\Delta/T}}{[1+e^{\Delta/T}]^2}. \tag{2.13}$$

Here, Δ is the energy between two levels and T is the temperature. We use this method in Chapter 5 to estimate the energy scale of antiferromagnetic exchange interactions.

2.9 Muon Spectroscopy

The muon is a fundamental particle classified as a lepton. This particle can have a charge of ± 1 and $S = \frac{1}{2}$, which means that it is capable of interacting with local magnetic fields much like the neutrons discussed above. In the case of experiment, the positive muon

(antimuon) is used, as it has a longer lifetime than its counterpart (averaging ~ 2.2 μs), as well as higher stability within matter. With incredible sensitivity to small perturbations in local fields, muons make excellent probes for elucidating the spin dynamics expected to emerge in QSL candidates [140]. An illustration of how a μSR measurement is conducted is given in Figure 2.9. As discussed, competing exchange interactions can suppress the ordering transition of a material, leading to difficulties in extracting useful information from convential bulk magnetometry techniques [141]. In these cases more specialised techniques are required such as muon spin relaxation spectroscopy. This technique can provide information on the spin dynamics present in these magnetically disordered phases, making it an excellent tool when used in conjunction with the other bulk methods [12, 142]. Muon spin relaxation spectroscopy, in principle, works by detecting positrons originating from decay of an antimuon parent, where the propagation vectors of decayed positrons are highly correlated to the local magnetic environment that perturbed the spin of the antimuon [143]. To understand this correlation, we must consider what is happening in this experimental setup. First, spin-polarised antimuons are implanted, stopping within close proximity to areas of high electron density because of their positive charge. At these stopping sites, the antimuon begins to precess at a frequency proportional to the internal field incident upon it. During this precession, the antimuon decays, producing a positron, an electron neutrino, and a muon antineutrino. The decayed positrons preferentially decay in the direction of the antimuon spin, meaning that we are able to track the depolarisation of the implanted muon over a range of decay lifetimes ranging between $0-30$ μs. Positron detectors are positioned in front and behind the sample, called front and back detectors, allowing muon asymmetry to be calculated using Equation 2.14.

$$A(t) = \frac{N_{\mathrm{B}}(t) - \alpha N_{\mathrm{F}}(t)}{N_{\mathrm{B}}(t) + \alpha N_{\mathrm{F}}(t)} \tag{2.14}$$

Here, α is the calibration constant, t is time and $N_{\mathrm{B}}/N_{\mathrm{F}}$ are the positron counts. In μSR measurements, magnetic fields can be applied transversely or longitudinally, with

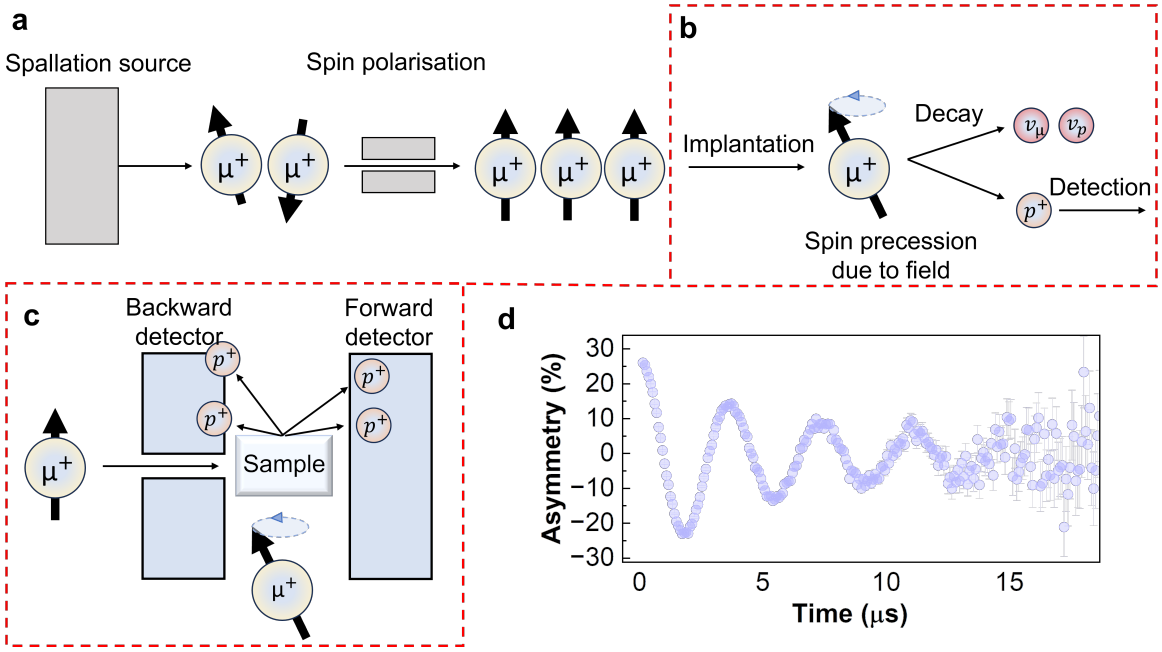


Figure 2.9: An illustration of how a μSR set-up works. **a)** Antimuons are generated at a spallation source, either continuously or by pulsing. The produced antimuons must be spin-polarised for use in the experiment as the perturbation of their spin indirectly provides us with magnetic information. **b)** Once these spin-polarised, antimuons are implanted within a sample, the presence of internal or applied magnetic fields cause a precession of their spin. **c)** Antimuons have a range of lifetimes, averaging 2.2 μs, and once decayed, produce a positron which can be detected at either a forward or backward detector. With a full spectrum of antimuon lifetimes generating positrons at many time points, we begin to observe an asymmetry between the forward and backward detectors due to continuous precession and decay. The decay lifetime and spin precession allow us to plot the detector asymmetry ratio vs. time, in which the changes in antimuon asymmetry with lifetime provide information on the magnetic fields that perturbed the implanted antimuon spin. **d)** Experimentally, a transverse field may be applied to the sample, the oscillations observed in these data of frequency, f, are directly proportional to the applied field strength felt by the antimuon, allowing for the calibration of the set-up for later observation of internal fields in a material. The peaks and troughs of this oscillation can be ascribed to a muon decaying at a time where it is directly facing one detector over the other.

applied transverse fields allowing us to extract the instrumental calibration constant α. As previously discussed, muons precess at a frequency proportional to the incident field and would therefore precess at a frequency equal to the applied transverse field. Muons also decay at ~2.2 μs on average, meaning that millions of muons will decay across a range of times averaging 2.2 μs. Due to this decay time distribution, a muon precessing in an applied transverse field will give an oscillatory signal, as the muon spin is decaying at different points of its precession illustrated in Figure 2.9c/d. Fitting this oscillating signal to a simple sine function allows us to extract α. Since the applied field is known, the frequency can be calculated. The relationship between applied field strength and frequency provides us with α, allowing the calculation of internal fields by fitting observed frequencies, which may evolve in further measurements. Some experimental data for a QSL candidate were obtained (Figure 2.10.), here we see that the observation of a plateau in relaxation rate vs. time data indicates spin dynamics in the system [144].

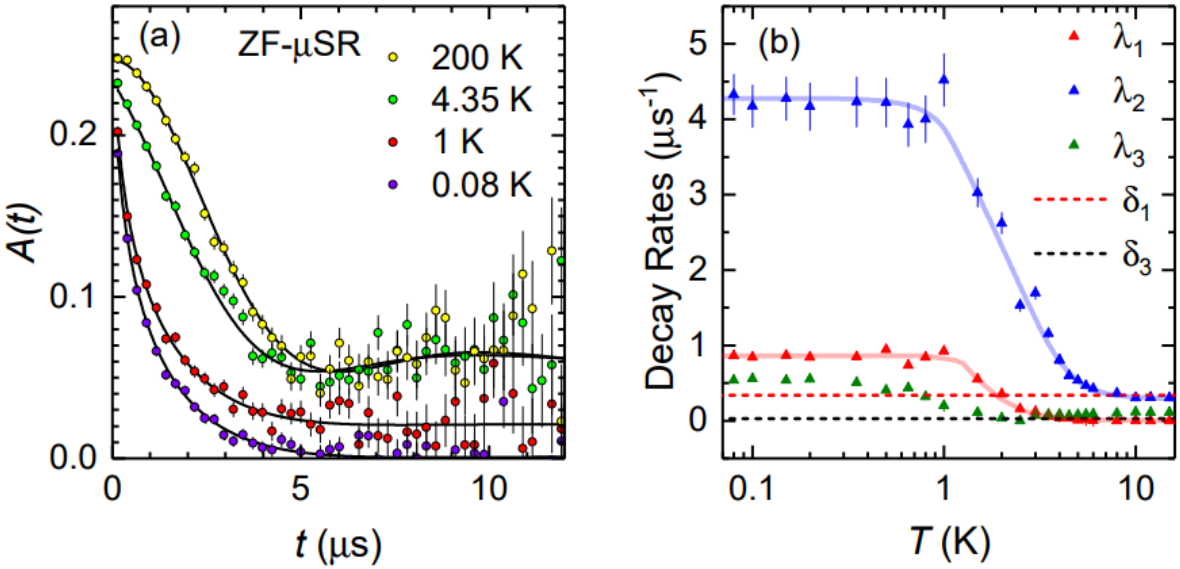


Figure 2.10: Some literature MuSR data for a QSL candidate system, $H_3LiIr_2O_6$. (left) muon asymmetry vs. time showing the fast relaxation of implanted muons across a range of temperatures. (right) Relaxation rate vs. time plot showing a low temperature plateau at ~ 1 K indicative of spin dynamics [144].

Similarly to neutrons, muons cannot be created in the lab, they require spallation sources. However, unlike neutron experiments, muons do not require sample deuteration, as the

muon stopping sites are unaffected by the incoherent scattering characteristics of hydrogen. The relationship of sample size on muon measurement is also not as closely linked as in a neutron experiment, meaning that much smaller samples can be used. The ISIS Neutron and Muon Source generates muons in pulses, which allows for fast collection times but poorer time resolution compared to continuous sources. However, this is only a drawback in cases where interesting phenomena are expected to occur at these short timescales, which is not the case in muon experiments discussed in Chapter 5.

2.9.1 Fitting μSR data

To extract meaningful information from μSR data we must often fit our experimental data to equations that well describe the muon behaviour. We do this using software packages such as WIMDA [145] which provides all functions necessary for the fitting of MuSR data. One of the most important functions in fitting muon data in the presence of a static field is the Kubo-Toyabe function, which we use in Chapter 5 to fit zero field MuSR data. When a muon spin resides within a randomly oriented field with a known root mean square value, the relaxation of this muon under these conditions are described by the Kubo-Toyabe function (Equation 2.15).

$$G_z(t) = \frac{2}{3}\left(1 - \Delta^2 t^2\right)\exp\left(-\frac{1}{2}\Delta^2 t^2\right) + \frac{1}{3} \tag{2.15}$$

One of the main features of this function is the recovery of a $\frac{1}{3}$ tail, within which, the model is exceptionally sensitive to external fields [146], such as those which spontaneously arise in magnetic systems at temperatures below their ordering transition. In cases where nuclear moments are decoupled by external fields, the relaxation of our muon asymmetry is directly influenced by the evolving or static internal field of the sample. In cases where static fields dominate, we apply simple fitting functions such as Lorentzian relaxation to extract the relaxation rate λ for temperature dependence studies we discuss in Chapter 5.

Chapter 3

Crystal and Magnetic Structure Determination of Kagome Containing Metal-Organic Frameworks

3.1 Introduction

In terms of novel "quantum materials discovery", metal-organic frameworks (MOFs) have become the route of choice for many. Featuring a high degree of tunability, MOFs facilitate structural modifications, minimising the challenges of magnetic site disorder. [12] Often occurring in inorganic materials [56, 147], magnetic site disorder leads to difficulty in elucidating the magnetic structure and, in some cases, leads to a breakdown of the desired magnetic topology [148]. Specific MOFs may be considered quantum spin liquid (QSL) candidates when their structures satisfy several properties expected to host such a state. The key properties expected to facilitate a QSL state are the use of $S = \frac{1}{2}$ magnetic atoms, approaching magnetic two-dimensionality and ensuring conventionally frustrated geometries, including triangular, honeycomb and kagome arrangements [9]. MOFs are exceptionally useful to this end because their structures can be modified and therefore tuned towards these desired properties. The ability to easily modify organic components

in MOFs also allows for the close study of broad families of materials sharing properties of interest. An example of how much the magnetism of MOFs can be tuned is given by a study into a family of bimetallic, manganese (II), chromium (III) MOFs, in which magnetic susceptibility was found to vary significantly with the change of solvation and counterions present [149]. By using MOF families for magnetic study, we are able to isolate the structural characteristics directly affecting the magnetic exchange, allowing us to modify and optimise the structures further to produce specific magnetic characteristics [25].

In recent years, there have been numerous examples of kagome-containing metal-organic frameworks that have the potential to host topological quantum states such as the QSL. Although, as discussed in Chapter 1, there has also been much debate in the literature over the magnetic ground states of some MOFs hosting a kagome arrangement of Cu^{2+} atoms [12, 82, 84, 86]. Due to this, we performed a comprehensive study, finding that the magnetic ground states of a family of copper carbonate kagome-containing MOFs with the formula $Cu_3(CO_3)_2(x)_3{\cdot}2ClO_4$, where x is a ditopic organic ligand, hosted a ferromagnetically ordered kagome arrangement. Fortunately, ferromagnetic kagome compounds are still sought after for their electronic properties and potential applications in spintronics [150]. Therefore, magnetically ordered kagome-containing systems found on the path to QSLs, are invariably interesting for study, making the search for QSL candidates highly fruitful regardless of the outcome. As introduced in Chapter 1, one of the first kagome-containing MOFs reported was Cu(1,3-benzenedicarboxylate), (Cu-*bdc*), featuring a kagome arrangement of $S = \frac{1}{2}$, Cu^{2+} ions chelated by *bdc* within the kagome planes and isophthalic acid between the planes. Curie-Weiss analysis of magnetic susceptibility data suggested dominant antiferromagnetic exchange coupling, with a θ_{CW} = -33 K, while the heat capacity confirmed an ordered transition occurring at 2 K, suggesting a degree of frustration [76]. Later, it was discovered through a neutron powder diffraction experiment that Cu-*bdc* was composed of ferromagnetic layers bound antiferromagnetically

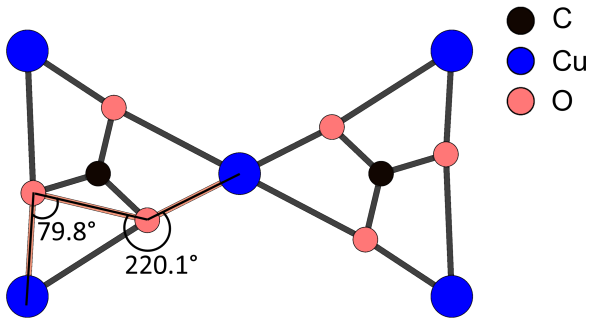


Figure 3.1: A section of a copper carbonate kagome lattice, the proposed exchange pathway and the associated angles are given by black lines, with this model outlined by Mulrooney et al. [83]

between the kagome planes [79]. With dominant ferromagnetic exchange within kagome layers observed in Cu-*bdc*, we hypothesised that alterations to the out-of-plane ligands may drive the magnetically ordered regime to an alternate ground state. To determine whether a similar antiferromagnetic kagome was present in MOFs containing different organic ligands, we isolated a family of materials to study; the first member of this family was $Cu_3(CO_3)_2(bpe)_3{\cdot}2ClO_4$, (MOF-*bpe*) where *bpe* = 1,2-bis(4-pyridyl)ethane.

In this MOF, Cu^{2+} ions form a kagome layer by ligating atmospheric CO_3^{2-} to form characteristic kagome triangles with carbonates simultaneously mediating magnetic exchange via the route proposed in Figure 3.1 above [83]. These copper kagome layers are then covalently bound by unconjugated *bpe* ligands yielding the three-dimensional MOF structure. Our initial hypothesis was that the unconjugated *bpe* ligand would not host exchange between the kagome planes, leaving quasi-two-dimensional, magnetically isolated kagome layers. Since original reports of this system were in disagreement over the magnetic ground state we chose to perform our own study into the magnetic ground state. With one group claiming short-range canted antiferromagnetic order based on AC magnetic susceptibility measurements [84], and others proposing ferromagnetic order at $T_C \approx$ 12 K, based on heat capacity and DC magnetic susceptibility measurements [85]. There was room for the magnetic structure of this system to be comprehensively assigned. To

achieve this, we collected NPD, μSR and SQUID DC magnetic susceptibility data; and with these, were able to produce a consistent model of the magnetic ground state of MOF-*bpe* [12]. Similarly to Cu-*bdc*, through NPD measurement, we find that MOF-*bpe* also orders ferromagnetically within the kagome layers and antiferromagnetically between them. This showed once again that despite a change in the organic ligand, the magnetic ground state remained consistent and that the *bpe* ligand was capable of hosting a superexchange pathway despite being unconjugated. Following our findings for MOF-*bpe*, we focused our attention on the closely related $Cu_3(CO_3)_2(bpy)_3{\cdot}2ClO_4$ (MOF-*bpy*) system, where *bpy* = 1,2-bis(4-pyridyl)ethylene. Comparisons in the literature between MOF-*bpe* and MOF-*bpy* suggested stronger exchange coupling as a result of conjugation in MOF-*bpy*, demonstrating the usefulness of MOF tunability in manipulating the magnetic response [82].

To further our understanding of the effects of interplane ligand exchange and the magnetic response, we began the study of a third member of the $Cu_3(CO_3)_2(x)_3{\cdot}2ClO_4$ family, where x = 4,4-azopyridine, (MOF-*azpy*). We synthesised single crystals for MOF-*bpe*, *bpy* and *azpy* which allowed us to us to refine structural models from SCXRD data before magnetic characterisation through magnetic susceptibility, NPD and μSR measurements used in Chapter 3. Our findings were, again, the presence of ferromagnetically coupled kagome layers, antiferromagnetically coupled between planes in all cases [12]. Because we observe a similar magnetic ground state in all cases, we must look at the finer details, ascertaining what is driving the superexchange across these three interplane ligands. Since it is challenging to confirm the direct effect of the changing interplanar (ethane, ethene and azo) bonds, we can propose, similarly to Ajeesh *et al*, that the conjugation and delocalisation of the *bpy* and *azpy* ligands may play a role. Considering that the NPD data for MOF-*bpe* indicates a canting of moments in the crystallographic *ab*-plane, our assumption was that this may be due to the lack of conjugation. Although inconclusive, our magnetic susceptibility data show small variations in Curie-Weiss temperatures as well as

small differences in the low-temperature susceptibility behaviour as a function of temperature between MOF-*bpe* and the others shown in Figure 3.5, discussed later. To further probe the magnetism, we must look at other characteristics of the $Cu_3(CO_3)_2(x)_3{\cdot}2ClO_4$ family.

One of these characteristics is the presence of ligand disorder, specifically the 50:50 rotational disorder observed in the three cases illustrated in Figure 3.2. We initially proposed that there may be a magnetic response driven by correlated disorder; however, we were unable to take this analysis further directly. Instead, we approached this indirectly, by synthesising another member of the $Cu_3(CO_3)_2(x)_3{\cdot}2ClO_4$ family. Featuring no chemical disorder about the interplane ligands we expected to outline the effect of ligand disorder on the magnetism observed. For this study, we grew single crystals of $Cu_3(CO_3)_2(bpa)_3{\cdot}2ClO_4$ (MOF-*bpa*) where *bpa* is 4,4-bipyridyl acetylene (Figure 3.2), this system features a 180° ethyne bond as well as conjugation, making it an excellent candidate for isolating a comparison to the non-conjugated MOF-*bpe* and the conjugated and disordered MOF-*bpy*, *azpy*. Previous reports of this system suggest an ordering temperature T_C = 9.5 K and a Curie-Weiss temperature θ_{CW} = +26.6(8) K, suggesting that the magnetic exchange interactions of MOF-*bpa* are relatively consistent with the other MOFs outlined [82, 85, 151]. We find consistent results in all cases, with positive values of θ_{CW} suggesting similar ferromagnetic dominance within the kagome plane. In this chapter, we present the synthesis of four kagome-containing MOFs, sharing Cu^{2+}, CO_3^{2-} kagome layers, interconnected by ditopic organic ligands. We then present the structural and magnetic characterisation of them clarifying the literature reports before our own comparisons between them. We aim to confirm the initial findings of Keene *et al* [86], for MOF-*bpa*, and build upon their magnetic characterisation through NPD methods. In doing so we hope to observe the effects, if any, of removing ligand disorder on the magnetic properties.

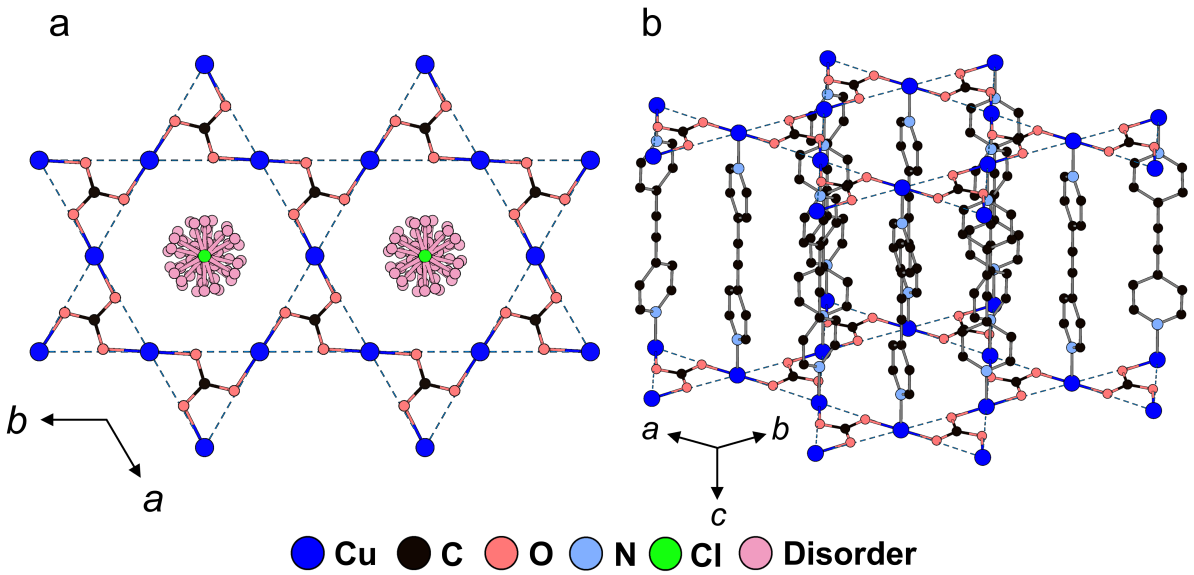


Figure 3.2: The structure of $Cu_3(CO_3)_2(bpa)_3{\cdot}2ClO_4$, illustrated from refined crystallographic information, the system is made up of Cu^{2+} carbonate kagome layers (a), covalently linked by the organic ligand 4,4-bipyridyl acetylene (b). Dashed lines represent Jahn-Teller distorted bonds while the perchlorate is shown to be heavily disordered removed from (b) for clarity.

3.2 Experimental Methods

3.2.1 Single-Crystal Synthesis

Samples of the $Cu_3(CO_3)_2(x)_3{\cdot}2ClO_4$ MOF family were, as discussed, synthesised by a modified Solvay process [103]. Single crystals of $Cu_3(CO_3)_2(x)_3{\cdot}2ClO_4$ (MOF-x), where x is *bpe* [1,2-bis(4-pyridyl)ethane, $C_{12}H_{12}N_2$], *bpy* [1,2-bis(4-pyridyl)ethylene, $C_{12}H_{10}N_2$], *azpy* [4,4'-azopyridine, $(C_{10}H_8N_4)$], *bpa* [bis(4-pyridyl)acetylene, $(C_{12}H_8N_2)$] were synthesised as follows:

MOF-*bpe*

For single crystals of MOF-*bpe*, $Cu(ClO_4)_2{\cdot}6H_2O$ (550 mg, 1.51 mmol) and *bpe* (270 mg, 1.51mmol) were added to aqueous NH_3 (15%, 200 cm^3). The mixture was stirred until fully dissolved and left to slowly evaporate for 3 days before a deep purple product was isolated by filtration and washed with H_2O (3×50 cm^3) and MeOH (3×50 cm^3). MOF-*bpe* (441

mg, 0.42 mmol, 84%) was isolated as purple hexagonal plate-like crystals. CHN elemental analysis data were measured on a Thermo Scientific FlashSmart CHNS/O Elemental Analyser, indicating sample purity from the expected values for $Cu_3(CO_3)_2(bpe)_3{\cdot}2ClO_4$: C, 43.0; H, 2.4; N, 7.9; found, C, 43.0; H, 2.4; N, 7.9.

MOF-*bpy*

For single crystals of MOF-***bpy***, $Cu(ClO_4)_2{\cdot}6H_2O$ (66 mg, 0.18 mmol) and ***bpy*** (33 mg, 0.18 mmol) were dissolved in a mixture of aqueous NH_3 (35%, 3.75 cm^3), methanolic NH_3 (7 N, 4 cm^3), and MeOH (7.25 cm^3). The mixture was stirred until fully dissolved and left to slowly evaporate over 7 days before a deep blue product was isolated by filtration and washed with H_2O (3 × 20 cm^3) and MeOH (3 × 20 cm^3). MOF-***bpy*** (48 mg, 0.05 mmol, 76%) was isolated as purple hexagonal plate-like crystals with the expected CHN analysis: C, 43.2; H, 2.9; N, 8.0; found, C, 43.2; H, 2.9; N, 7.8.

MOF-*azpy*

For single crystals of MOF-***azpy*** was prepared by dissolving $Cu(ClO_4)_2{\cdot}6H_2O$ (185 mg, 0.5 mmol) in aqueous NH_3 (35%, 7 cm^3) and H_2O (5 cm^3). To this was added dropwise a solution of azpy (92 mg, 0.5 mmol) in EtOH (5 cm^3) and aqueous NH^3 (35%, 7 cm^3). The resulting black solution was stirred for 30 min, allowed to evaporate slowly for 12 days before a black product was isolated by filtration and washed with H_2O (3 × 20 cm^3) and EtOH (3 × 20 cm^3). MOF-***azpy*** (152 mg, 0.14 mmol, 87%) was isolated as black needle-shaped crystals with the expected CHN analysis: C, 33.7; H, 2.5; N, 15.8; found, C, 33.3; H, 2.5; N, 15.8.

MOF-*bpa*

Finally, For single crystals of MOF-***bpa***, $Cu(ClO_4)_2{\cdot}6H_2O$ (514 mg, 1.39 mmol) and ***bpa*** (250 mg, 1.39 mmol) were added to aqueous NH_3 (16%, 200 cm^3). The mixture was stirred until fully dissolved and left to slowly evaporate for 5 days before a deep purple

product was isolated by filtration and washed with H_2O (3×50 cm^3) and MeOH (3×50 cm^3). MOF-*bpa* (402 mg, 0.38 mmol, 78%) was isolated as purple hexagonal plate-like crystals with the expected CHN analysis: C, 43.5; H, 2.3; N, 8.0; found, C, 43.5; H, 2.3; N, 7.9.

3.2.2 Powder X-ray Diffraction

A laboratory powder X-ray diffractometer was used in conjunction with the samples in this chapter. These measurements were taken on a Bruker D8 diffractometer with a monochromated Cu $K_\alpha 1$ radiation source of wavelength $\lambda = 1.54056$ Å. Around 200 mg of sample was ground to a homogeneous powder and mounted on a low background silicon holder for analysis. Scans were taken between $4 - 50°$ 2θ, with a step size of 0.00164° at room temperature.

3.2.3 Single-Crystal X-ray Diffraction

Single crystal X-ray diffraction data were collected on the I19 beamline at Diamond Light Source with a radiation wavelength of 0.6889 Å. The collected data were then processed using CrysAlis PRO171.42.49 [152] and Olex2 software packages [120]. Structural determination was achieved via a direct methods approach using the ShelXS package [153], then refined using the ShelXL [154] package using a full-matrix, least-squares approach based on F^2. Hydrogen positions and thermal parameters were restrained to values consistent with the atoms they were bound to, as X-ray scattering data does not provide high enough resolution to solve these hydrogen atoms individually. The bond lengths and angles of the heavily disordered perchlorate anions were restrained using RIGU in the fit of MOF-*bpy* and MOF-*bpa*, with the addition of fixed occupancies providing a stable refinement. In the cases of MOF-*bpe*, MOF-*azpy* refinement of the perchlorates was not possible due to low data quality. These data were Rietveld refined using a twenty term Chebyschev, with instrumental peak shapes refined using A LaB_6 standard.

3.2.4 Magnetic Susceptibility

Zero field cooled (ZFC) and field cooled (FC) magnetic susceptibility measurements were collected on a Quantum Design magnetic property measurement system 3 (MPMS 3) SQUID magnetometer in DC mode, measuring between 1.8−300 K. A palladium standard was used to calibrate the instrument prior to measurement. Samples were mounted using gelatin capsules which were sealed with G-varnish before being secured in plastic sample holders. Magnetic susceptibility vs. temperature measurements were collected for all samples in an applied field of 100 Oe or 1000 Oe. Magnetic susceptibility vs. field measurements were performed up to 7 T and full magnet resets were run to eliminate any remnant fields within the SQUID magnet. These measurements were taken between -7 T and 7 T, which were the upper limits of the SQUID instrument.

3.2.5 Neutron Powder Diffraction

Neutron powder diffraction measurements were taken on the WISH beamline at the ISIS Neutron and Muon source. A sample of MOF-*bpa* (~ 1.5 g) was mounted in a vanadium can and secured in a sample holder. These measurements were taken in a helium cryostat at temperature points of 1.4 K and 25 K. The raw data were then extracted and refined against the CIF data obtained by single crystal XRD using the Rietveld method in GSAS2 and Fulprof software [155, 156]. These data were Rietveld refined using a twenty term Chebyschev, with peak shapes refined to the instrument using a NaCaAlF standard sample.

3.3 Results and Discussion

3.3.1 Crystal Growth

At the time of starting this project, the current literature on MOF-*bpe* and MOF-*bpy* featured crystallographic data collected via single crystal and powder diffraction methods, respectively. As single-crystal growth of MOF-*bpy* was not yet reported [82]. This literature was used to assist in the growth of large single crystals of both systems, improving the current crystallographic understanding of MOF-*bpy* specifically. Interestingly, the grown morphologies of these two MOFs differed significantly. While MOF-*bpe* formed intergrown plate-like crystals, MOF-*bpy* formed needles. This preferential growth in opposing crystallographic planes was a point of interest, as needle crystals are more challenging to collect SCXRD data for.

As MOF-*bpy* required the use of methanol due to water solubility issues, it was expected to be the main source of this preferential growth. To mitigate this, we optimised solvent ratios for purpose, minimising the use of methanol, which we found led to the growth of MOF-*bpy* crystals in a plate-like regime. It can be extracted from this experiment that the concentration of water during nucleation has a direct impact on the crystal morphology. A simple explanation for this is that water has a higher surface tension, which facilitates (observed) crystal growth at the liquid-air interface in MOF-*bpe* syntheses. The use of a "minimum" methanol and "maximum" water in MOF-*bpy* synthesis facilitated the growth of diffraction-quality plate-like single crystals.

In the case of MOF-*azpy*, no previous literature outlined the synthetic route or crystal structure; however, it was assumed that it would form similarly to MOF-*bpe* and MOF-*bpy*. To some extent this was the case however, similarly to *bpy*, *azpy* was insoluble in water. This meant that a screening was necessary to find solvents that dissolved *azpy* while simultaneously remaining miscible with water. Ethanol was isolated as the optimal

solvent. This facilitated the growth of needle-shaped crystals of MOF-*azpy*. Optimisation of the method to produce plate-like MOF-*azpy* crystals was not fruitful; however, the growth of large enough needle-like crystals on a growth time scale of 3 months proved to be sufficient for diffraction experiment.

The final MOF studied in this chapter is MOF-*bpa* [151]. This MOF is synthesised identically to MOF-*bpe* and forms large block crystals with well-defined domains. The synthesis of high-quality crystals in all cases directly improved the diffraction data acquired, since peak intensity is closely linked to crystallite domain size, facilitating the conclusive crystallographic study reported herein.

3.3.2 Single-Crystal Structural Determination

As discussed, the $Cu_3(CO_3)_2(x)_3{\cdot}2ClO_4$ MOF family is characterised by kagome layers of Cu^{2+} cations chelated by CO_3^{2-} anions, covalently bound along the *c*-axis by long, ditopic bipyridyl ligands. Generally, the kagome lattice is made up of interconnected equilateral triangles. However, in the case of these MOFs, a distorted kagome lattice is observed, made up of alternating, inequivalent, equilateral triangles forming a "breathing" kagome lattice. The growth of large single crystals facilitated the production of individual crystallographic information files (CIFs) for each MOF system. The previous analysis had relied on the modification of the reported MOF-*bpe* CIF for the Rietveld analysis of powder diffraction data, which assumed the conservation of unit cell symmetry across the MOF family, which was not necessarily correct.

Initially, the literature report of MOF-*bpe* by Kanoo *et al* presented a crystallographic information file (CIF) model of MOF-*bpe* in the $P\bar{6}$ space group. This assignment of a primitive cell, featuring a centre of inversion and a six-fold rotational symmetry, translates to a model that cannot possibly describe the chemistry of the *bpe* ligand. The assignment of $P\bar{6}$ would orient the central ethane bond, perpendicular to the orienta-

tion of the pyridyl groups, which goes against the established bond geometry rules of bond-hybridisation theory. Therefore, we proposed the assignment of the $P3$ space group, which provides excellent agreement with experimental data, along with the observation of chemically sensible bonding geometries. To achieve the fits we report here, an inversion twin law was applied about the a-axis, RIGU restraints were applied to the Cl-O bonds to prevent divergence, and SADI and EADP restraints were applied to carbon atoms and C-C bonds to ensure homogeneous atomic displacement and thermal parameters within the organic ligands, again preventing divergence.

For MOF-*bpa* the higher symmetry hexagonal space group $P6/m$ was assigned, capturing the lack of ligand disorder and increased symmetry. These assignments were only made possible by the growth of high-quality single crystals, with the structures and crystallographic data outlined in Figure 3.3 and Table 3.1 respectively. We see here that the

Table 3.1: Summarised crystallographic data for MOF-*bpe*, -*bpy*, -*azpy* and -*bpa* from the refinement of data collected on the I19 beamline at Diamond Light Source at 298 K.

MOF	*bpe*	*bpy*	*azpy*	*bpa*
formula	$C_{38}H_{36}Cl_2Cu_3N_6O_{14}$	$C_{38}H_{30}Cl_2Cu_3N_6O_{14}$	$C_{32}H_{24}Cl_2Cu_3N_12O_{14}$	$C_{38}H_{24}Cl_2Cu_3N_6O_{14}$
M_r (g mol^{-1})	1062.25	1056.20	1062.15	1050.15
temperature (K)	298	298	298	298
crystal system	trigonal	trigonal	trigonal	hexagonal
space group	$P3$	$P3$	$P3$	$P6/m$
a (Å)	9.4043(1)	9.3058(1)	9.2929(1)	9.2453(1)
c (Å)	13.3063(1)	13.3653(2)	12.9593(1)	13.5788(2)
V (Å^3)	998.92(5)	987.22(5)	951.39(1)	984.26(2)
Z	1	1	1	1
ρ_{calc} (g cm^{-3})	1.785	1.750	1.820	1.735
μ (Cu Kα) (mm^{-1})	3.766	3.811	4.006	1.678
$F(000)$	539.0	533.0	533.0	527.0
crystal size (mm^3)	0.16 × 0.07 × 0.06	0.31 × 0.04 × 0.04	0.18 × 0.12 × 0.09	0.009 × 0.008 × 0.004
radiation wavelength (Å)	0.6889	0.6889	0.6889	0.6889
R_{int} (%)	8.98	6.93	11.47	10.16
GooF	1.02	1.00	1.19	1.22
R_1,[a] wR_2[b] ($I > 2\sigma(I)$) (%)	4.55, 13.11	6.29, 17.80	5.47, 18.02	3.67, 10.41
R_1,[a] wR_2[b] (all data) (%)	4.75, 13.43	6.71, 18.39	6.30, 18.88	5.88, 14.56
$\Delta\rho_{max}$, $\Delta\rho_{min}$ (eÅ^{-3})	0.47, -0.50	1.30, -0.81	0.60, -0.95	0.79, -0.53
Flack parameter	0.47(1)	0.38(2)	0.41(2)	0

values for the Flack parameter are closer to 0.5 than 0 or 1 in MOF-*bpe*, *bpy* and *azpy*, indicating a non-centrosymmetric cell. The Flack parameter is the measure of agreement between the data and model in situations where the absolute structure cannot be

unambiguously

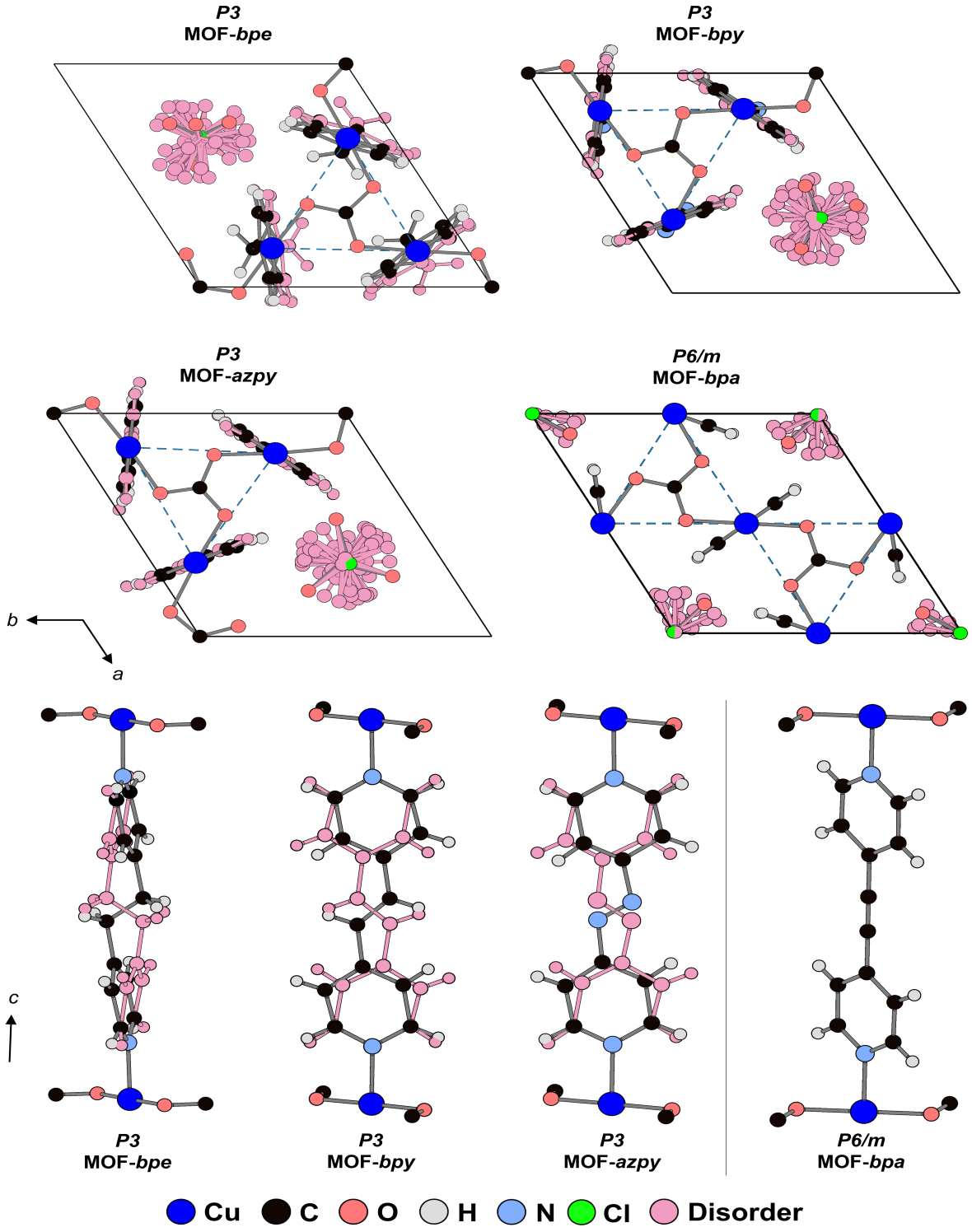


Figure 3.3: A comparison of each MOF system, MOF-*bpe*, *bpy* and *azpy* are in the $P\bar{3}$ while MOF-*bpa* is in the higher symmetry $P6/m$ space group. The pink atoms and bonds represent disorder about their respective sites, while we see that MOF-*bpa* contains disorder only in the perchlorate counterions.

refined with one consistent cell. This may be the case when; chirality, low data quality or where twinning is present such as our assignment of an inversion twin in the three outlined MOFs. Values close to 0 or 1 indicate an accurate absolute structure with a value of 1 indicating an absolute structure inverse to that of the one refined, while values approaching 0.5 indicate a disagreement between the modelling of the present reflections to one absolute structure. In fitting the SCXRD data, we used a twin law for MOF-*bpe*, *bpy* and *azpy*. The equal and opposite matrices were (1 0 0, 0 1 0, 0 0 1) and (−1 0 0, 0 −1 0, 0 0 −1), giving the Flack parameters in Table 3.1. These structures were solved using room-temperature synchrotron data collected on the I19 beamline (DLS).

As illustrated, rotational ligand disorder is present in MOF-*bpe*, *bpy* and *azpy*, wherein the ratios are close to 50:50, suggesting that there is no preferential ligand orientation. These models also show that the "breathing" kagome network is present in all cases, with elongated Cu-O bonds originating from Jahn-Teller distortion (represented by dotted lines in Figure 3.2) in the *ab* plane. The planar, disorder-free acetylene ligands present in MOF-*bpa* facilitate the higher symmetry space group assignment. In addition to the data presented, we also collected at 30 K, providing us with more representative crystallographic models for the Rietveld refinement of the low-temperature neutron powder diffraction data discussed later.

3.3.3 Laboratory Powder X-Ray Structure Confirmation

To confirm phase purity and refine cell parameters in all cases, laboratory PXRD data were collected at room temperature and fit using the Le Bail method, illustrated in Figure 3.4. MOF-*bpe*, *bpy*, *azpy* were refined against the $P\bar{3}$ model and MOF-*bpa* against $P6/m$, with refined lattice parameters presented in Table 3.2.

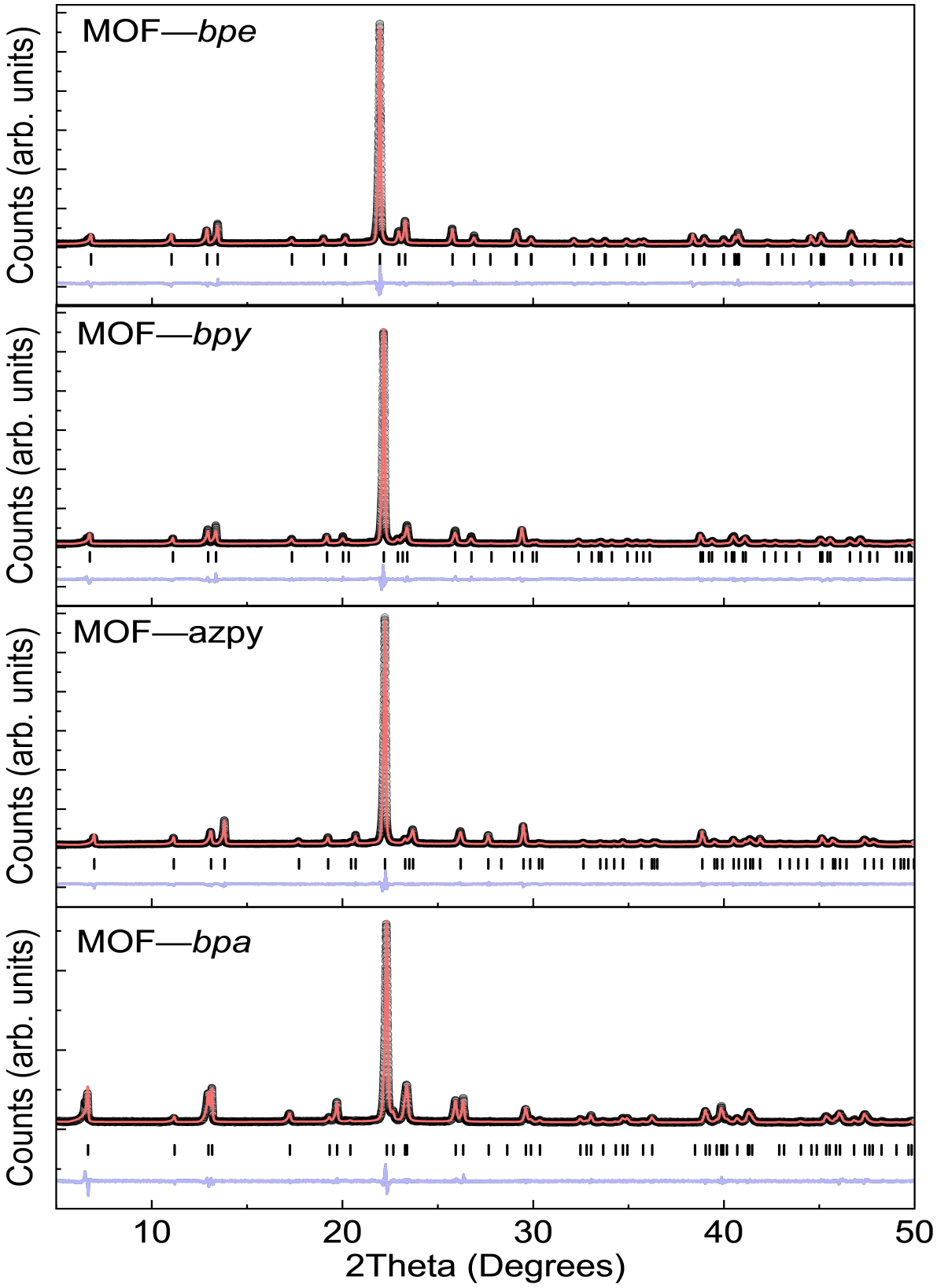


Figure 3.4: Le Bail fits using; the $P3$ model for MOF-bpe, bpy and $azpy$, alongside the $P6/m$ model for MOF-bpa, against laboratory collected PXRD data Cu$K\alpha$.

Table 3.2: Summary of refined lattice parameters collected on a Panalytical Empyrean at 300 K.

MOF	a/ Å	c/ Å
bpe	9.410(15)	13.328(20)
bpy	9.315(6)	13.391(20)
azpy	9.299(6)	12.974(14)
bpa	9.256(5)	13.610(13)

Since the asymmetric unit cells of these MOFs contain over 60 atoms including disorder, refining atomic positions and thermal parameters freely using laboratory data was not reliable. As a result, analysis of these data should also be approached with caution, since data of this quality are generally only used to confirm the phase purity and cell dimensions of the synthesised systems. As such, we collect high-resolution PXRD data on the I11 beamline (DLS) for MOF-*bpa* to more comprehensively refine our structural model.

3.3.4 High-Resolution Powder X-Ray Structure Determination

While SCXRD provides us with a structural model for a single crystal sample, this cannot always be considered representative of the bulk composition. Single-crystal data often fails to capture bulk phenomena such as; amorphous content, preferred orientation, and differing phase fractions in samples. As such, PXRD data facilitate the study of the average structure of a given material, taking into account all effects that may influence the observed powder pattern. High-resolution data provide us with more information and therefore the opportunity for a more comprehensive statistical analysis with reduced error. As discussed previously, more accurate structural models allow more accurate magnetic characterisation, so we used synchrotron X-ray data for the Rietveld analysis of MOF-*bpa* shown in Figure 3.5. For this refinement the thermal parameters for the perchlorates were not refined as the high levels of disorder led to an unstable refinement. For the remaining atoms, excluding hydrogen, isotropic thermal parameters and atomic

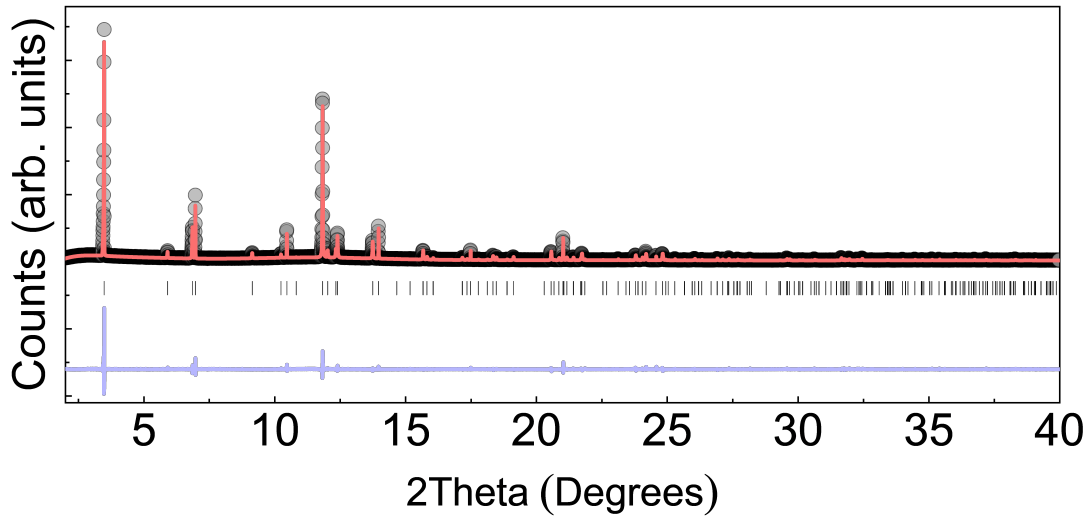


Figure 3.5: Rietveld refinement of MOF-*bpa* against the *P*6/m model obtained from SCXRD analysis with a weighted R value, R_{WP} = 8.793 %

coordinates were allowed to refine freely. Instrument parameters were obtained through the Rietveld refinement of a silicon NIST 640c standard, against the collected data. One point outstanding from this refinement is the reduced intensity of several reflections. All 0 0 *l* reflections are under-fit which may indicate a preferred orientation effect; however, there is also reduced intensity at (0 2 0), (0 2 1) and (0 2 4) suggesting a different source of this phenomenon. Similar Rietveld powder analysis was carried out prior to this study on other members of the kagome-containing MOF family, with similar intensity underfitting suggested to arise due to preferred orientation of "rod-like" crystals [66]. The data presented here however, were collected from crystals with no obvious preferential growth since we were able to optimise crystal morphology synthetically. The lack of a clear distinction between data collected on "rod-like" crystals and well-proportioned crystals suggests that the intensity issues observed in all cases do not arise from preferred orientation. There are several alternative explanations for the slight disagreement between fit and data; ligand disorder driven peak-broadening, of course, does not apply to MOF-*bpa*, also implying that this may not be the source of similar under-fit data in the other MOF family members. The most likely possibility that satisfies for all four kagome-containing MOFs is that the SCXRD models do not fully capture the long-range disorder

of the breathing kagome network, which we have seen artificially inflates the U_{iso} values of copper and carbonate sites [12, 66]. The crystal structure parameters for the Rietveld refinement of MOF-*bpa* are shown in Table 3.3.

Table 3.3: Refined structure parameters for the $P6/m$ model of MOF-*bpa* fit to XRD data collected on I11, Diamond, at 300 K. Final refined lattice parameters were a = 9.2503(4) Å and c = 13.5812(5) Å, R_{WP} = 8.637 % and reduced χ^2 = 1.56.

Atom	Site	x	y	z	Occupancy	U_{iso}
Cu1	2/m(001)	1.0000	0.5000	0.0000	1	0.051(7)
			Carbonate			
O1	m(001)	0.7824(7)	0.4861(2)	0.0000	1	0.011(1)
C1	-6	0.6666	0.3333	0.0000	1	0.001(8)
			Bipyridyl acetylene			
N1	2(001)	1.0000	0.0000	0.1468(6)	1	0.050(1)
C2	1	0.9463(4)	0.588(8)	0.1971(4)	1	0.069(1)
H2	1	0.908(1)	0.6497(6)	0.1623(7)	1	0.056(8)
C3	1	0.9457(6)	0.5930(6)	0.2986(4)	1	0.086(8)
H3	1	0.9095(6)	0.6573(5)	0.3316(5)	1	0.063(2)
C4	2(001)	1.0000	0.5000	0.3507(8)	1	0.051(1)
C5	2(001)	1.0000	0.5000	0.4563(1)	1	0.113(3)
			Perchlorates			
Cl1	1	1.0056(9)	0.0003(1)	-0.0090(1)	0.0833	0.050(6)
O11	1	1.0208(6)	0.0707(4)	-0.1081(6)	0.0833	0.070(1)
O12	1	1.1699(9)	0.0388(3)	0.0269(8)	0.0833	0.066(3)
O13	1	0.9095(8)	-0.1824(5)	-0.0131(5)	0.0833	0.050(5)
O14	1	0.9225(5)	0.0633(1)	0.0550(1)	0.0833	0.101(2)
Cl2	1	0.9979(7)	1.0160(9)	0.4927(3)	0.0833	0.054(8)
O21	1	0.8733(2)	1.0580(9)	0.5238(3)	0.0833	0.072(1)
O22	1	1.1523(4)	1.1770(8)	0.4891(7)	0.0833	0.071(1)

O23	1	0.9537(2)	0.9416(9)	0.3938(9)	0.0833	0.081(7)
O24	1	0.0241	0.1617	-0.01089	0.0833	0.087(1)

With single-crystal and powder diffraction methods in agreement on the $P6/m$ assignment of MOF-*bpa* we can move on to further characterise the system via magnetic susceptibility measurements. To compare Rietveld refinement and single crystal XRD solutions to the structure we compare the jahn-teller distorted Cu-O bond length error. For the single crystal data the bond length is 2.67799(3) Å, while the Rietveld refined model is 2.67961(12) Åsuggesting reduced bond length error in the SCXRD data acquired.

3.3.5 Comparisons of Magnetic Susceptibility Data

DC SQUID temperature-dependent magnetic susceptibility data were collected for MOF-*bpe*, *bpy*, *azpy* and *bpa* shown in Figure 3.6. A temperature-independent background subtraction was performed using a diamagnetic palladium standard provided by Quantum Design. The purpose of these comparisons is to ascertain whether the MOF-*bpa* has a magnetic response different from that of the previously reported MOFs [12]. From these data alone, we struggle to find clear differences between the four, aside from the magnetic response of MOF-*bpe* being a factor of 10 higher. In lieu of heat capacity data, we performed further analysis via Fisher's specific heat calculations, providing estimations of transition temperature, T_C, through derivative plots of susceptibility data (Figure 3.7). In Fisher's specific heat plots, inflection points indicate the presence of a spontaneous change in the bulk magnetic susceptibility. Interestingly, one could argue that there are two inflection points in MOF-*bpy* and MOF-*bpa*, in these graphs. If we were to consider this at face value, it may indicate an increase in bulk susceptibility followed by a decrease in susceptibility within the 1.5 K range. Although this could be interpreted as ferromagnetic order occurring at a temperature higher than that of the antiferromagnetic counterpart, it would be challenging to draw this conclusion from these isolated measurements alone. Another point of interest here is that a trend begins to emerge. Across the series; *bpe*

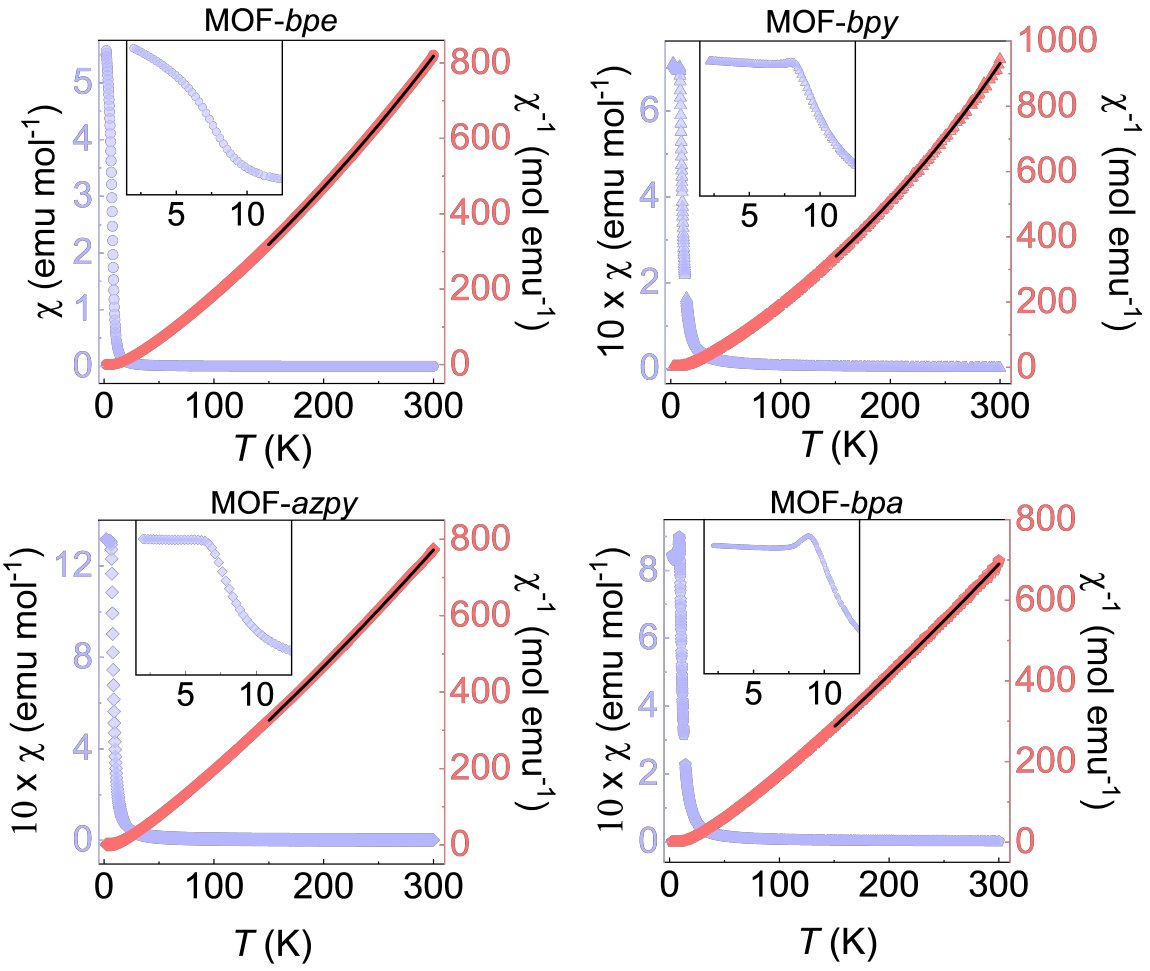


Figure 3.6: Temperature dependent magnetic susceptibility measured in an applied field of 0.1 T. Curie-Weiss fits (black) of the inverse susceptibility (red) were performed across temperature ranges above 100 K using Equation 2.5. The insets show the low-temperature behaviour in each case. Note: an instrumental error led to a loss of data in MOF-*bpy* and MOF-*bpa* between 13 – 14 K.

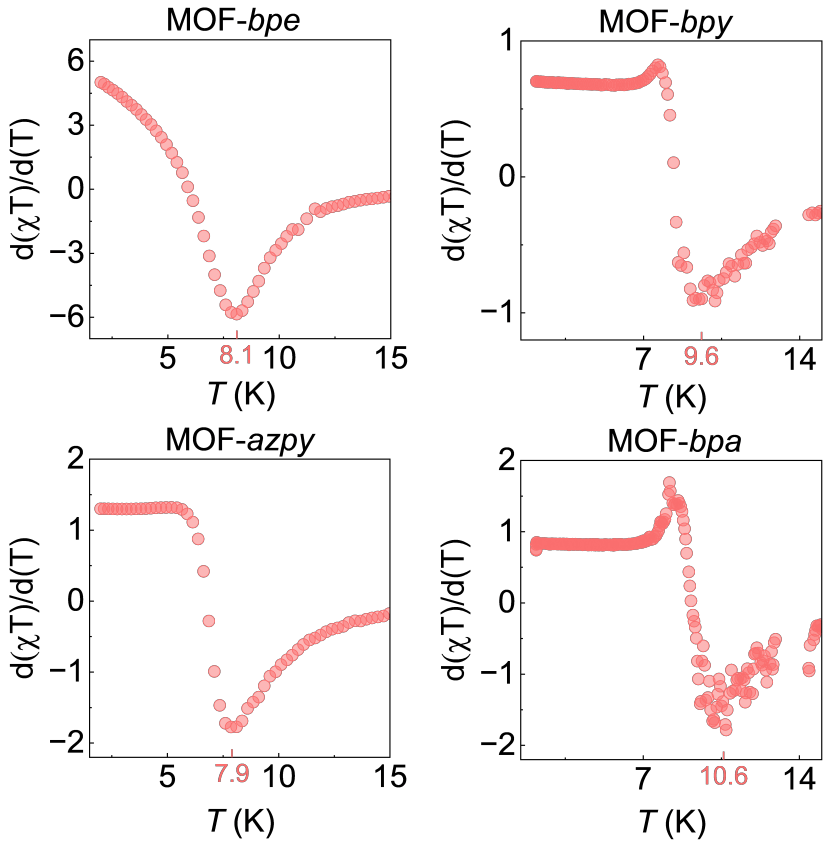


Figure 3.7: Derivative plots of temperature dependent magnetic susceptibility measured in an applied field of 0.1 T for MOF-*bpe*, *bpy*, *azpy* and *bpa*. These plots indicate the presence of inflection points corresponding to spontaneous change in the magnetic susceptibility of internal moments.

$< azpy < bpy < bpa$, inflection corresponding to a reduction in susceptibility becomes more intense, that is, the negative inflection around 8 K in MOF-*bpa* is significantly sharper than the smooth curve observed in MOF-*bpe* at around 6 K. A summary of magnetic data derived from susceptibility and Fisher-specific heat is given in Table 3.4 below. Although, we see no evidence that MOF-*bpa* deviates significantly from the motif

Table 3.4: Comparisons of key data from magnetic susceptibility and Fisher specific heat measurements.

MOF	θ_{CW}/ K	μ_{eff}/ μ_b	χ_0/emu mol^{-1}	T_C/ K
bpe	26.067(1)	1.86(01)	$-3.53x10^{-6}$	8.1
bpy	24.910(54)	1.85(02)	$-4.889x10^{-6}$	9.6
azpy	25.036(27)	1.80(02)	$-1.82x10^{-6}$	7.9
bpa	26.627(3)	1.87(1)	$-2.22x10^{-6}$	10.6

of dominant ferromagnetic exchange interactions through Curie-Weiss analysis, we observe a higher T_C = 10.6 K extracted from Fisher's specific heat data. Despite small deviations between systems, it is likely that MOF-*bpa* behaves analogously. To further elucidate the magnetic ground state of MOF-*bpa* we collected and analysed NPD data, confirming whether the long-range ordered regime of the other MOFs are consistent with MOF-*bpa*.

3.3.6 Determination of the Magnetic Structure of MOF-*bpa* by Neutron Powder Diffraction

Data for MOF-*bpa* were collected at 1.5 and 25 K on the WISH diffractometer at ISIS Neutron and Muon source. Instrumental parameters were calculated using the Rietveld refinement of a $NaCaAlH_2OF_6$ standard across the five detector banks. Although it is often desirable to deuterate hydrogen-containing samples, incoherent scattering in MOF-*bpa* did not prevent nuclear and magnetic refinements from being successfully carried out. To reliably conduct a magnetic refinement, the scale factor must be extracted from a nuclear refinement. This is necessary because the intensity fitting of a magnetic Bragg reflection is directly proportional to both the magnetic structure being refined against and the scale factor. Therefore, obtaining a scale factor from a nuclear refinement al-

lows us to fix this value during magnetic refinement, which is standard practice. In the case of MOF-*bpa* a multibank Rietveld refinement was performed without constraints or restraints on data collected at 25 K. These data were refined against the 30 K SCXRD refined CIF for MOF-*bpa* as this provides a temperature-consistent model for the 25 K measurement unlike the 300 K I11 refined CIF. The isotropic thermal parameters and atomic displacements were allowed to be freely refined in all atoms except for the disordered perchlorate, the fits and data are shown in Figure 3.8 and Table 3.5 respectively.

Table 3.5: Refined structure parameters for the $P6/m$ model of MOF-*bpa* fit to NPD data collected on WISH, ISIS, at 25 K. Final refined lattice parameters were a = 9.1552(5)Å and c = 13.6104(3) Å, global R_{WP} = 3.20 % and reduced χ^2 = 170.82.

Atom	Site	x	y	z	Occupancy	U_{iso}
Cu1	2/m(001)	0.5000	0.0000	0.5000	1	0.067(9)
			Carbonate			
O1	m(001)	0.5156(6)	0.2263(3)	0.5000	1	0.018(1)
C1	-6	0.6667	0.3333	0.5000	1	0.028(8)
			Bipyridyl acetylene			
N1	2(001)	0.5000	0.0000	0.3441(8)	1	0.055(3)
C2	1	0.4105(1)	0.0543(1)	0.3029(2)	1	0.041(8)
H2	1	0.3409(1)	0.0932(2)	0.1676(1)	1	0.032
C3	1	0.4063(1)	0.0554(1)	0.2013(2)	1	0.046(6)
H1	1	0.3479(1)	0.0933(1)	0.3385(1)	1	0.032
C4	2(001)	0.5000	0.0000	0.1494(2)	1	0.039(9)
C5	2(001)	0.5000	0.0000	0.0444(3)	1	0.050(7)
			Perchlorates			
Cl1	1	0.0060	0.005	0.4875	0.0833	0.025
O11	1	-0.0060	-0.0610	0.3918	0.0833	0.049
O12	1	0.1770	0.1170	0.5120	0.0833	0.041

O13	1	-0.0670	-0.1310	0.5556	0.0833	0.061
O14	1	-0.0880	0.0910	0.4890	0.0833	0.050
Cl2	1	0.0190	0.0061	-0.0076	0.0833	0.021
O21	1	0.1810	0.0290	0.0113	0.0833	0.054
O22	1	-0.0990	-0.1080	0.0614	0.0833	0.048
O23	1	-0.0290	-0.0560	-0.1053	0.0833	0.038
O24	1	0.0280	0.1660	-0.0011	0.0833	0.051

The multibank Rietveld refinement of MOF-*bpa* provides us with a scale factor in Bank 1 of 5.604(4), which will be used in the magnetic refinement. First however, we must perform a subtraction of Bank 1, 25 K data from 1.5 K data to highlight any magnetic Bragg intensity. This subtraction is performed using Bank 1 as this is the only bank with a long enough d-spacing range to observe the magnetic intensity, shown in Figure 3.9. The Bragg reflection observed at 27.21 Å is at precisely double the refined crystallographic c-axis of 13.6104 Å suggesting a doubling of this crystallographic c-axis in the magnetic unit cell and therefore a propagation vector of $\boldsymbol{K} = (0\ 0\ \frac{1}{2})$. This is a feature consistent with the analysis of WISH data for MOF-*bpe*, *bpy*, and *azpy* performed within the group [12]. The results of our analysis suggested the presence of ferromagnetically coupled copper carbonate kagome planes, which are antiferromagnetically coupled along the c-axis.

The magnetic structure determination was carried out using Fullprof software in the magnetic space group $P1$. The $P1$ space group allows modelling of both ferromagnetic and antiferromagnetic components expected within MOF-*bpa*, which would not be captured by higher-symmetry space group assignment, as their symmetry would be broken to allow these two components. The fitting of subtracted data to the $P1$ space group is shown in Figure 3.9. The $P1$ space group has no symmetry constraints, and as a result, a refinement against this space group using so few magnetic Bragg reflections requires multiple constraints. To begin, we observe that only $(0\ 0\ l)$ reflections are present, meaning

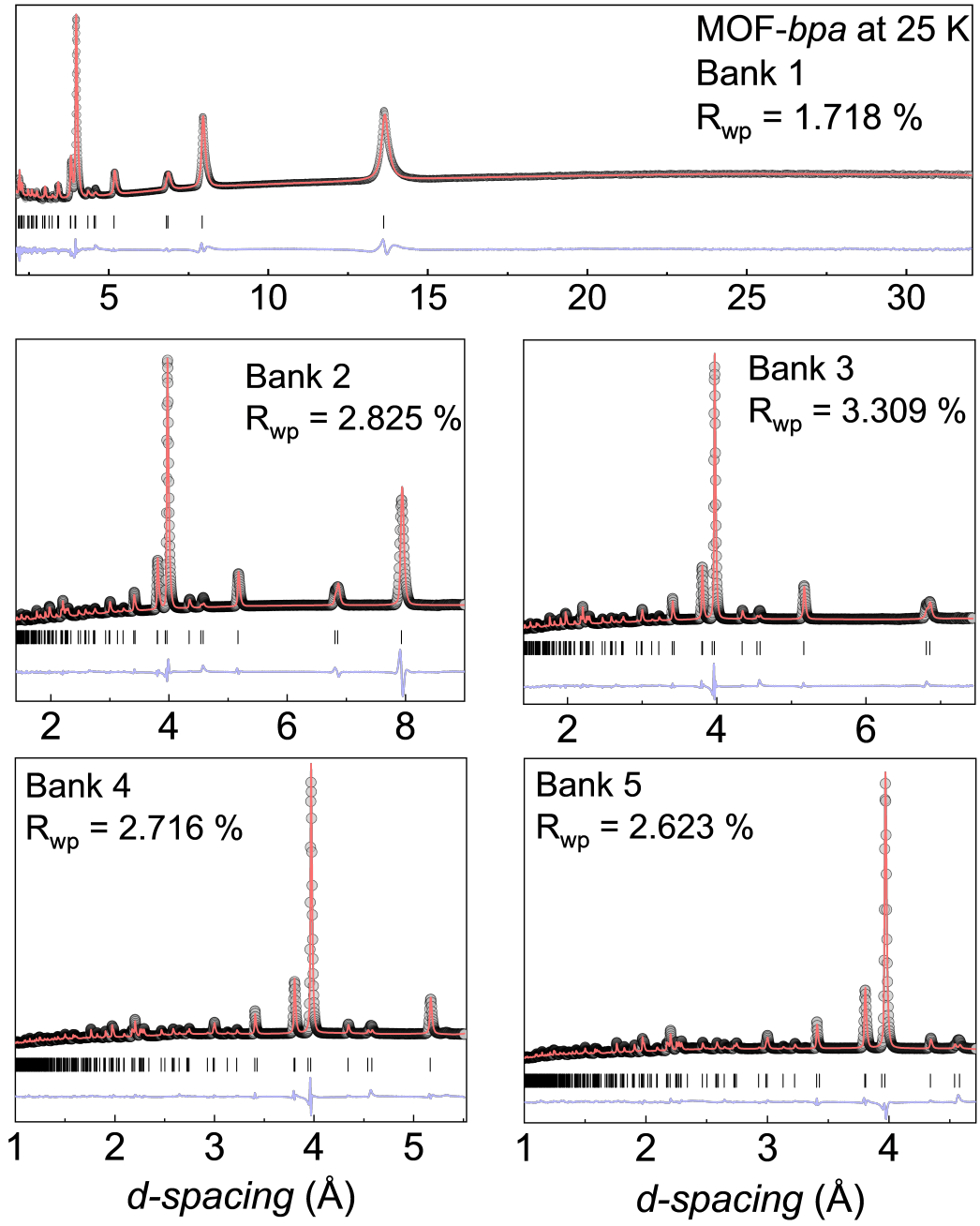


Figure 3.8: Rietveld refinement of the $P6/m$ model of MOF-*bpa* against 25 K data collected on the WISH diffractometer. Refined lattice parameters are a = 9.1552(5) and c = 13.6104(3) with a global R_{WP} = 3.20 %

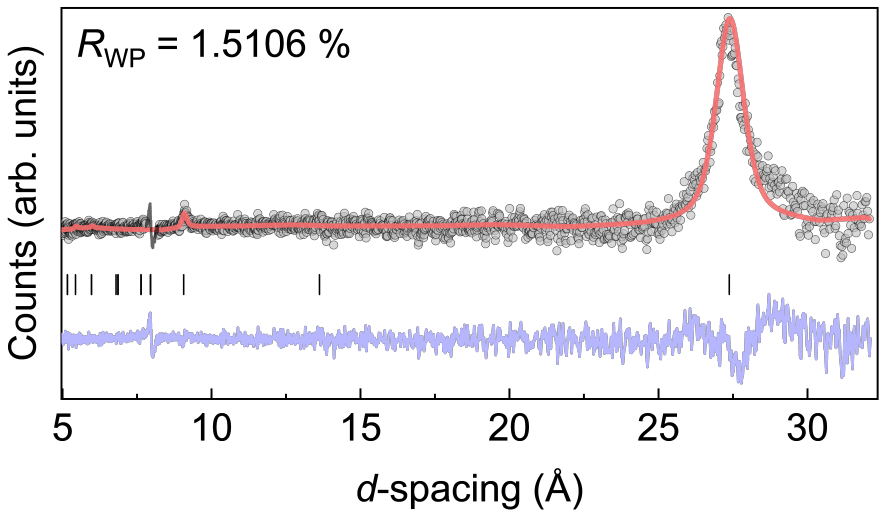


Figure 3.9: Magnetic Rietveld refinement of the $P1$ structure against subtracted NPD data from 1.4 and 25 K collections. A gap in the fit around 8 Å was applied due to a thermal contraction feature. Here, the red line is the fit, blue is the difference between fit and data and points are data.

that any information extracted cannot be related to a moment oriented outside of the kagome planes, therefore moment contributions in the c plane are fixed to zero. Since there is also no magnetic Bragg intensity at the (0 0 2) position we can also rule out the canting of magnetic moments we observed in MOF-*bpe* [12]. These features imply that MOF-*bpa* behaves similarly to MOF-*bpy* and MOF-*azpy* in terms of its ordered magnetic structure. Thus featuring ferromagnetically coupled Cu^{2+} kagome planes, coupled antiferromagnetically to adjacent layers (Figure 3.10). Since there is not enough data to refine the moment orientations freely, another constraint was applied to ensure that moments in adjacent planes are both equal and opposite in magnitude, with moments allowed to refine only along the a-axis. These constraints resulted in a good fit to the data and a refined magnetic moment size of 0.373(7) μ_B per copper site. A comparison of the magnetic moment sizes of each system is outlined in Table 3.6. We see from this comparison that the moment size of MOF-*bpa* is significantly lower in magnitude to the rest of the family. There are two possibilities for this result; one is a reduction in dimensionality of MOF-*bpa* caused by reduced susceptibility to exchange through the acetylene bond (which is contrary to our prior assessment), the second more likely cause is an in-

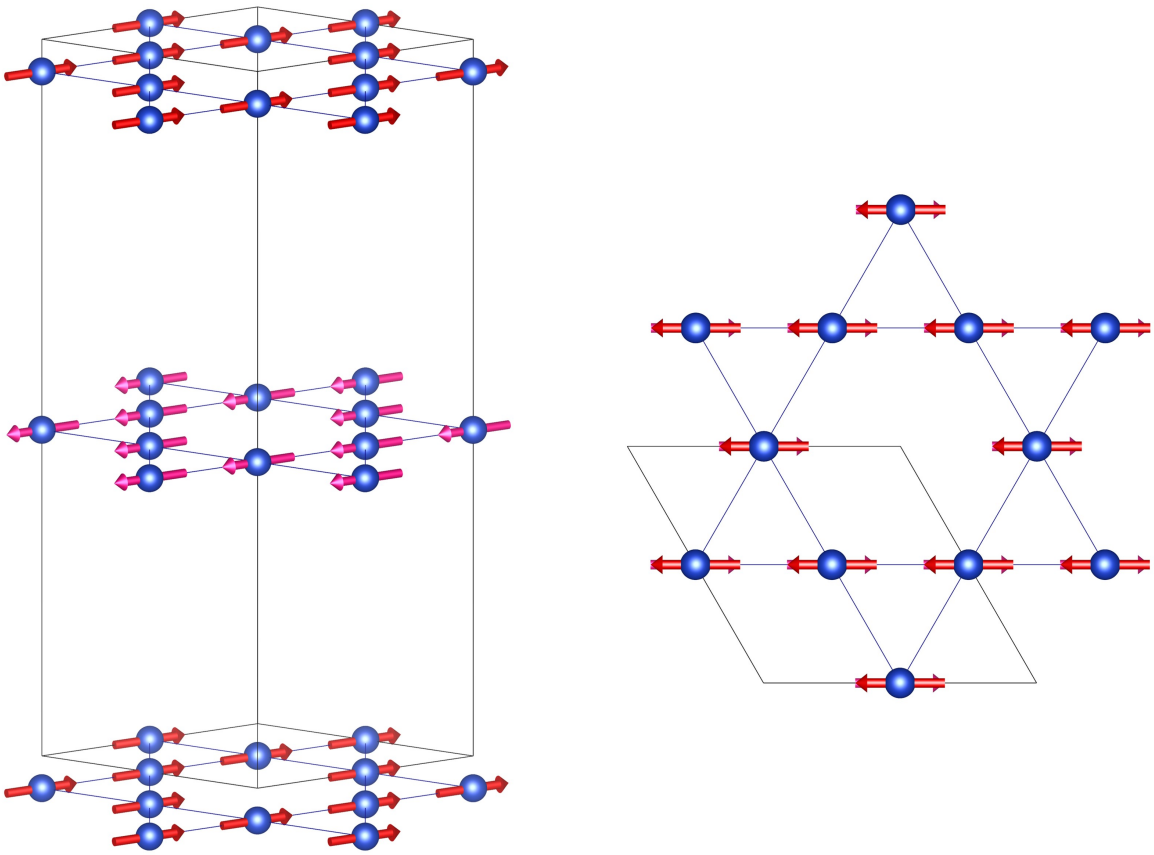


Figure 3.10: The proposed magnetic structure of MOF-*bpa*, in which we see ferromagnetically coupled kagome planes, antiferromagnetically coupled, giving us a *c*-axis length of 27.24 Å in the assigned magnetic unit cell.

Table 3.6: Summary of magnetic moment size refined from subtracted NPD data, data collected for MOF-*bpe*, *bpy* and *azpy* refined by Katherine Tustain*. [12]

MOF	Moment size/ μ_B
bpe	Approximately 0.5*
bpy	0.497(4)*
azpy	0.495(3)*
bpa	0.373(7)

consistency between the scale factors of the previously fit, modelled and refined data. The ordered moment sizes for MOF-*bpe*, *bpy* and *azpy* were extracted from data acquired by a former group member, while MOF-*bpa* was not, there is a strong possibility that the data quality and nuclear refinements performed on MOF-*bpa* are of a different standard, leading to uncertainty over the scale factor assignments used in magnetic refinements. Since the results discussed previously appear to support the conclusion that magnetism in MOF-*bpa* does not deviate significantly from the MOF family, we can be confident that uncertainty over the ordered moment comes from this source.

3.4 Conclusions

The synthesis and comprehensive structural and magnetic characterisation of a family of Cu^{2+}, CO_3^{2-} kagome-containing MOFs have been reported. Three of these, MOF-*bpe*, *bpy* and *azpy* have been studied either within the group or in the literature, with their structural and magnetic characteristics confirmed in this chapter. A fourth member of this family of materials was synthesised and compared using X-ray and neutron sources to determine whether there were any significant differences in the long-range, magnetically ordered ground state. The analysis of MOF-*bpa* resulted in several key findings.

1 – Variations in the synthetic route of all systems allowed us to grow larger single crystals than previously reported, allowing us to perform a comprehensive crystallographic study in all four systems.

2 – Synchrotron X-ray analysis provides us with the highest quality data for the structural refinement of MOF-*bpa*, allowing us to confirm the lack of ligand disorder and the assignment of the space group $P6/m$.

3 – Bulk magnetic susceptibility measurements indicate that our measurements for MOF-

bpa are consistent with the literature [86], and that only minute variations in the bulk susceptibility are observed across the four systems. This confirms that small structural changes can be used to manipulate the magnetic response on a fine scale, which is a promising finding for other MOF systems nearing the optimal conditions to host the QSL.

4 – Measurements taken on the WISH diffractometer at the ISIS Neutron and Muon source have allowed us to collect data with sufficient *d*-spacing to observe magnetic Bragg reflections at a position double the crystallographic unit cell. Importantly, MOF-*bpa* data are consistent with our reports of MOF-*bpe*, *bpy* and *azpy*, confirming that the motif of ferromagnetic kagome layers, coupled antiferromagnetically persists within several variations of the inter-plane ligand [12].

5 – MOF-*bpa* across all magnetic measurements presents small indications that the exchange interactions differ slightly in comparison to the rest of the MOF family. However, a conclusive assignment of what drives these differences cannot be obtained using the current data.

In summary, we present that MOFs allow for the manipulation of the chemical structure to an exceptionally fine degree in the context of modifying the magnetic response without significantly modifying the magnetic ground state. These kagome-containing MOFs also present material realisations of the interesting magnetic topology sought after for unconventional magnetic properties [25, 9]. These properties make these materials excellent candidates for study as kagome ferromagnets, especially if these systems require tuning for use. Additional work is ongoing to study MOF-*bpy* by inelastic neutron scattering to find any evidence for the quantum hall effect. Further measurements for MOF-*bpa* could be taken to elucidate the interplay between the selection of inter-plane ligands and magnetic order, such as single-crystal magnetometry measurements. These may provide further insight into the magnitudes of magnetic exchange observed both ferromagnetically and

antiferromagnetically. Here we could quantify the strength of exchange coupling, directly observing the extent to which these varying ligands facilitate superexchange. However, this relies upon the synthesis of larger single-crystals, which is a particularly challenging task as the optimisation of synthesis has been extensively studied in this Thesis. Another method would be to perform DFT calculations to predict the differences in these superexchange pathways, however previously, we have found that the energy scales of the antiferromagnetic components of exchange are too small to predict reliable values. In terms of expanding upon this work further, we explore inter-plane ligands which may be cleaved, providing us with magnetic nanosheets (Chapter 4) and in-plane ligands which mediate antiferromagnetic superexchange (Chapter 5) pushing us towards the ideal antiferromagnetic kagome expected to host the QSL state. Work moving beyond the scope of this thesis may involve conductivity measurements and screening to find whether these materials are viable for use in computation, with their fragile magnetically ordered states bearing promise for spintronics applications [11, 84].

Chapter 4

Approaching the Two-Dimensional Limit of the $S = \frac{1}{2}$ Kagome Ferromagnet Within Two Metal-Organic Frameworks

4.1 Introduction

Prior to 2018 the existence of a material hosting two-dimensional ferromagnetism was deemed impossible [157]. This was based upon the Mermin-Wagner theorum, stating that the spontaneous symmetry-breaking mechanism of magnetic order could not be facilitated by ≤ two-dimensional systems at $T > 0$. This was thought to be the case because the broken symmetry of a two-dimensional system would generate quantum fluctuations which diverge at dimensions ≤ 2 preventing the symmetry breaking mechanism. This was not strictly the reality however, in cases where a low-energy gap is introduced through single ion anisotropy, long-range order is expected to be stabilised in a similar way to a two-dimensional Ising model with two degrees of freedom [46, 47]. Since the discovery of two-dimensional long-range ferromagnetic order in CrI_3 [45], there has been increasing interest in two-dimensional magnetic materials [158, 159, 160]. With the study of two-dimensional magnetic materials growing in interest since their recent discovery, novel

materials are at the forefront of advancing our understanding [161, 162]. As we have previously discussed, kagome-containing materials are expected to host some interesting magnetic phenomena, and so the study of two-dimensional kagome-containing systems may be a key avenue of study, especially when considering an ideal kagome should feature only in-plane nearest neighbour exchange coupling [163, 164]. Since they are ultra-thin by design, two-dimensional magnets are expected to be ideal candidates for use in future technologies; from high-density data storage [165, 166], to quantum computing [167]. With such promise, routes to synthesise new and exciting materials are being explored [162, 161]. This also includes the exploration of two-dimensional and quasi-two-dimensional magnetic MOFs for the observation of their intriguing low-temperature physics [83, 96]. As we have discussed in Chapter 3, the kagome lattice presents an exciting magnetic topology for the study of interesting magnetic phenomena, with the potential to generate high levels of frustration in the antiferromagnetic kagome, as well as potential to host exotic magnetic states in the ferromagnetic kagome, hosting further neighbour exchange coupling than the nearest neighbour [163]. Previously, we have studied MOFs of formula $Cu_3(CO_3)_2(x)_3{\cdot}2ClO_4$, where x represents a ditopic organic ligand that produces a three-dimensional framework consisting of copper carbonate kagome layers covalently bridged by these ditopic ligands [12, 82, 84].

Since these systems were observed to host antiferromagnetic exchange interactions between kagome layers [12], this chapter aims to isolate the magnetic exchange of the copper carbonate kagome. We do this through structural design, selecting interplane ligands which are monodentate, in doing so we form magnetically isolated kagome layers within a three-dimensional MOF, hence quasi-two dimensional magnetic MOFs. While the work reported in Chapter 3 provides a synthetic route to realising possible quasi-two-dimensional magnetic systems, the novelty of the materials studied within this chapter goes beyond just "extending a family of magnetic MOFs". In this chapter we instead aim to characterise systems likely to host two-dimensional magnetic exchange, making them exciting

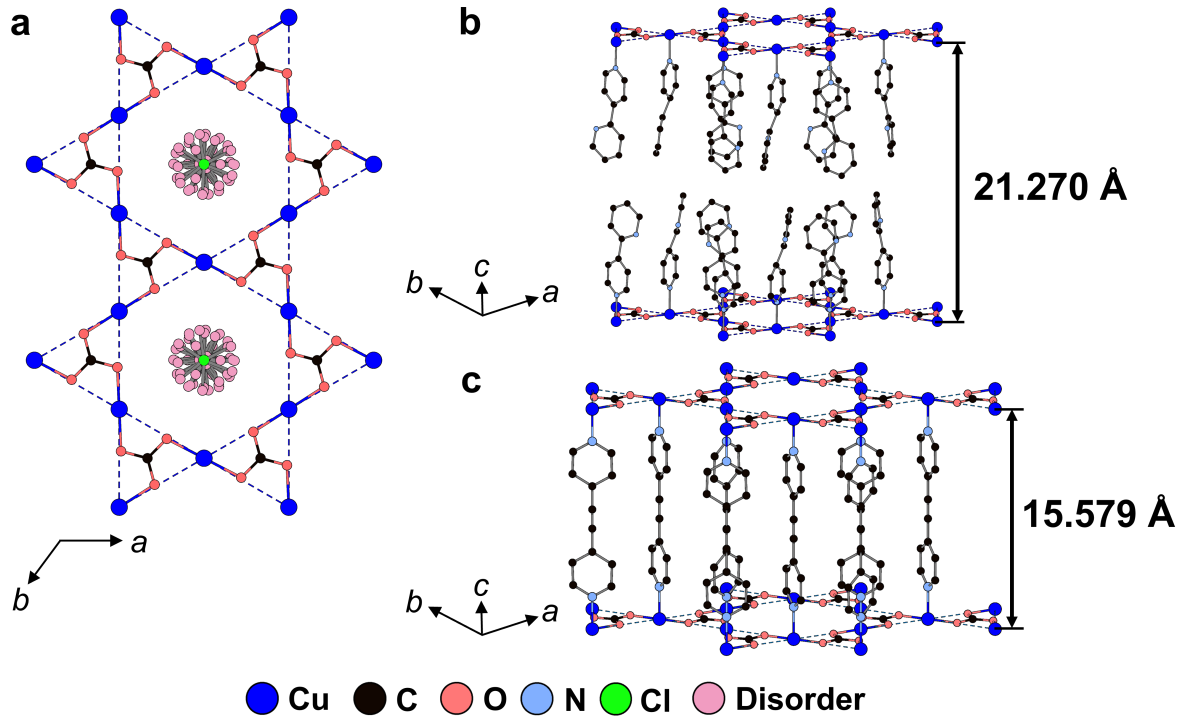


Figure 4.1: Structural models of MOF-*bipy* and MOF-*bpa*. a) Here we see the copper carbonate kagome lattice, shared by both MOF-*bipy* and MOF-*bpa*, where disordered perchlorate occupies the hexagonal channels of the framework. b) Here, we see how the copper carbonate kagome layers are stacked by monodentate *bipy* ligands, which leads to a structure featuring no covalent inter-plane linkage at a separation distance of 21.270 Å between kagome layers. c) Here we see MOF-*bpa*, previously studied in Chapter 3, the copper kagome layers present are covalently bound resulting in antiferromagnetic exchange coupling studied by neutron powder diffraction methods, the inter-layer distance here is 13.579 Å.

targets for further study. In addition to broadening our understanding of the copper carbonate ferromagnetic kagome, we also approach a better general understanding of two-dimensional magnetism. A promising system reported in the literature was MOF-*bipy*, where *bipy* is 2,4-bipyridine [83] and the MOF formula was $Cu_3(CO_3)_2(bipy)_6{\cdot}2ClO_4$. Here, *bipy* acts as a monodentate ligand, binding to a single copper atom. MOF-bipy contains copper carbonate kagome layers with terminal ligands that stack through non-covalent interactions. This stacking is believed to be stabilised by hydrogen bonding interactions between nitrogen and hydrogen from neighbouring ligands due to their proximity [83]. A comparison of the layering present in MOF-*bipy* and MOF-*bpa* studied in Chapter 3 is illustrated in Figure 4.1 above. The reported Curie-Weiss analysis for MOF-

bipy found a Curie constant $C = 0.403(3)$ cm^3 K mol^{-1}, corresponding to an effective moment $\mu_{\text{eff}} = 1.795(2)$ and a Curie-Weiss temperature $\theta_{\text{CW}} = 21.5(8)$ K, suggesting a spin only moment consistent with a $S = \frac{1}{2}$ system and dominant ferromagnetic exchange coupling [6, 83]. These magnetic properties were of similar order to the results found for the covalently bound kagome-containing MOFs outlined in Chapter 3, suggesting that the copper carbonate kagome continues to host ferromagnetic exchange coupling in these non-covalently bound MOFs. From this literature report we chose to begin our own study of MOF-***bipy***, not only as an obvious extension of the MOF family, well studied in Chapter 3, but primarily as a route towards two-dimensional kagome-containing MOFs.

Alongside MOF-***bipy*** we began working on the synthesis and characterisation of a novel system following the $Cu_3(CO_3)_2(x)_6{\cdot}2ClO_4$ formula. To find a suitable candidate, we began synthetic experimentation using other monodentate ligands such as isonicotinimide, tert-butyl-pyridine, pyridine and methylpyridine. Through experimentation we were successful in synthesising MOF-***mp***, $Cu_3(CO_3)_2(mp)_6{\cdot}2ClO_4$ where ***mp*** is methypyridine. The success of this synthesis was tracked by single-crystal X-ray structural analysis, confirming the expected copper kagome lattice stacked with methylpyridine ligands which we expect to have weaker interlayer interactions than MOF-***bipy*** due to a lack of potential hydrogen bonding, illustrated in Figure 4.2. Importantly, in both cases, the non-covalent stacking of MOF-***bipy*** and MOF-***mp*** also facilitate a further avenue of study, exfoliation to magnetic nanosheets. We aim to study MOF-***bipy*** and MOF-***mp*** in tandem to discover whether there is evidence to suggest that the copper carbonate kagome layers present are indeed magnetically isolated and can be exfoliated down to the monolayer limit. If our studies suggest that these two MOFs host quasi-two-dimensional magnetic exchange they may be excellent candidates for the improvement and development of characterising such materials, while additionally holding potential for applications in future technologies. Especially since exfoliation to a magnetic monolayer extends the scope of the study of these materials further [114, 168]. With the kagome layers stacking via

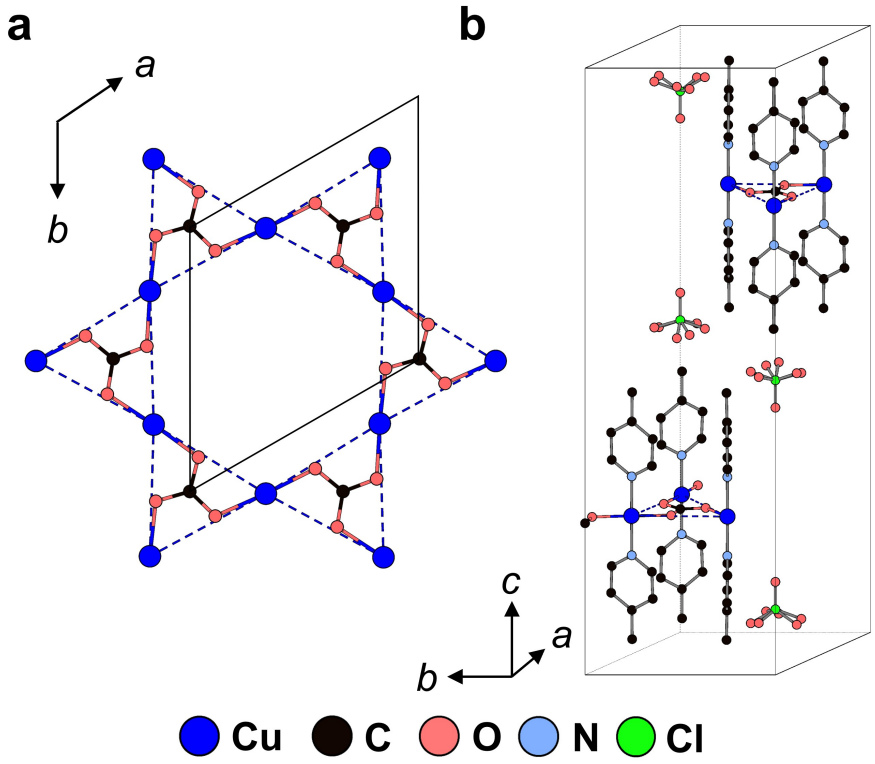


Figure 4.2: Crystallographic models of MOF-*mp* generated from SCXRD data. a) One layer of MOF-*mp* confirming the presence of the copper carbonate kagome lattice. b) One unit cell of MOF-*mp* showing that kagome layers stack through weak inter-layer interactions where layers do not stack directly on top of each other, instead an *abab* pattern where layers are related, rotated through 60°.

weak intermolecular forces and not covalent bonding, the opportunity to mechanically exfoliate such materials to magnetic nanosheets becomes a possibility [104]. Defined as a "top-down" approach, nanosheets can be obtained from a bulk three-dimensional system through multiple routes, most famously with scotch tape for graphene [169]. Using exfoliation techniques such as ultrasonication [170], we aimed to exfoliate MOF-*bipy* and MOF-*mp* to magnetic kagome nanosheets. This presents a highly novel route of study into these materials featuring ferromagnetic kagome layers. Our initial characterisation will be from atomic force microscopy confirming successful exfoliation to nanomaterial by height profile analysis. In this chapter, we aim to characterise and compare the structural and bulk magnetic properties of MOF-*bipy* and the novel system MOF-*mp*, using single-crystal X-ray diffraction, neutron powder diffraction, heat capacity and magnetic susceptibility methods. We then aim to present evidence for the successful exfoliation of MOF-*bipy* and MOF-*mp* to metal-organic nanosheets (MONs) confirming this via atomic force microscopy.

4.2 Experimental Methods

4.2.1 Single-Crystal Synthesis

Samples of the two systems were synthesised by the same modified Solvay process outlined in Chapter 3. [103] Single crystals of $Cu_3(CO_3)_2(x)_6{\cdot}2ClO_4$, (MOF-$x$), where x is *bipy* (2,4'-bipyridine, $(C_5H_4N)_2$) and *mp* (4-methylpyridine, (C_6H_7N)) were synthesised as follows.

MOF-*bipy*

For single crystals of MOF-*bipy*, $Cu(ClO_4)_2{\cdot}6H_2O$ (926 mg, 2.5 mmol) and 2,4'-bipyridine (781 mg, 5 mmol) were dissolved in aqueous NH_3 (35%, 200 cm^3). The resultant blue solution was bubbled with CO_2 for five minutes with stirring. The mixture was then evaporated at 70 °C in a two litre crystallisation dish until blue crystals formed on the

surface (after approximately 4 hours). These crystals were then isolated by filtration with the excess mother liquor returned to the crystallisation dish yielding more crystals. The crystals were washed with H_2O (3 × 20 cm^3) and MeOH (3 × 20 cm^3). After repeating the crystallisation process 3 times we combine the crystals to give MOF-*bipy* (872 mg, 0.6 mmol, 70%) as blue hexagonal plate-shaped crystals. CHN elemental analysis data indicated sample purity from the expected values for $Cu_3(CO_3)_2(bipy)_6{\cdot}2ClO_4$: C, 49.6; H, 3.6; N, 11.2; found, C, 50.1; H, 3.0; N, 11.2.

MOF-*mp*

For single crystals of $Cu_3(CO_3)_2(mp)_6{\cdot}2ClO_4$ (MOF-mp), $Cu(ClO_4)_2{\cdot}6H_2O$ (700 mg, 1.9 mmol) was dissolved in aqueous NH_3 (32%, 100 cm^3), alongside this, 4-methylpyridine (0.5 cm^3, excess, 6 mmol) was dissolved in 100 cm^3 methanol and added to the copper solution dropwise with stirring. The resultant mixture was then stirred for 1 hour to ensure homogeneity. The mixture was transferred to a clean crystallisation dish before heating at 45 °C. Within 4 hours, a layer of deep blue hexagonal plate-like crystals formed on the surface of the mixture. These crystals were then isolated by vacuum filtration and washed with H_2O (3 × 50 cm^3) and acetone (3 × 50 mL) before drying in vacuo at 70 °C. MOF-mp (450 mg, 0.85 mmol, 65%) was isolated as hexagonal plate-like crystals. CHN elemental analysis data indicated sample purity from the expected values for $Cu_3(CO_3)_2(mp)_6{\cdot}2ClO_4$: C, 41.33; H, 3.83; N, 7.61; found, C, 41.52; H, 3.94; N, 7.55.

4.2.2 Exfoliation Method

To acquire metal-organic nanosheets (MONs) the exfoliation of three-dimensional MOF crystals was carried out using an ultrasonication method [106]. A crystalline sample was added to ultrapure acetone at a concentration of 1 mg/ cm^3 in a 15 cm^3 vial and placed in a water bath ultrasonicator at 80 kHz for four hours. Acetone was used after a solvent screening found that this was the most promising solvent in terms of the Tyndall effect observed. These samples were then centrifuged to remove large particulates and

the remaining suspension was tested for Tyndall scattering, confirming the presence of suspended nanoparticles by their reflection of applied laser light [105]. These samples were then centrifuged and decanted to isolate the smallest material present for further analysis. We were able to begin optimising the exfoliation process by tracking success from collected AFM images, although a robust method of nanosheet synthesis is still ongoing.

4.2.3 Powder X-ray Diffraction

A laboratory powder X-ray diffractometer was used for the initial characterisation of both MOF-*bipy* and MOF-*mp* samples. These measurements were taken on a Panalytical Empyrean diffractometer with a monochromated Cu $K_{\alpha 1}$ radiation source of wavelength $\lambda = 1.54056$ Å and a selected beam slit size of $\frac{1}{8}°$. Around 200 mg of sample was ground to a homogeneous powder and mounted on a low-background silicon holder for analysis. Scans were taken between $4 - 50$ ° 2θ, with step sizes of 0.00138 ° at room temperature. Alongside these laboratory measurements, high-resolution X-ray data were collected on the I11 beamline at Diamond Light Source, using radiation of wavelength, 0.8258 Å at room temperature in a 0.3 mm borosilicate glass capillary. These data were collected over a 2θ range of $2.033 - 120.352$ ° with a step size of 0.004 °. These data were analysed by the Le Bail and Rietveld methods using GSAS2 software [155].

4.2.4 Single-Crystal X-ray Diffraction

Single-crystal X-ray diffraction data were collected for MOF-*bipy* at 30 and 300 K using the I19 beamline at Diamond Light Source, with an incident radiation wavelength of 0.6889 Å. SCXRD data were collected for MOF-*mp* using a Rigaku Synergy-S dual source with a PhotonJet-S X-ray source and a HyPix-6000 detector. Data were collected at 100 K using an Oxford Cryosystems cryostream device, while samples were mounted using MiTeGen sample holding loops. For both MOF-*bipy* and MOF-*mp* the collected data were processed using CrysAlis PRO171.42.49 and Olex2 software packages [120].

Structural determination was achieved using a direct methods approach using the ShelXS package [153], then refined using the ShelXL [154] package using a full-matrix, least-squares approach based on F^2.

4.2.5 Magnetic Susceptibility

Magnetic susceptibility measurements were collected on a Quantum Design Magnetic Property Measurement System 3 (MPMS 3) SQUID magnetometer in DC mode, measuring between 1.8 – 300 K. A palladium standard was used to calibrate the instrument prior to measurement. For these measurements 18 and 24 mg samples of MOF-*bipy* and MOF-*mp* respectively were mounted in gelatin capsules which were sealed with G-varnish before being secured in straw sample holders. Temperature-dependent magnetic susceptibility data were collected in zero field and in a 0.1 T applied field for ZFC and FC measurements. Field-dependent magnetic susceptibility measurements were performed on the same samples at 2 K up to 7 T applied field, with full magnet resets employed between measurements to eliminate remnant fields within the SQUID magnet. Ultra-low field-dependent magnetic susceptibility measurements were also taken on these samples between 0 – 2.5 mT at 2 K.

4.2.6 Heat Capacity

Heat capacity measurements were performed by Dr Angel Arevalo-Lopez at the Ecole Nationale Supérieure de Chimie de Lille. For these measurements the relaxation method in the Dynacool PPMS from Quantum Design was employed on a 1.83 mg sample of MOF-*bipy* and a 2.42 mg sample of MOF-*mp*. Data were measured in zero field between 1.8 and 301.9 K before fitting a linear region using the Debye equation outlined in Chapter 2. The fit was then extrapolated to simulate the low temperature phonon response for its subtraction from experimental data providing the magnetic heat capacity for the system and, by extension, the magnetic entropy.

4.2.7 Neutron Powder Diffraction

Neutron powder diffraction measurements were collected on the WISH beamline at ISIS Neutron and Muon Source, Didcot. For the measurement of MOF-*bipy* a 1.97 g sample was mounted into a vanadium can and inserted with Cryostat for measurements at 1.5 and 14 K. For the measurement of MOF-*mp* a 2.16 g sample was mounted in a vanadium can and inserted with cryostat for measurements at 1.5 and 15 K. The data obtained were then refined using GSAS II against structural models generated from our SCXRD data [155]. Magnetic models were generated through refinements performed using the Fulprof software suite [156]. These data were Rietveld refined using a twenty term Chebyschev, with instrumental peak shapes refined to the instrument using a NaCaAlF standard sample

4.2.8 Atomic Force Microscopy

Atomic force microscopy images were collected on a Keysight 9500 AFM, using non-contact high resonance silicon cantilevers, with 320 kHz operating frequency, the images were then processed using Gwyddion software [171]. Samples of MOF-*bipy* and MOF-*mp* were exfoliated and nanosheets were isolated using the exfoliation method outlined above. For both MOF systems a 0.05 cm^3 aliquot was taken using a micropipette, these aliquots were then drop cast under ambient conditions, or spin coated under nitrogen on freshly cleaved mica sheets. The surfaces of these mica sheets were then imaged by AFM.

4.3 Results and Discussion

4.3.1 Crystal Growth

The methods used for the growth of MOF-*bipy* and MOF-*mp* were developed from the synthetic successes of the MOFs outlined in Chapter 3. MOF-*bipy* is a reported material with an outlined synthetic method [83] however, we instead chose to optimise our own previously established methods for the growth of large single-crystals of

MOF-*bipy*. MOF-*mp* is a previously unreported kagome MOF following the MOF-*bipy*, $Cu_3(CO_3)_2(bipy)_6{\cdot}2ClO_4$ formula, substituting *bipy* for *mp*. The main synthetic optimisation for these two stacked kagome MOFs was the use of a crystallisation dish held at 45°C for MOF-*mp* and 70°C for MOF-*bipy* reflecting the water content of each reaction. We found that this favoured the nucleation of crystals at the air-liquid phase boundary, helping us isolate phase pure, crystalline samples. Attempts to grow crystals for both systems proved to be ineffective at room temperature, with amorphous impurity phases forming in both cases. We also discovered in the optimisation process of synthesising MOF-*bipy* that bubbling CO_2 during the mixing stage significantly improved the crystal quality, enabling us to perform SCXRD on samples formed by this method. Thanks to these experimental optimisations we were able to grow crystals on the milimetre scale, with single domains approaching 0.5 mm observed in polarised optical microscope images and scanning electron microscope images (Figure 4.3).

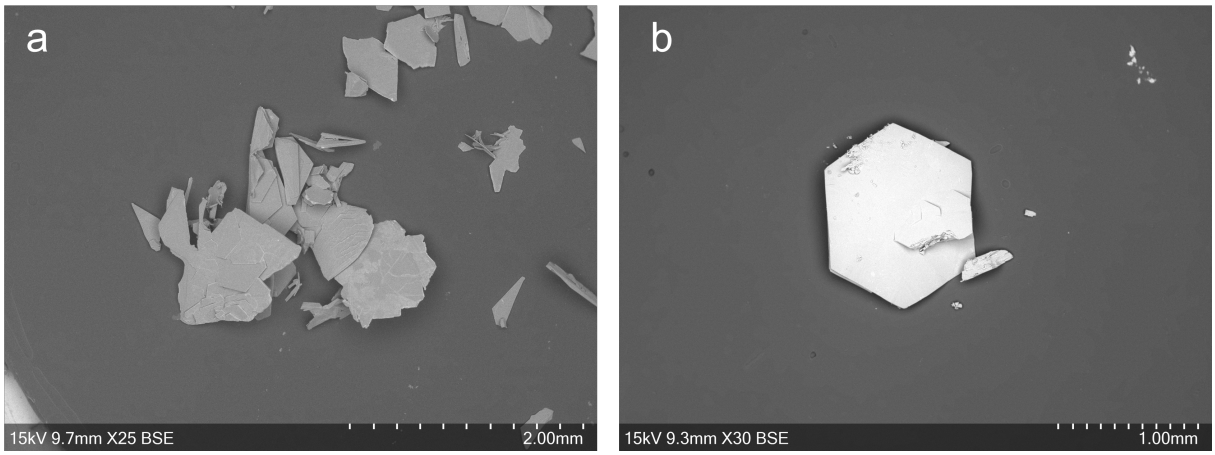


Figure 4.3: Two SEM images taken on crystals of (a) MOF-*bipy* at a magnification of 20x and (b) MOF-*mp* at a magnification of 30x. These images show the size of crystals formed by our optimised synthetic methods, as well as the ability to observe discrete crystal domains confirmed by polarised optical microscopy.

4.3.2 Structural Determination by Single Crystal X-ray Diffraction

MOF-*bipy*

As discussed, structural characterisation of MOF-*bipy* was reported by Mulrooney *et al* [83] at 100 K. Here, they report MOF-*bipy* in the $P\bar{3}$ space group with cell parameters of $a = b = 15.929(2)$ Å and $c = 21.291(4)$ Å. One of our first objectives in our own structural characterisation of MOF-*bipy* was to replicate the 100 K literature report. Taking the reported structural analysis further, by modelling SCXRD data at 30 and 300 K collected on the I19 beamline at Diamond Light Source and modelling our data in Olex 2 [120]. From our structural modelling, we were able to confirm the $P\bar{3}$ space group assignment for MOF-*bipy* at 30 K. Although we also collected data at 100 K, we were unable to model these data, we suspect that the data quality of this temperature point was compromised, likely due to lower crystal quality for this experiment making a stable refined structure challenging to obtain, and so instead we model 300 K data to the $P\bar{3}$ space group, the key difference in these data was a distortion of the kagome lattice, leading to a doubling of the c-axis as adjacent distorted kagome layers are inequivalent, related by a 180° rotation about the a-axis (Figure 4.4).

We were also able to confirm that Cu-O and Cu-N bond lengths in the 30 K model were consistent with the literature, Cu-N = 2.009 Å, and Cu-O = 1.961 and 2.616 Å , confirming the report of equatorial-axial Cu-O bonds, with one Jahn-Teller distorted [83]. This effect has also been observed MOF-*bpa*, *bpe*, *bpy* and *azpy* suggesting that this unconventional Jahn-Teller distortion is likely to be a characteristic propery of the octahedrally coordinated copper carbonate kagome lattice. Since the magnetic activity of MOF-*bipy* is studied well into the undistorted kagome regime, the high-temperature distortion is of little concern in terms of magnetism, although this distortion may produce a peak associated with a phase transition in heat capacity data. As seen in Table 4.1,

our 30 K model for MOF-*bipy* is in agreement with the literature report at 100 K Å [83]. We produced our models using several restraints due to the disorder of the perchlorate anions and ligands.

Table 4.1: Summarised SCXRD data for MOF-*bipy* collected at 30 and 300 K on the I19 beamline at Diamond Light Source and 100 K modelled by Mulrooney *et al* [83]. We observe a change in cell parameters between 30 and 300 K data due to a distortion of the kagome lattice through carbonate rotation.

Temperature (K)	30	100 [83]	300
formula	$C_{62}H_{48}Cl_2Cu_3N_{12}O_{14}$	$C_{62}H_{54}Cl_2Cu_3N_{12}O_{17}$	$C_{32}H_{24}Cl_2Cu_3N_{12}O_{14}$
M_r (g mol^{-1})	1451.31	1501.01	1446.64
crystal system	trigonal	trigonal	trigonal
space group	$P\bar{3}$	$P\bar{3}$	$P\bar{3}$
a (Å)	15.8531(1)	15.929(2)	15.9285(2)
c (Å)	21.2609(2)	21.291(4)	42.7175(6)
V (Å^3)	1541.37(8)	4678.5(16)	9386.1(3)
Z	3	3	6
ρ_{calc} (g cm^{-3})	1.557	1.591	1.536
μ (mm^{-1})	1.097	1.182	1.081
$F(000)$	738.0	2283.0	4422.0
crystal size (mm^3)	0.055 × 0.050 × 0.040	0.150 × 0.150 × 0.020	0.055 × 0.050 × 0.040
radiation wavelength (Å)	0.6889	0.71075	0.6889
R_{int} (%)	7.31	6.44	9.71
GooF	1.099	1.077	1.292
R_1,[a] wR_2[b] ($I > 2\sigma(I)$) (%)	8.58, 25.86	7.80, 23.12	12.75, 39.25
R_1,[a] wR_2[b] (all data) (%)	10.93, 28.96	10.73, 25.49	19.33, 43.27
$\Delta\rho_{max}$, $\Delta\rho_{min}$ (eÅ^{-3})	1.92, -0.88	0.85, -1.06	1.42, -1.42

To achieve the fits we report here, thermal displacement (RIGU) restraints were applied to Cl-O bond lengths, while bond length (SADI) restraints were applied to C-C and C-N bonds and equivalent thermal displacement (EADP) restraints on C and N atoms within the bipyridyl ligands, as these could not be refined independently. We must also consider that the model we report for MOF-*bipy* at 300 K is of lower quality to our

30 K refinement, both models given by Figure 4.4. Several factors have led to this; the complexity added with the larger unit cell, greater thermal vibration energy (Debye-Waller) at high temperatures and the poorer model quality (R_{int} = 9.71 %).

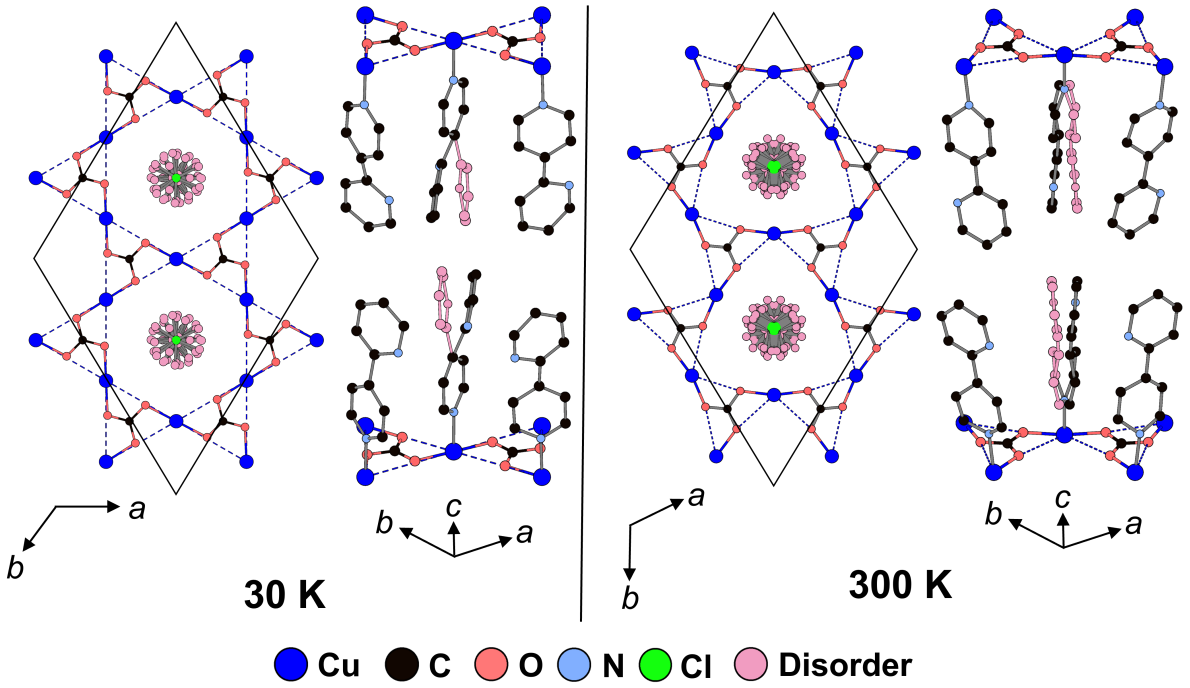


Figure 4.4: Crystallographic models for MOF-*bipy* generated from data taken on the I19 beamline at Diamond Light Source at 30 and 300 K. In 30 K data we observe a kagome arrangement of corner sharing triangles made up of Cu^{2+} ions chelated by CO_3^{2-} ligands, here, 2,4'-bipyridine, (*bipy*) bridges the gap between kagome layers, stacking them via weak intermolecular forces. These ligands are rotationally disordered about the ring containing the 4' position nitrogen in a refined ratio of 65:35. In the 300 K data, corner sharing triangles are maintained, however, they are larger due to the distortion to the kagome. This leads to a change in Cu-Cu distances (4.574 Å at 30 K and 4.801 Å at 300 K). The *bipy* ligands at 300 K are also rotationally disordered in a fixed ratio of 50:50.

In both the 30 and 300 K data, we ruled out the possibility of twinning via an automatic twin peak search in CrysAlisPro [152], finding $>$ 95 % of Bragg reflections are accounted for by our space group and unit cell assignments in both cases. From our SCXRD analysis we confirm the $P\overline{3}$ space group describes the structure of MOF-*bipy* at 30 K, and note the emergence of distortion to the kagome lattice which is not characterised by disorder, but rather a stable conformation of the copper carbonate lattice analogous to common copper carbonate chain motifs illustrated in Figure 4.5. In any case, we assign the 300 K

MOF-*bipy* phase to the $P\bar{3}$ space group with lattice parameters of $a = b = 15.9285(2)$ Å and $c = 42.7175(6)$ Å. To confirm that our 30 K model for MOF-*bipy* is representative of the bulk structure we performed a Rietveld refinement of neutron powder diffraction data discussed later.

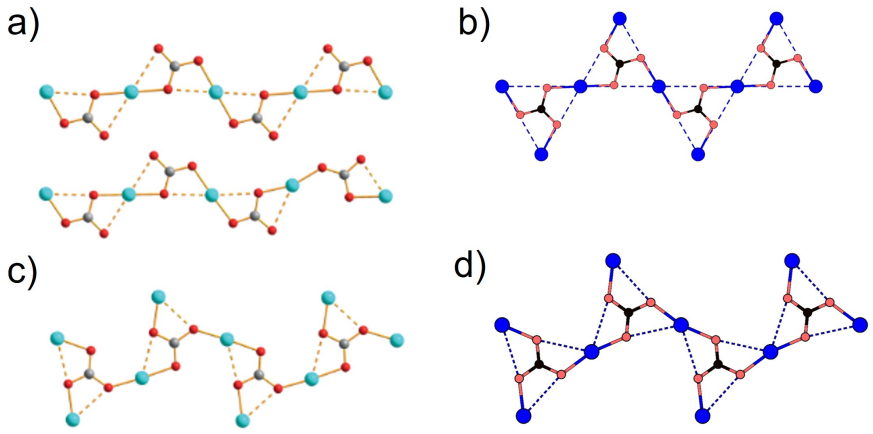


Figure 4.5: Some sections of copper carbonate chains taken from the literature and from generated models of MOF-*bipy* SCXRD data. a) Two similar chain motifs commonly adopted by copper carbonate [172], analogous to b) a section of the copper carbonate kagome lattice modelled for MOF-*bipy* from 30 K data. c) Another possible copper carbonate chain motif [173], this time analogous to a section of d) a section of MOF-*bipy* modelled from 300 K data.

MOF-*mp*

For the structural modelling of MOF-*mp* we do not have a literature structure for reference, and so here, we outline the first structural report. For MOF-*mp* we collected SCXRD data at 100 K and modelled these data using OLEX2 [120]. The SCXRD data acquired to model MOF-*mp* at 300 K was insufficient for a reasonable model to be generated, and so the direct comparison between MOF-*mp* and the distorted kagome of MOF-*bipy* at 300 K was not possible. The summarised crystallographic data are outlined in Table 4.2, where we see the differences between some of our generated models. Our first model assigned MOF-*mp* to the $P6_3/m$ space group, here no ligand disorder was considered, as we were using this simply to confirm the space group symmetry, cell parameters and structure. Similarly to MOF-*bipy*, Jahn-Teller distortion affects one of the Cu-O bonds

where Cu-O = 1.965 and 2.789 Å and Cu-N = 2.018 Å. This initial model confirmed that we had been successful in synthesising a $Cu_3(CO_3)_2(mp)_6{\cdot}2ClO_4$ species, featuring copper carbonate kagome layers stacked by terminal ligands, much like MOF-*bipy*. Further analysis in our second model provided a better fit to the data, also confirming our space group assignment, while describing a disorder effect generated by the rotational freedom of the carbonate ligand.

This disorder was a novel observation in MOF-*mp*, however, this carbonate rotation is likely to facilitate the distortion of the kagome lattice in MOF-*bipy*. Similarly to MOF-*bipy*, MOF-*mp* does not covalently bond to adjacent kagome layers, meaning these layers instead stack via weak intermolecular forces facilitating the crystal growth along the *c*-axis. Additionally, copper carbonate layers in MOF-*mp* are not aligned, meaning that the nearest neighbour copper atoms between layers are separated by varying distances, further reducing the likelihood of exchange being facilitated (Figure 4.6b). The weak stacking in MOF-*mp* and MOF-*bipy* is the most likely factor facilitating carbonate rotation, an effect we do not observe in the covalent coordinated MOFs outlined in Chapter 3. This was calculated in MOF-*mp* as a rotation of 22.4(6)°, (Figure 4.6c,d). The inclusion of this disorder in our models of MOF-*mp* provides a significant improvement in fit quality, with a reduction in R_1 for reflections greater than 2σ from 10.84 % to 5.94 % with similar goodness-of-fit (1.14 and 1.15). The third model we chose to apply to our data was a disordered monoclinic space group , $P2_1/m$ since the reflections we observed in our raw data also fit this space group assignment. However, in this model, significant levels of electron density outside of the MOF required assignment, with the only possibilities being water, methanol, or another species, in any case, there is no evidence in organic elemental analysis for these being present. Even with the assignment of four water molecules per formula unit, electron density remained, which could not be well fit to water. This fit serves as a reminder that a well-fitting model does not always equal a chemically sensible structure.

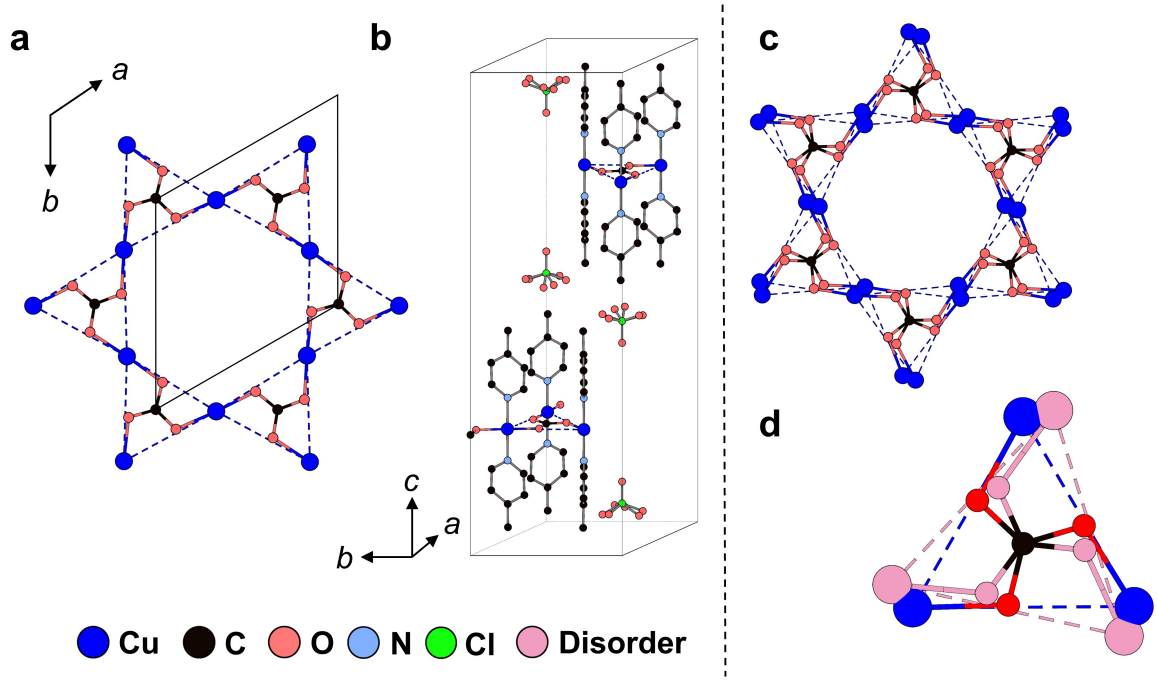


Figure 4.6: Crystallographic models of MOF-*mp* generated from SCXRD data collected at 100 K. Here, a and b are taken from data processed without the inclusion of disorder, while c and d are modelled inclusive of disorder. a) MOF-*mp* viewed along the *c*-axis, showing the copper carbonate kagome lattice, perchlorate omitted for clarity. b) A single unit cell of MOF-*mp*, this shows the stacking of kagome layers by weak intermolecular forces, hydrogen omitted for clarity. c) Here, we observe the effects of including disorder to our model, leading to the emergence of two overlain distorted kagome lattices. d) Here, we observe a section of the disordered MOF-*mp* model, from which we observe that disorder is facilitated by the rotation of the carbonate ligand through 22.46(2)°

Table 4.2: Summarised SCXRD data for MOF-*mp* collected at 100 K. We observe that the collected data can be modelled in different ways.

Model	$P6_3/m$	disordered ($P6_3/m$)	disordered ($P2_1/m$) + H_2O
formula	$C_{38}H_{42}Cl_2Cu_3N_6O_{13.5}$	$C_{38}H_{42}Cl_2Cu_3N_6O_{13.5}$	$C_{38}H_{44.1}Cl_2Cu_3N_6O_{18}$
M_r (g mol^{-1})	1052.31	1052.31	1148.42
crystal system	hexagonal	hexagonal	monoclinic
temperature (K)	100	100	100
space group	$P6_3/m$	$P6_3/m$	$P2_1/m$
a (Å)	9.4081(3)	9.41259(11)	9.4099(2)
b (Å)	9.4081(3)	9.41259(11)	31.0479(3)
c (Å)	31.0350(8)	31.0475(3)	9.4113(2)
V (Å^3)	2378.95(16)	2382.18(6)	2382.19(9)
Z	2	2	2
ρ_{calc} (g cm^{-3})	1.393	1.479	1.601
μ (mm^{-1})	2.997	3.147	3.262
$F(000)$	1017.0	1083.0	1186.0
crystal size (mm^3)	0.117 × 0.089 × 0.037	0.12 × 0.10 × 0.02	0.12 × 0.10 × 0.02
radiation wavelength (Å)	1.5418	1.5418	1.5418
R_{int} (%)	3.49	3.75	3.38
GooF	1.140	1.151	1.103
R_1,[a] wR_2[b] ($I > 2\sigma(I)$) (%)	10.84, 30.72	5.94, 18.11	6.69, 20.51
R_1,[a] wR_2[b] (all data) (%)	11.59, 31.45	6.38, 18.82	7.44, 21.66
$\Delta\rho_{max}$, $\Delta\rho_{min}$ (eÅ^{-3})	1.65, -2.73	1.13, -0.59	1.42, -0.50

Comparisons of MOF-*bipy* and MOF-*mp*

At 100 K the structures of MOF-*bipy* and MOF-*mp*, share the copper carbonate triangles synonomous with the kagome lattice, as well as the non-covalent stacking of these kagome layers originating from monodentate ligands. One of the first clear differences between the two systems is the stacking motif, kagome layers in MOF-*bipy*, at 30 K and 100 K stack in parallel with each other, while the kagome layers in MOF-*mp* at 100 K stack in an *abab* pattern related by a 60 ° rotation (Figure 4.7). There is however, the unanswered question of why we observe a structural distortion between 30 and 300

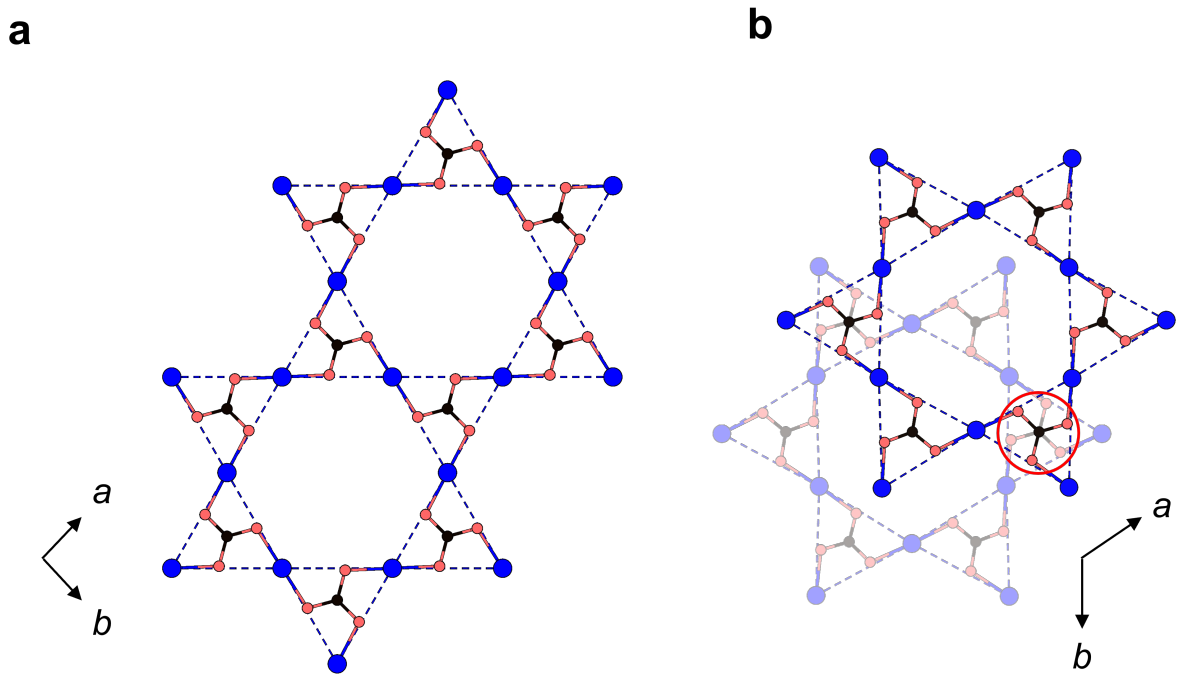


Figure 4.7: Two stacked kagome layers with all other atoms removed for clarity. a) Here we see MOF-*bipy*, where we are unable to see the second layer due to a parallel stacking motif characterised by the pattern, *aa*. b) Here we see MOF-*mp*, where two layers are observed to stack in a motif characterised by the pattern, *abab*, we also observe here that the layers are linked by a symmetry operation, a 60° rotation about the centre of the circled carbonate ligand.

K models of MOF-*bipy*. Since we observe no such effect in the conjugated MOFs outlined in Chapter 3, we can infer that this effect is facilitated by freedom provided by the weak stacking of kagome layers. Our structural analysis of MOF-*mp* and MOF-*bipy* has shown that there is a possibility for carbonate ligands to rotate, leading to disorder in MOF-*mp* at 100 K but a stable, distorted kagome structure in MOF-*bipy* at 300 K. We do not have SCXRD data for MOF-*mp* at 30 or 300 K making a direct comparison to MOF-*bipy* impossible. There are few literature reports specific to disordered copper carbonate kagome-containing MOFs however, there are discussions by Mulrooney *et al* [83], in which copper carbonate chains are observed to fall into multiple binding motifs.

Two binding motifs of interest from the literature are compared with the copper carbonate binding motifs observed in our MOF-*bipy* data, illustrated in Figure 4.5. Here, MOF-*bipy* adopts the distorted kagome at 300 K with no sign of rotational disorder of the carbonate ligand. The stability of this state may arise due to several factors; first, bipyridine is larger, heavier, and more sterically hindered than methylpyridine, meaning that the ability of the kagome lattice to move between distorted states would likely be less energetically favourable than it would be in MOF-*mp*. Second, we observe evidence suggesting that hydrogen bonding may exist between neighbouring bipyridine ligands, specifically between 4-pyridyl nitrogen and neighbouring hydrogen of adjacent ligands at distances of $\sim 2.2 - 3.3$ Å. If hydrogen bonding was present between these ligands it may make a specific repeated conformation more energetically favourable. Based upon these factors, MOF-*bipy*, at 300 K, likely has enough thermal energy to facilitate the expansion of the kagome to an energetically favourable distorted arrangement, while at lower temperatures, such as 30 K, the structure contracts to the near-perfect kagome we observe.

As discussed for MOF-*bipy*, the reason MOF-*mp* exhibits this disordered behaviour likely stems from the smaller energy barrier to structural distortion the smaller methylpyridine ligands provide. These ligands are unlikley to host hydrogen bonding and are significantly

less sterically hindered than bipyridine. The collection of 300 K data for MOF-*mp* would prove invaluable in discovering whether the distorted kagome lattice observed in 300 K MOF-*bipy* models are a characteristic property of MOF-*bipy* and whether the disorder in MOF-*mp* is more so an order-by-disorder mechanism facilitated by the methylpyridine ligand. Since we do not observe these kagome distortion effects in the covalently bound MOFs outlined in Chapter 3 we have further evidence to suggest this is an effect of the weak interlayer stacking. The distortion observed however, appears to be sensitive to the inter-plane ligands, which further validates the claims that MOFs facilitate the study of small structural change on the bulk properties of materials [25, 12]. Ultimately, to draw further conclusions, we require the collection of 30 and 300 K SCXRD data for MOF-*mp*, allowing for a direct comparison with MOF-*bipy*. The main points of interest here however, are that at 30 K, MOF-*bipy* features a perfect kagome arrangement and at 100 K, MOF-*mp*, through disorder has an average structure characterised by the perfect kagome. We therefore remain confident that, when approaching the temperatures in which magnetic phenomena emerge, the structures will be in the expected kagome arrangement, which we confirm through structural refinement of low-temperature neutron powder diffraction data.

4.3.3 Powder X-ray Diffraction Analysis of MOF-*mp*

In PXRD studies of MOF-*mp* we found an intriguing effect which was believed to stem from preferred orientation. In Figure 4.8 we see lab PXRD data collected at 300 K which we Le Bail fit to the disordered MOF-*mp* model outlined previously. We observe here that intensity is dominated by even (0 0 2l) reflections, with odd (0 0 l) reflections forbidden due to the $P6_3/m$ symmetry. A second set of data were collected using a 1° beam slit increasing the intensities of the (h k 0) reflections, we then Le Bail fit these data (Figure 4.9), our fit was in reasonable agreement to the observed peaks (with lattice parameters $a = b = 9.4081(3)$ Å and $c = 31.0479(3)$ Å). Across multiple samples we found that peak intensity and peak width effects dominated the (h k 0) and (0 0 2l)

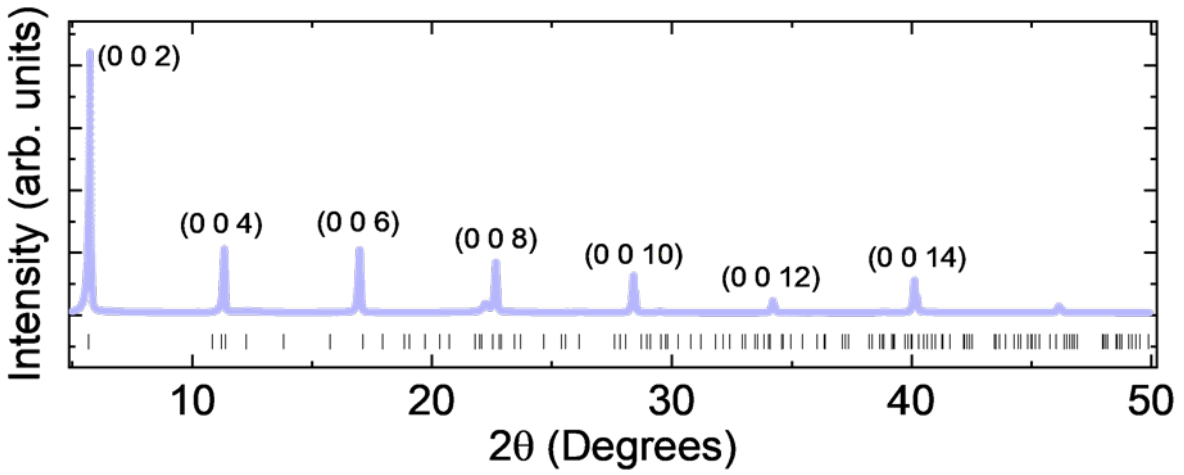


Figure 4.8: Laboratory PXRD data for MOF-*mp* collected at 300 K. Here we see almost no intensity besides the (0 0 2l) reflections, (0 0 l) reflections are forbidden here due to the symmetry of the $P6/m$ space group.

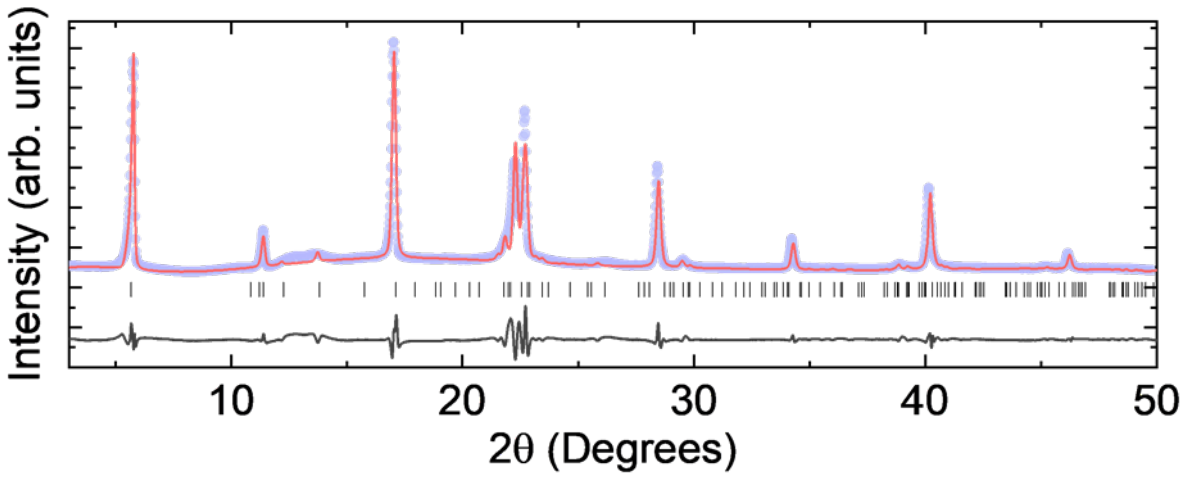


Figure 4.9: Laboratory PXRD data collected for MOF-*mp* at 300 K refined using the Le Bail method, extracted lattice parameters were $a = b = 9.5861(2)$ Å and $c = 31.2699(9)$ Å with an $R_{WP} = 12.75$

reflections of laboratory data and so we collected synchrotron PXRD data, giving us a better chance of performing a Rietveld refinement. The peak shape characteristics observed in laboratory powder data which could not be captured by Rietveld refinement were also observed in data collected on the I11 beamline at Diamond Light Source (Figure 4.10). Typically, preferred orientation effects are more intense when using flat plate sample

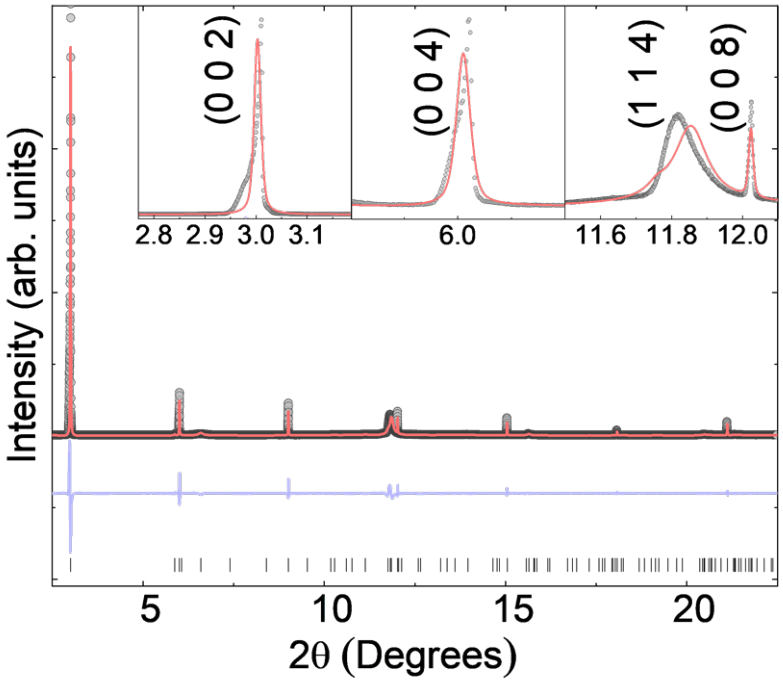


Figure 4.10: High-resolution PXRD data collected on the I11 beamline at Diamond Light Source at 300 K fit to the $P6_3/m$ space group using the Le Bail method. We are able to fit all peaks to the 100 K model of MOF-*mp* with lattice parameters $a = b = 9.2998(2)$ Å and $c = 31.5186(6)$ Å, $R_{WP} = 38.04$ %. Here, the peak intensities of all (0 0 2l) are under-fit by the model, with peak shoulders present in the (0 0 2) and (0 0 4) reflections leading to a peak shift which likely affects our extracted lattice parameters. We also observe in the rightermost inset that (h k 0) reflections are severely broadened which may originate from ligand disorder in the (h k 0) plane.

holders, however we still see the dominance of (0 0 2l) reflections in the capillary sample holder data collected on the I11 beamline. There are several possible explanations for these intensity problems, and, interestingly, some of these are shared with the covalently bound MOFs reported in Chapter 3 [12, 66]. One of these similar peak intensity effects was that (h k 0) peak intensity was largely reduced in cases where disorder dominates these planes, which may also explain our observations of peak broadening in non-(0 0

2l) Bragg reflections MOF-mp. Another effect leading to the poor fit of MOF-mp is the appearance of peak shoulders on several low-angle peaks, leading to a peak shift in the refinement that leads to lattice parameters which are not representative of the sample. A similar effect is observed in yttria-stabilised zirconia, where the study concluded that the peak shoulders originated from structural distortion of the material, since these shoulders are only observed on the (0 0 2) and (0 0 4) positions, we suggest that this effect may be observed due to stacking faults [174]. In the case of MOF-mp, it is not impossible that the grinding process also distorts the structure, with layers so weakly stacked in the crystal structure, one explanation may be that a partial exfoliation of MOF-mp during this grinding process produces a mixed phase which we cannot model. This may explain the intense (0 0 2l) reflections we observe. To further study the bulk structural properties of a powder sample of MOF-mp we performed a neutron powder diffraction study.

4.3.4 Structural Confirmation by Neutron Powder Diffraction

MOF-mp

Considering the limitations posed by the peak effects in our PXRD data, we aim to better characterise the bulk through a neutron powder diffraction study. Although we do not expect neutron diffraction to mitigate the previously discussed peak shape/intensity effects, as they likely originate from any combination of chemical disorder, stacking faults or preferred orientation, finding these peak effects to be consistent rules out the possibility of sample dependence. As expected, we observed similar peak broadening effects in non-(0 0 2l) reflections, as well as in further order (0 0 2l) reflections making a stable Rietveld refinement challenging, even in higher-resolution detector banks. We were however able to perform a Rietveld refinement on Bank 1 where we refine the strain, size lattice parameters, scale factor and March-Dolasse ratio. The refinement of the March-Dolasse ratio helps us model preferred orientation by reducing the relative intensity of specific (h k l) planes, we found a ratio of 0.746 for (0 0 2) reflections was sufficient to better fit our data. Our Rietveld refinement captured the most intense (0 0 2) reflection well, allowing us to

extract a scale factor for the calibration of our magnetic refinement discussed later. The less intense peaks were not as well fit due to their peak shapes and significant reductions in intensity. The hybrid Rietveld-Le Bail refinement is given in Figure 4.11, where Bank 1 was fit by the Rietveld method and Banks 2 - 5 were fit by the Le Bail method.

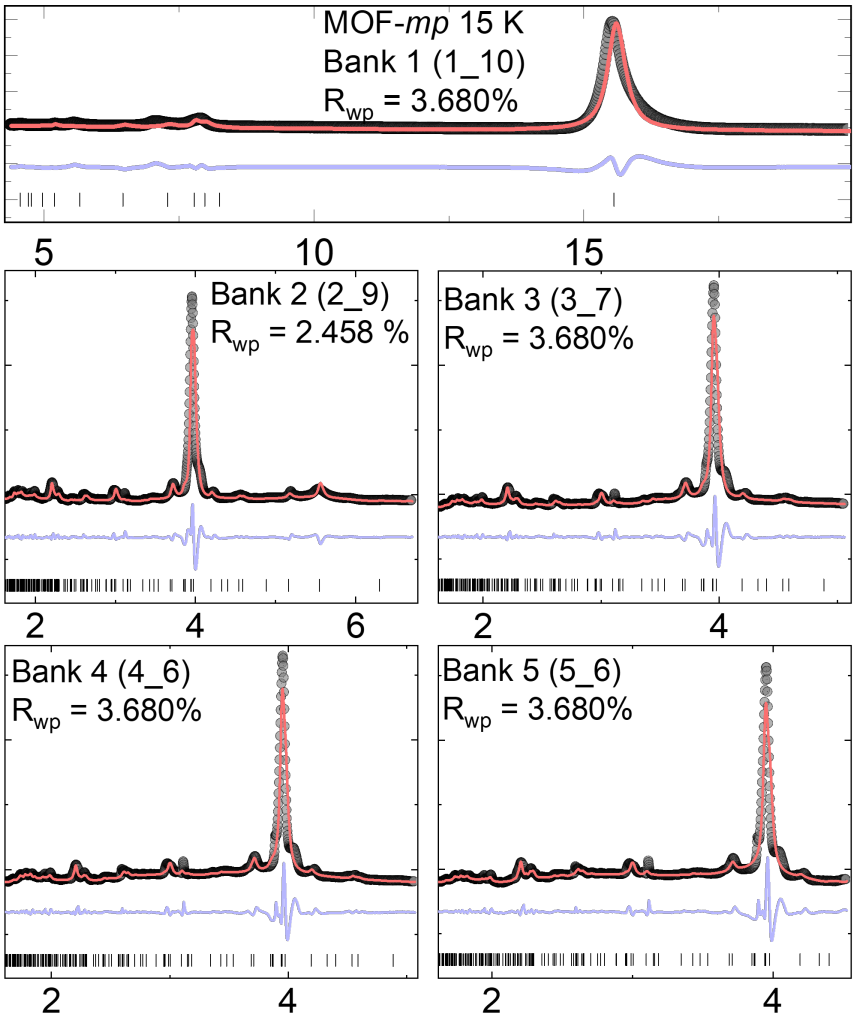


Figure 4.11: Rietveld and Le Bail refinement of the $P6_3/m$ structure of MOF-*mp* against data collected on the WISH diffractometer at 15 K. Here Bank 1 is fit using the Rietveld method and Banks $2-5$ were fit simultaneously using the Le Bail method, with refined lattice parameters $a = b = 9.5281(1)$ Å and $c = 31.119(2)$ Å and the scale factor = 4.3347(2), $R_{\mathrm{WP}} = 3.680$ %

MOF-*bipy*

To confirm the structure of MOF-*bipy* we performed a Rietveld refinement of NPD data collected on the WISH diffractometer at ISIS Neutron and Muon Source. The data collected for this refinement were obtained at 14 K and so we refined these data against the 30 K structural model outlined previously to ensure comparable data. The refinement and data are summarised in Figure 4.12. For this refinement several restraints and

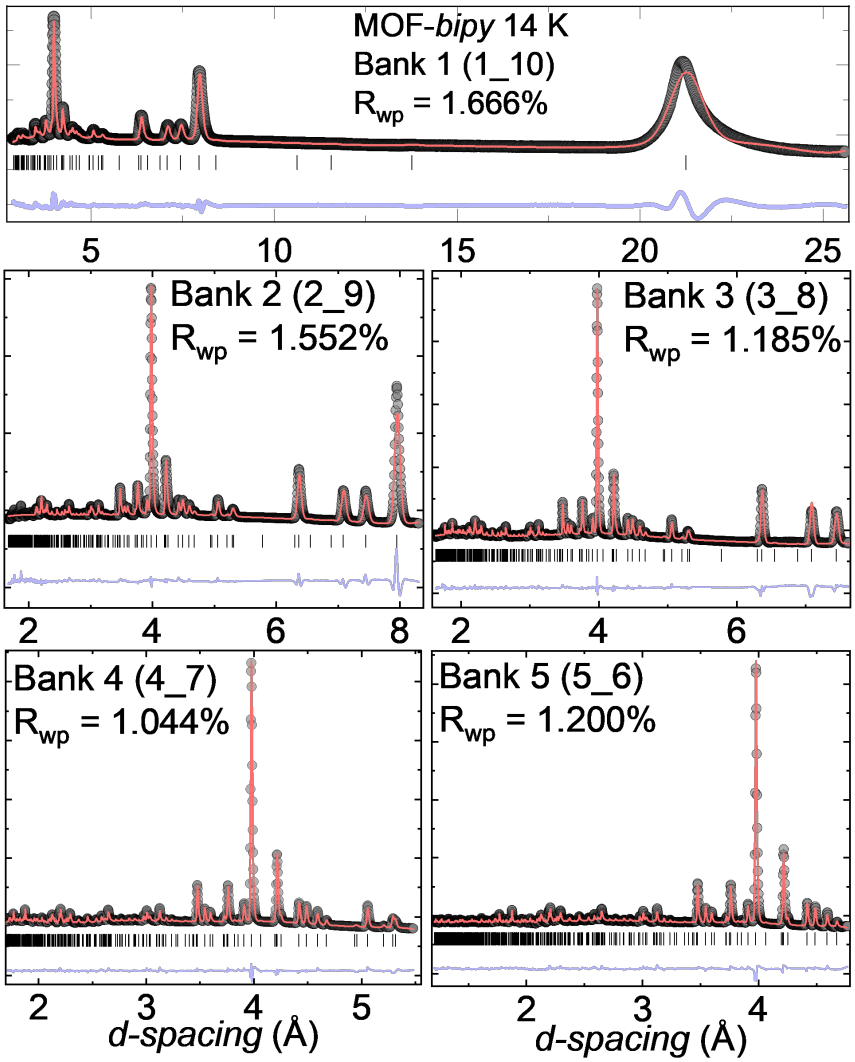


Figure 4.12: Rietveld refinement of the $P\bar{3}$ structure of MOF-*bipy* against data collected on the WISH diffractometer at 14 K. Here we simultaneously refine all five banks to give lattice parameters $a = b = 15.8848(4)$ Å and $c = 21.2240(3)$ Å and the scale factor = 4.9478(7), $R_{\mathrm{WP}} = 2.855$ %

constraints were employed to achieve this fit. Firstly, all bipyridyl ligands and their disor-

dered components were assigned to separate rigid bodies, with their fractional occupancies freely refined, providing a 63:37 ratio for the two disordered ligand components. Next, we refined the positions of perchlorate counter ions, we did this by refining the atomic coordinates of chlorine and constraining oxygen to a fixed bond length allowing us to refine the fractional coordinates of the perchlorate molecule while allowing the oxygen coordinates to refine alongside. We then restrain the Cu-N bonds to be equivalent and the bond angles in the carbonates to be equivalent preventing them from rotating in our model, as this commonly caused divergence. Finally, we constrained the copper sites to have equivalent thermal parameters, as these could not be refined independently. We find that our refinement is in excellent agreement with our 30 K model for MOF-*bipy* generated from SCXRD data, with a global R_{WP} = 2.855 % across five bank detectors. Our refined lattice parameters were $a = b$ = 15.8848(4) Å and c = 21.2240(3) Å, in the $P\bar{3}$ space group summarised by Table A.2.

Comparisons of MOF-*bipy* and MOF-*mp*

We find that we are able to more completely model neutron powder diffraction data for MOF-*bipy*, when compared to MOF-*mp*. It is likely that this is due to the stacking stability facilitated by hydrogen bonding in MOF-*bipy*. This would lead to a reduction in stacking faults, which are likely to be the reason for the peak intensity and peak shape inconsistencies we observe in MOF-*mp*. This may be backed up qualitatively when we consider the crystals themselves. To emphasise this point we provide two SEM images of some crystals which are representative of crystallisation in each case (Figure A.1). We can see here how inter-grown and layered MOF-*mp* is when compared to MOF-*bipy* and the likelihood for this to introduce stacking faults.

4.3.5 Bulk Magnetic Characterisation by Magnetic Susceptibility

DC SQUID temperature-dependent magnetic susceptibility data were collected for MOF-*bipy* and MOF-*mp* at 0.1 T, shown in Figure 4.13. A temperature-independent back-

ground subtraction was performed using a diamagnetic palladium standard provided by Quantum Design. Here, we report the bulk magnetic properties of the two MOF systems along with all the extracted magnetic information.

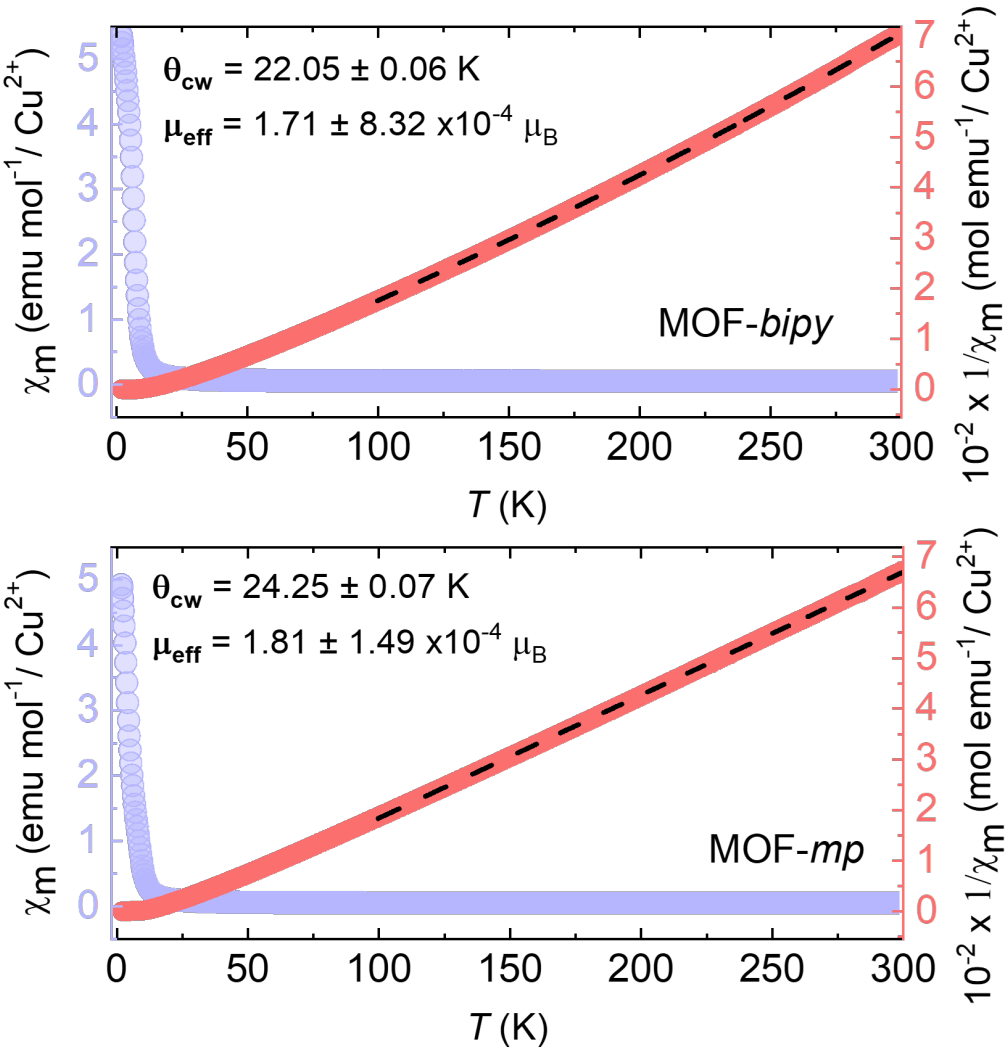


Figure 4.13: Temperature-dependent magnetic susceptibility data for MOF-*bipy* and MOF-*mp* at 0.1 T. Here we plot the magnetic and inverse magnetic susceptibility for both systems, upon fitting the data to the Curie-Weiss equation we obtain values for the Curie-Weiss temperatures (θ_{CW}) which were 22.05(6) and 24.25(7) K for MOF-*bipy* and MOF-*mp* respectively. These values suggest dominant ferromagnetic exchange interactions within both MOFs [12, 6]. We also extract values for the effective moment (μ_{eff}) which, in both cases, are consistent with the expected 1.72 μ_B for a $S = \frac{1}{2}$ system.

Initially we collected ZFC and FC measurements for MOF-*bipy* and MOF-*mp* to determine whether any bifurcation is observed to rule out signs of spin freezing or the onset of

ferromagnetic order (Figure A.2). The next measurements we took were magnetisation vs. temperature for both systems (Figure 4.13). In both cases we observe Curie-like behaviour until the potential transition temperatures, characterised by a deviation from the smooth curve. We then fit inverse susceptibility data to the Curie-Weiss equation. For MOF-*bipy* we extract a θ_{CW} = 22.05(6) K, and the Curie constant C = 0.3684(5) emu K mol^{-1} corresponding to a μ_{eff} = 1.71 ± 8.32 x 10^{-4} μ_B, in close agreement with the expected value for a $S = \frac{1}{2}$ system (1.73 μ_B). For MOF-*mp* we extract a θ_{CW} = 24.25(7) K, and the Curie constant C = 0.4114(1) emu K mol^{-1} corresponding to a μ_{eff} = 1.81 ± 1.49 x 10^{-4} μ_B, also in close agreement with the expected value for a $S = \frac{1}{2}$ system (1.73 μ_B). From these data we infer that the dominant exchange interactions present in both systems are likely ferromagnetic in nature, which we would expect for the copper carbonate kagome lattice [12]. To estimate the ordering temperature (T_C) of both systems we performed Fisher's specific heat calculations, plotting the derivatives of temperature multiplied magnetic susceptibility (Figure 4.14). Here, we are able to observe ordering temperatures $T_C \approx$ 8.5 and 5.7 K for MOF-*bipy* and MOF-*mp*, respectively, given by an inflection point.

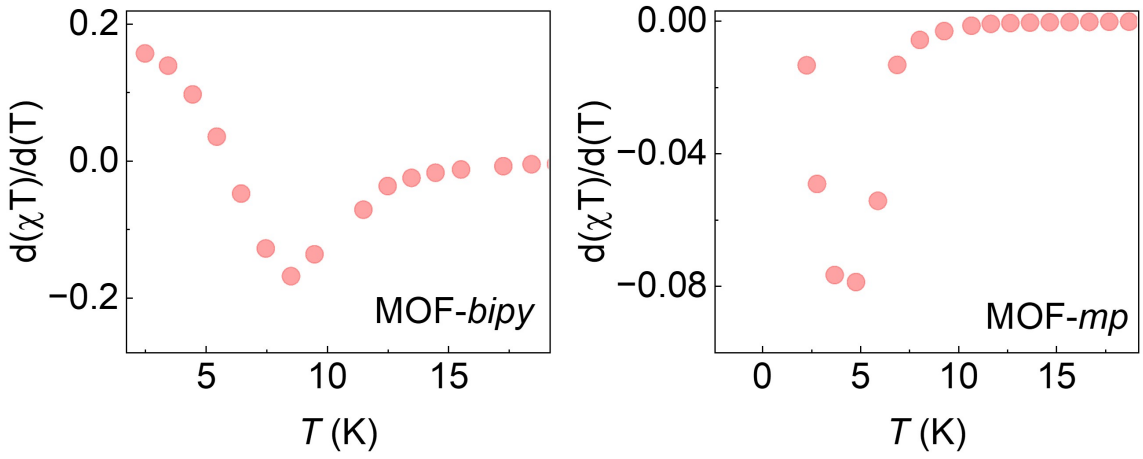


Figure 4.14: Derivative plots of temperature dependant magnetic susceptibility data collected in an applied field of 0.1 T for both MOF-*bipy* and MOF-*mp*. From these data we are able to extract an estimate for T_C from the point of inflection in each case. Ordering temperatures extracted were T_C = 8.529(2) and 4.798(6) K for MOF-*bipy* and MOF-*mp* respectively.

We also collect field-dependent measurements for MOF-*mp* and MOF-*bipy* at 2 K (Figure 4.15), finding that, 100 % of moments are saturated by an applied 7 T field respectively, and that no clear magnetic hysteresis is observed in either case, although we have found previously that the systems reported by Ivko *et al* hosted soft ferromagnetism, meaning the hysteresis is very weak. It is possible that these systems are also soft ferromagnets however we may need ultra low field measurements to tease these curves apart [25, 101].

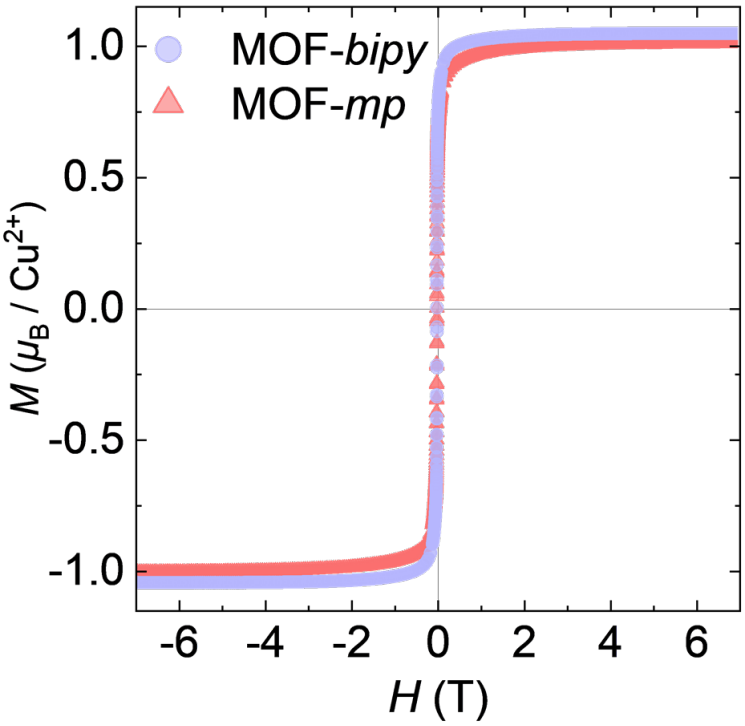


Figure 4.15: Magnetisation vs. field data for both MOF-*bipy* and MOF-*mp* overlain. Here we see no significant signs of magnetic hysteresis and a 1 T applied field appears to fully saturate both systems. Both systems near saturation at 1 T, with MOF-*bipy* approaching full saturation at lower field to MOF-*mp*.

4.3.6 Differences in Magnetic Heat Capacity Data

To further probe the bulk magnetism of these MOFs we collected heat capacity data. We collected these data in zero applied field between 1.8 and 300 K shown in Figure 4.16 and 4.18. Since the heat capacity we observe is the sum of the magnetic, phononic, electronic and nuclear heat capacity we must attempt to isolate the magnetic contribution [136]. Attempts were made to synthesise diamagnetic zinc analogues of the two systems, with the

formula $Zn_3(CO_3)_2(x)_6{\cdot}2ClO_4$ where x is $bipy$ or mp, as these would provide a better estimate of nonmagnetic contributions to heat capacity. These attempts were unsuccessful, so instead we use a simulated approximation derived from the Debye-Einstein relationship discussed in Chapter 2. To fit the high-temperature, phonon dominating region of the data ($T \geq 25$ K) we applied three Debye functions as follows:

$$C_{Debye} = \sum_{i=1}^{3}\left[9NR\left(\frac{T}{\theta_{Debye}}\right)^3 \int_0^{\frac{\theta_{Debye}}{T}} \frac{x^4 e^x}{(e^x-1)^2}dx\right]. \tag{4.1}$$

Each Debye function applied accounts for an atom type within the unit cell based on its respective mass (Cu, Cl, O/N/C) corresponding to x. N is the number of atoms in the formula unit and θ_{Debye} is the Debye temperature. The incorporation of a fourth Debye function to account for hydrogen was unstable, generating extreme errors. Ideally, we require a diamagnetic analogue for a more accurate approach to determining the magnetic contribution to heat capacity, which still does not guarantee a perfect subtraction.

MOF-*bipy*

For MOF-*bipy* we use Equation 4.1 to fit a data range of 25 − 300 K expected to host a dominant phononic contribution to the data (C_{pho}). This model had an excellent fit to the data with $R^2 = 0.999$ and reduced $\chi^2 = 9.512$, suggesting a reliable model to extrapolate to the 0 − 25 K region of the data (Figure 4.16 a, b). This extrapolation is subtracted from the data to isolate the magnetic contribution to the heat capacity (C_{mag}) (Figure 4.16 c). For a conventional magnetically ordered system we would expect to see a sharp peak indicative of the onset of long-range order around T_C [175]. For MOF-*bipy* however, we observe a broad feature with a maximum at ~7 K. There are many factors that may lead to a broad feature in magnetic heat capacity data, some include chemical disorder, the emergence of the Schottky anomaly (Equation 2.13), low dimensional magnetism [136, 176], and systematic errors due to the subtraction. We cannot determine which of these factors give rise to this feature, although considering the possibility that the kagome

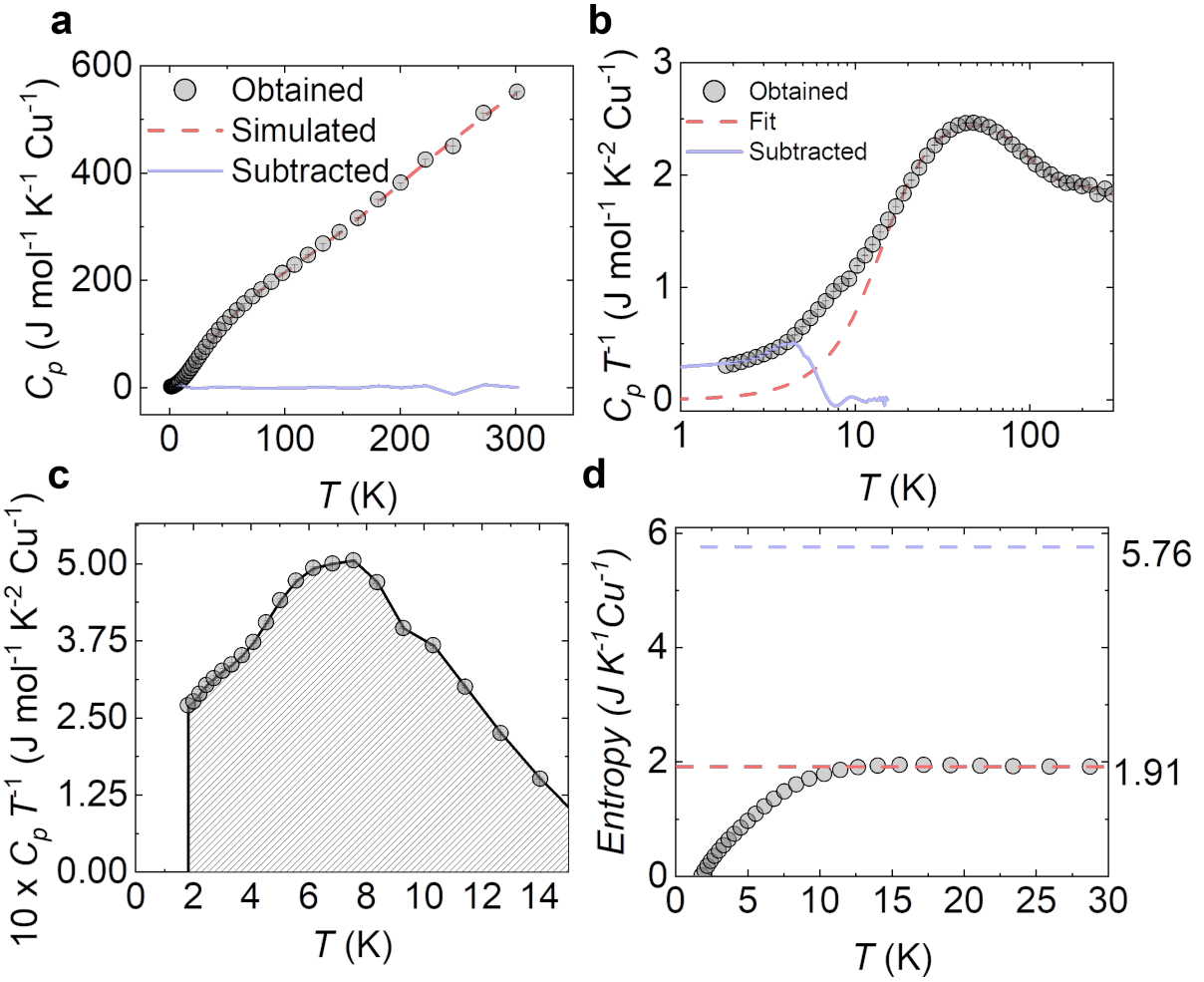


Figure 4.16: Heat capacity data for MOF-*bipy* collected in zero-applied field between 1.8 and 300 K. (a) A plot of zero field heat capacity vs. temperature data fit to three Debye functions across a temperature range of 25 – 300 K, this approximates the phonon contribution to total heat capacity given by the simulated curve. (b) A log plot of temperature-dependent heat capacity vs. temperature, with the subtraction of the simulated curve from obtained data giving (c) the magnetic temperature-dependent heat capacity. Here, a broad feature is observed below 12 K with a peak at ~7 K. (d) The total magnetic entropy release can be calculated by taking the integral of the temperature-dependent magnetic heat capacity indicating an entropy release of 33.05 % of the expected entropy release of a single, ($S = \frac{1}{2}$), Cu^{2+} ion.

layers present in MOF-*bipy* are magnetically isolated and has ligand disorder modelled previously (Figure 4.4), we may begin to outline the possible sources of such a broad feature. We also observe 76.95 % of magnetic entropy remains unaccounted for (Figure 4.16d), which may be another indication that three-dimensional magnetic order is not fully adopted. We can also be confident here that 76.95 % of magnetic entropy will not be recovered at temperatures below 1.8 K. Of course, to further corroborate these claims we require complementary results from other methods of characterisation, we obtain this from the observation and analysis of magnetic Bragg intensity in subtracted neutron powder diffraction data discussed later. Importantly, these data are our first indication that the magnetic characteristics present in MOF-*bipy* may not be three-dimensional in nature [177]. Additionally, we perform a Schottky fit to our magnetic heat capacity using Equation 2.13 to extract an energy gap as discussed in Chapter 2 (Figure 4.17). We find for MOF-*bipy* an energy gap of 1.38(17) meV for a two-level $S = \frac{1}{2}$ system, a value that may be compared experimentally in an inelastic neutron scattering experiment.

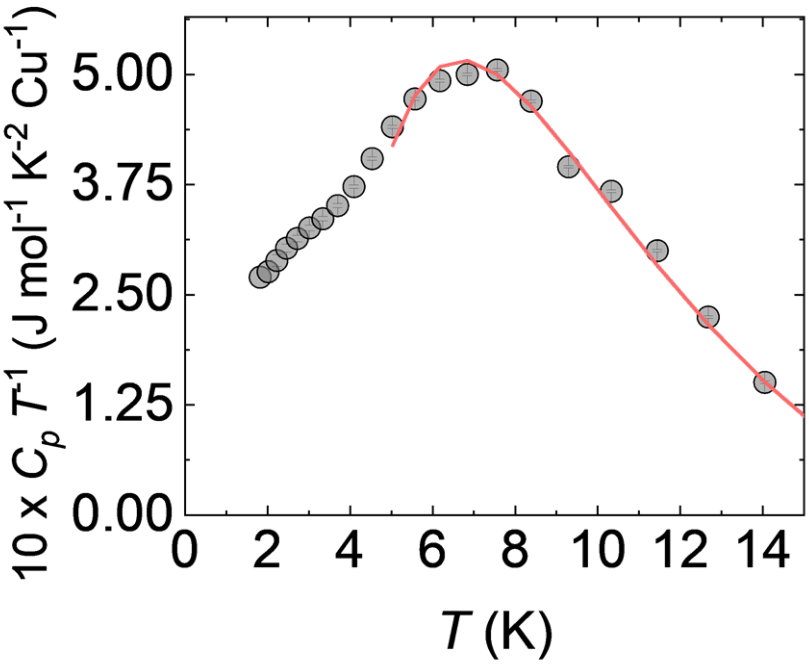


Figure 4.17: Magnetic heat capacity data for MOF-*bipy* fit to the Schottky anomoly, providing an extracted energy gap of 1.38(17) meV for a two-level $S = \frac{1}{2}$ system.

MOF-*mp*

We treated the heat capacity data for MOF-*mp* in a similar way to MOF-*bipy*, fitting our data to Equation 4.1 through a temperature range of 25 – 300 K to extrapolate a simulated curve for the subtraction of C_{pho} (Figure 4.18).

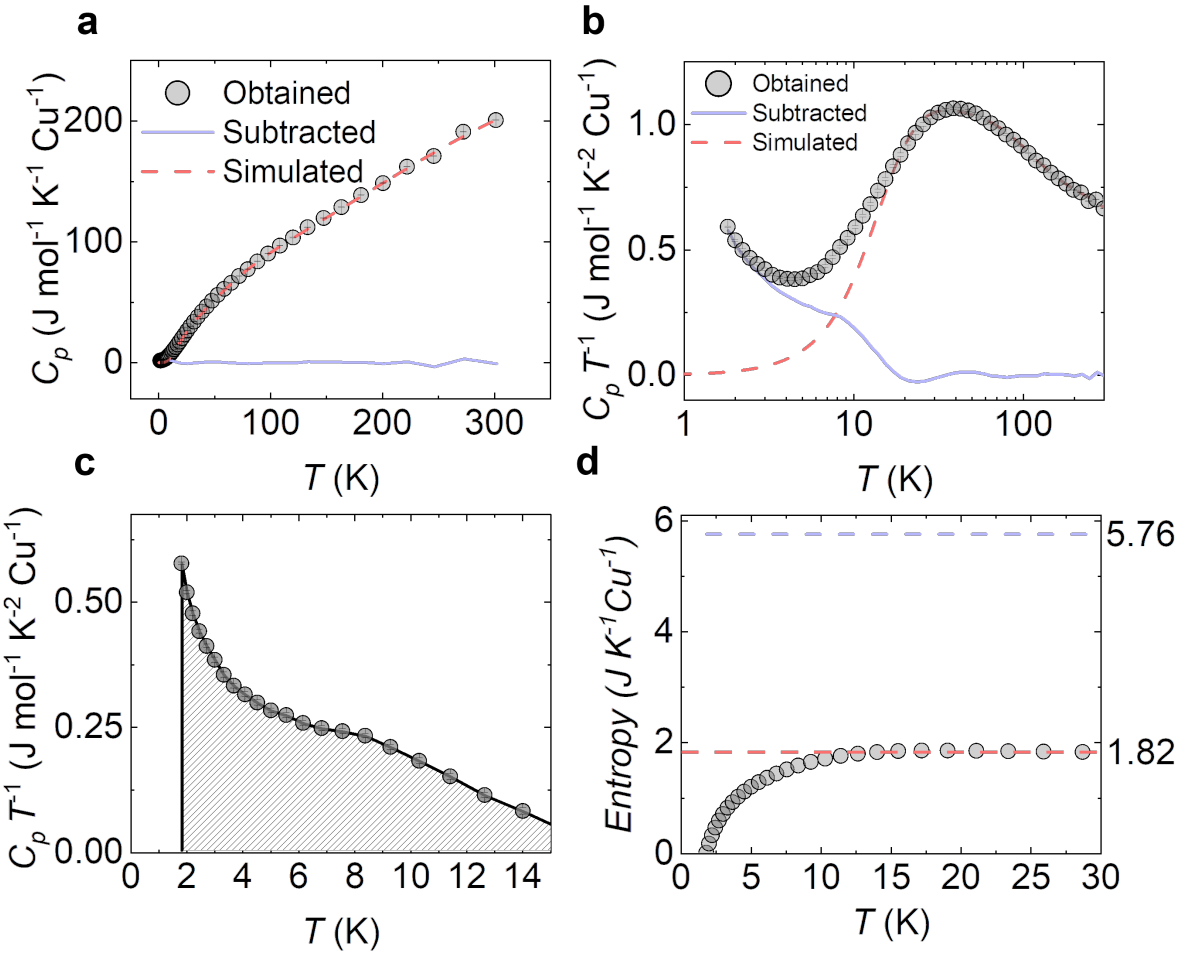


Figure 4.18: Heat capacity data for MOF-*mp* collected in zero-applied field between 1.8 and 300 K. (a) A plot of zero field heat capacity vs. temperature data fit to three Debye functions across a temperature range of 25 – 300 K, this approximates the phonon contribution to total heat capacity given by the simulated curve. (b) A log plot of temperature-dependent heat vs. temperature, with the subtraction of the simulated curve from obtained data giving (c) the magnetic temperature-dependent heat capacity. Here, a broad feature appears to be dominated by a rise in magnetic heat capacity below ~8 K which rises until the lowest collected temperature of 1.8 K. (d) The total magnetic entropy release can be calculated by taking the integral of the temperature-dependent magnetic heat capacity indicating an entropy release of 31.59 % of the expected entropy release of a single, ($S = \frac{1}{2}$), Cu^{2+} ion.

In our subtracted magnetic heat capacity data (Figure 4.18c), we observe a difference between the two MOFs. The curve appears to deviate from its trajectory at ~8 K rising to a peak at 1.8 K. Since our data end at 1.8 K, we cannot be sure of the magnetic heat capacity at lower temperatures; although this curve may indicate the onset of an ordered state, it is also possible that another phenomenon is dominating the low-temperature region of the data, such as the nuclear heat capacity (C_{Nuc}). With no definitive evidence for a transition to a magnetically ordered state outside of Fisher's specific heat. As we do not know how much further this peak increases below 1.8 K we cannot be sure how accurate our calculation of the magnetic entropy released would be, therefore we require a repeat measurement of MOF-*mp* at lower temperatures to be sure this is a real feature, and the extent of which it increases. If we were able to determine the source of this sharp feature, we may be able to subtract it to observe a similar broad feature to MOF-*bipy* however we cannot be sure. Similarly to MOF-*bipy* we also observe a significant portion of magnetic entropy missing (72.5 %), also suggesting that MOF-*mp* may not have adopted a fully magnetically ordered state down to 1.8 K however these assertions are only as strong as the quality of our phonon subtraction. [177].

Missing Magnetic Entropy in MOF-*bipy* and MOF-*mp*

The proceeding discussion outlines some possible reasons for the observations of these heat capacity data. From our Fishers' specific heat plots discussed previously, we find estimations for the T_{C} of both systems, 8.529(2) and 4.798(6) K for MOF-*bipy* and MOF-*mp* respectively. In the magnetic heat capacity for MOF-*bipy* we see that the T_{C} calculation matches up to the broad feature we observe in our magnetic heat capacity data, we also propose here that the intense upturn in MOF-*mp* will require a repeat measurement to confirm. In MOF-*bipy* we observe that a significant portion of magnetic entropy is missing, suggesting that the system may not undergo a transition from an uncorrelated, paramagnetic regime, to a three-dimensional long-range-ordered one. If MOF-*bipy* is indeed quasi-two-dimensional, then two-dimensional ferromagnetic correlations may ex-

ist above T_C, meaning that as we cool below T_C a smaller portion of magnetic entropy is required for an ordered state to be adopted which may explain this lack of entropy. Another possible explanation for this lack of entropy is that conventional long-range ferromagnetic order is not adopted by the copper carbonate kagome lattice. In the literature it is stated that for a ferromagnetic kagome lattice featuring nearest-neighbour exchange only, where J1/|J2| ≈ 0, long-range ferromagnetic order would likely be adopted [163]. In cases where next-nearest-neighbour exchange is facilitated, the magnetic ground state may shift toward an unconventional state [163]. Since we are confident that the nature of exchange present within the copper carbonate kagome lattice will be ferromagnetic from comparisons to the copper carbonate MOFs outlined in Chapter 3, we may explain our unexpected heat capacity results for MOF-*bipy* by suggesting that further neighbour exchange coupling is facilitated within the kagome layers for these systems. Ultimately, we require repeat measurements for both systems to confirm that the features observed are indeed real effects or that these features do not simply arise through instrumental or data processing errors. Additionally, applying a simple Lorentzian function to low temperature MOF-*mp* data may allow for the subtraction of the upturn leaving behind a similar broad feature to MOF-*bipy*, however there is no way of knowing whether the data collected for MOF-*mp* is valid for these comparisons and so a repeat measurement is the main suggestion here.

4.3.7 Magnetic characterisation by Neutron Powder Diffraction

Since the neutron is capable of interacting via both strong nuclear force and by dipole-dipole interactions, we are able to collect data containing both nuclear and magnetic information. To isolate the magnetic information we require data collected above and below the estimated T_C of a system. Subtracting these data provide a pattern containing only magnetic information which we may analyse. We can then extract information on the moment sizes and orientations in an ordered lattice, which allows us to refine a magnetic unit cell similarly to the nuclear refinements of the nuclear cell discussed previously. For

both MOF-*bipy* and MOF-*mp* we observe one magnetic Bragg reflection which we fit in the magnetic space group $P1$. The $P1$ space group has no symmetry constraints and so moments within the cell have the freedom to point in any direction, since this does not reflect the data, we must apply a constraint consistent with the observed pattern. For this, we constrain all the moments to be parallel in the the ab-plane, as the single observed (0 0 l) reflection does not provide information on the moments pointed outside of the ab-plane. In the subtracted data for both MOF-*bipy* and MOF-*mp*, we observe one broad peak at a d-spacing consistent with the crystallographic c-axis of the unit cell. Unlike MOF-*bpa*, discussed in Chapter 3 we observe no doubling of the c-axis for our magnetic unit cell, and therefore infer a k vector = (0 0 0), corresponding to a magnetic cell with dimensions equivalent to the nuclear cell. This was our first indication that no antiferromagnetic inter-plane exchange coupling was present in MOF-*bipy*. For MOF-*mp* however, this assertion cannot be made because the crystallographic unit cell contains a bilayer, and a reflection at ~31 Å only provides information on the next-nearest neighbouring plane and not the nearest-neighbour layer within a single unit cell.

MOF-*bipy*

The magnetic component of WISH data for MOF-*bipy* was obtained through the subtraction of 1.5 K data from 14 K data (above the suspected T_C ≈8 K obtained from Fisher's specific heat and heat capacity measurements). Fitting these data to the $P1$ space group with a cell containing 11 copper atoms, a scale factor obtained from our nuclear refinement of 4.9478(7) and fixed lattice parameters of $a = b = 15.8760(4)$ Å and $c = 21.2175(8)$ Å, provides us with a good fit to the data, $\chi^2 = 0.7798$. These data are shown in Figure 4.19 and 4.20. Due to the signal to noise ratio, only one weak, broad magnetic Bragg reflection, (0 0 1), is observed, this limits what may be constrained in the model. We performed three refinements with the moment size allowed to vary solely along the a-axis, b-axis and both combined. We found no difference in the moment size propagating either the a or b-axis with a divergence observed in the refinement of both simultaneously. Therefore, we report

a moment size of 0.32(5) μ_B along the a-axis producing the magnetic unit cell illustrated in Figure 4.20. This is a lower value than the related copper carbonate kagome MOFs

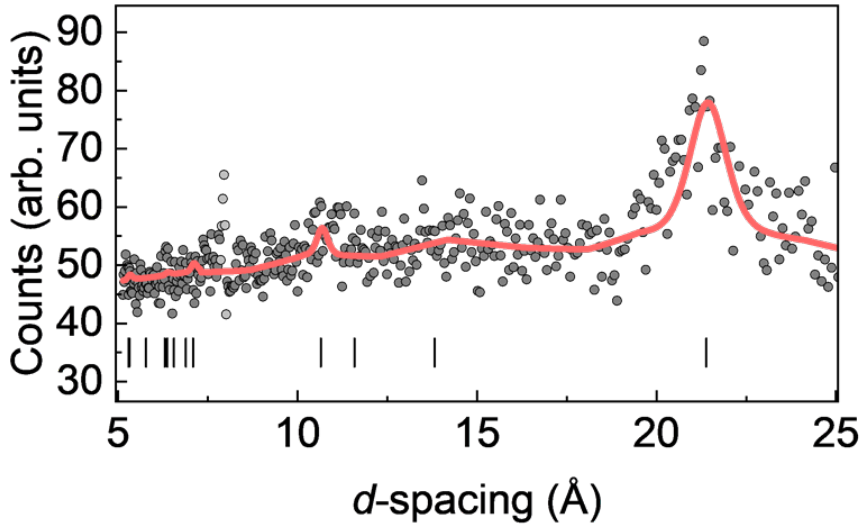


Figure 4.19: The magnetic refinement of subtracted MOF-*bipy* WISH neutron powder diffraction data to the constrained $P1$ model. The refinement was performed by constraining the moment orientation of 11 copper sites to the ab-plane, fixing cell parameters to $a = b = 15.8760(4)$ Å and $c = 21.2175(8)$ Å with a scale factor of 4.9478(7). A thermal contraction can be observed between 7.8 and 8.2 Å.

outlined in Chapter 3, summarised in Table 3.5, however similar low values also arise in systems featuring $S = \frac{1}{2}$ two-dimensional magnetism, as quantum fluctuations suppress the ordered moment [178]. Importantly, no magnetic intensity was observed at a doubling of the c-axis which we have found previously indicates the presence of antiferromagnetic exchange coupling between kagome planes [12]. This provides us with evidence that the magnetic exchange coupling in MOF-*bipy* may be isolated to the kagome plane however there is little direct evidence for this besides the fact that magnetic exchange is highly unlikely to propagate this gap. This is still an exciting discovery, as the use of non-covalent ligands like 2,4'-bipyridine was driven by our hypothesis that they would not mediate magnetic exchange between kagome layers which is a possibility from these data. As the largest magnetic Bragg peak is observed at 21.2175(8) Å , the length of the c-axis, we can be confident that we have a ferromagnetically correlated system. More evidence supporting our assignment of ferromagnetic kagome layers is the lack of spontaneous downturn in

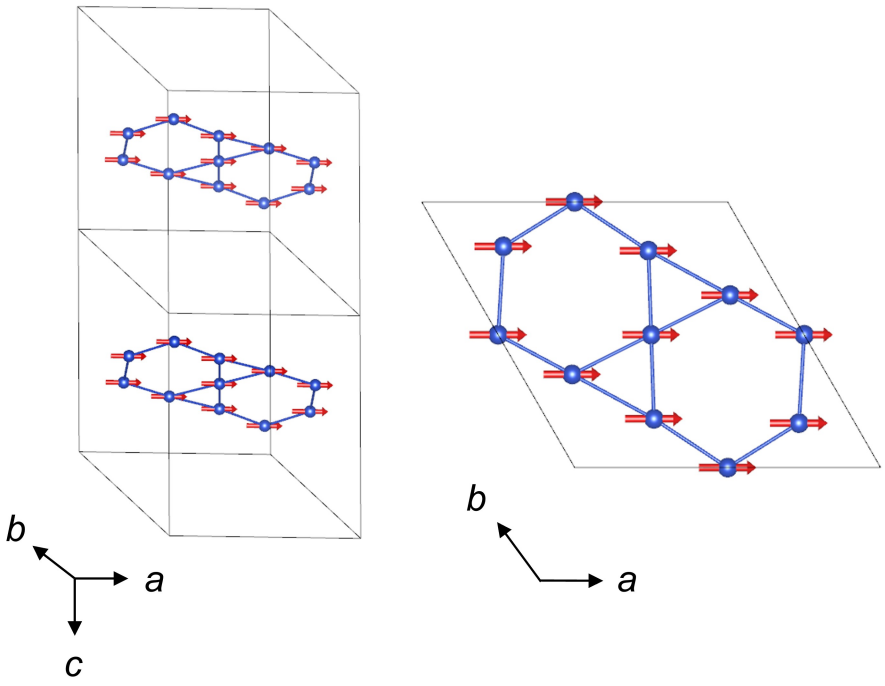


Figure 4.20: In the proposed magnetic structure of MOF-*bipy* ferromagnetically coupled Cu^{2+} atoms within the *ab*-plane lie within kagome planes, with no sign of antiferromagnetic coupling between kagome layers. This model may suggest the presence of isolated magnetic kagome layers, however ferromagnetic coupling between these layers cannot be ruled out.

temperature dependant magnetic susceptibility indicative of antiferromagnetic exchange coupling, which is observed in all covalently bound kagome MOFs discussed in Chapter 3 [12], all of which feature antiferromagnetic exchange coupling between kagome planes.

MOF-*mp*

The magnetic component of WISH data for MOF-*mp* was obtained through the subtraction of 15 K data from 1.5 K data (above the suspected T_C ≈5 K obtained from Fisher's specific heat calculations). We fit these data to the *P*1 space group with a cell containing 6 copper atoms, with fixed lattice parameters of $a = b = 9.4080(9)$ Å and $c = 31.0350(1)$ Å and a scale factor of 4.33472(6), extracted from the Rietveld refinement of comparable Bank 1 data. We were able to index a *k*-vector of (0 0 0) from the observation of a magnetic Bragg reflection consistent with the nuclear cell symmetry. Similarly to MOF-*bipy*, the magnetic Bragg reflection was observed for the (0 0 *l*) position only, and so moment

propagation was constrained to point within the *ab*-plane. Interestingly, we are able to fit our subtracted data to three models (Figure 4.21), with this complexity arising due to the presence of two magnetic planes within the cell. Another consideration is that the magnetic Bragg reflection observed is at ~31.39 Å which would only provide us with information on magnetic layers separated by an entire unit cell.

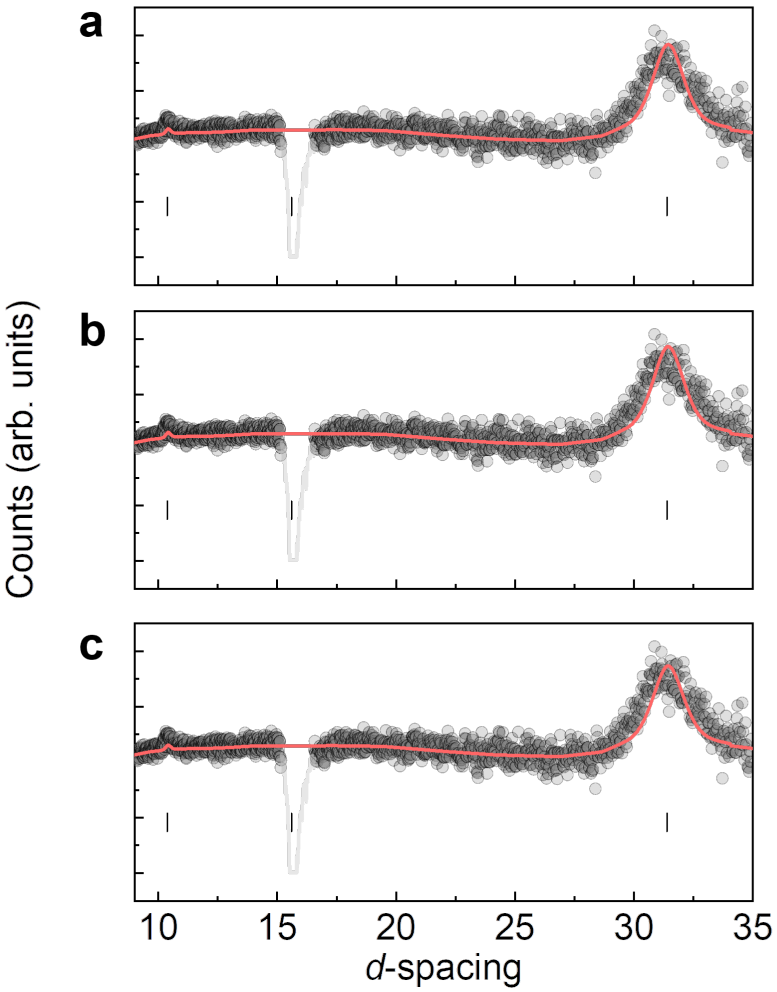


Figure 4.21: Magnetic fits to temperature subtracted neutron powder diffraction data, with a thermal contraction removed between 15.05 – 16.61 Å. a) For this fit, one layer containing three copper atoms was allowed to refine constrained to the *a*-axis producing an ordered moment of 0.76(8) μ_B. b) In this fit the complete unit cell containing six copper atoms was allowed to refine with each layer constrained to be equal but opposite in the *a*-axis producing an ordered moment for the layers of 0.38(8) and -0.38(8) μ_B. c) In this fit, the complete unit cell containing six copper atoms was allowed to refine, with each layer pointing in a different crystallographic plane with ordered moments of 0.428 μ_B in the *a*-axis and 0.42(8) μ_B in the *b*-axis.

We therefore gain no information on the nature of magnetic exchange between layers within the cell separated by ~ 15.17 Å. A thermal contraction is observed at this *d*-spacing which may mask magnetic Bragg intensity here. Due to these factors, our magnetic models for MOF-*mp* can only infer the nature of exchange with nearest neighbour layers based upon the exchange interactions viewed upon one kagome layer, hence we are able to fit these data to the three different models summarised in Figure 4.22.

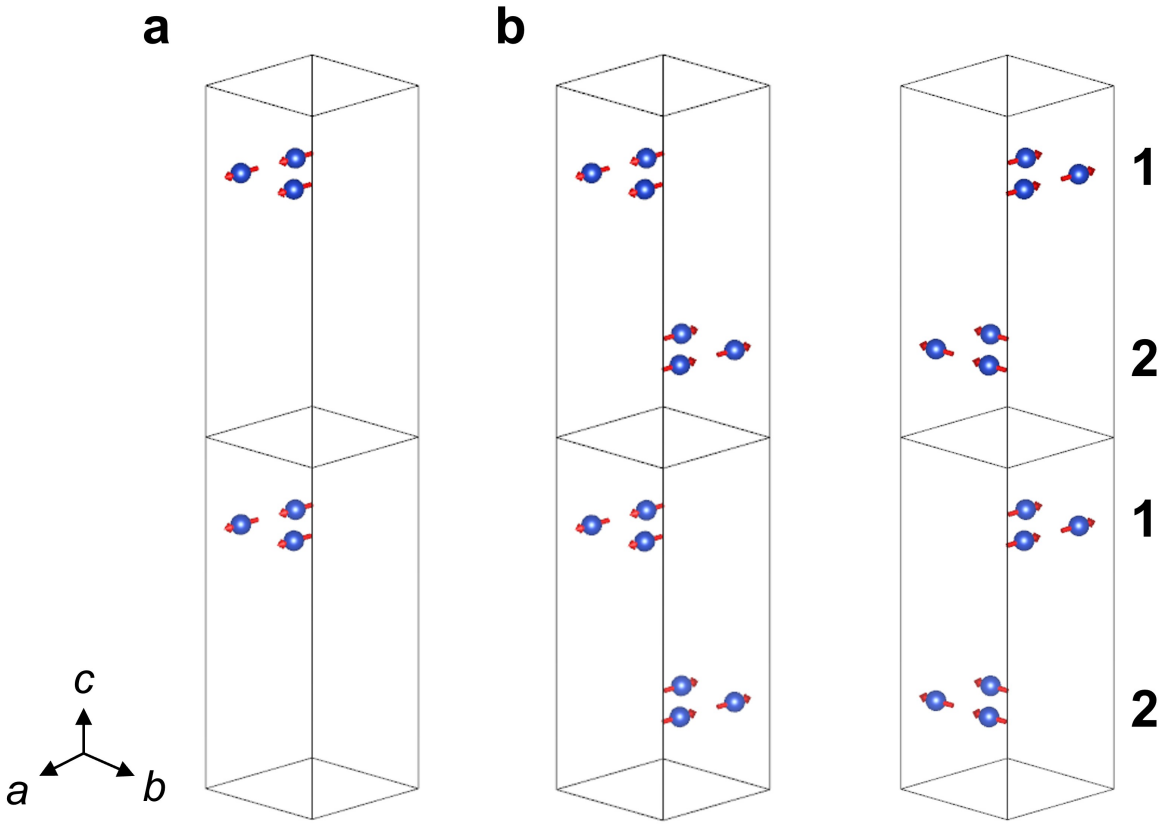


Figure 4.22: Proposed magnetic structures for MOF-*mp* based upon the magnetic fits performed. a) In this model three magnetic moments per cell are coupled ferromagnetically pointing in the *a*-axis; b) In these models we observe layers of ferromagnetically coupled moments, the nearest-neighbour layers may be modelled pointing in any direction in the *ab*-plane, as the fit only provides information on two layers separated by one unit cell. The numbers denote equivalent layers.

As discussed the single magnetic Bragg peak which we fit to each of these models provides us with information solely for two planes separated by ~31 Å. It is therefore possible for two planes separated by ~15 Å to be refined in any direction in the *ab*-plane provided it is

consistent with its neighbouring unit cell. If we consider two unit cells stacked along the *c*-axis, we would observe four kagome layers. Using Figure 4.23b as a reference, we can label these distinct layers one and two, our data would be fit by any model in which the moments in layer one are equivalent and the moments in layer two point in the *ab*-plane. As a consequence, attempts to fit these data to models incorporating nearest-neighbour layer interactions did not fit the data, as these fits require the presence of a magnetic Bragg reflection within the region dominated by a thermal contraction. Because of this, we are unable to make any claims about the magnetic interactions which may occur between nearest-neighbour layers within the unit cell.

Comparisons of MOF-*bipy* and MOF-*mp*

For these systems, we find ordered magnetic moments for a single layer of the copper carbonate kagome to be consistent and within error. With the refined moment for MOF-*bipy* = 0.32(5) μ_B, and the ordered moment for a bilayer of MOF-*mp* = 0.76(7) μ_B, and a monolayer = 0.38(7) μ_B. The values obtained for the two MOFs are lower than those for the related copper carbonate kagome MOFs outlined in Chapter 3, summarised in Table 3.5. It is possible that the reductions in moment size come from the quasi-two-dimensionality of the moments within MOF-*bipy* and MOF-*mp*. This assertion may also be supported by our heat capacity data, where the missing entropy observed in both cases may arise due to increased quantum fluctuations due to lower dimensionality [178], or due to the presence of two-dimensionally correlated ferromagnetic moments at temperatures higher than our expected T_C. In the case of the latter, our temperature subtraction would not fully capture the onset of magnetic order from a fully paramagnetic regime to a ferromagnetically ordered one, hence the reduced moment size. A well-known limitation of neutron powder diffraction refinements is the challenge of finding a temperature high enough to yield the paramagnetic information required for proper subtraction, but low enough to minimise thermal contractions, which may mask the magnetic Bragg intensity. Importantly, despite some uncertainty on the exact cause of the reduced moment sizes

for MOF-*bipy* and MOF-*mp*, we do observe evidence of ferromagnetic exchange coupling within $S = \frac{1}{2}$ kagome layers, which may be isolated from adjacent layers.

4.3.8 Nanosheet characterisation by Atomic Force Microscopy

As we discussed at the beginning of this chapter, magnetically isolated two-dimensional ferromagnetic kagome layers were proposed to exist in MOF-*bipy* and MOF-*mp* due to the lack of covalent bonding between the kagome layers. Based upon our findings for MOF-*bipy* we expect ferromagnetic exchange coupling within these kagome layers which is correlated between the nearest-neighbour layer, and so exfoliation of the system to the monolayer would, in theory, afford ferromagnetic kagome nanosheets. In the case of MOF-*mp* we cannot rule out the presence of antiferromagnetic nearest neighbour layer correlations; however, the most likely case is that, similarly to MOF-*bipy* the kagome layers are ferromagnetically coupled in plane and ferromagnetically correlated between them. As such, exfoliated monolayers or bilayers of MOF-*mp* would likely still be examples of ferromagnetic kagome nanosheets.

As discussed, we approach the exfoliation of these MOFs by ultrasonication methods [170], tracking the thicknesses of the exfoliated materials by atomic force microscopy (AFM) measurements. We were able to begin optimising the exfoliation process through varying our nanosheet preparation and tracking these results by AFM study. When using this method, nanosheets are often characterised by a sharp rise, a long plateau, and a sharp fall with a height equal to the expected height of a monolayer or bilayer of the three-dimensional parent system. In the case of MOF-*bipy* the expected height of one layer was 21.270 Å or 2.13 nm, while the height of one bilayer of MOF-*mp* was 31.035 Å or 3.04 nm. AFM data collected for both systems is shown in Figure 4.23. We can see here that in both cases, features consistent with nanosheets are present, and for MOF-*bipy* we observe features with height profiles ~1.9 nm, which are close to the expected value of 2.1 nm for a single layer and within the error of the instrument. For MOF-*mp*

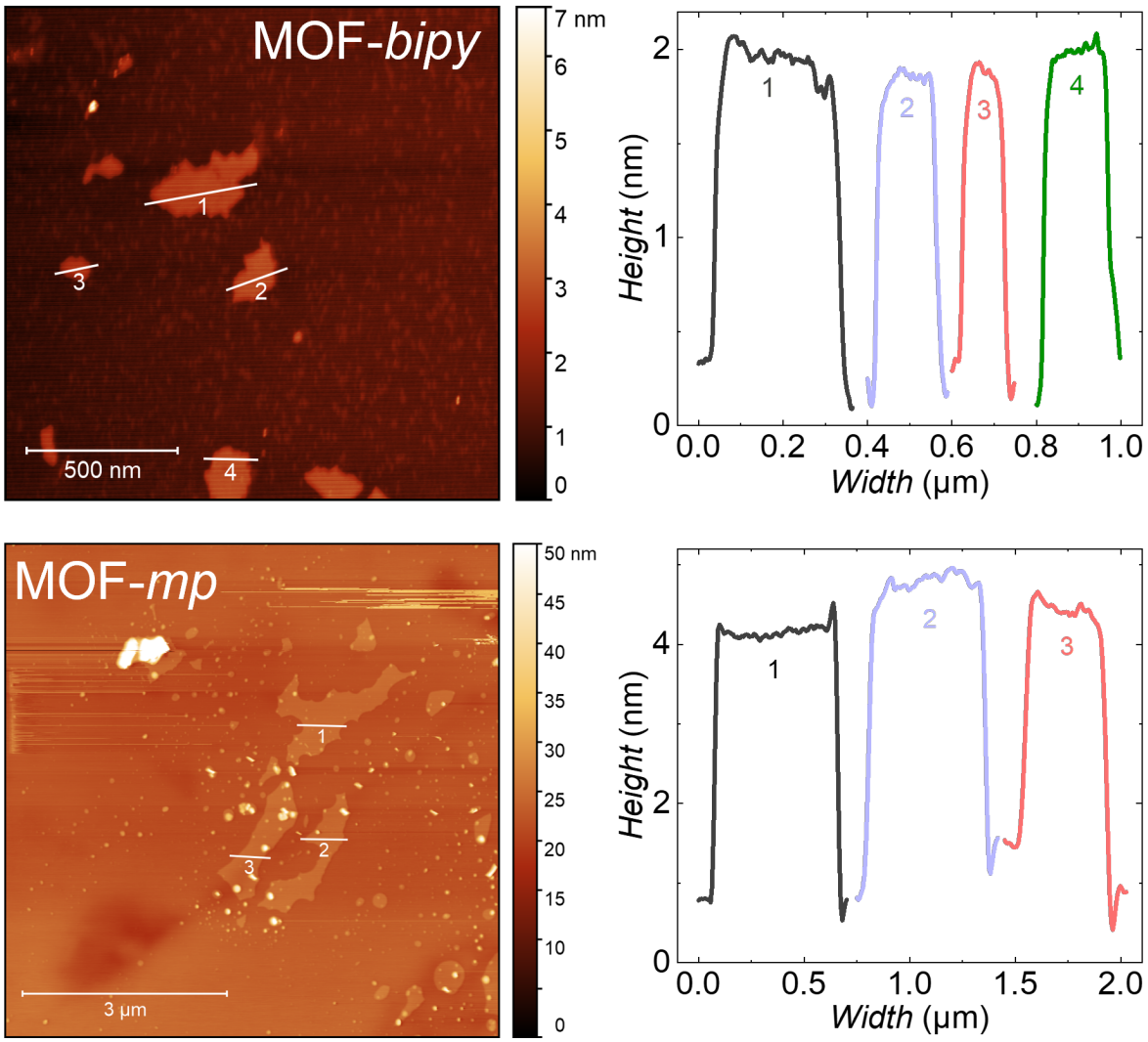


Figure 4.23: Atomic force microscope images and respective height profile maps for specified points for (top) MOF-*bipy* where we see height profiles ~2 nm with a lateral scale of 500 nm, and (bottom) MOF-*mp* where we see height profiles ~3 nm with a lateral scales up to 3 μm.

we see height profiles ~ 3.4 nm again, within a reasonable range of the expected height profile of a MOF-*mp* bilayer. From these data we have a strong indication that we have been successful in producing nanosheets, however there are limitations of our samples which must be considered for these systems. One of these limitations was the difficulty in developing a rigorous exfoliation method that guarantees the selective production of nanosheets. What is often observed in AFM images of the two systems are circular features consistent with clumps of crystalline material with height profiles ranging between $10-100$ nm dominating the sample area. Despite the centrifugation of exfoliated samples,

it is apparent that nanosheets have an affinity for clumping together. As such, distinguishing nanosheets from clumped nanoparticulate material, or finding nanosheets even in cases where nanoparticulates are largely removed was challenging. For context, we were successful in observing material consistent with nanosheets on three occasions across the collection of more than 400 images.

Along the way, we attempted several exfoliation optimisations; first, we experimented with the concentration of the MOF, then the time of exfoliation, the speed of centrifugation, the number of rounds of centrifugation and the type of sample deposition. None of these alterations definitively provided a robust method to isolate pure nanosheet material however, we were able to find nanosheet material along the way. The challenges of isolating nanosheets are echoed in further characterisation techniques, as the methods commonly used to confirm bulk structural and magnetic properties are not appropriate for such small samples. With no way of isolating large quantities of pure nanosheet material, the majority of bulk characterisation techniques cannot be used, making further characterisation of the nanosheets challenging. Ideally, we would need to confirm that the observed nanosheets are still crystalline, before confirming whether they are magnetically active through methods such as X-ray circular dichroism (XMCD) or magneto-optic kerr effect (MOKE) [179]. Regarding this, XMCD beamtime is scheduled for July 2024 providing us with an opportunity to confirm the magnetic activity of our exfoliated material. Realistically, the challenge of nanosheet characterisation comes from their novelty. We are still in the developmental stages of characterising this emerging class of materials. As such, more challenging materials will aid in the optimisation, development and discovery of suitable techniques capable of fully elucidating the structures and magnetic behaviour of nanosheet magnets.

4.4 Conclusions

Here, we report the synthesis and comprehensive structural and magnetic characterisation of two non-covalently stacked, Cu^{2+}, CO_3^{2-} kagome-containing MOFs, sharing the $Cu_3(CO_3)_2(x)_6{\cdot}2ClO_4$ formula, where x is methylpyridine or 2,4-bipyridine have been reported. Of these two systems MOF-*mp* was new to the literature, making this study an exciting insight into the magnetic behaviours of a new kagome-containing MOF. The use of neutron and XRD has allowed us to structurally characterise the bulk of both systems alongside giving us insights into the magnetic ground states hosted by the MOFs. The analysis of these two systems sharing the characteristics of a kagome lattice stacked by weak intermolecular forces has allowed us to draw some comparisons between them, helping us understand the effects of structural change on systems with non-trivial magnetic ground states. Some of the key findings from this chapter are summarised here:

1 – The crystal structure of MOF-*bipy* was confirmed, and modelled in the $P\overline{3}$ via SCXRD, this assignment was then confirmed to be representative of the bulk through the Rietveld refinement of NPD data.

2 – The crystal structure of MOF-*mp* was modelled through the use of SCXRD data, with the $P6_3/m$ space group and cell parameters confirmed by characterisation of the bulk in the Le Bail refinements of lab and synchrotron X-rays as well as neutrons. From the bulk analysis we highlight several features of MOF-*mp* which make its bulk characterisation challenging, the presence of preferred orientation, anisotropic particle sizes, stacking faults structural deformation and disorder all contribute to the difficulty in performing Rietveld analysis on MOF-*mp*. We conclude that these features are more pronounced in comparison to MOF-*bipy* due to weaker interlayer stacking interactions.

3 – From bulk magnetic susceptibility measurements, we found that both systems do not show a clear sign of adopting a conventional long-range magnetically ordered state.

Despite this, transition temperatures of ≈ 8.5 and 4.7 K for MOF-*bipy* and MOF-*mp* were extracted respectively from Fisher's specific heat calculations suggesting that these systems do undergo a magnetic transition.

4 – From our NPD measurements, we model ferromagnetic kagome layers in MOF-*bipy* and MOF-*mp* which we would expect upon a copper carbonate kagome lattice [12]. In the subtracted magnetic data in each case, we extract a lower-order moment than the related systems studied in Chapter 3. This may originate from subtracted data that do not describe a transition from fully paramagnetic to long-range ordered state, indicating that higher temperature magnetic correlations are present. In addition to this, we may expect a lower ordered moment due to the presence of two-dimensional exchange interactions. For MOF-*mp* we cannot rule out the possibility that the bilayer contained within the unit cell is not antiferromagnetically coupled, although the distance and stacking motif devoid of covalent linkage makes this unlikely.

5 – Finally, we provide evidence by AFM that it is possible to delaminate both MOFs to the two-dimensional limit. This makes these systems ideal candidates for further study of their magnetic characteristics on the two-dimensional scale, as low dimensionality is said to provide an excellent foundation for the observation of exotic magnetic states due to the increased effects of quantum fluctuations [104].

During this study, we have shown once again that MOFs are incredibly versatile in nature, allowing us to design networks of magnetically interacting atoms likely to feature interesting exchange interactions. One of the key points of interest with these two systems was the fact that magnetic kagome layers are stacked by weak intermolecular forces, since covalently linked copper carbonate kagome lattices were studied in Chapter 3, this chapter provides an insight into the added complexity of structural and magnetic characterisation of stacked MOFs expected to host quasi-two-dimesnional exchange interactions.

We report evidence here, that the magnetic ground states of this, now extended, family of kagome-containing MOFs are not conventionally ordered ferromagnets.

To overcome the challenge of magnetically characterising these systems, computational calculations of the likely magnetic exchange pathways are likely required, as only so much can be said about the acquired data. Again, the growth of large single crystals would facilitate single crystal magnetic characterisation, eliminating many of the issues plaguing our bulk characterisation attempts especially in MOF-*mp*. In terms of exfoliation to nanosheets, we must confirm the crystallinity of the nanosheets observed by AFM. We may do this through the use of electron diffraction, electron backscattering or even the collection of a bulk sample of pure nanosheets, however all of these require the development of a robust method of pure nanosheet production.

If a robust method was developed, and the crystallinity of these nanosheets was confirmed, we may perform measurements such as MOKE or X-ray magnetic circular dichroism techniques to confirm that our nanosheets were magnetically active. In this chapter, we have outlined two magnetic MOFs which likely host quasi-two-dimensional exchange interactions. These also show promise to be exfoliated to the monolayer, reiterating the strength of MOF chemistry for the discovery of interesting magnetic materials and pushing the emerging field of two-dimensional magnetic materials forward. Additionally, we present two candidates that host a ferromagnetic kagome arrangement of $S = \frac{1}{2}$ atoms with the strong potential to host interesting band structures arising from the strong quantum fluctuations generated from the small energy scales and low dimensionality [11, 178, 180].

Chapter 5

Realising the $S = \frac{1}{2}$ Kagome Antiferromagnet in a Metal-Organic-Framework

5.1 Introduction

As we have previously discussed, magnetic MOFs are an incredibly versatile class of materials, with some of their tunability and unconventional ferromagnetism exemplified in Chapters 3 and 4. In this chapter however, we begin to explore another avenue, approaching the two-dimensional model of the $S = \frac{1}{2}$ kagome antiferromagnet in a MOF. In previous chapters, we attempted to generate magnetically isolated kagome layers through out-of-kagome-plane ligand selection; however, due to the dominant ferromagnetic exchange in these systems we could not study them as QSL candidates despite their intriguing properties. In this chapter, we focus on changing the in-kagome-plane ligand while ensuring that these planes are non-covalently stacked, in hopes of generating isolated, antiferromagnetic exchange coupling within a kagome MOF. We expect that a two-dimensional, antiferromagnetically coupled kagome MOF would bring us closer than ever before to the ideal conditions expected for the observation of a QSL state in a MOF. To reiterate these

optimal conditions; $S = \frac{1}{2}$ magnetic atoms, isolated two-dimensional antiferromagnetic exchange pathways within a frustrated geometry such as the kagome [82]. Here, we use $S = \frac{1}{2}$, Cu^{2+}, with multiple theoretical and experimental studies in the literature suggesting that various ligands would be suitable for mediating antiferromagnetic exchange coupling, while preserving a kagome arrangement within a MOF [94, 97, 98, 181]. In the literature, these prospective ligands appear to host antiferromagnetic exchange coupling, while simultaneously forming MOFs with no covalent inter-kagome-plane linkage [94]. With these antiferromagnetic kagome layers often stacking without conventional covalent bonding, we expect these three-dimensional MOFs to host magnetic exchange exclusive to the kagome layers.

One theoretical study on such MOFs indicated that the use of C_6O_6, C_6S_6 and C_6Se_6 ligands, bound to a magnetic metal ion, in a kagome arrangement, would likely yield exciting magnetic phenomena for experimental study [181]. In an experimental study a $Cu_3(C_6S_6)_2$ species was characterised though combined heat capacity and magnetic susceptibility studies. These indicated a lack of magnetic order down to 50 mK, with $\theta_{CW} = -1400$ K suggesting strong antiferromagnetic exchange coupling [182]. Similarly, computational studies on $Fe_3(C_6O_6)_2$ suggested antiferromagnetic exchange coupling in magnetically isolated kagome layers through DFT calculations, however, they were unable to prove this experimentally [94]. These studies established that the $M_3(C_6X_6)_2$ formula is appropriate for approaching the QSL state in a two-dimensional MOF. Here, we introduce $Cu_3(C_6O_6)_2 \cdot xH_2O$, (Cu-HHB), where HHB is a dehydrogenated hexahydroxybenzene ligand, following the $M_3(C_6X_6)_2$ formula. This system has been studied primarily for its conductive properties [97], with the most recent reports determining a robust synthetic method and Curie-Weiss analysis $\theta_{CW} = -26.1$ K, where no signs of long-range order were found in magnetic susceptibility data down to 1.8 K [98].

The structure of Cu-HHB (Figure 5.2) is unconventional, with kagome layers made up of

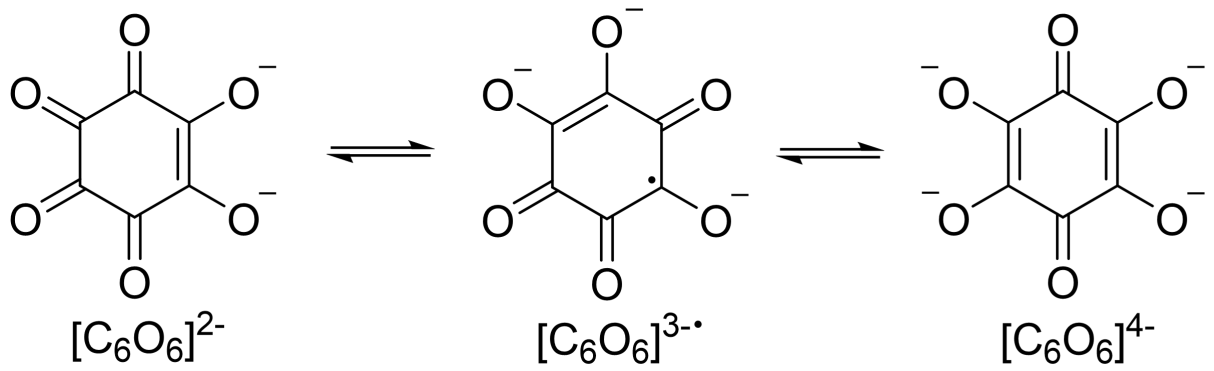


Figure 5.1: The proposed resonant forms of the C_6O_6 ligand. For the charge of the Cu-HHB to be balanced, an average charge of 3- must be upheld, this was confirmed through electron diffraction (ED) and X-ray photoemission spectroscopy (XPS) studies by Meng *et al* [98].

Cu^{2+} ions, chelated by C_6O_6 which is proposed to exist in a state of resonance (Figure 5.1) balancing the charge to form a kagome network of corner sharing triangles. For Cu-HHB, ED methods were employed by Meng *et al*, determining that Cu-HHB adopts the $C2/m$ space group with refined lattice parameters of a = 21.86(3), b = 12.950(5) and c = 6.120(7) Å [98]. In their report, they also collected powder X-ray diffraction (XRD) data for a sample of Cu-HHB, refining this against the $P2/m$ model by the Le Bail method. This suggested some uncertainty in the space group assignment, which we later clarify using high-resolution synchrontron powder XRD. In Cu-HHB, the kagome layers are proposed to be stacked by unconventional π-π, "pancake bonds" previously unobserved in MOFs [98, 183, 184]. These "pancake bonds" are generally found to occur between radical species with highly delocalised π electrons, such as in radical benzene species [185]. In such pancake-bonded systems, radicals are free to dimerise, making them spin-neutral. Since Cu-HHB may feature $[C_6O_6]^{3-\cdot}$ as the dominant resonant ligand form, and a strong link between such radical forms and charge stabilisation in the MOF (outlined by Meng *et al* [98]), we agree that it is possible for pancake bonds to exist in Cu-HHB. Experimentally, we can also infer the presence of pancake bonds by magnetic susceptibility measurements, as present radical species would increase the experimentally obtained spin-only moment of Cu-HHB above the expected spin-only contribution of Cu^{2+}. The theoretical and experimental literature suggest that Cu-HHB would be a prime candidate to host a QSL

state [94, 97, 98, 181]. Therefore, we chose to explore the magnetism of this system at the lowest possible temperatures using NPD, MuSR, magnetic susceptibility and heat capacity measurements to determine whether a QSL-like state lies within Cu-HHB. In addition, the synthesis of Cu-HHB was optimised from literature reports, with structural determination carried out via high-resolution powder XRD and NPD. Together, the complementary measurements are used to elucidate the crystal structure and unconventional magnetic ground state of Cu-HHB, a promising QSL candidate.

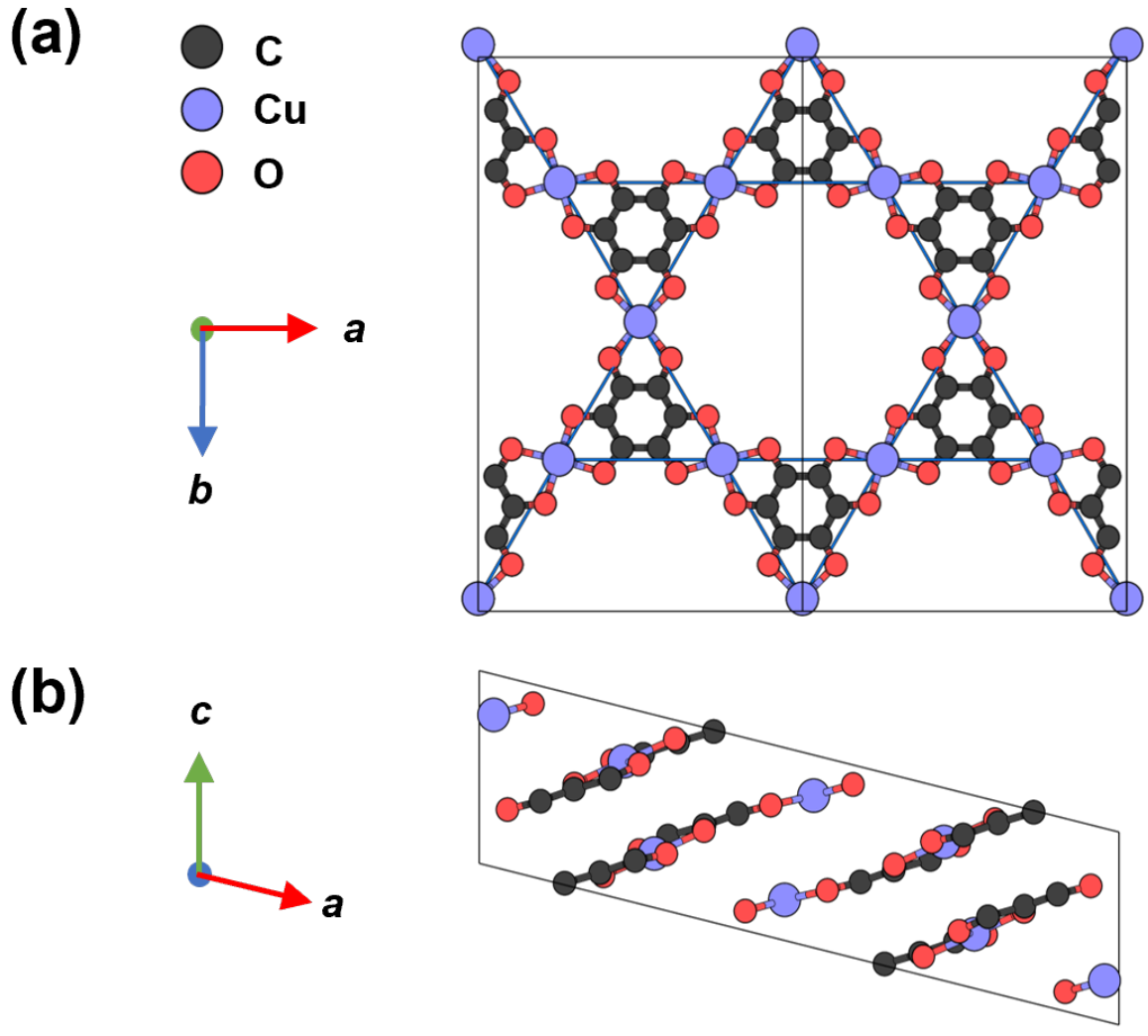


Figure 5.2: A crystallographic model of Cu-HHB viewed along (a) the c-axis, here we observe the kagome lattice, generated by the affixation of the HHB liagnds to copper. In (b), the b-axis, we observe no covalent bonds bridging the kagome layers separated by ~ 3 Å, we would instead expect pancake bonds to occupy this space, water is omitted here for clarity.

5.2 Experimental Methods

Finding favourable experimental conditions for the synthesis of $Cu_3(C_6O_6)$ was non-trivial. We attempted synthesis of Cu-HHB using literature reports prior to 2022, and after several iterations of various experimental conditions, we were unable to produce the pure phases outlined [97]. However, the report from 2022 included a comprehensive study of the formation of Cu-HHB which we used as a foundation for our synthetic procedure [98].

The one-pot synthesis of $Cu_3(C_6O_6)_2{\cdot}xH_2O$ (Cu-HHB) was performed in a 500 cm^3 round bottom flask. First, 200 cm^3 of deionised water was degassed at room temperature for 30 minutes, before adding 6.132 g (32.69 mmol) of $CuNO_3{\cdot}2.5H_2O$. Once dissolved, 20 g (excess) of ammonium acetate was added, allowing the acetate to fully dissolve before slow addition of 2.8 g (16.27 mmol) of tetrahydroxyquinone (THQ) solid. After plugging with a suba seal, the mixture is stirred at the lowest rpm setting possible and heated to 80 °C. During this heating, a balloon filled with air is dispersed through the mixture via needle at a flow rate of approximately 5 bubbles per second. The reaction vessel is then left in this state for 3 days ensuring maximum yield, where a dark navy precipitate, too fine to filter is formed. The resultant mixture is cooled to room temperature and left for a few hours, during which time the solid product settles to the bottom, allowing excess solvent and dissolved starting materials to be removed by a syringe. The product was then washed thoroughly, as much solid THQ remains unreacted amongst the powder product.

The washing steps were carried out with methanol, in 50 cm^3 centrifuge tubes, with the most efficient technique being the addition of methanol, vigorous shaking to dissolve THQ, followed by centrifugation to separate the dissolved THQ and the MOF product. This step is then repeated until the methanol removed is colourless as the dissolved THQ in methanol is bright yellow in colour. The relatively low yield ($\sim$ 10%) of Cu-HHB is

likely a result of using less than minimum solvent, coupled with the sparing solubility of THQ in water, as both of these factors lead to slower dissolution of solid THQ during the reaction and subsequently the formation of Cu-HHB, resulting in better crystallinity as shown by the sharpness of the Bragg peaks in powder XRD data alongside corresponding SEM images (Figure 5.4). The final product is then collected as a dark navy powder (2.18 g, 3.92 mmol, 25 %) with expected CHN analysis: C, 22.70; H, 1.91; N, 0; found, C, 19.35; H, 1.80; N, 1.63 with the differences and nitrogen content are believed to originate from the presence of NH_4^+ and NO_3^- ions balancing charge at the extremities of the crystallites, consistent with CHNS, XPS and Raman performed by Meng *et al* [98].

5.2.1 Powder X-ray Diffraction

A laboratory powder X-ray diffractometer was used to initially characterise the samples in this chapter. These measurements were taken on a Panalytical Empyrean diffractometer with a monochromated Cu $K_{\alpha 1}$ radiation source of wavelength $\lambda = 1.54056$ Å and a selected beam slit size of 1°. Around 200 mg of sample was ground to a homogeneous powder and mounted on a low-background silicon holder for analysis. Scans were taken between 4−50 ° 2θ, with step sizes of 0.0001 ° at room temperature. This is a nondestructive method, and the powder samples analysed were re-collected and used in further measurements such as magnetic susceptibility. Alongside these laboratory measurements, high-resolution X-ray data were collected on the I11 beamline at Diamond Light Source, using radiation of wavelength, 0.8258 Å at room temperature in a 0.3 mm silicon capillary. These data were collected over a 2θ range of 2.033 – 120.352 ° with a step size of 0.004 °. The data were then analysed against a published CIF to obtain a new refined model for the average structure of Cu-HHB [98]. These data were Rietveld refined using a twenty term Chebyschev, with instrumental peak shapes refined using A LaB_6 standard.

5.2.2 Magnetic Susceptibility

Magnetic susceptibility measurements were collected on a Quantum Design Magnetic Property Measurement System 3 (MPMS 3) SQUID magnetometer in DC mode, measuring between $1.8 - 300$ K. A palladium standard was used to calibrate the instrument prior to measurement. A 23 mg sample was mounted in a gelatin capsule which was sealed with G-varnish before being secured in a straw sample holder. Temperature-dependent magnetic susceptibility data were collected in zero field and in a 0.01 T applied field for this sample. Field dependent magnetic susceptibility measurements were performed at 0.4, 2 and 5 K up to 7 T applied field, with full magnet resets employed between measurements to eliminate remnant fields within the SQUID magnet. Furthermore, He^3 measurements were collected on an 11 mg sample, prepared as above. This set-up utilises a dilution fridge insert, facilitating data acquisition at temperatures as low as 0.4 K.

5.2.3 Heat Capacity

Heat capacity measurements were performed by Dr Angel Arevalo-Lopez at the Ecole Nationale Supérieure de Chimie de Lille. For these measurements, they used the relaxation method in the Dynacool PPMS from Quantum Design on a 6.09 mg sample of Cu-HHB. We measured in zero field between 1.8 and 301.9 K before fitting a linear region using the Debye equation outlined in the Chapter 2. This fit was then extrapolated to simulate the phonon response of Cu-HHB for its subtraction from experimental data providing the magnetic heat capacity for the system and, by extension, the magnetic entropy.

5.2.4 Scanning Electron Microscopy

Scanning electron microscope (SEM) images were obtained on a Hitachi TM4000 plus tabletop microscope, with a maximum magnification of 1000x. Images were collected on washed and unwashed samples of Cu-HHB at room temperature for the confirmation of crystal growth and a crystallinity assessment in a qualitative way.

5.2.5 Neutron Powder Diffraction

Neutron powder diffraction measurements were taken on WISH at ISIS Neutron and Muon Source, Didcot. Two samples of Cu-HHB (~1.8 g and ~1.4 g) were mounted and measured separately in a copper can and secured in a sample holder. These measurements were taken in a dilution fridge, at various temperature points between 68 mK and 40 K. The raw data were then extracted and modelled against a refined CIF model from synchrotron X-ray data collected on the I11 beamline (DLS). These data were Rietveld refined using a twenty term Chebyschev, with peak shapes refined to the instrument using a NaCaAlF standard sample

5.2.6 Muon Spin Relaxation

Muon spin relaxation and rotation (MuSR) spectra for Cu-HHB were collected on the MuSR instrument at the ISIS Neutron and Muon Source, Didcot. A 1.8 g sample was sealed in a silver packet approximately 3 x 3 cm and screwed to a silver backing plate at the end of the dilution fridge insert. Measurements were taken in zero, transverse, and longitudinal fields to acquire instrumental parameters and magnetic features of Cu-HHB. Measurements were taken at a range of temperatures between 0.1 and 148.4 K for the observation of temperature-dependent magnetic behaviour.

5.3 Results and Discussion

5.3.1 Optimisation of Synthesis

The methods described in the literature for the synthesis of Cu-HHB by [98], were crucial in our ability to reliably produce the MOF. During the process of optimising this synthetic route, we discovered that the crystallite sizes were unlikely to be big enough for single-crystal analysis and that several factors influenced the crystallinity. Our first observation was the nucleation of Cu-HHB, we find that Cu-HHB forms at the surface of large

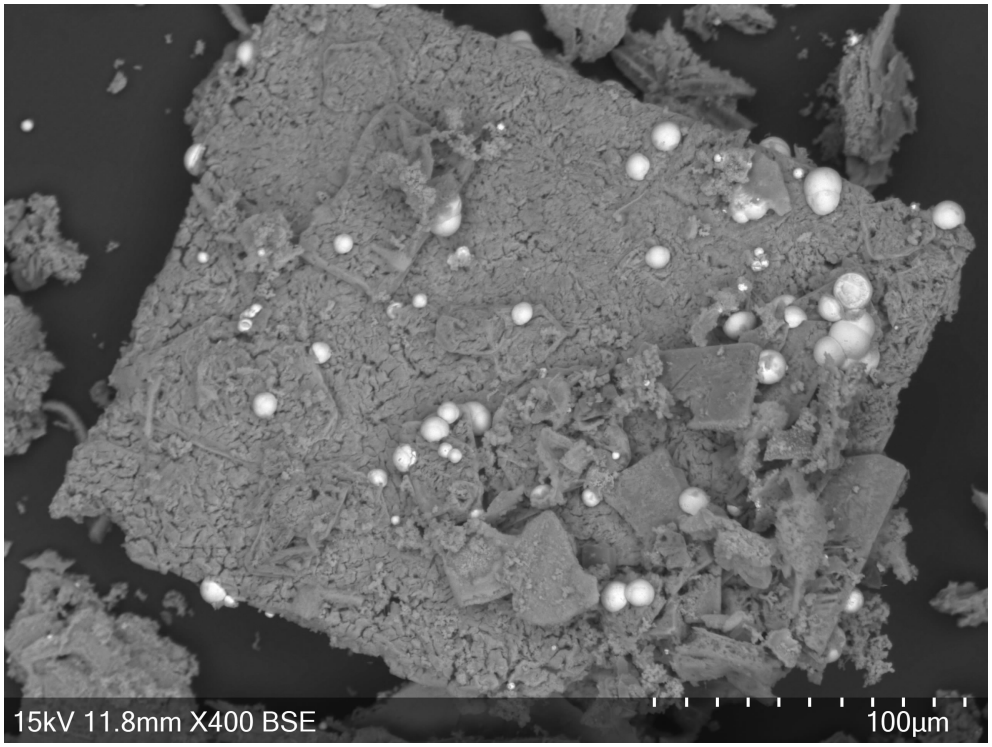


Figure 5.3: An image of unwashed Cu-HHB, the large square morphology is a THQ crystal upon which Cu-HHB nucleates, covering the entire crystal. The white spheres can be attributed to a soluble amorphous copper ammonium species formed during the reaction, which is not present in the washed samples. Copper was confirmed to be on the surface by energy-dispersive X-ray (EDX) analysis (Figure A.4) of this sample. The lack of crystals of this scale and morphology in all washed samples further confirm that this is a THQ crystal.

THQ crystals which are added to the reaction mixture as a solid. We can confirm this by observing scanning electron microscope (SEM) images, where structures with the morphology and size of THQ crystals are removed after washing, the nucleation of Cu-HHB on a 200 μm THQ crystal is shown in Figure 5.3 above. Furthermore, we track crystallite size by SEM and powder XRD, allowing us to optimise the synthesis towards synthesising larger crystallites. One of the major breakthroughs in this synthesis involved increasing the concentration of tetrahydroxyquinone (THQ). With THQ sparingly soluble in water, large THQ crystals acted as nucleation points for the growth of Cu-HHB as observed in the SEM images taken of prewashed samples shown in Figure 5.4. Comparisons between a sample synthesised using 7 mg and 14 mg of THQ in a volume of 15 cm^3 of water yielded significantly different crystal morphologies. More angular crystals $\sim$ 10x larger

were observed in the higher concentration reaction, and less well-defined crystallites were observed in the other. These observations are compounded by laboratory XRD, which presents sharper, more intense Bragg peaks, believed to be associated with better crystallinity in the data given in Figure 5.4. Here, we have successfully tracked the crystallite size, allowing us to optimise our synthetic method toward a better quality material for further characterisation.

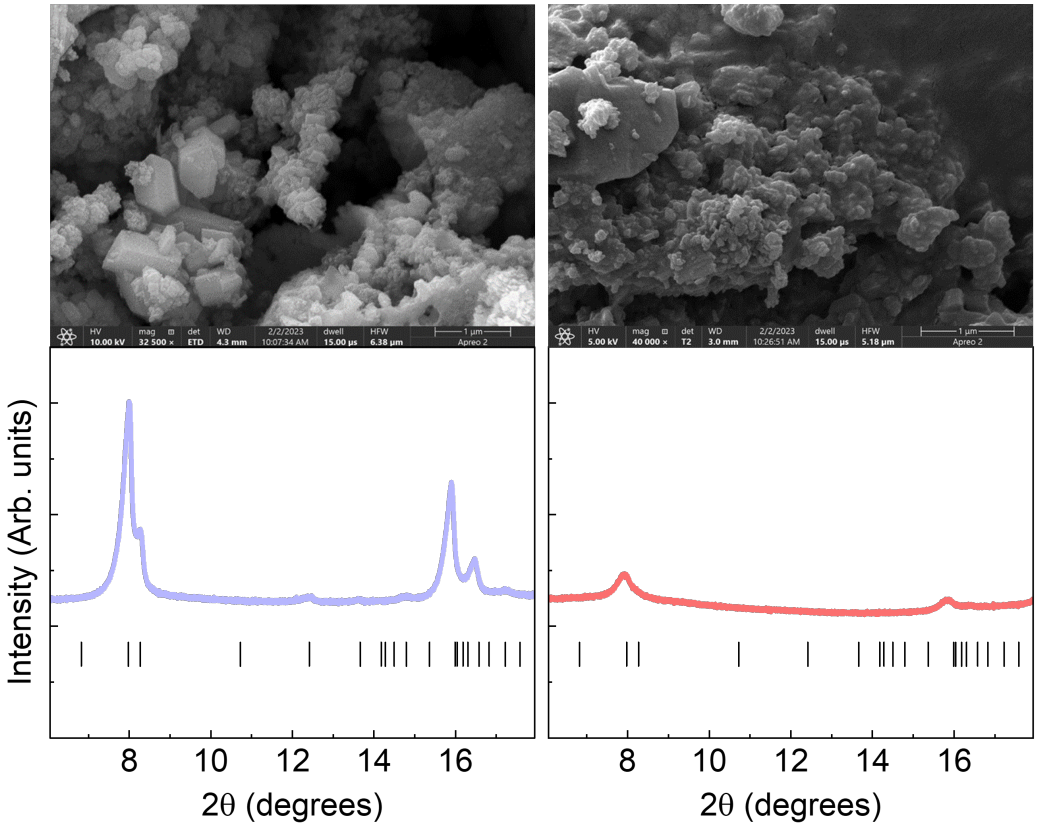


Figure 5.4: Two fixed scale SEM and powder XRD plots for two samples with the $C2/m$ structure of Cu-HHB (left) 14 mg per 15 cm^3, featuring sharper peaks along a comparable x and y axis to (right) a 7 mg per 15 cm^3 sample. In both cases we confirmed the presence and purity of Cu-HHB by Le Bail refinement.

5.3.2 Water Content Analysis by Fourier Transform Infrared Spectroscopy and Thermogravimetric Analysis

To confirm the presence of water in our samples of Cu-HHB we performed Fourier transform infrared (FTIR) analysis. We confirm the presence of water from the broad feature

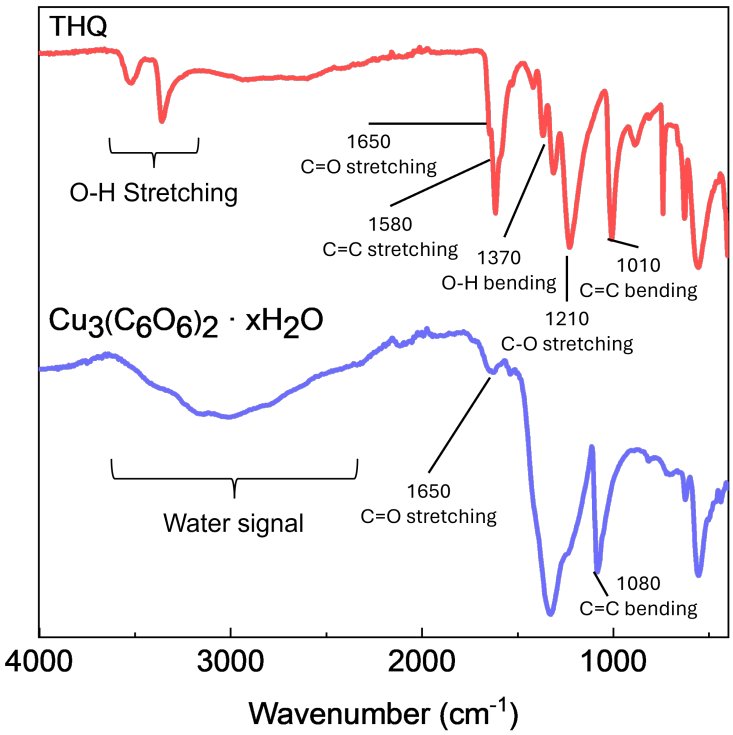


Figure 5.5: FTIR spectra for THQ (red) and Cu-HHB (blue), here we observe a clear signal due to water in Cu-HHB along, a significant reduction in C=O stretching observed at 1650 cm^{-1} and the loss of O-H stretching in our Cu-HHB sample indicating the complete removal of THQ from our sample.

in the data at high wavenumber. The FTIR data for THQ ligand and a Cu-HHB sample are outlined in Figure 5.5. Here, we see the presence of a water feature, as well as the reduction in peak intensity for THQ peaks in the Cu-HHB sample, which also suggests a complete reaction and removal of THQ via washing stages. Since previous reports of Cu-HHB outline the presence of six water molecules per formula unit, we chose to perform our own analysis via thermogravimetric analysis (TGA) (Figure 5.6). We found a mass loss of 0.338 mg from a 4.38 mg sample, a mass loss of 8.36 %. This mass loss can be ascribed to the removal of 3.7 water molecules per formula unit. We performed a repeat measurement on a 5.299 mg sample, finding a mass loss of 0.534 mg, 10.01 % mass loss corresponding to 4.44 water molecules. We can approximate from these data (accounting for instrumental error) that in our synthesised Cu-HHB samples we have approximately four molecules of water, $Cu_3(C_6O_6)_2{\cdot}4H_2O$, further confirmed via diffraction methods discussed later.

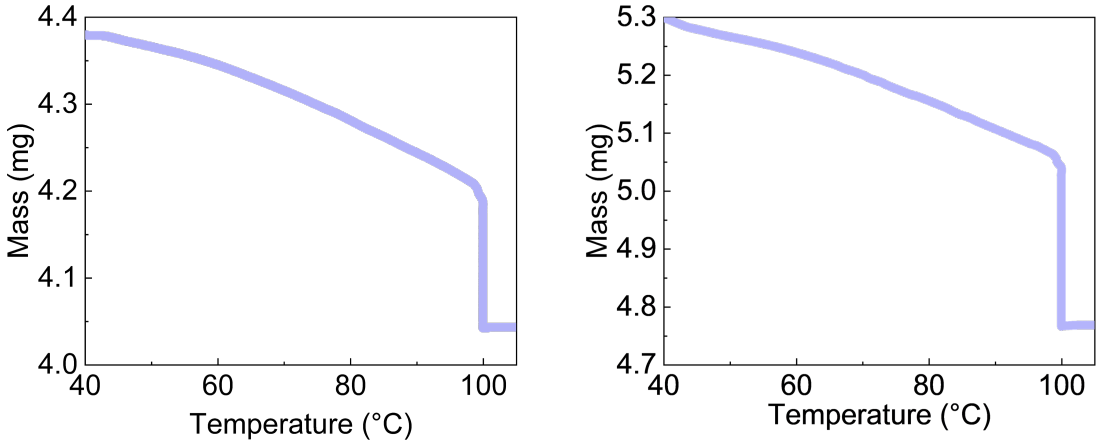


Figure 5.6: Two TGA datasets collected from a sample of Cu-HHB, indicating a mass loss due to water of 0.338 mg (Left) and 0.534 mg (Right). These data suggest a loss of 4.4 and 3.7 molecules of water per formula unit of Cu-HHB respectively.

5.3.3 Structure Determination by High-Resolution X-ray Diffraction

Since there was uncertainty in the space group assignment of Cu-HHB in the literature, we decided to perform our own study using high-resolution XRD on the I11 beamline at the Diamond Light Source. Because the X-ray data collected by Meng *et al*, were laboratory data, they were only able to perform a Le Bail refinement on such a complex MOF. We chose to collect synchrotron XRD data that allowed us to perform Rietveld analysis, providing us with the highest quality data for the Rietveld refinement of Cu-HHB, which confirmed the assignment of the $C2/m$ space group. Synchrotron powder XRD data were collected at 298 K for a powder sample of Cu-HHB as presented in Figure 5.7. A Rietveld fit was performed against the $C2/m$ structural model using the published ED CIF [98]. The refined lattice parameters extracted were a = 22.3016(7), b = 13.1465(1) and c = 6.2218(6) Å, where bond restraints were applied to all Cu-O and C-C to prevent them from refining to unreasonable values. Rigid bodies restraints were also applied to the two fragments of the organic ligand described as "fragments" because of symmetry elements which split them into halves, hydrogen was removed from four water molecules consistent with our TGA analysis, as the refinement of hydrogen could not be performed

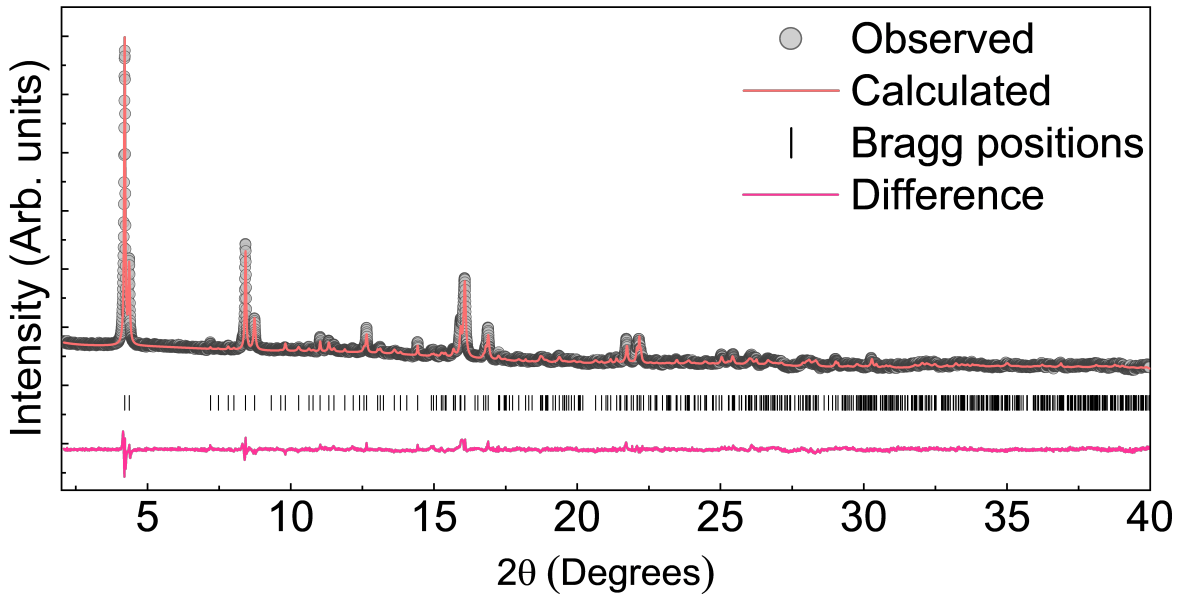


Figure 5.7: The Rietveld refinement of Cu-HHB against the $C2/m$ model, weighted R factor, R_{WP} = 4.395 %, where refined lattice paramters are a = 22.3016(7), b = 13.1465(1) and c = 6.2218(6) Å. In this refinement, four molecules of water with their hydrogen atoms removed were included, their atomic coordinates were allowed to refine freely providing us with a significantly better fit than in models where these water positions were not refined.

accurately by X-ray measurement. The thermal parameters for both copper atoms were constrained to be equal as they could not be consistently refined independently. These data are summarised in Table 5.1. Furthermore, additional evidence for our choice of $C2/m$ model is given by Figure 5.8, showing that all Bragg reflections are captured by the $C2/m$ assignment.

Table 5.1: Refined structural parameters for the $C2/m$ model of Cu-HHB fit to XRD data collected on I11, Diamond, at 298 K. Rigid bodies were defined for two HHB ligand halves (1) and (2); with refined origins of [0.2554(6), 0.0665(6), 0.2310(9)] and [0.2604(3), 0.4009(7), 0.2964(6)]. Thermal parameters for these rigid bodies could not be refined stably. The final refined lattice parameters were a = 22.3016(7), b = 13.1465(1) and c = 6.2218(6) Å, R_{WP} = 4.439 % and reduced χ^2 = 489.35.

Atom	Site	x	y	z	Occupancy	U_{iso}
Cu1	m(y)	0.5288(4)	0.5000	0.7955(1)	1	0.004(1)
Cu2	1	0.2711(1)	0.2540(3)	0.2806(3)	1	0.004(1)
Ligand fragment 1						
C1	1	0.4157(8)	0.4428(3)	0.6244(9)	1	0.012

O1	1	0.4662(6)	0.3993(9)	0.7088(9)	1	0.009
C2	1	0.3621(7)	0.3939(5)	0.5159(3)	1	0.011
O2	1	0.3585(4)	0.2951(1)	0.4832(2)	1	0.009
C3	1	0.3069(4)	0.4518(1)	0.4171(6)	1	0.004
O3	1	0.2601(9)	0.4002(2)	0.3014(6)	1	0.005
Ligand fragment 2						
C4	1	0.3069(4)	0.4518(1)	0.0.4171(6)	1	0.004
O4	1	0.3024(1)	0.1188(5)	0.3069(4)	1	0.011
C5	1	0.1988(5)	0.1169(9)	0.1226(9)	1	0.003
O5	1	0.2015(1)	0.2152(7)	0.1169(9)	1	0.005
C6	1	0.1446(9)	0.0611(1)	0.0241(2)	1	0.006
O6	1	0.0942(4)	0.1044(6)	-0.0880(8)	1	0.005
Oxygen						
O7	m(y)	0.0761(6)	0.5000	0.4478(3)	1	0.050
O8	1	0.5434(8)	0.1835(1)	-0.1118(7)	1	0.050
O9	m(y)	0.3998(2)	0.0000	0.9728(4)	1	0.050
O10	1	0.5512(3)	0.197(7)	0.4316(4)	1	0.050

We can see in the inset of Figure 5.8 that both peaks around 4° are in no way accounted for by the Bragg positions in the $P2/m$ assignment, these additional peaks are not observed in experimental data allowing us to make a confident assignement. Due to these observations, we are confident in the space group assignment of $C2/m$. From this refined model we are able to explore important characteristics of the system; for instance, the nearest-neighbour Cu-Cu distances expected to mediate exchange were found to be 6.577 and 6.518 Å. We also find that neighbouring kagome layers are separated by ~ 3 Å, supporting our assertions that pancake bonds are responsible for the stacking observed, as pancake bonds are expected to be as long as 3.05 Å [187]. We also find that the Cu-O bond lengths are 1.941 and 1.934 Å, suggesting that Jahn-Teller distortion may be so extreme that

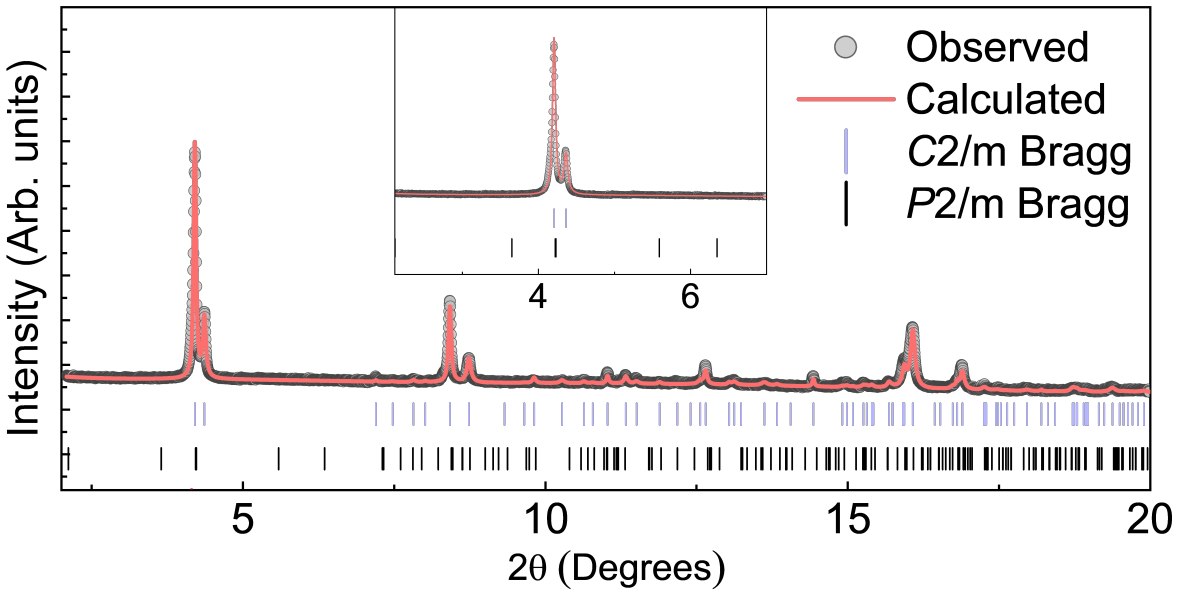


Figure 5.8: Evidence for the assignment of the $C2/m$ model in the Le Bail refinement of Cu-HHB. We see here that Bragg intensity is not observed at many of the low 2θ Bragg reflections expected for the $P2/m$ space group for Cu-HHB. The Bragg reflections corresponding to the $P2/m$ model of Cu-HHB were generated using ISODISTORT [186].

axial bonds stretch beyond a bonding range yielding an effective square planar geometry. Although we cannot confirm the positional coordinates of hydrogen from these refinements we can confirm that the oxygen atoms from these water molecules reside as close as 2.93(4) Å, which is within the range of possible hydrogen bonding interactions including error, expected, between 2.2 – 3.3 Å [188].

5.3.4 Magnetic Characterisation by Magnetic Susceptibility

Initially, field cooled and zero field cooled temperature-dependent magnetic susceptibility measurements were collected for Cu-HHB (Figure 5.9), using an MPMS3 SQUID in DC mode. These data were collected using a cryostat between 1.8−300 K and with a He^3 insert for measurements taken under 1.8 K. The MPMS3 was calibrated for these measurements using a palladium standard prior to measurement. Using an applied field of 0.1 T in FC and ZFC measurements, we observe no bifurcation, indicating no spin freezing. An upturn in the susceptibility can be observed below around 40 K with inverse susceptibility following Curie-Weiss behaviour at higher temperatures characterised by linearity. We

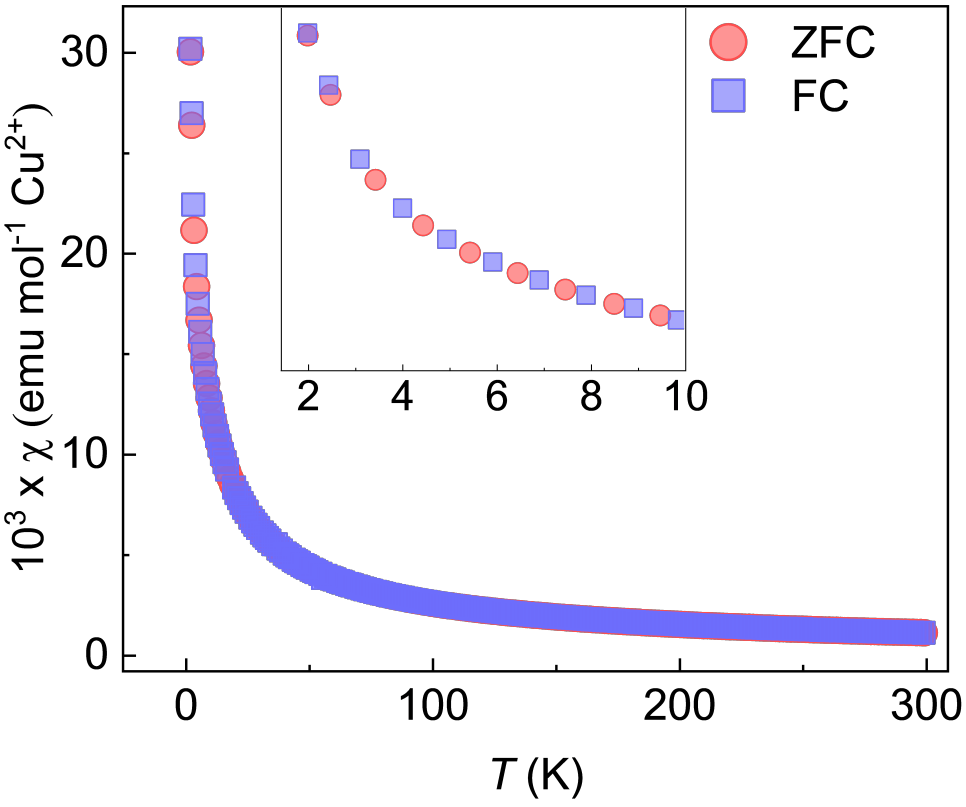


Figure 5.9: Field cooled and zero field cooled data taken at 0.1 T for a sample of Cu-HHB Here we see no bifurcation of the two datasets, suggesting no field-induced spin freezing or transition to an ordered state.

chose a Curie-Weiss fitting range of $100 - 300$ K based on the increase in error observed in smaller and larger fitting ranges. Curie-Weiss analysis provided us with a $\theta_{\mathrm{CW}} = -35.0(1)$ K suggesting dominant antiferromagnetic exchange interactions consistent with the literature ($\theta_{\mathrm{CW}} = -26.1$ K) [98]. Our extracted Curie constant was 0.348(1) emu K mol^{-1} corresponding to a spin-only contribution of $\mu_{eff} = 1.66(5)\ \mu_B$, within a reasonable range of the theoretical value for a single unpaired electron $\mu_{eff} = 1.73\ \mu_B$. These values support the hypothesis that the magnetic response observed in Cu-HHB originates from the Cu^{2+} ions. These data are shown in Figure 5.10, where there is no clear sign of magnetic order characterised by the Curie-like curve observed down to 0.4 K.

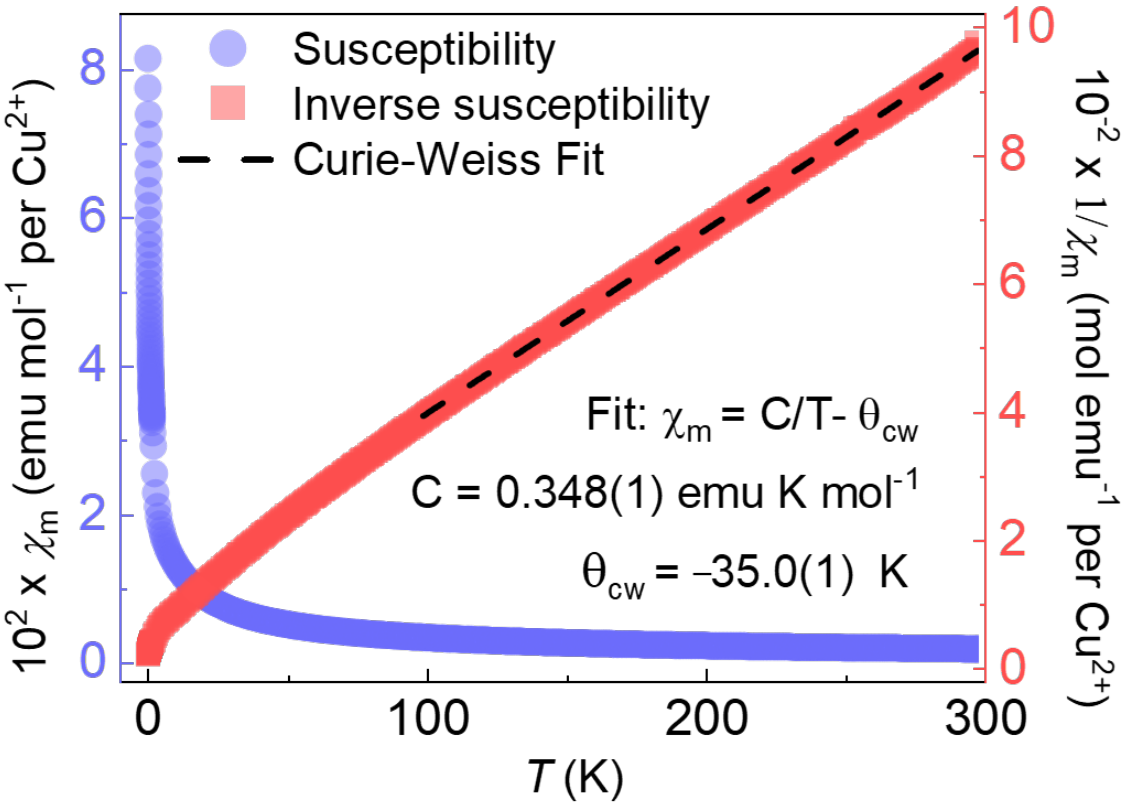


Figure 5.10: Temperature dependant magnetic susceptibility data for Cu-HHB in a 0.01 T applied field between $0.4 - 300$ K, inverse susceptibility data were fit to the Curie-Weiss equation providing a $\theta_{\mathrm{CW}} = -35.0(1)$, alongside a Curie constant of 0.384(1) corresponding to a $\mu_{\mathrm{eff}} = 1.66(5)\ \mu_{\mathrm{B}}$. We see no clear evidence for a long-range ordered transition in these magnetic susceptibility data, characterised by a deviation from the smooth curve.

From these data, we have our first evidence of antiferromagnetic exchange coupling on a kagome MOF with no clear evidence for long-range magnetic order. Further supporting this evidence, magnetisation vs. field data collected at 5, 2 and 0.4 K show no signs of magnetic hysteresis (Figure 5.11.). Here, we see a ~ 50% reduction in the saturation of our magnetic moment at a 7 T applied field between the three datasets. We also observe that at lower temperature magnetic moments more rapidly align with the weaker applied field up to around 800 mT. As we see no evidence of magnetic order in our temperature dependence study, it is unlikely that the observations in magnetisation vs. field data are due to the onset of long-range order, instead we propose that these features originate from short-range antiferromagnetic coupling, synonymous with the resonating valence bond model [3].

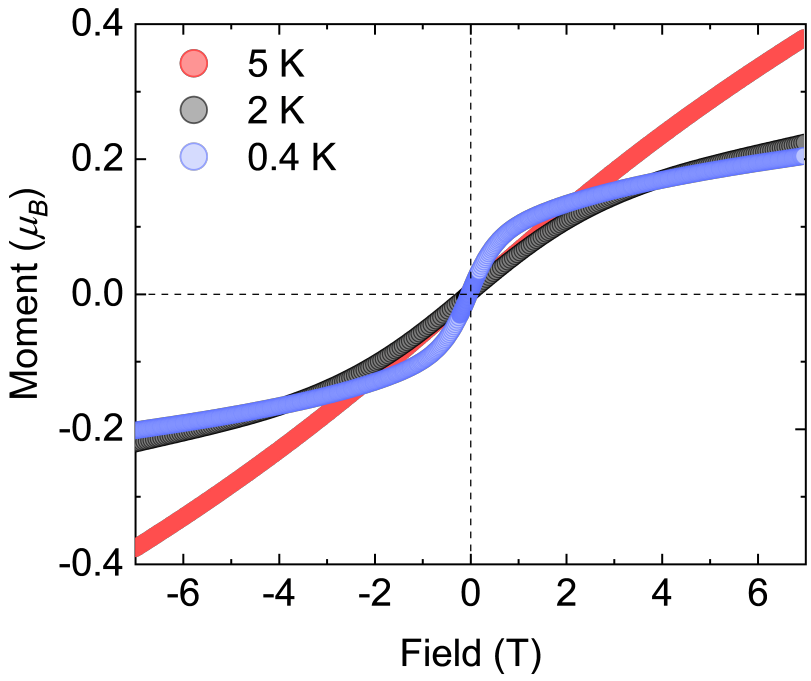


Figure 5.11: Field dependance of the magnetic moment collected at 5, 2 and 0.4 K. These data show a reduced saturation of moments to the applied field at lower temperatures, suggesting the onset of short-range antiferromagnetic correlations, further supported by the sharper increase in saturation at lower field in 0.4 K data.

5.3.5 Missing Entropy in Magnetic Heat Capacity

Heat capacity measurements were taken in zero applied field between 1.8 and 301 K, as shown in Figure 5.12. Generally, to observe the magnetic contribution to heat capacity C_{mag} we must subtract the estimated phonon contribution in lieu of data from a non-magnetic analogue. In cases such as ours, where a non-magnetic analogue cannot be synthesised, a simulation can be achieved through fitting high-temperature regions of data to Debye functions, we used three Debye functions as follows:

$$C_{Debye} = \sum_{i=1}^{3}\left[9NR\left(\frac{T}{\theta_{Debye}}\right)^3 \int_0^{\frac{\theta_{Debye}}{T}} \frac{x^4 e^x}{(e^x-1)^2} dx\right]. \tag{5.1}$$

Each Debye function applies to each atom by mass in the unit cell (Cu, O/C and H) through x, the ratio between atom size and thermal contribution, while N is the number of atoms in the formula unit and θ_{Debye} is the Debye temperature. We use Equation 5.1 as a fitting function at higher temperatures where the phonon contribution will dominate. The temperature range of $25 - 300$ K was selected due to this being well above any likely magnetic contribution providing us with an excellent fit to the data, $R^2 = 0.999$, reduced $\chi^2 = 0.260$. It could be considered that the θ_{CW} = -35 would require a fit taken at higher temperatures for a better fit however, this would not account for a significant portion of the missing entropy we observe. A low-temperature phonon simulation can then be extrapolated from this fit to provide us with an estimate for the phonon heat capacity (C_{pho}) below 25 K. With this simulated curve we could subtract the experimental data providing us with C_{mag}. In these subtracted magnetic heat capacity data, we would expect to see a sharp feature indicating order for an ordered system; however, in the case of Cu-HHB we observe a broad feature evolving below 10 K with a peak maximum at 3.34 K. The magnetic entropy release can then be calculated by taking the integral of the magnetic heat capacity. This corresponds to the entropy release as this system enters its magnetic ground state, with the full entropy release for a single ion of a $S = \frac{1}{2}$ system being equal to $\Delta S = R\ln(2S+1)$, $\Delta S = 5.762$ J K^{-1}. When performing the integration of

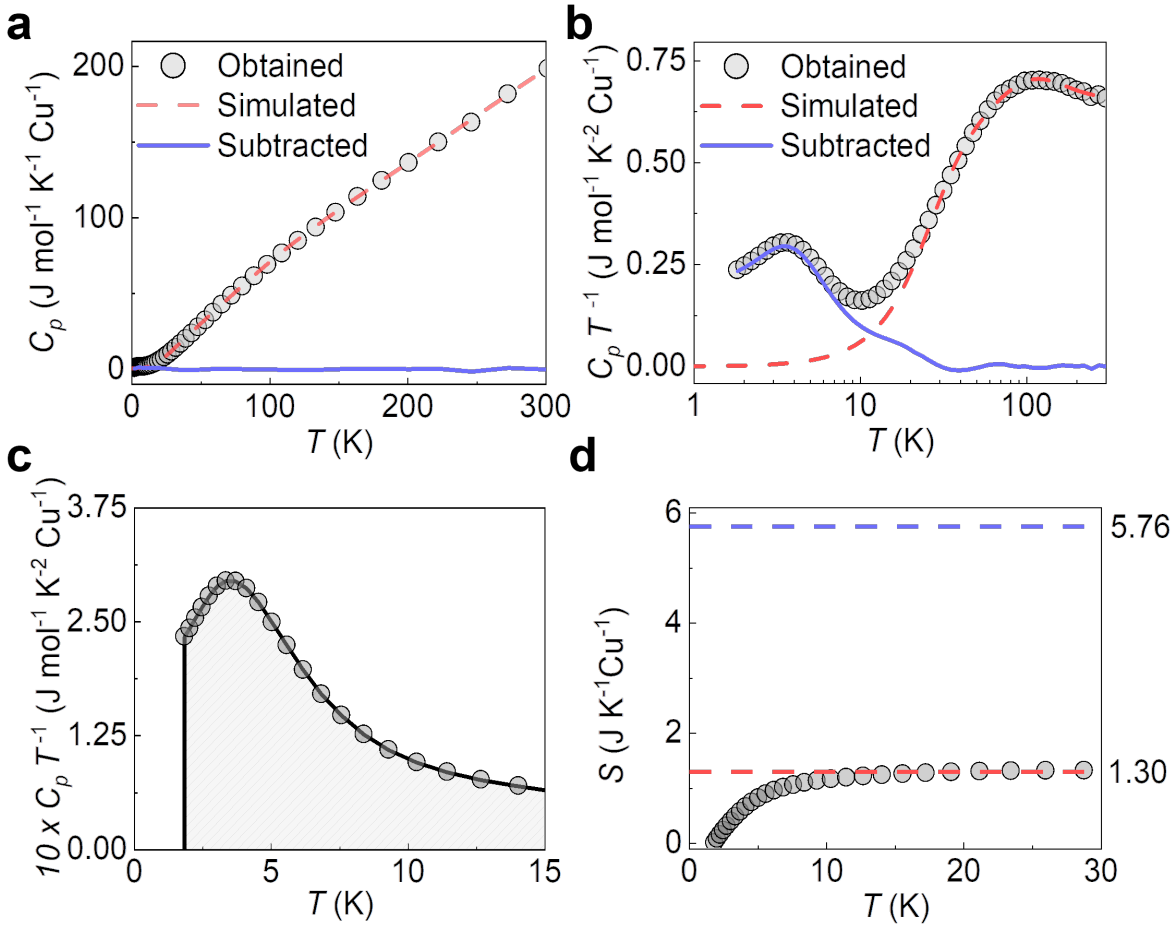


Figure 5.12: Heat capacity data for Cu-HHB collected between 1.8 and 301 K. (a) Temperature dependence of zero field specific heat capacity data fit to three Debye functions to approximate the phonon contribution given by the simulated curve. (b) A log plot of temperature-divided specific heat, with the subtraction of simulated from experimental data providing the magnetic contribution to specific heat. (c) Subtracted data reveals a broad feature below 5 K. (d) Calculated magnetic entropy release indicates that only 22.57 % of magnetic entropy is taken into account when compared to the calculated magnetic entropy of a single ($S = \frac{1}{2}$), Cu^{2+} ion. We cannot rule out the fact that some additional magnetic entropy would be gained from a lower temperature dataset however the amount of entropy would not recover the missing 73 %.

C_{mag} we find that only 22.57% of the magnetic entropy is accounted for, meaning that 73.43% of magnetic entropy is yet to be released down to 1.8 K. This is another strong indication that magnetic order is not adopted by the system down to low temperatures, since a conventionally ordered system would have a far greater portion of magnetic entropy accounted for below the ordering temperature [189, 190]. This may be similar to the missing magnetic entropy we observe in Chapter 4, where short range correlations may have been responsible for this. With further evidence for a disordered magnetic state down to 1.8 K, we decided to perform an elastic neutron scattering experiment to confirm a lack of magnetic order in Cu-HHB. These heat capacity data however highlight the limitations of performing phonon subtractions through simulation, although we see no evidence of a sharp peak indicating the emergence of long-range order we cannot be certain that the missing entropy does not arise due to the subtraction. In hopes of gleaning further information from these data, we applied a Schottky function to the magnetic heat capacity data (Figure 5.13).

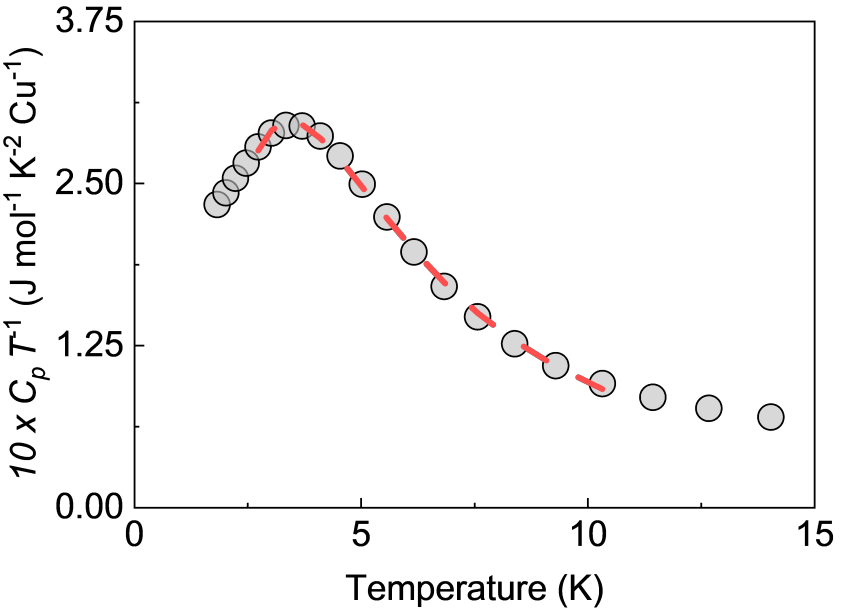


Figure 5.13: Magnetic heat capacity data obtained from the phonon subtraction method outlined above. We fit this data using a Schottky function (Equation 2.13) between 2.5 and 10 K, yielding a good fit to the data and a calculated energy gap of 0.71(5) meV.

As discussed in Chapter 2, this fit provides information on the energy scale of magnetic interactions within the system, given by the calculated energy gap. The energy gap calculated for this two-level $S{=}\frac{1}{2}$ system was found to be 0.71(5) meV, a value which can be compared experimentally in an inelastic neutron scattering study which have been collected for fitting at a later date.

5.3.6 Indications of a Lack of Long-Range Order by Neutron Powder Diffraction

NPD data were collected on the WISH diffractometer at ISIS Neutron and Muon Source, Didcot for a 1.8 g sample of Cu-HHB referred to as (1) and a 1.4 g sample of Cu-HHB which had been vacuum dried referred to as (2). Since we have confirmed the presence of water, we can expect incoherent scattering from hydrogen to affect the background of data for (1), hence the synthesis of the further dried (2). In our measurement of (1), we discovered that the copper can sample holder dominated the powder pattern as a copper impurity, making Rietveld refinement challenging. Instead, we were able to perform a Le Bail refinement; an example of this copper dominance is given in Figure 5.14, where a two-phase Le Bail refinement was performed on Bank 4 data. Due to the copper impurity

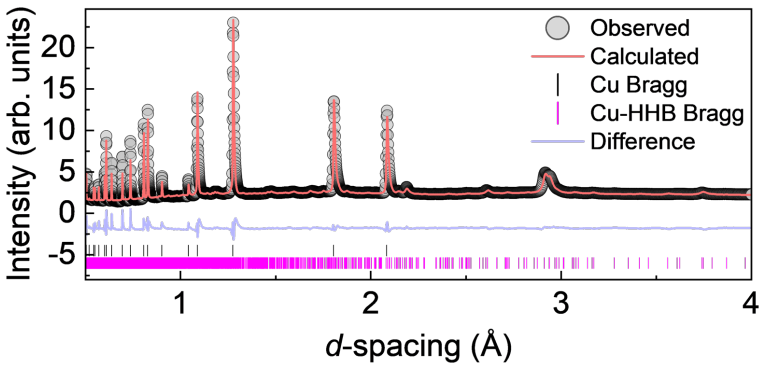


Figure 5.14: In these Bank 4 data, we observe sharp copper peaks at Bragg positions denoted in black, these peaks dominate the powder pattern up to around 2.1 Å. Very few peaks beyond 2.1 Å d-spacing, the refinement against the $C2/m$ Cu-HHB model is unlikely to provide more information on Cu-HHB than our high-resolution powder X-ray diffraction data.

we performed a Le Bail fit to data outside of the low d-space range of copper across all five banks shown in Figure 5.15.

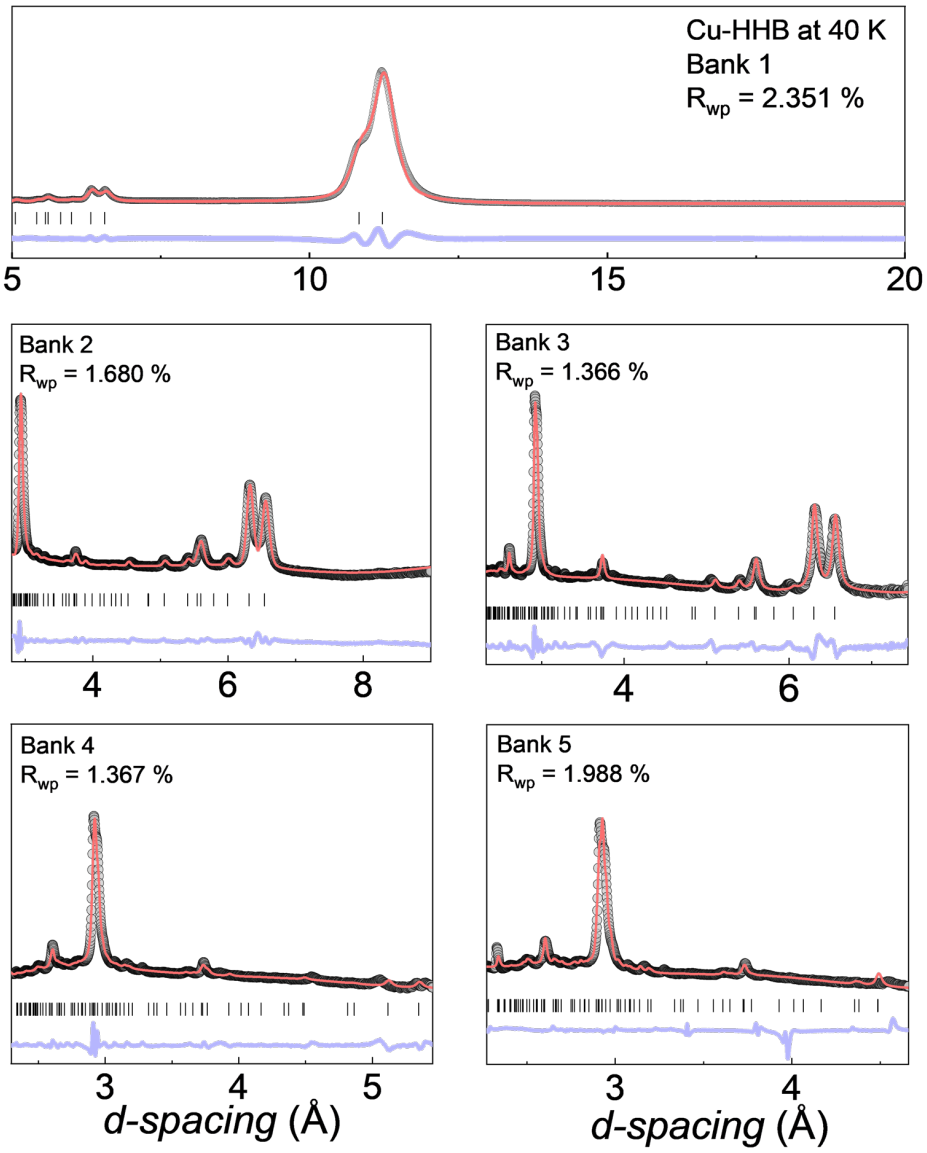


Figure 5.15: Le Bail refinement of the $C2/m$ structure of Cu-HHB against data collected on the WISH diffractometer at 40 K. For this, the lattice parameters were refined across 5 banks to a = 22.0753(2), b = 13.1799(7) and c = 6.2258(7) Å. We were unable to fit regions dominated by copper Bragg reflections and so limits were set on these data to ensure the inclusion of Bragg reflections solely originated from Cu-HHB.

Our next step was to measure at low temperature to perform a subtraction of nuclear Bragg scattering (high T) from the nuclear + magnetic Bragg scattering (low T). As we

used a dilution fridge, we were able to reach temperatures as low as ~ 68 mK for this subtraction. Usually, in subtracting high temperature NPD data from low temperature data, we are left with only the magnetic contribution to Bragg intensity observed; however, in the case of (1) we see a significant anomalous shift in the background between 40 K and 68 mK data coming from an unknown origin. In Figure 5.16 we plot the high- and low-temperature datasets, allowing us to observe this "shift" in these data.

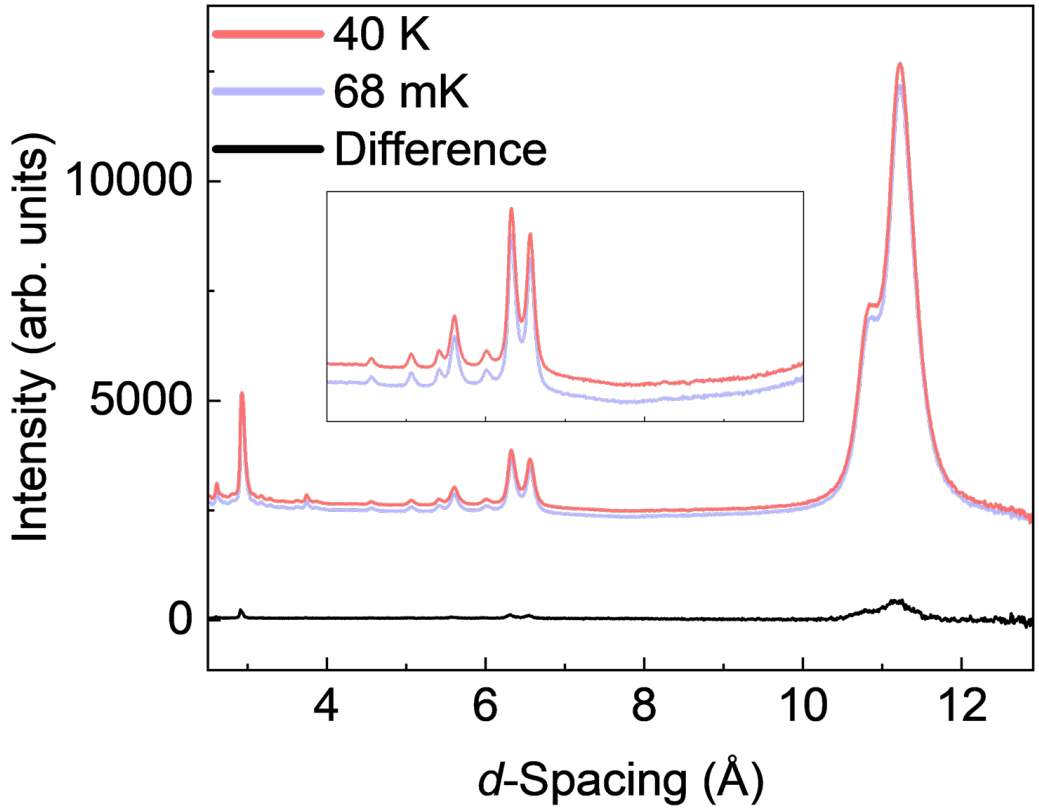


Figure 5.16: Neutron powder diffraction data collected for Cu-HHB (1) at 40 and 68 mK, here we observe a significant shift between the two datasets which we initally proposed came from the switching between cryostat and dilution fridge sample holder.

Our main finding in these data are the lack of Bragg intensity in the 68 mK scan at non-nuclear positions, this means that any magnetic Bragg intensity that does exist, must be consistent with a propagation vector K = (0, 0, 0). Since the observable differences in these data are unlikely to originate from a magnetic source, we are unable to derive

any more useful information from (1) beyond a magnetic refinement of the skewed data, which we provide for (2) later. To investigate whether this phenomenon was simply an experimental error, we performed measurements at a later stage on the separate sample (2). Sample (2) was synthesised identically to (1), with the purity and structure confirmed through in-house powder XRD and elemental analysis. Therefore, we use (2) as a repeat measurement, which confirms whether our unconventional data for (1) were of instrumental origin. For (2) we chose to collect data at multiple points between 40 K and base temperature to observe the evolution of any similar temperature-dependent behaviour of the sample, as we had observed in (1). We were again faced with significant Bragg intensity from the copper can in our NPD data for (2) so we were unable to perform a Rietveld refinement. Instead, we performed another Le Bail refinement to confirm consistency between the two samples in terms of their refined lattice parameters shown in Figure 5.15. Our next step was to plot data at all temperature points collected, observing whether the "shifting" of data occurred spontaneously at a given temperature, evolved gradually or was not observed at all in (2) (Figure 5.17).

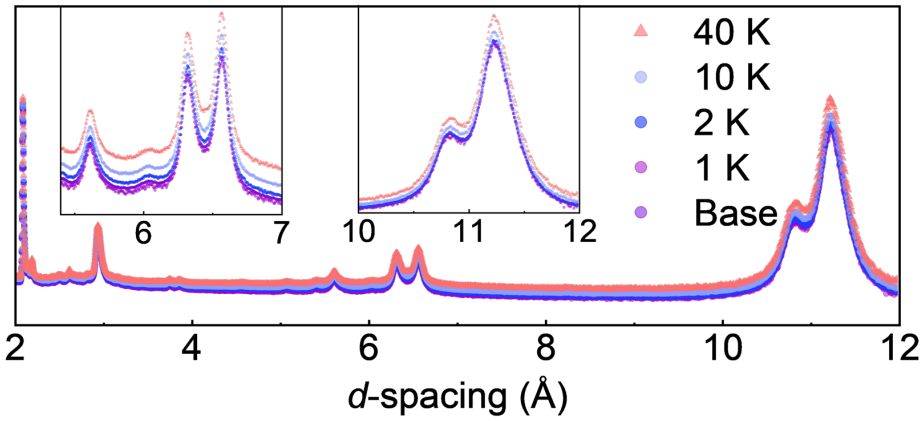


Figure 5.17: Neutron powder diffraction data collected for Cu-HHB (2) across five temperature points, taken between 40 and 68 mK (Base). Here we observe the anomolous increase in background intensity with increasing temperature, the consistency of this background throughout nuclear and non-nuclear positions of the pattern make it unlikley to be an effect of atomic thermal motion (Debye-Waller) [191].

In these data, we see that the "shift" appears gradual across the temperature points between 40 and 0.1 mK with a plot of temperature point vs. intensity at a fixed *d*-

spacing suggesting an exponential decrease with decreasing temperature shown in Figure 5.18.

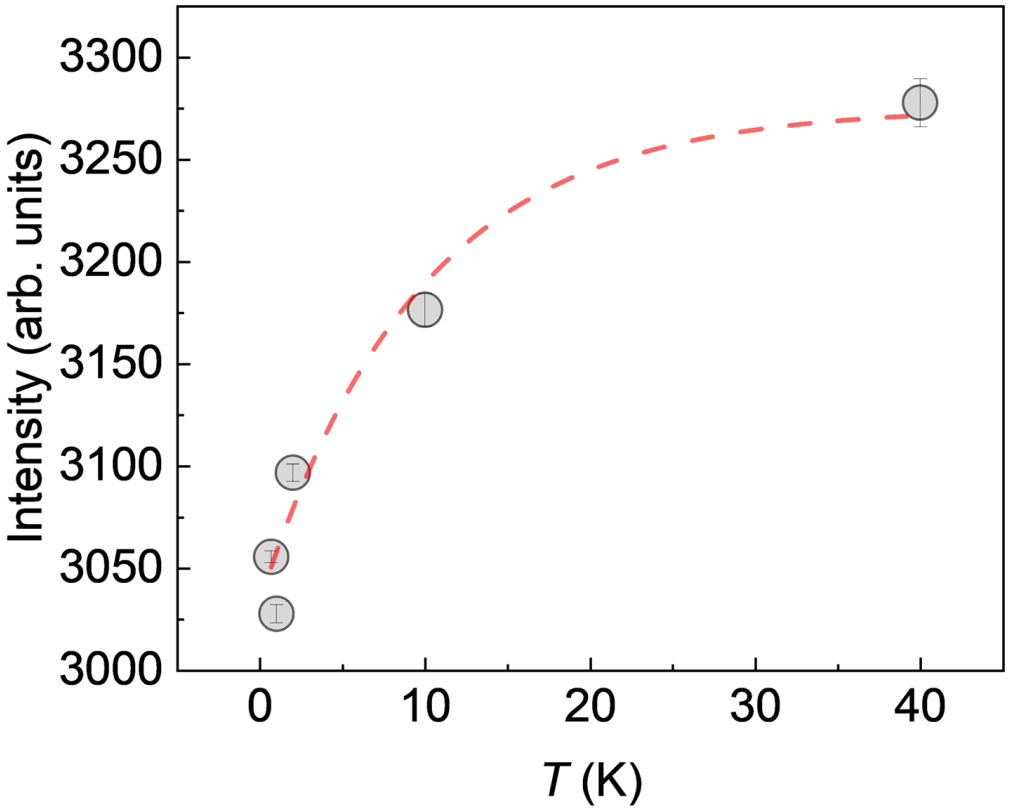


Figure 5.18: Plot of intensity against temperature point at 3.999 Å d-spacing, fit to a simple exponential function ($\chi^2 = 12.3435$). This plot suggests that the increase in background intensity due to temperature becomes less pronounced as temperatures increase beyond 40 K.

From these data we observe that the temperature dependence of intensity will likely be less prominent at temperatures higher than 40 K. Furthermore, the consistency between the measurements of (1) and (2) suggest that the observed effect is a real characteristic of Cu-HHB however, its source is unknown. The collection of data for (1) and (2) also allowed us to observe any effects due to drying of (2). First we simulated Bank 2 NPD patterns from the crystallographic model generated by the Rietveld refinement of high-resolution powder XRD data with and without water molecules present. We were then able to observe any difference in the dataset, finding that a difference in the intensity ratio

between two peaks was observed at around 6.5 Å d-spacing. We see in Figure 5.19 that the experimentally obtained data for (1) and (2) are in fact consistent with the simulated patterns.

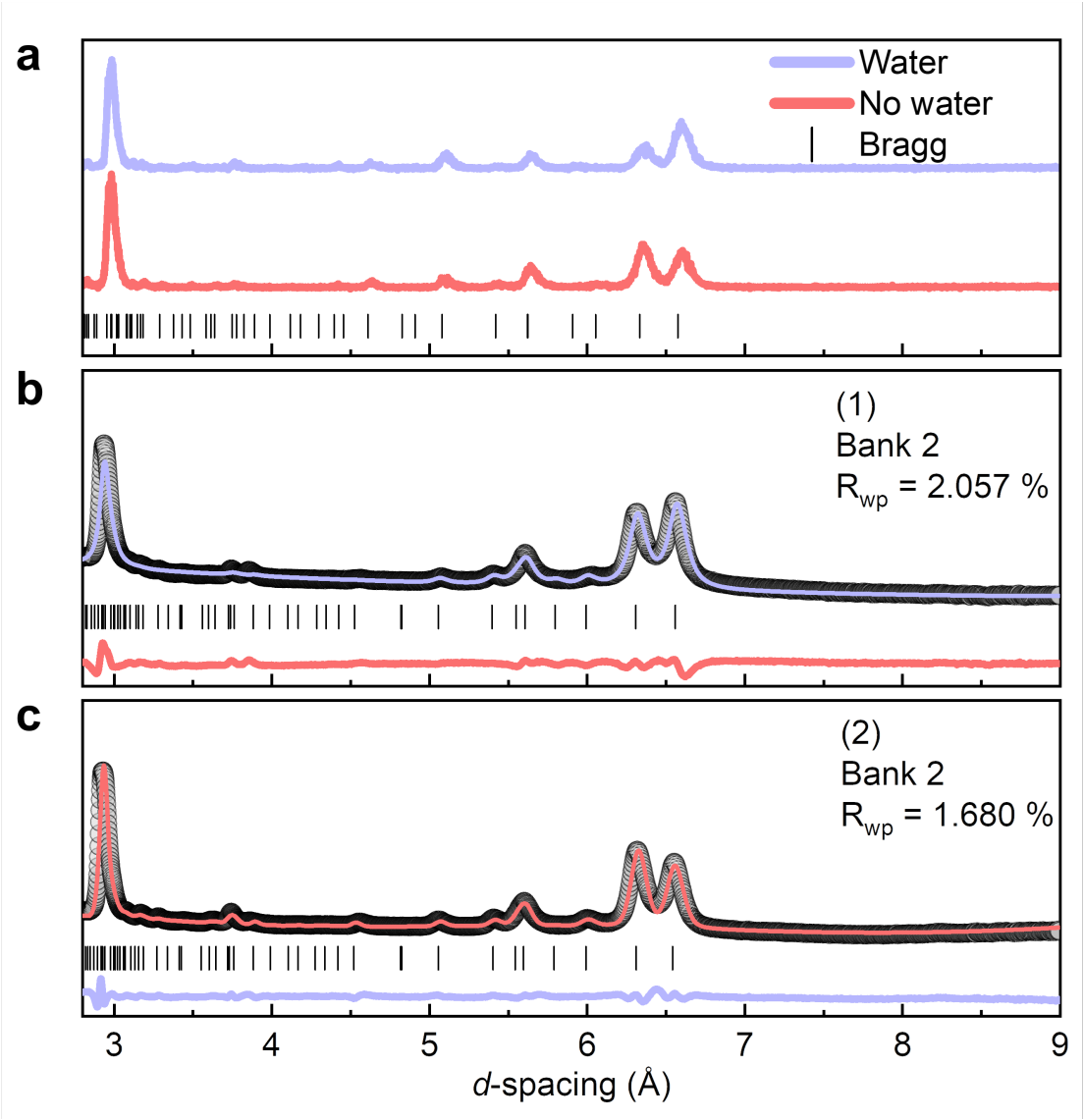


Figure 5.19: NPD patterns for Bank 2 WISH data. a) Two simulated diffraction patterns using the $C2/m$ model for Cu-HHB, with all water molecules present, and with them all removed, we notice here that the ratio between the peaks $\sim 6 - 6.7$ Å are unique to the presence of water. b) We see here that for sample (1) the peak ratio more closely matches the simulated pattern where water is present. c) We see here that for sample (2) the peak ratio follows the simulated pattern without water more closely.

Since we could not perform a stable Rietveld refinement of the NPD data, we cannot confirm the extent of dehydration in (2). However, this is a promising result suggesting

that water, at least to some extent, can be removed from the framework. From our two studies of Cu-HHB we see that there is no sign of Bragg intensity outside of the nuclear cell, and that differences in the peak intensity due to the unknown source may mask any magnetic Bragg intensity that was present. To confirm that the difference between 40 and 0.1 K data was not from a magnetic source, we perform a Rietveld refinement on a small d-space range containing the most prominent peak in Bank 1 data to extract a scale factor for use in a magnetic refinement (Figure 5.20).

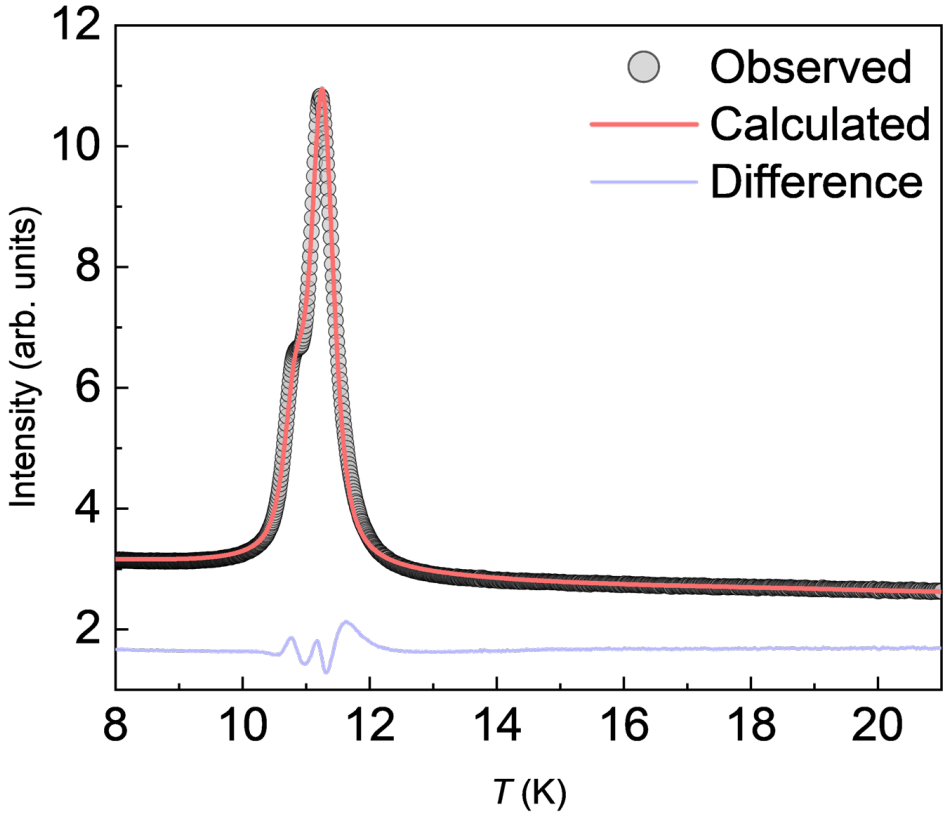


Figure 5.20: The Rietveld refinement of one feature in Bank 1, Cu-HHB data to the $C2/m$ model, collected on the WISH diffractometer. R_{wp} = 2.368%, scale factor = 2.4476(5). We are unable to fit multiple peaks to the model here while simultaneously obtaining a consistent scale factor, therefore we select the most intense Bragg peak for refinement.

In extracting this scale factor we are then able to perform a magnetic refinement of Cu-HHB (Figure 5.21). We select Bank 1 data for subtraction as this is the longest d-spacing range that contains the large feature at $\sim$ 11 Å. Upon performing a magnetic refinement

against the subtracted data in the lowest possible symmetry space group $P1$ (Figure 5.20), we found that the Bragg peaks could be fit to an ordered magnetic magnetic moment of 7.71(47) μ_B which was significantly higher than the 1.73 μB expected for a $S = \frac{1}{2}$, Cu^{2+} system. We therefore conclude that the Bragg intensity in the subtracted dataset is an artefact of temperature-dependent variations and not magnetic in origin and therefore refinements in higher symmetry magnetic space groups was not necessary. With the analysis of these NPD data, we come to the conclusion that there is no clear evidence for magnetic order in either sample of Cu-HHB across the two separate measurements, since the observed temperature-dependent phenomenon dominates all data, making a reasonable assignment of the underlying magnetism is impossible.

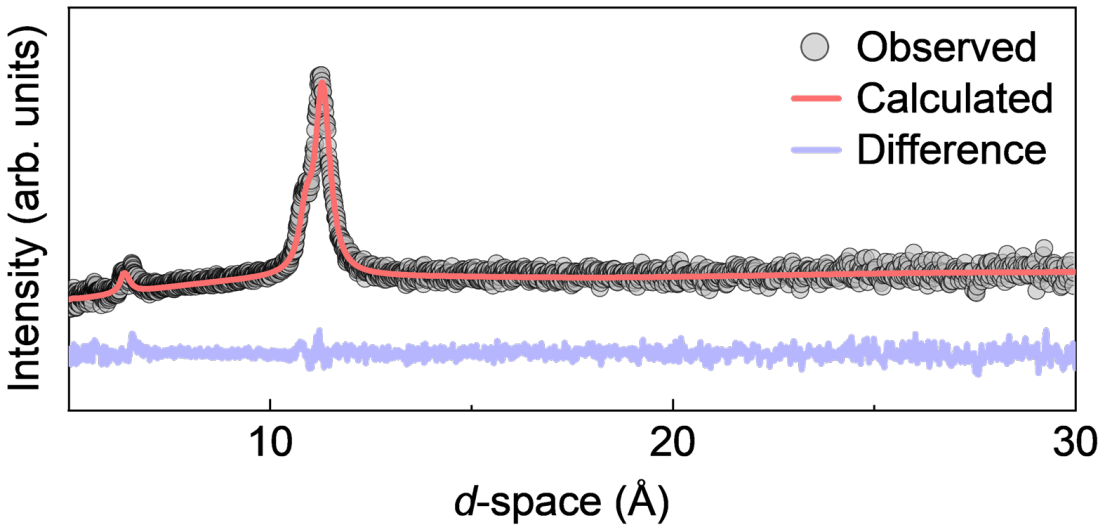


Figure 5.21: Temperature subtracted data from Bank 1, fit to the $P1$ structure providing an extracted moment of 7.71(47) μ_b which is significantly greater than the expected moment of 1.73 μ_b for Cu^{2+}.

To further probe Cu-HHB for magnetic phenomena we move towards performing muon spin relaxation spectroscopy with the aim of highlighting any features of local magnetism and any other temperature dependent effects.

5.3.7 Muon Spin Relaxation Spectroscopy for the Confirmation of Spin Dynamics down to 98 mK

With a large portion of magnetic entropy missing in heat capacity data at 1.8 K and no clear indication of an onset of magnetic order down to sub-Kelvin temperatures in our magnetometry and NPD measurements, we have significant evidence for an unconventional magnetic ground state in Cu-HHB. With all measurements corroborating a lack of long-range ordered ground state, we performed a muon spin relaxation study on MuSR at ISIS Neutron and Muon Source to obtain another insight into the local magnetism of Cu-HHB and whether these data suggest that a QSL state is hosted therein. The first data collected on MuSR were transverse field (TF) measurements, allowing us to fit, and extract the calibration parameter, α, correcting data for inconsistencies between the forward and backward detectors (Figure 5.22).

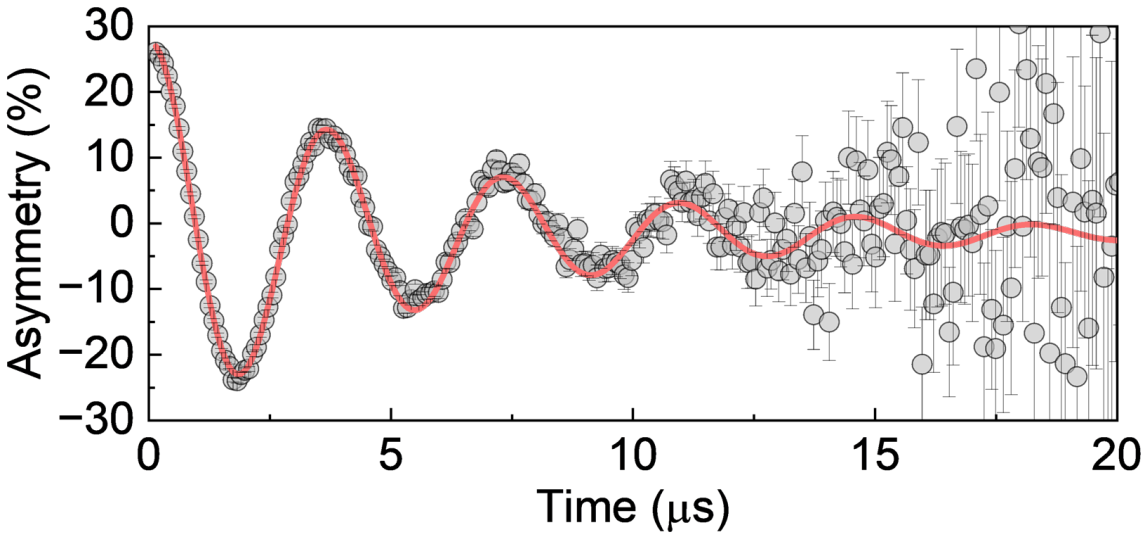


Figure 5.22: MuSR data collected at 120 K in an applied transverse field of 20 G for Cu-HHB, these data are fit to an oscillatory function combined with a Lorentzian relaxation function providing a good fit to the data. From this fit we can extract the frequency corresponding directly to the applied field which then allows us to calculate the detector calibration constant α = 1.4400.

We then begin to measure the magnetic response of the sample at base temperature (0.098 K) in zero applied field to probe the magnetic response. Here, we expect to see a magnetic

response from both the nuclear moment and local magnetic fields of the sample. We fit these data to one Gaussian Kubo-Toyabe function (Equation 5.2) this function describes the distribution of muon stopping sites in a static field. The ability to fit these MuSR data using one function indicates the presence of one muon stopping site. However, we are unable to determine the position of this muon stopping site without further DFT calculations.

$$G_z^G(t) = \frac{2}{3}\left(1 - \Delta^2 t^2\right)\exp\left(-\frac{1}{2}\Delta^2 t^2\right) + \frac{1}{3} \tag{5.2}$$

Where Δ is the width of the Gaussian distribution of magnetic fields and t is time, from this fitting function we are able to extract a field from Δ using software packages such as WIMDA [145]. The next step was to decouple the nuclear field using an applied longitudinal field (LF) leaving behind only the contribution to relaxation from any other magnetic source in the sample. We do this by analysing data across a range of LF's at 0.098 K to find the smallest applied field which fully decouples the nuclear moment of Cu-HHB. The full decoupling of nuclear moments would be indicated by a flattening of the MuSR signal we observe in Cu-HHB, (Figure 5.23).

From this, we are sure we have decoupled the nuclear moment, we can begin a temperature dependence study at a fixed longitudinal field of 111 G. However, one factor to consider during these studies is the use of two different sample holders (cryostat and dilution fridge) for measurements above and below $\sim$ 4 K. To assess the potential differences in the data acquired on each, we collected some zero-field and applied LF data in each sample holder (Figure A.3). The difference between the two datasets is minimal, however this will be taken into account in further studies later. We then collected data at temperature points ranging from $0.098 - 150$ K to assess the temperature dependence of muon relaxation in the sample. We find that the data in all cases can be fit to a single Lorentzian relaxation function, providing us with the relaxation rate (λ).

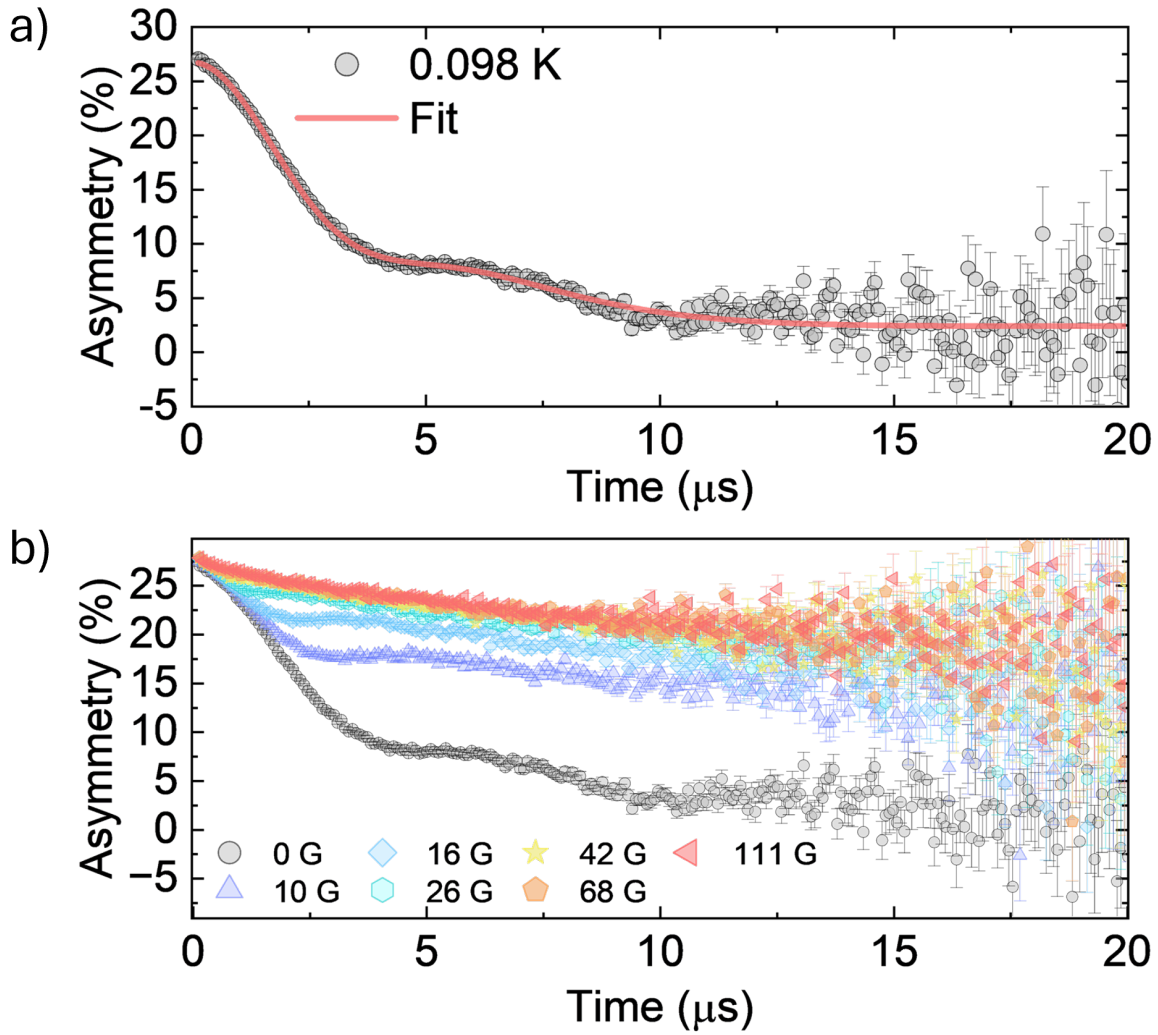


Figure 5.23: MuSR data collected at 0.098 K in a) zero field, fit to Kubo-Toyabe and Gaussian relaxation functions, providing a relaxation rate of 0.2009(23) cm^{-1} and a static field of -6.33(3) mT. b) Several longitudinal fields were applied across the sample to ascertain the field required to fully decouble the nuclear moments of the system, we find that 111 G is ample for the full decoupling of nuclear moments, characterised by a flattening of the zero-field signal.

In Figure A.5 we fit multiple datasets to a single Lorentzian with extracted values for λ summarised in Table A.1. The study of relaxation rate as a function of temperature can tell us whether a spin glass or magnetic transition is occurring, characterised by a sharp feature at the transition temperature and no sign of a plateau at lower temperature [142, 192]. For a dynamic magnetic ground state however, we would expect to see a plateau where the relaxation rate is independant of temperature, which is exactly what we observe in our plot of these relaxation rate data (Figure 5.24).

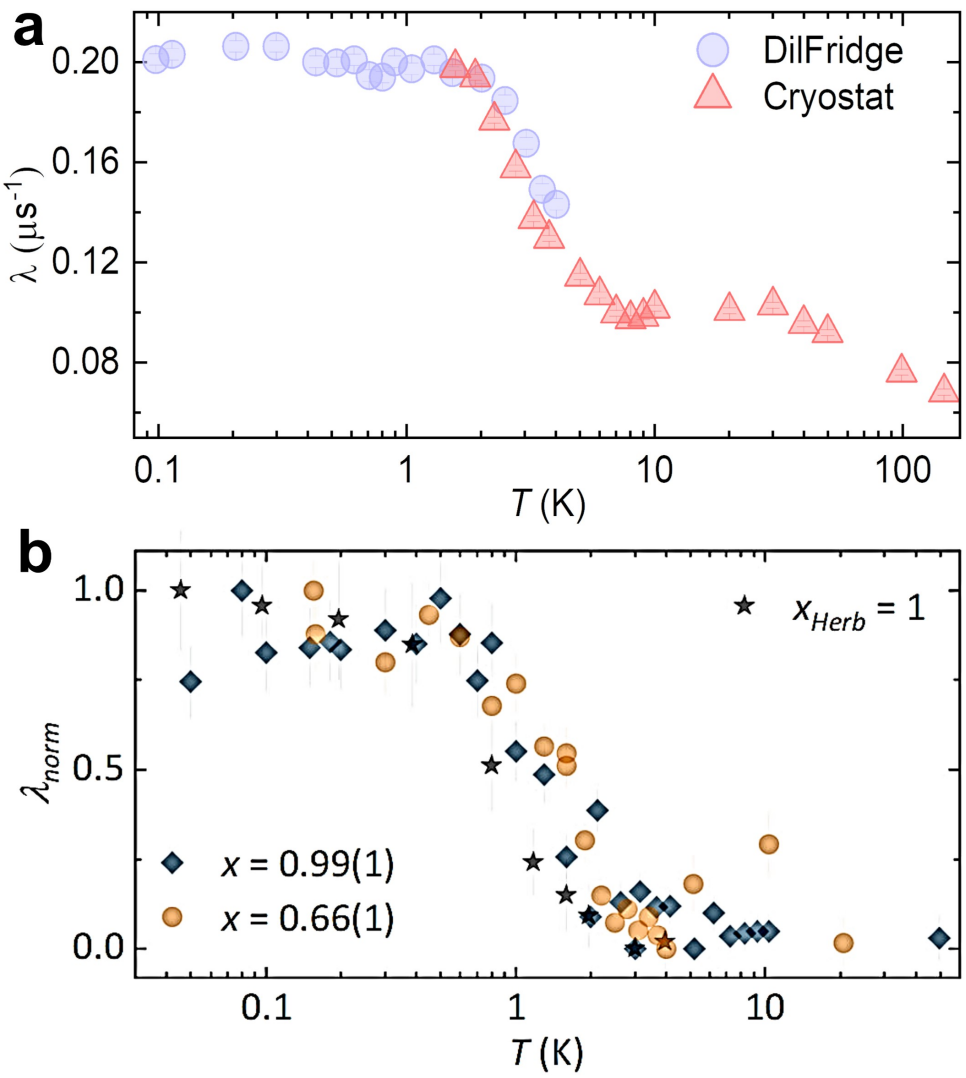


Figure 5.24: Two plots of MuSR temperature dependent relaxation rate data. a) In Cu-HHB, we see a sharp increase in relaxation rate from ~ 8 K corresponding to a slowing of muon precession, followed by a plateau from 1.9 – 0.098 K indicating spin dynamics [60, 142, 192]. b) Here we see temperature-dependent normalised muon spin relaxation rate data for substituted Zn-barlowite where x = 0.99(1) and 0.66(1), alongside overlain, published data for herbertsmithite ($X_{\mathrm{Herb}} = 1$) [60]. We observe in all cases a sharp rise in muon relaxation rate beginning at ~3 K, rising to a plateau ~0.6 K indicative of spin dynamics [67].

Since there are no indications of spontaneous oscillations in de-coupled asymmetry vs. time data (Figure 5.24), we cannot derive any further information from our data without the use of DFT. Often, fitting the spontaneous oscillations in decoupled data to wave functions can provide the frequency and therefore magnetic fields felt by the muon; however,

no such oscillations are observed in our sample. Therefore, we are only able to comment on the lack of features, and how these further support our hypothesis that Cu-HHB may host a QSL state. When we compare our findings to kagome $S{=}\frac{1}{2}$ antiferromagnets also studied by MuSR, such as herbertsmithite an Zn-barlowite, we observe similar plateaus thought to arise due to the unchanging static fields felt by the muon [60, 67].

5.3.8 Conclusions

The synthesis of an antiferromagnetic Cu^{2+} kagome MOF has been described. We have identified the space group of Cu-HHB through the first structural refinement utilising synchrotron X-rays and neutrons. The combination of our structural characterisation and magnetic analysis have provided an unprecedented insight into the complex magnetic phenomena hosted by Cu-HHB. Our goal of elucidating the magnetic ground state of Cu-HHB has been successful and despite the challenges faced in neutron powder diffraction analysis, we observe several indications of a magnetically disordered state in Cu-HHB despite the antiferromagnetic exchange interactions inferred by magnetometry measurements. In doing so we have showcased the extreme difficulty and the necessity of using many complementary techniques in the analysis of QSL candidates. We accept that in using almost all magnetic characterisation techniques, the expected outcome is a lack of magnetic signal from the onset of long-range order, making a QSL-like state exceptionally challenging to unambiguously assign. However, we present our findings as the strongest evidence to date that a QSL-like state exists within Cu-HHB, a Cu^{2+} kagome MOF, down to at least 0.098 K.

1– We confirm the presence of water in Cu-HHB qualitatively and quantitatively through FTIR and TGA analysis, suggesting a water content of 4 molecules per formula unit.

2– We present synchrotron powder XRD data, which facilitated the unambiguous assignment of the $C2/m$ space group for Cu-HHB during our Rietveld analysis of the data.

3– We present evidence supporting the hypothesis that Cu-HHB does not exhibit a long-range ordered transition despite the antiferromagnetic correlations indicated by magnetic susceptibility of the energy scale 0.71(5) meV obtained from heat capacity data. Furthermore we present NPD featuring no clear non-nuclear magnetic Bragg intensity and a low-temperature plateau in MuSR both pointing towards the existence of a spin-dynamic and possibly spin-liquid ground state down to 0.098 K.

The $M_3(C_6X_6)_2$ has proven to be a useful motif for research in several fields including superconductivity, semiconductivity, and complex magnetic phenomena [94, 96, 98, 181, 182]. Due to the lack of magnetic Bragg intensity and temperature-dependent background features of Cu-HHB in NPD measurements, we are unable to propose a magnetic structure. However, we can confirm that the dominant magnetic exchange in Cu-HHB is antiferromagnetic in nature, theoretically through the bonding geometries of likely nearest-neighbour exchange pathways and experimentally through the calculation of a θ_{CW} from magnetic susceptibility measurements. With such a promising system, several additional measurements may provide better insight into the interesting magnetism present in this system:

1– The optimisation of synthesis and further study of the underlying crystallinity may facilitate better single-crystal structural models and magnetic analysis of Cu-HHB. The synthesis of dehydrated and deuterated Cu-HHB may also prove useful in neutron experiments, confirming whether the protons are responsible for our temperature-dependent background issues.

2– The deuteration or full dehydration of Cu-HHB would also allow for inelastic neutron scattering experiments as these highly sensitive measurements suffer from incoherent scattering masking the data. We have since used this technique on Cu-HHB (2) finding

that the level of dehydration is satisfactory for these measurements where we confirmed the absence of dispersive spin waves corresponding to antiferromagnetic order. We are however yet to find or observe broad continuous excitation signals expected to arise for QSL's as data is still being processed for publication [193, 194].

3– Since Cu-HHB does not show any signs of adopting long-range magnetic order at low temperatures, it would be interesting to test the material in proof-of-concept studies, finding whether the material is a suitable candidate for applications in the technologies QSL's are proposed to advance, such as quantum computing [195]. This would be best approached via conductivity studies or graphene doping studies as recently explored in the literature [196].

Furthermore, we see evidence in the literature for the feasibility of "bottom-up" approaches to synthesising Cu-HHB, involving the deposition of HHB onto a pristine copper (111) surface allowing for characterisation of single layers of Cu-HHB [80]. This may also allow Cu-HHB to be studied for applications in thin-film technologies [197]. It is clear from this study of one MOF with the general formula $M_3(L)_2$ is highly interesting for the study of unconventional magnetism. With the findings contained within this chapter making up the most complete characterisation of Cu-HHB to date, we move towards inelastic neutron scattering to uncover further magnetic information on this exciting material.

Chapter 6

Chapter Summaries and Outlook

In this thesis, we have investigated four metal-organic frameworks containing copper(II) in a kagome arrangement. We have identified three distinct magnetic ground states, showcasing the capability of MOF chemistry in studying magnetic structures hosting both long-range order and unconventional magnetic ground states, arising from geometries such as the kagome. This thesis is divided into three chapters that focus on; the unconventional long-range ordered ground state of a three-dimensional copper carbonate kagome MOF, the impact of changing the magnetic dimensionality through ligand selection between ferromagnetic copper carbonate kagome planes, and the low-temperature magnetic properties of a two-dimensional kagome-containing MOF with antiferromagnetic exchange correlations. The summary and outlook for these findings are given below:

6.1 Chapter Summaries

$Cu_3(CO_3)_2(bpa)_3{\cdot}2ClO_4$, MOF-*bpa*: In Chapter 3, we explore a fourth member of a MOF family previously reported to host ferromagnetic copper kagome layers, which antiferromagnetically couple to nearest neighbour layers through ditopic organic ligands. We present the first magnetic neutron diffraction study for MOF-*bpa* and find

that small differences in the ordered moment size and ordering transition temperature are present. However, these do not change the characteristics of the magnetically ordered ground state we model. Additionally, we find only slight variations in the magnetic susceptibility data collected for the four MOFs. This suggests that the structural changes facilitated by MOF chemistry are useful in fine-tuning magnetic exchange interactions. However, the limitations of our analytical techniques make the characterisation of these minute changes challenging.

If we were to further analyse our data through high-temperature series expansion of magnetic susceptibility data, or through computational study on the inter-plane superexchange pathway, we may be able to draw some conclusions on the superexchange mediated by these inter-plane ligands and whether disorder and conjugation play a role. As we optimize the structure of magnetic MOFs to achieve specific characteristics, it will be essential to comprehend the influence that particular ligands have on magnetism for further intelligent design. Ultimately, this work demonstrates the usefulness of MOF chemistry in the study of specific magnetic geometries such as the kagome and provides us with the insight to explore different systems utilising different ligands such as those studied in the later chapters. For the four MOFs discussed in this chapter, our ligand selection for the three-dimensional structure preserved the kagome lattice, allowing us to confirm that the magnetic ground states remain largely unchanged. From this we conclude that $Cu_3(CO_3)_2(x)_3{\cdot}2ClO_4$ systems, where x is a ditopic organic ligand, are likely to be comprised of ferromagnetic kagome layers, coupled antiferromagnetically to neighbouring layers, whether ligand disorder and conjugation are present between layers or not. The future work being undertaken for MOF-*bpa* is the deuteration of samples and the collection of inelastic neutron scattering data in the hopes of studying the flat bands associated with the magnon Hall effect.

$Cu_3(CO_3)_2(x)_6{\cdot}2ClO_4$, x = *mp*, *bipy*: In Chapter 4, we built on the foun-

dations laid out in Chapter 3, extending the discussed MOF family to include those with magnetically isolated copper carbonate kagome layers through ligand selection. To achieve this we used the monodentate ligands 4-methylpyridine and 2,4'-bipyridine, which we confirmed to yield non-covalent, stacked kagome layers in a three-dimensional MOF. Since we expected the kagome layers to be ferromagnetic, this chapter aimed to explore whether there was evidence for these ferromagnetic layers being magnetically isolated, yielding two-dimensional kagome layers. First, we confirm the crystal structures of these systems. Since MOF-*mp* was a previously unreported system, the acquisition of SCXRD data were crucial in outlining the structure. Through magnetic susceptibility measurements we found Curie-Weiss temperatures consistent with those reported for the covalent, coordinated MOFs outlined in Chapter 3, suggesting that the ferromagnetic exchange coupling present in the copper kagome lattice was preserved. Our analysis of magnetic heat capacity data suggested that significant portions of magnetic entropy magnetic entropy maybe missing for both MOFs. The possibility that ferromagnetic two-dimensional exchange correlations describe the magnetic structure above the suspected ordering transition temperature may explain this missing magnetic entropy, which we observe in heat capacity data.

This was a hypothesis supported by our neutron powder diffraction data, where we find no evidence for magnetic exchange between layers and no evidence for antiferromagnetic exchange coupling. It was therefore possible that we have discovered quasi-two-dimensional ferromagnetic layers in both cases, with exchange propagating between planes unlikely and lacking experimental evidence. It is clear from our analysis however that limitations in our data make specific claims challenging however there are several indications that we may have synthesised systems hosting two-dimensional exchange interactions. This was an exciting discovery as the two-dimensional ferromagnetic kagome was expected to host exotic magnetic phenomena in cases where competing interactions between the nearest and the next nearest-neighbour are present [163]. Due to the promise of magnetically

isolated kagome layers, we exfoliate these MOFs, confirming the presence of single-layer height profiles by atomic force microscopy. These systems pose attractive candidates for further investigation of their two-dimensional magnetic behaviour. However, before doing this, we must first confirm the crystallinity and magnetic activity of the exfoliated material. This would likely be possible through electron diffraction, X-ray circular dichroism and magneto optic kerr effect studies on the suspected nanosheets.

$Cu_3(C_6O_6)_2$, Cu-HHB: In Chapter 5, we use our findings from previous chapters to help find a system likely to host a QSL state. First, the copper carbonate kagome, was found to host ferromagnetic exchange, and second, the stacked kagome-containing MOFs in Chapter 4 showed no signs of inter-plane exchange, these two findings led us to the system we report in Chapter 5. This system features magnetically isolated copper hexahydroxybenzene kagome layers and was initially reported to host antiferromagnetic exchange interactions, making it an excellent candidate for study as a QSL candidate material in terms of dimensionality and exchange interactions present. Initially, we confirmed the crystal structure through Rietveld refinement of high-resolution PXRD data, as conflict in the literature suggested two space group assignments. Next, we confirmed that no evidence for the adoption of long-range magnetic order was visible in magnetic susceptibility, confirming the presence of antiferromagnetic exchange interactions by Curie-Weiss analysis.

We also discovered that a significant portion of magnetic entropy maybe missing, much like the systems reported in Chapter 4. However, as an antiferromagnetically correlated system with no clear signs of order, this lack of magnetic entropy may simply arise from the lack of long-range ordered transition down to 1.8 K. We further confirm the lack of long-range magnetic order by analysing neutron powder diffraction data. Although the subtraction of these data were limited by an unknown source of background, we observe no indications of the onset of a long-range ordered state emerging from non-nuclear

Bragg positions. Finally, to probe the low-temperature spin dynamics, we performed a temperature-dependent muon study, finding no evidence for the adoption of long-range order or transition to a spin-glass state. It is hoped that the collection of inelastic neutron scattering data will further elucidate the low-temperature magnetism hosted by Cu-HHB, extracting an energy scale comparable to the calculated Schottky anomaly, and defining whether it is a gapless or gapped quantum spin liquid [198], is hosted within a MOF.

6.2 Outlook

An overarching theme of this thesis is one of discovering unconventional magnetic ground states in MOFs. Whether adopting both ferromagnetic and antiferromagnetic order simultaneously in Chapter 3, signs of a lack of three-dimensional order in Chapter 4 and a complete lack of long-range order in Chapter 5, the $S = \frac{1}{2}$ kagome model has been rigorously studied in a material setting. The three-dimensional long range ordered MOFs discussed in Chapter 3 mark over 10 years of research into the complex magnetic ground states featured within these materials. Alongside the unambiguous characterisation of their magnetic structures, we also found that inter-plane ligand selection plays a crucial role in their low-temperature, long-range ordered state. This chapter acts as a comprehensive study into the magnetic behaviours of the $Cu_3(CO_3)_2(x)_3{\cdot}2ClO_4$ family of MOFs, presenting a foundation for future research into similar systems. If we had not been able to elucidate the magnetic ground state of this family of materials, we may still be under the same impression that the copper carbonate kagome is antiferromagnetic [82, 84, 85].

The work carried out in Chapter 4 was based on the idea of tuning the magnetic properties of these MOFs by implementing different organic ligands. With two-dimensional magnets expected to be excellent candidates for novel spintronics devices [11], approaching

a less well studied magnetic topology such as the two-dimensional kagome may elucidate whether they are good candidates for such applications. Alongside this, the ferromagnetic kagome holds additional promise, as it has been seen to host topological magnon bands in the literature, a phenomenon expected to aid in the application to novel spintronics, due to the fact that magnons do not produce "joule heating" [11, 80, 199]. It is for these reasons that the discovery of new systems with the potential to host such phenomena are sought after. In Chapter 4 we report a kagome-containing MOF previously unreported in the literature, marking a brand new system which may host exciting physics with the added benefit of facilitating delamination to nanosheets. The potential for delamination make both MOF-*bipy* and MOF-*mp* exciting materials for experimentation in both ultrathin technologies and in the elucidation of exotic magnetic phenomena such as these discussed topological magnon bands. As such, future work on these systems will involve the characterisation of magnetic nanosheets alongside the study of the unexfoliated, magnetically quasi-two dimensional systems.

In Chapter 5 we approached a different model of interest, opting to build upon the current literature for a $S = \frac{1}{2}$ antiferromagnetic kagome-containing MOF, better outlining its potential as a QSL hosting material. Since the QSL cannot be characterised directly, it is of great importance that several techniques are used in conjunction to characterise the sought after state. We improve upon the existing literature for this system and find that there is no evidence for the emergence of a long-range ordered state within. Similar evidence has been reported for members of the $Cu_3(L)_2$ family, for instance, $Cu_3(HHTP)_2$, where HHTP is 2,3,6,7,10,11-hexahydroxytriphenylene, has been reported in 2024 to host a robust quantum spin liquid state [95]. In this case they go beyond just studying the spin dynamics and approach the applications of quantum spin liquids. They do this by constructing the $S = \frac{1}{2}$ two-dimensional kagome antiferromagnet upon graphene, which has been shown to massively increase conductivity, therefore allowing this material to be considered for components in electronics. This may be the logical next step for the study

of Cu-HHB.

Since elucidating the Quantum Spin Liquid in a material context remains a difficult task, there may be a point in the future where the benefits of further characterisation become limited by the current state-of-the-art. At that stage, focussing on optimising these systems for practical applications may become more useful to progression than fully grasping the fundamental physics behind them. Similarly to lodestone, which was used in the first compasses long before its underlying physics were understood [7]. Perhaps promising quantum spin liquid containing materials should be optimised for use in emergent technologies, with the underlying physics better understood within the context of their functional properties.

References

[1] Martin Jansen. "Solid State Chemistry and its Applications". In: *Angewandte Chemie* 97.7 (July 1985), pp. 616–616. ISSN: 0044-8249. DOI: 10.1002/ange.19850970741.

[2] Mingming Ma et al. "A review of all-solid-state electrolytes for lithium batteries: high-voltage cathode materials, solid-state electrolytes and electrode–electrolyte interfaces". In: *Materials Chemistry Frontiers* 7.7 (2023), pp. 1268–1297. ISSN: 2052-1537. DOI: 10.1039/D2QM01071B.

[3] Kyung-Su Kim. "Exact hole-induced resonating-valence-bond ground state in certain U Hubbard models". In: *Physical Review B* 107.14 (Apr. 2023), p. L140401. ISSN: 2469-9950. DOI: 10.1103/PhysRevB.107.L140401.

[4] Le Gao et al. "4D Ultra-High-Density Long Data Storage Supported by a Solid-State Optically Active Polymeric Material with High Thermal Stability". In: *Advanced Optical Materials* 9.17 (Sept. 2021). ISSN: 2195-1071. DOI: 10.1002/adom.202100487.

[5] Herb Goronkin and Yang Yang. "High-Performance Emerging Solid-State Memory Technologies". In: *MRS Bulletin* 29.11 (Nov. 2004), pp. 805–813. ISSN: 0883-7694. DOI: 10.1557/mrs2004.232.

[6] S Blundell. *Magnetism in Condensed matter*. 2001.

[7] Allan A. Mills. "The Lodestone: History, Physics, and Formation". In: *Annals of Science* 61.3 (July 2004), pp. 273–319. ISSN: 0003-3790. DOI: 10.1080/000337903100-01642812.

[8] Lucile Savary and Leon Balents. "Quantum spin liquids: a review". In: *Reports on Progress in Physics* 80.1 (Jan. 2017), p. 016502. ISSN: 0034-4885. DOI: 10.1088/0034-4885/80/1/016502. URL: https://iopscience.iop.org/article/10.1088/0034-4885/80/1/016502.

[9] C. Broholm et al. "Quantum spin liquids". In: *Science* 367.6475 (Jan. 2020). ISSN: 0036-8075. DOI: 10.1126/science.aay0668.

[10] Jia-Xin Yin et al. "Quantum-limit Chern topological magnetism in TbMn6Sn6". In: *Nature* 583.7817 (July 2020), pp. 533–536. ISSN: 0028-0836. DOI: 10.1038/s41586-020-2482-7.

[11] Guojing Hu and Bin Xiang. "Recent Advances in Two-Dimensional Spintronics". In: *Nanoscale Research Letters* 15.1 (Dec. 2020), p. 226. ISSN: 1556-276X. DOI: 10.1186/s11671-020-03458-y.

[12] Samuel A. Ivko et al. "Uncovering the S=12 Kagome Ferromagnet within a Family of Metal–Organic Frameworks". In: *Chemistry of Materials* 34.12 (June 2022), pp. 5409–5421. ISSN: 0897-4756. DOI: 10.1021/acs.chemmater.2c00289.

[13] Mohadeseh Safaei et al. "A review on metal-organic frameworks: Synthesis and applications". In: *TrAC Trends in Analytical Chemistry* 118 (Sept. 2019), pp. 401–425. ISSN: 01659936. DOI: 10.1016/j.trac.2019.06.007.

[14] Ayesha Rehman et al. "Synthesis and effect of metal–organic frame works on CO2 adsorption capacity at various pressures: A contemplating review". In: *Energy & Environment* 31.3 (May 2020), pp. 367–388. ISSN: 0958-305X. DOI: 10.1177/0958305X19865352.

[15] Linjian Zhang, Fangqin Liand, and Liangfei Luo. "Preparation Methods of Metal Organic Frameworks and Their Capture of CO2". In: *IOP Conference Series: Earth and Environmental Science* 108 (Jan. 2018), p. 042104. ISSN: 1755-1307. DOI: 10.1088/1755-1315/108/4/042104.

[16] Chao-Wei Huang et al. "Metal–organic frameworks: preparation and applications in highly efficient heterogeneous photocatalysis". In: *Sustainable Energy & Fuels* 4.2 (2020), pp. 504–521. ISSN: 2398-4902. DOI: 10.1039/C9SE00972H.

[17] Sanju Soni, Parmendra Kumar Bajpai, and Charu Arora. "A review on metal-organic framework: Synthesis, properties and application". In: *Characterization and Application of Nanomaterials* 3.2 (Sept. 2020), p. 87. ISSN: 2578-1995. DOI: 10.24294/can.v3i2.551.

[18] Vadia Foziya Yusuf, Naved I. Malek, and Suresh Kumar Kailasa. "Review on Metal–Organic Framework Classification, Synthetic Approaches, and Influencing Factors: Applications in Energy, Drug Delivery, and Wastewater Treatment". In: *ACS Omega* 7.49 (Dec. 2022), pp. 44507–44531. ISSN: 2470-1343. DOI: 10.1021/acsomega.2c05310.

[19] Mosaed S. Alhumaimess. "Metal–organic frameworks and their catalytic applications". In: *Journal of Saudi Chemical Society* 24.6 (June 2020), pp. 461–473. ISSN: 13196103. DOI: 10.1016/j.jscs.2020.04.002.

[20] Rahime Eshaghi Malekshah et al. "MOFs as Versatile Catalysts: Synthesis Strategies and Applications in Value-Added Compound Production". In: *ACS Omega* 8.35 (Sept. 2023), pp. 31600–31619. ISSN: 2470-1343. DOI: 10.1021/acsomega.3c02552.

[21] Joseph F. Olorunyomi et al. "Metal–organic frameworks for chemical sensing devices". In: *Materials Horizons* 8.9 (2021), pp. 2387–2419. ISSN: 2051-6347. DOI: 10.1039/D1MH00609F.

[22] Hessamaddin Sohrabi et al. "Metal-organic frameworks (MOF)-based sensors for detection of toxic gases: A review of current status and future prospects". In: *Materials Chemistry and Physics* 299 (Apr. 2023), p. 127512. ISSN: 02540584. DOI: 10.1016/j.matchemphys.2023.127512.

[23] Harrison D. Lawson, S. Patrick Walton, and Christina Chan. "Metal–Organic Frameworks for Drug Delivery: A Design Perspective". In: *ACS Applied Materials & Interfaces* 13.6 (Feb. 2021), pp. 7004–7020. ISSN: 1944-8244. DOI: 10.1021/acsami.1c01089.

[24] V. Stavila, A. A. Talin, and M. D. Allendorf. "MOF-based electronic and opto-electronic devices". In: *Chem. Soc. Rev.* 43.16 (2014), pp. 5994–6010. ISSN: 0306-0012. DOI: 10.1039/C4CS00096J.

[25] Agnes E. Thorarinsdottir and T. David Harris. "Metal–Organic Framework Magnets". In: *Chemical Reviews* 120.16 (Aug. 2020), pp. 8716–8789. ISSN: 0009-2665. DOI: 10.1021/acs.chemrev.9b00666.

[26] Guojun Zhou, Yang Wang, and Zhehao Huang. "Structure and function tailored metal-organic frameworks for heterogeneous catalysis". In: *Chem Catalysis* 2.12 (Dec. 2022), pp. 3304–3319. ISSN: 26671093. DOI: 10.1016/j.checat.2022.10.023.

[27] Walther Gerlach and Otto Stern. "Der experimentelle Nachweis der Richtungsquantelung im Magnetfeld". In: *Zeitschrift fur Physik* 9.1 (Dec. 1922), pp. 349–352. ISSN: 1434-6001. DOI: 10.1007/BF01326983.

[28] N. Bohr. "On the constitution of atoms and molecules". In: *The London, Edinburgh, and Dublin Philosophical Magazine and Journal of Science* 26.151 (July 1913), pp. 1–25. ISSN: 1941-5982. DOI: 10.1080/14786441308634955.

[29] Ilya G Kaplan. "Pauli Exclusion Principle and its theoretical foundation". In: (Jan. 2019). URL: https://arxiv.org/abs/1902.00499v3.

[30] Klaus Hentschel. "Atomic Models, J.J. Thomson's "Plum Pudding" Model". In: *Compendium of Quantum Physics*. Berlin, Heidelberg: Springer Berlin Heidelberg, 2009, pp. 18–21. DOI: 10.1007/978-3-540-70626-7{_}9.

[31] H. Nagaoka. "Kinetics of a system of particles illustrating the line and the band spectrum and the phenomena of radioactivity". In: *The London, Edinburgh, and Dublin Philosophical Magazine and Journal of Science* 7.41 (May 1904), pp. 445–455. ISSN: 1941-5982. DOI: 10.1080/14786440409463141.

[32] E. Schrödinger. "An Undulatory Theory of the Mechanics of Atoms and Molecules". In: *Physical Review* 28.6 (Dec. 1926), pp. 1049–1070. ISSN: 0031-899X. DOI: 10.1103/PhysRev.28.1049.

[33] "Libre texts - Electronic orbitals". In: (). URL: https://libretexts.org/.

[34] S F Edwards and P W Anderson. "Theory of spin glasses". In: *Journal of Physics F: Metal Physics* 5.5 (May 1975), pp. 965–974. ISSN: 0305-4608. DOI: 10.1088/0305-4608/5/5/017.

[35] Steven T Bramwell and Mark J Harris. "The history of spin ice". In: *Journal of Physics: Condensed Matter* 32.37 (Sept. 2020), p. 374010. ISSN: 0953-8984. DOI: 10.1088/1361-648X/ab8423.

[36] Philippe Mendels and Fabrice Bert. "Quantum kagome frustrated antiferromagnets: One route to quantum spin liquids". In: *Comptes Rendus Physique* 17.3-4 (Mar. 2016), pp. 455–470. ISSN: 16310705. DOI: 10.1016/j.crhy.2015.12.001.

[37] Frédéric Mila. "Quantum spin liquids". In: *European Journal of Physics* 21.6 (Nov. 2000), pp. 499–510. ISSN: 0143-0807. DOI: 10.1088/0143-0807/21/6/302. URL: https://iopscience.iop.org/article/10.1088/0143-0807/21/6/302.

[38] G. Misguich C. Lhuillier. *Introduction to Frustrated Magnetism*. Ed. by Claudine Lacroix, Philippe Mendels, and Frédéric Mila. Vol. 164. Berlin, Heidelberg: Springer Berlin Heidelberg, 2011. ISBN: 978-3-642-10588-3. DOI: 10.1007/978-3-642-10589-0.

[39] Bodong Lv et al. "Anomalous Hall effect in kagome ferromagnet YbMn6Sn6 single crystal". In: *Journal of Alloys and Compounds* 957 (Sept. 2023), p. 170356. ISSN: 09258388. DOI: 10.1016/j.jallcom.2023.170356.

[40] Changmin Lee et al. "Spin wavepackets in the Kagome ferromagnet Fe3Sn2: Propagation and precursors". In: *Proceedings of the National Academy of Sciences* 120.21 (May 2023). ISSN: 0027-8424. DOI: 10.1073/pnas.2220589120.

[41] Sandy Adhitia Ekahana et al. "Anomalous electrons in a metallic kagome ferromagnet". In: *Nature* 627.8002 (Mar. 2024), pp. 67–72. ISSN: 0028-0836. DOI: 10.1038/s41586-024-07085-w.

[42] Linda Ye et al. "Massive Dirac fermions in a ferromagnetic kagome metal". In: *Nature* 555.7698 (Mar. 2018), pp. 638–642. ISSN: 0028-0836. DOI: 10.1038/nature25987.

[43] Hidenori Takagi et al. "Concept and realization of Kitaev quantum spin liquids". In: *Nature Reviews Physics* 1.4 (Mar. 2019), pp. 264–280. ISSN: 2522-5820. DOI: 10.1038/s42254-019-0038-2.

[44] P. W. Anderson. "The Resonating Valence Bond State in La2CuO4 and Superconductivity". In: *Science* 235.4793 (Mar. 1987), pp. 1196–1198. ISSN: 0036-8075. DOI: 10.1126/science.235.4793.1196.

[45] Bevin Huang et al. "Electrical control of 2D magnetism in bilayer CrI3". In: *Nature Nanotechnology* 13.7 (July 2018), pp. 544–548. ISSN: 1748-3387. DOI: 10.1038/s41565-018-0121-3.

[46] Bevin Huang et al. "Layer-dependent ferromagnetism in a van der Waals crystal down to the monolayer limit". In: *Nature* 546.7657 (June 2017), pp. 270–273. ISSN: 0028-0836. DOI: 10.1038/nature22391.

[47] Cheng Gong et al. "Discovery of intrinsic ferromagnetism in two-dimensional van der Waals crystals". In: *Nature* 546.7657 (June 2017), pp. 265–269. ISSN: 0028-0836. DOI: 10.1038/nature22060.

[48] J.-Y. You and Y.P. Feng. "A two-dimensional kagome magnet with tunable topological phases". In: *Materials Today Chemistry* 30 (June 2023), p. 101566. ISSN: 24685194. DOI: 10.1016/j.mtchem.2023.101566.

[49] Youngjun Ahn et al. "Progress and Prospects in Two-Dimensional Magnetism of van der Waals Materials". In: (Jan. 2024).

[50] P. Khuntia et al. "Gapless ground state in the archetypal quantum kagome antiferromagnet ZnCu3(OH)6Cl2". In: *Nature Physics* 16.4 (Apr. 2020), pp. 469–474. ISSN: 1745-2473. DOI: 10.1038/s41567-020-0792-1.

[51] Z Hiroi et al. "Spin-1/2 kagome compounds: Volborthite vs Herbertsmithite". In: *Journal of Physics: Conference Series* 145 (Jan. 2009), p. 012002. ISSN: 1742-6596. DOI: 10.1088/1742-6596/145/1/012002.

[52] Matthew P. Shores et al. "A Structurally Perfect S = 1 /2 Kagomé Antiferromagnet". In: *Journal of the American Chemical Society* 127.39 (Oct. 2005), pp. 13462–13463. ISSN: 0002-7863. DOI: 10.1021/ja053891p. URL: https://pubs.acs.org/doi/10.1021/ja053891p.

[53] J. S. Helton et al. "Spin Dynamics of the Spin- 1/2 Kagome Lattice Antiferromagnet ZnCu3(OH6Cl2)". In: *Physical Review Letters* 98.10 (Mar. 2007), p. 107204. ISSN: 0031-9007. DOI: 10.1103/PhysRevLett.98.107204.

[54] Zenji Hiroi et al. "Orbital Transitions and Frustrated Magnetism in the Kagome-Type Copper Mineral Volborthite". In: *Inorganic Chemistry* 58.18 (Sept. 2019), pp. 11949–11960. ISSN: 0020-1669. DOI: 10.1021/acs.inorgchem.9b01165.

[55] Wen-Jun Hu et al. "Fractionalized Excitations Revealed by Entanglement Entropy". In: *Physical Review Letters* 124.23 (June 2020), p. 237201. ISSN: 0031-9007. DOI: 10.1103/PhysRevLett.124.237201.

[56] Danna E. Freedman et al. "Site Specific X-ray Anomalous Dispersion of the Geometrically Frustrated Kagomé Magnet, Herbertsmithite, ZnCu3(OH)6Cl2". In:

Journal of the American Chemical Society 132.45 (Nov. 2010), pp. 16185–16190. ISSN: 0002-7863. DOI: 10.1021/ja1070398.

[57] G J Nilsen et al. "Low-energy spin dynamics of the S = 1/2 kagome system herbertsmithite". In: *Journal of Physics: Condensed Matter* 25.10 (Mar. 2013), p. 106001. ISSN: 0953-8984. DOI: 10.1088/0953-8984/25/10/106001.

[58] M. Fu et al. "Evidence for a gapped spin-liquid ground state in a kagome Heisenberg antiferromagnet". In: *Science* 350.6261 (Nov. 2015), pp. 655–658. ISSN: 0036-8075. DOI: 10.1126/science.aab2120. URL: https://www.sciencemag.org/lookup/doi/10.1126/science.aab2120.

[59] Tian-Heng Han et al. "Correlated impurities and intrinsic spin-liquid physics in the kagome material herbertsmithite". In: *Physical Review B* 94.6 (Aug. 2016), p. 060409. ISSN: 2469-9950. DOI: 10.1103/PhysRevB.94.060409.

[60] P. Mendels et al. "Quantum Magnetism in the Paratacamite Family: Towards an Ideal Kagomé Lattice". In: *Physical Review Letters* 98.7 (Feb. 2007), p. 077204. ISSN: 0031-9007. DOI: 10.1103/PhysRevLett.98.077204.

[61] Rebecca W. Smaha et al. "Materializing rival ground states in the barlowite family of kagome magnets: quantum spin liquid, spin ordered, and valence bond crystal states". In: *npj Quantum Materials* 5.1 (Apr. 2020), p. 23. ISSN: 2397-4648. DOI: 10.1038/s41535-020-0222-8.

[62] Hiroyuki Yoshida et al. "Orbital switching in a frustrated magnet". In: *Nature Communications* 3.1 (May 2012), p. 860. ISSN: 2041-1723. DOI: 10.1038/ncomms1875.

[63] K. M. Ranjith et al. "Magnetic resonance as a local probe for kagomé magnetism in Barlowite". In: *Scientific Reports* 8.1 (Dec. 2018), p. 10851. ISSN: 2045-2322. DOI: 10.1038/s41598-018-29080-8. URL: http://www.nature.com/articles/s41598-018-29080-8.

[64] Tian-Heng Han et al. "Anisotropy: Spin order and magnetization of single-crystalline Cu4(OH)6FBr barlowite". In: *Physical Review B* 93.21 (June 2016), p. 214416. ISSN: 2469-9950. DOI: 10.1103/PhysRevB.93.214416.

[65] Tian-Heng Han, John Singleton, and John A. Schlueter. "Barlowite: A Spin-1/2 Antiferromagnet with a Geometrically Perfect Kagome Motif". In: *Physical Review Letters* 113.22 (Nov. 2014), p. 227203. ISSN: 0031-9007. DOI: 10.1103/PhysRevLett.113.227203.

[66] Katherine Tustain. "Inorganic and Hybrid Analogues of Kagome and Triangular Magnets". In: *Thesis* (2021).

[67] Katherine Tustain et al. "From magnetic order to quantum disorder in the Zn-barlowite series of S=1/2 kagomé antiferromagnets". In: *npj Quantum Materials* 5.1 (Oct. 2020), p. 74. ISSN: 2397-4648. DOI: 10.1038/s41535-020-00276-4.

[68] Jiaming Wang et al. "Emergence of spin singlets with inhomogeneous gaps in the kagome lattice Heisenberg antiferromagnets Zn-barlowite and herbertsmithite". In: *Nature Physics* 17.10 (Oct. 2021), pp. 1109–1113. ISSN: 1745-2473. DOI: 10.1038/s41567-021-01310-3.

[69] Dan Zhao et al. "Tuning the Topology and Functionality of MetalOrganic Frameworks by Ligand Design". In: *Accounts of Chemical Research* 44.2 (Feb. 2011), pp. 123–133. ISSN: 0001-4842. DOI: 10.1021/ar100112y.

[70] Miguel Cortijo et al. "Modulation of the Magnetic Properties of Two-Dimensional Compounds [NiX2(N–N)] by Tailoring Their Crystal Structure". In: *Inorganic Chemistry* 52.12 (June 2013), pp. 7087–7093. ISSN: 0020-1669. DOI: 10.1021/ic400632c.

[71] Danil W. Boukhvalov et al. "Effect of Ligand Substitution on the Exchange Interactions in (Mn12)-Type Single-Molecule Magnets". In: *Inorganic Chemistry* 49.23 (Dec. 2010), pp. 10902–10906. ISSN: 0020-1669. DOI: 10.1021/ic101229p.

[72] Pieremanuele Canepa, Yves J. Chabal, and T. Thonhauser. "When metal organic frameworks turn into linear magnets". In: *Physical Review B* 87.9 (Mar. 2013), p. 094407. ISSN: 1098-0121. DOI: 10.1103/PhysRevB.87.094407.

[73] Daniel R. Harcombe et al. "One-dimensional magnetic order in the metal-organic framework Tb(HCOO)3". In: *Physical Review B* 94.17 (Nov. 2016), p. 174429. ISSN: 2469-9950. DOI: 10.1103/PhysRevB.94.174429.

[74] Alexander Vasiliev et al. "Milestones of low-D quantum magnetism". In: *npj Quantum Materials* 3.1 (Mar. 2018), p. 18. ISSN: 2397-4648. DOI: 10.1038/s41535-018-0090-7.

[75] Brian Moulton et al. "Crystal Engineering of a Nanoscale Kagomé Lattice". In: *Angewandte Chemie International Edition* 41.15 (Aug. 2002), pp. 2821–2824. ISSN: 14337851. DOI: 10.1002/1521-3773.

[76] Emily A. Nytko et al. "A Structurally Perfect S = 1/2 MetalOrganic Hybrid Kagomé Antiferromagnet". In: *Journal of the American Chemical Society* 130.10 (Mar. 2008), pp. 2922–2923. ISSN: 0002-7863. DOI: 10.1021/ja709991u.

[77] Vinodkumar Etacheri et al. "Visible-light activation of TiO2 photocatalysts: Advances in theory and experiments". In: *Journal of Photochemistry and Photobiology C: Photochemistry Reviews* 25 (Dec. 2015), pp. 1–29. ISSN: 13895567. DOI: 10.1016/j.jphotochemrev.2015.08.003.

[78] Wei-Zheng Shen et al. "A Structural and Magnetic Investigation of Ferromagnetically Coupled Copper(II) Isophthalates". In: *European Journal of Inorganic Chemistry* 2005.12 (June 2005), pp. 2297–2305. ISSN: 1434-1948. DOI: 10.1002/ejic.200401022.

[79] R. Chisnell et al. "Topological Magnon Bands in a Kagome Lattice Ferromagnet". In: *Physical Review Letters* 115.14 (Sept. 2015), p. 147201. ISSN: 0031-9007. DOI: 10.1103/PhysRevLett.115.147201.

[80] Ran Zhang et al. "On-surface Synthesis of a Semiconducting 2D Metal–Organic Framework Cu3 (C6O6) Exhibiting Dispersive Electronic Bands". In: *Angewandte Chemie* 132.7 (Feb. 2020), pp. 2691–2695. ISSN: 0044-8249. DOI: 10.1002/ange.201913698. URL: https://onlinelibrary.wiley.com/doi/10.1002/ange.201913698.

[81] Yu-Ling Wang et al. "Syntheses and Characterizations of Two 3D CobaltOrganic Frameworks from 2D Honeycomb Building Blocks". In: *Crystal Growth & Design* 5.5 (Sept. 2005), pp. 1849–1855. ISSN: 1528-7483. DOI: 10.1021/cg0501128.

[82] M. O. Ajeesh et al. "Tuning of magnetic frustration in S = 1 / 2 Kagomé lattices [Cu3(CO3)2(bpe)3](ClO4)2 and [Cu3(CO3)2(bpy)3](ClO4)2 through rigid and flexible ligands". In: *Solid State Communications* 207 (Apr. 2015), pp. 16–20. ISSN: 00381098. DOI: 10.1016/j.ssc.2015.01.018.

[83] David Z. T. Mulrooney et al. "Phase Control of Ferromagnetic Copper(II) Carbonate Coordination Polymers through Reagent Concentration". In: *European Journal of Inorganic Chemistry* 2018.48 (Dec. 2018), pp. 5223–5228. ISSN: 1434-1948. DOI: 10.1002/ejic.201801041. URL: https://chemistry-europe.onlinelibrary.wiley.com/doi/10.1002/ejic.201801041.

[84] A. Jain et al. "Fragile magnetic ground state of a spin- 1/2 metal-organic kagome lattice". In: *Physical Review B* 101.14 (Apr. 2020), p. 140413. ISSN: 2469-9950. DOI: 10.1103/PhysRevB.101.140413. URL: https://link.aps.org/doi/10.1103/PhysRevB.101.140413.

[85] Prakash Kanoo et al. "A planar Cu2+ (S = 1/2) kagomé network pillared by 1,2-bis(4-pyridyl) ethane with interesting magnetic properties". In: *Dalton Transactions* 26 (2009), p. 5062. ISSN: 1477-9226. DOI: 10.1039/b905229a. URL: http://xlink.rsc.org/?DOI=b905229a.

[86] Tony D. Keene et al. "Tuning of magnetic frustration in S = 1 / 2 Kagomé lattices Cu3(CO3)2(bpe)3(CLO4)2 and Cu3(CO3)2(bpy)3(CLO4)2 through rigid and

flexible ligands". In: *Dalton Trans.* 43.39 (Oct. 2014), pp. 14766–14771. ISSN: 1477-9226. DOI: 10.1039/C4DT02205J. URL: http://xlink.rsc.org/?DOI=C4DT02205J.

[87] Jiang-Feng Song et al. "Five metal imidazole dicarboxylate-based compounds comprising M3(MIDC)2 entities (M=Zn2+, Co2+, Mn2+): syntheses, structures and properties". In: *Journal of Coordination Chemistry* 68.20 (Oct. 2015), pp. 3651–3666. ISSN: 0095-8972. DOI: 10.1080/00958972.2015.1071483.

[88] Partha Mahata, Debajit Sarma, and Srinivasan Natarajan. "Magnetic behaviour in metal-organic frameworks—Some recent examples". In: *Journal of Chemical Sciences* 122.1 (Jan. 2010), pp. 19–35. ISSN: 0974-3626. DOI: 10.1007/s12039-010-0001-3.

[89] John B. Goodenough. "Magnetism and the Chemical Bond." In: *Berichte der Bunsengesellschaft für physikalische Chemie* 68.10 (Dec. 1964), pp. 996–996. ISSN: 0005-9021. DOI: 10.1002/bbpc.19640681015.

[90] Pedro Mateus et al. "A Trinuclear Copper(II) Cryptate and Its μ3-CO3 Cascade Complex: Thermodynamics, Structural and Magnetic Properties". In: *Chemistry - A European Journal* 17.40 (Sept. 2011), pp. 11193–11203. ISSN: 09476539. DOI: 10.1002/chem.201101372. URL: http://doi.wiley.com/10.1002/chem.201101372.

[91] Chandrima Chakravarty, Bikash Mandal, and Pranab Sarkar. "Bis(dithioline)-Based Metal–Organic Frameworks with Superior Electronic and Magnetic Properties: Spin Frustration to Spintronics and Gas Sensing". In: *The Journal of Physical Chemistry C* 120.49 (Dec. 2016), pp. 28307–28319. ISSN: 1932-7447. DOI: 10.1021/acs.jpcc.6b09416.

[92] Chandrima Chakravarty, Bikash Mandal, and Pranab Sarkar. "Bis(iminothiolato)-Based One-Dimensional Metal–Organic Framework: Robust Bipolar Magnetic Semiconductor with Reversal of Spin Polarization". In: *The Journal of Physical Chemistry C* 124.1 (Jan. 2020), pp. 37–43. ISSN: 1932-7447. DOI: 10.1021/acs.jpcc.9b08456.

[93] Mingwen Zhao, Aizhu Wang, and Xiaoming Zhang. "Half-metallicity of a kagome spin lattice: the case of a manganese bis-dithiolene monolayer". In: *Nanoscale* 5.21 (2013), p. 10404. ISSN: 2040-3364. DOI: 10.1039/c3nr03323f.

[94] Muqing Hua et al. "Highly Degenerate Ground States in a Frustrated Antiferromagnetic Kagome Lattice in a Two-Dimensional MetalOrganic Framework". In: *J. Phys. Chem. Lett. 2021* 12 (2021), pp. 3733–3739. DOI: 10.1021/acs.jpclett.1c00598. URL: https://doi.org/10.1021/acs.jpclett.1c00598.

[95] Pranay Ninawe et al. "Robust Spin Liquidity in 2D Metal-Organic Framework Cu3(HHTP)2 with S = $\frac{1}{2}$ Kagome Lattice". In: *Chemistry – A European Journal* (Nov. 2023). ISSN: 0947-6539. DOI: 10.1002/chem.202303718.

[96] Yuki Misumi et al. "Quantum Spin Liquid State in a Two-Dimensional Semiconductive Metal–Organic Framework". In: *Journal of the American Chemical Society* 142.39 (Sept. 2020), pp. 16513–16517. ISSN: 0002-7863. DOI: 10.1021/jacs.0c05472. URL: https://pubs.acs.org/doi/10.1021/jacs.0c05472.

[97] Jihye Park et al. "Synthetic Routes for a 2D Semiconductive Copper Hexahydroxybenzene Metal-Organic Framework". In: *Journal of the American Chemical Society* 140.44 (2018). ISSN: 15205126. DOI: 10.1021/jacs.8b06666.

[98] Zheng Meng et al. "Unraveling the Electrical and Magnetic Properties of Layered Conductive Metal-Organic Framework With Atomic Precision". In: *Angewandte Chemie* 134.6 (Feb. 2022), e202113569. ISSN: 1521-3757. DOI: 10.1002/ANGE.202113569. URL: https://onlinelibrary.wiley.com/doi/full/10.1002/ange.202113569%20https://onlinelibrary.wiley.com/doi/abs/10.1002/ange.202113569%20https://onlinelibrary.wiley.com/doi/10.1002/ange.202113569.

[99] Lucy Clark and Aly H. Abdeldaim. "Quantum Spin Liquids from a Materials Perspective". In: *https://doi.org/10.1146/annurev-matsci-080819-011453* 51 (July 2021), pp. 495–519. ISSN: 15317331. DOI: 10.1146/ANNUREV-MATSCI-080819-

011453. URL: https://www.annualreviews.org/doi/abs/10.1146/annurev-matsci-080819-011453.

[100] Vinod Kumar Dwivedi and Soumik Mukhopadhyay. "Suppression of long range magnetic ordering and electrical conduction in Y1.7Bi0.3Ir2O7 thin film". In: *Journal of Magnetism and Magnetic Materials* 484 (Aug. 2019), pp. 313–319. ISSN: 0304-8853. DOI: 10.1016/J.JMMM.2019.04.049.

[101] J A M Paddison et al. "Hidden order in spin-liquid Gd3Ga5O12". In: *Science* 6257 (2015), pp. 179–181. DOI: 10.1126/science.aaa5326. URL: http://wrap.warwick.ac.uk/87963http://dx.doi.org/10.1126/science.aaa5326.

[102] Wenshan Hong et al. "Extreme Suppression of Antiferromagnetic Order and Critical Scaling in a Two-Dimensional Random Quantum Magnet". In: (2021). DOI: 10.1103/PhysRevLett.126.037201.

[103] Klaus S. Lackner. "Carbonate Chemistry for Sequestering Fossil Carbon". In: *Annual Review of Energy and the Environment* 27.1 (Nov. 2002), pp. 193–232. ISSN: 1056-3466. DOI: 10.1146/annurev.energy.27.122001.083433.

[104] David J. Ashworth and Jonathan A. Foster. "Metal–organic framework nanosheets (MONs): a new dimension in materials chemistry". In: *Journal of Materials Chemistry A* 6.34 (2018), pp. 16292–16307. ISSN: 2050-7488. DOI: 10.1039/C8TA03159B. URL: http://xlink.rsc.org/?DOI=C8TA03159B.

[105] Jin-Chong Tan et al. "Hybrid Nanosheets of an Inorganic–Organic Framework Material: Facile Synthesis, Structure, and Elastic Properties". In: *ACS Nano* 6.1 (Jan. 2012), pp. 615–621. ISSN: 1936-0851. DOI: 10.1021/nn204054k.

[106] Anastasia V. Tyurnina et al. "Ultrasonic exfoliation of graphene in water: A key parameter study". In: *Carbon* 168 (Oct. 2020), pp. 737–747. ISSN: 00086223. DOI: 10.1016/j.carbon.2020.06.029.

[107] J. Šafránková et al. *20th Annual Conference of Doctoral Students, WDS'11 "Week of Doctoral Students 2011", Charles University, Faculty of Mathematics and Physics, Prague, Czech Republic, May 31, 2011 to June 3, 2011 : [proceedings of contributed papers]. Pt. 2 Physics of plasmas and ionized media*. Matfyzpress, 2011. ISBN: 9788073781859.

[108] Aastha Dutta. "Fourier Transform Infrared Spectroscopy". In: *Spectroscopic Methods for Nanomaterials Characterization*. Elsevier, 2017, pp. 73–93. DOI: 10.1016/B978-0-323-46140-5.00004-2.

[109] Qiang Ma et al. "Analytical Understanding of the Materials Design with Well-Described Shrinkages on Multiscale". In: *Chemistry – A European Journal* 24.27 (May 2018), pp. 6886–6904. ISSN: 0947-6539. DOI: 10.1002/chem.201704198.

[110] Fangqin Cheng et al. "FTIR analysis of water structure and its influence on the flotation of arcanite (K2SO4) and epsomite (MgSO4·7H2O)". In: *International Journal of Mineral Processing* 122 (July 2013), pp. 36–42. ISSN: 03017516. DOI: 10.1016/j.minpro.2013.04.007.

[111] Azad Mohammed. *Scanning electron microscopy (SEM): A review*. Tech. rep. URL: https://www.researchgate.net/publication/329990577.

[112] Iryna Andrusenko and Mauro Gemmi. "3D electron diffraction for structure determination of small-molecule nanocrystals: A possible breakthrough for the pharmaceutical industry". In: *WIREs Nanomedicine and Nanobiotechnology* 14.5 (Sept. 2022). ISSN: 1939-5116. DOI: 10.1002/wnan.1810.

[113] Waqas Ahmad et al. "A review of the synthesis, fabrication, and recent advances in mixed dimensional heterostructures for optoelectronic devices applications". In: *Applied Materials Today* 30 (Feb. 2023), p. 101717. ISSN: 23529407. DOI: 10.1016/j.apmt.2022.101717.

[114] Luis León-Alcaide et al. "2D magnetic MOFs with micron-lateral size by liquid exfoliation". In: *Chemical Communications* 56.55 (July 2020), pp. 7657–7660. ISSN:

1359-7345. DOI: 10.1039/D0CC02982C. URL: http://xlink.rsc.org/?DOI=D0CC02982C.

[115] Meipeng Jian et al. "Ultrathin water-stable metal-organic framework membranes for ion separation". In: *Science Advances* 6.23 (June 2020). ISSN: 2375-2548. DOI: 10.1126/sciadv.aay3998.

[116] Naoyuki Ishida. "Atomic force microscopy". In: *Non-Destructive Material Characterization Methods*. Elsevier, 2024, pp. 89–125. DOI: 10.1016/B978-0-323-91150-4.00011-2.

[117] M. Aliofkhazraei and N. Ali. "AFM Applications in Micro/Nanostructured Coatings". In: *Comprehensive Materials Processing* 7 (Jan. 2014), pp. 191–241. DOI: 10.1016/B978-0-08-096532-1.00712-3.

[118] E. S. Ameh. "A review of basic crystallography and x-ray diffraction applications". In: *The International Journal of Advanced Manufacturing Technology* 105.7-8 (Dec. 2019), pp. 3289–3302. ISSN: 0268-3768. DOI: 10.1007/s00170-019-04508-1.

[119] Anthony R. West. "Basic solid state chemistry". In: (1984), p. 480.

[120] Oleg V. Dolomanov et al. "OLEX2: a complete structure solution, refinement and analysis program". In: *Journal of Applied Crystallography* 42.2 (Apr. 2009), pp. 339–341. ISSN: 0021-8898. DOI: 10.1107/S0021889808042726.

[121] D.S. Sivia. *Elementary Scattering Theory*. Oxford University PressOxford, Jan. 2011. ISBN: 0199228671. DOI: 10.1093/acprof:oso/9780199228676.001.0001.

[122] H. Dittrich and A. Bieniok. "MEASUREMENT METHODS | Structural Properties: X-Ray and Neutron Diffraction". In: *Encyclopedia of Electrochemical Power Sources*. Elsevier, 2009, pp. 718–737. DOI: 10.1016/B978-044452745-5.00074-5.

[123] Tetsuya Ishikawa. "Accelerator-based X-ray sources: synchrotron radiation, X-ray free electron lasers and beyond". In: *Philosophical Transactions of the Royal Society A: Mathematical, Physical and Engineering Sciences* 377.2147 (June 2019), p. 20180231. ISSN: 1364-503X. DOI: 10.1098/rsta.2018.0231.

[124] Armel Le Bail. "Whole powder pattern decomposition methods and applications: A retrospection". In: *Powder Diffraction* 20.4 (Dec. 2005), pp. 316–326. ISSN: 0885-7156. DOI: 10.1154/1.2135315.

[125] H. M. Rietveld. "A profile refinement method for nuclear and magnetic structures". In: *Journal of Applied Crystallography* 2.2 (June 1969), pp. 65–71. ISSN: 00218898. DOI: 10.1107/S0021889869006558.

[126] Kenneth D. M. Harris, Maryjane Tremayne, and Benson M. Kariuki. "Contemporary Advances in the Use of Powder X-Ray Diffraction for Structure Determination". In: *Angewandte Chemie International Edition* 40.9 (May 2001), pp. 1626–1651. ISSN: 1433-7851. DOI: 10.1002/1521-3773(20010504).

[127] G. J. Long. "Neutron Diffraction". In: *Comprehensive Coordination Chemistry II* 2 (June 2004), pp. 83–90. DOI: 10.1016/B0-08-043748-6/01073-2.

[128] M. Viswanathan et al. "Neutron Diffraction Study on the Magnetic Structure of the Promised Multiferroic Hybrid Perovskite [C(ND2)3]Cu(DCOO)3 and Its Centrosymmetric Analogues". In: *The Journal of Physical Chemistry C* 123.30 (Aug. 2019), pp. 18551–18559. ISSN: 1932-7447. DOI: 10.1021/acs.jpcc.9b04368.

[129] Andrew T. Boothroyd. "Magnetic Diffraction". In: *Principles of Neutron Scattering from Condensed Matter*. Oxford University Press, Oxford, July 2020, pp. 213–256. DOI: 10.1093/oso/9780198862314.003.0007.

[130] D. Drung et al. "Highly Sensitive and Easy-to-Use SQUID Sensors". In: *IEEE Transactions on Applied Superconductivity* 17.2 (June 2007), pp. 699–704. ISSN: 1051-8223. DOI: 10.1109/TASC.2007.897403.

[131] Michael E. Fisher. "Relation between the specific heat and susceptibility of an antiferromagnet". In: *Philosophical Magazine* 7.82 (Oct. 1962), pp. 1731–1743. ISSN: 0031-8086. DOI: 10.1080/14786436208213705.

[132] Sam Mugiraneza and Alannah M. Hallas. "Tutorial: a beginner's guide to interpreting magnetic susceptibility data with the Curie-Weiss law". In: *Communications Physics* 5.1 (Apr. 2022), p. 95. ISSN: 2399-3650. DOI: 10.1038/s42005-022-00853-y.

[133] H. Zu, W. Dai, and A.T.A.M. de Waele. "Development of dilution refrigerators—A review". In: *Cryogenics* 121 (Jan. 2022), p. 103390. ISSN: 00112275. DOI: 10.1016/j.cryogenics.2021.103390.

[134] Yu.G. Pashkevich et al. "Magnetic ordering in Co2+-containing layered double hydroxides via the low-temperature heat capacity and magnetisation study". In: *Applied Clay Science* 233 (Mar. 2023), p. 106843. ISSN: 01691317. DOI: 10.1016/j.clay.2023.106843.

[135] R. E. Watson and M. Weinert. "Contribution of electronic excitations to the entropy of crystals: The relative stabilities of the hcp, fcc, and bcc structures among the transition metals". In: *Physical Review B* 30.4 (Aug. 1984), pp. 1641–1645. ISSN: 0163-1829. DOI: 10.1103/PhysRevB.30.1641.

[136] Ulrich Köbler and Andreas Hoser. "Magnetic Heat Capacity". In: 2010, pp. 167–184. DOI: 10.1007/978-3-642-02487-011.

[137] A. KH. Alassafee and M.S. Omar. "Debye–Einstein approximation approach to calculate the lattice specific heat and related parameters for a Si nanowire". In: *Journal of Taibah University for Science* 11.6 (Nov. 2017), pp. 1226–1231. ISSN: 1658-3655. DOI: 10.1016/j.jtusci.2016.11.002.

[138] C. Kittel. "Introduction to Solid State Physics ". In: *Acta Crystallographica* 7.1 (Jan. 1954), pp. 144–144. ISSN: 0365-110X. DOI: 10.1107/S0365110X54000448.

[139] Harunobu Akiyama and Daisuke Jido. "Systematic study of hadronic excitation energy using the Schottky anomaly". In: *Physical Review D* 104.11 (Dec. 2021), p. 114014. ISSN: 2470-0010. DOI: 10.1103/PhysRevD.104.114014.

[140] P Dalmas de Réotier and A Yaouanc. "Muon spin rotation and relaxation in magnetic materials". In: *Journal of Physics: Condensed Matter* 9.43 (Oct. 1997), pp. 9113–9166. ISSN: 0953-8984. DOI: 10.1088/0953-8984/9/43/002.

[141] Megan R Rutherford. *Weak transverse field μSR measurements as an experimental probe of magnetic materials*. Tech. rep. URL: https://phas.ubc.ca/~berciu/TEACHING/PHYS502/PROJECTS/21-Megan.pdf.

[142] O. Mustonen et al. "Spin-liquid-like state in a spin-1/2 square-lattice antiferromagnet perovskite induced by d10–d0 cation mixing". In: *Nature Communications* 9.1 (Mar. 2018), p. 1085. ISSN: 2041-1723. DOI: 10.1038/s41467-018-03435-1.

[143] Stephen Blundell. *Muon Spectroscopy*. Ed. by Stephen J. Blundell et al. Oxford University PressOxford, Nov. 2021. ISBN: 0198858957. DOI: 10.1093/oso/9780198858959.001.0001.

[144] Yan-Xing Yang et al. "Muon Spin Relaxation Study of Spin Dynamics in Quantum Spin Liquid Candidate H3LiIr2O6". In: (Jan. 2022). URL: http://arxiv.org/abs/2201.12978.

[145] F.L Pratt. "WIMDA: a muon data analysis program for the Windows PC". In: *Physica B: Condensed Matter* 289-290 (Aug. 2000), pp. 710–714. ISSN: 09214526. DOI: 10.1016/S0921-4526(00)00328-8.

[146] Toshimitsu Yamazaki. "Ryogo Kubo and muSR". In: *Hyperfine Interactions* 104.1/4 (1997), pp. 3–13. ISSN: 03043834. DOI: 10.1023/A:1012696615710.

[147] Zhenyue Zhu et al. "Disorder-Induced Mimicry of a Spin Liquid in YbMgGaO4". In: *Physical Review Letters* 119.15 (Oct. 2017), p. 157201. ISSN: 0031-9007. DOI: 10.1103/PhysRevLett.119.157201.

[148] K. Tustain et al. "Nuclear and magnetic structures of the frustrated quantum antiferromagnet barlowite". In: *Physical Review Materials* 2.11 (Nov. 2018), p. 111405. ISSN: 2475-9953. DOI: 10.1103/PhysRevMaterials.2.111405. URL: https://link.aps.org/doi/10.1103/PhysRevMaterials.2.111405.

[149] Mario Palacios-Corella et al. "Influence of Proton Conducting Cations on the Structure and Properties of 2D Anilate-Based Magnets". In: *Inorganic Chemistry* 56.22 (Nov. 2017), pp. 13865–13877. ISSN: 0020-1669. DOI: 10.1021/acs.inorgchem.7b01965.

[150] Wei Jiang, Xiaojuan Ni, and Feng Liu. "Exotic Topological Bands and Quantum States in Metal–Organic and Covalent–Organic Frameworks". In: *Accounts of Chemical Research* 54.2 (Jan. 2021), pp. 416–426. ISSN: 0001-4842. DOI: 10.1021/acs.accounts.0c00652.

[151] Tony D. Keene et al. "Multifunctional MOFs through CO2 fixation: a metamagnetic kagome lattice with uniaxial zero thermal expansion and reversible guest sorption". In: *Dalton Trans.* 43.39 (2014), pp. 14766–14771. ISSN: 1477-9226. DOI: 10.1039/C4DT02205J.

[152] *CrysAlisPRO, Oxford Diffraction /Agilent Technologies UK Ltd, Yarnton, England.*

[153] George M. Sheldrick. "A short history of SHELX". In: *Acta Crystallographica Section A Foundations of Crystallography* 64.1 (Jan. 2008), pp. 112–122. ISSN: 0108-7673. DOI: 10.1107/S0108767307043930.

[154] George M. Sheldrick. "Crystal structure refinement with SHELXL". In: *Acta Crystallographica Section C Structural Chemistry* 71.1 (Jan. 2015), pp. 3–8. ISSN: 2053-2296. DOI: 10.1107/S2053229614024218.

[155] Brian H. Toby and Robert B. Von Dreele. "GSAS-II: the genesis of a modern open-source all purpose crystallography software package". In: *Journal of Applied Crystallography* 46.2 (Apr. 2013), pp. 544–549. ISSN: 0021-8898. DOI: 10.1107/S0021889813003531.

[156] Juan Rodriguez-Carvajal. "Magnetic Structure Determination From Powder Diffraction Using The Program FullProf". In: *Applied Crystallography*. WORLD SCIEN-

TIFIC, May 2001, pp. 30–36. ISBN: 978-981-02-4613-6. DOI: 10.1142/978981281132-50005.

[157] N. D. Mermin and H. Wagner. "Absence of Ferromagnetism or Antiferromagnetism in One- or Two-Dimensional Isotropic Heisenberg Models". In: *Physical Review Letters* 17.22 (Nov. 1966), pp. 1133–1136. ISSN: 0031-9007. DOI: 10.1103/PhysRevLett.17.1133.

[158] M. Gibertini et al. "Magnetic 2D materials and heterostructures". In: *Nature Nanotechnology* 14.5 (May 2019), pp. 408–419. ISSN: 1748-3387. DOI: 10.1038/s41565-019-0438-6. URL: http://www.nature.com/articles/s41565-019-0438-6.

[159] Mongur Hossain et al. "Synthesis, characterization, properties and applications of two-dimensional magnetic materials". In: *Nano Today* 42 (Feb. 2022), p. 101338. ISSN: 17480132. DOI: 10.1016/j.nantod.2021.101338.

[160] Yang Li et al. "Emergent Phenomena in Magnetic Two-Dimensional Materials and van der Waals Heterostructures". In: *ACS Applied Electronic Materials* 4.7 (July 2022), pp. 3278–3302. ISSN: 2637-6113. DOI: 10.1021/acsaelm.2c00419.

[161] Yuyu Yao et al. "Recent progress on emergent two-dimensional magnets and heterostructures". In: *Nanotechnology* 32.47 (Nov. 2021), p. 472001. ISSN: 0957-4484. DOI: 10.1088/1361-6528/ac17fd.

[162] Rui-Zi Zhang et al. "Novel two-dimensional magnets with an in-plane auxetic effect". In: *Nanoscale* 15.21 (2023), pp. 9365–9371. ISSN: 2040-3364. DOI: 10.1039/D3NR01458D.

[163] D. Boldrin et al. "Haydeeite: A spin- 12 kagome ferromagnet". In: *Physical Review B* 91.22 (June 2015), p. 220408. ISSN: 1098-0121. DOI: 10.1103/PhysRevB.91.220408. URL: https://link.aps.org/doi/10.1103/PhysRevB.91.220408.

[164] Subir Sachdev. "Kagome- and triangular-lattice Heisenberg antiferromagnets: Ordering from quantum fluctuations and quantum-disordered ground states with unconfined bosonic spinons". In: *Physical Review B* 45.21 (June 1992), pp. 12377–

12396. ISSN: 01631829. DOI: 10.1103/PhysRevB.45.12377. URL: https://journals.aps.org/prb/abstract/10.1103/PhysRevB.45.12377.

[165] Dong Chen et al. "Variation of magnetism in two-dimensional MnS2 thin films". In: *Journal of Magnetism and Magnetic Materials* 563 (Dec. 2022), p. 169966. ISSN: 03048853. DOI: 10.1016/j.jmmm.2022.169966.

[166] David Soriano. "Uncovering magnetic interactions in moiré magnets". In: *Nature Computational Science* 3.4 (Apr. 2023), pp. 282–284. ISSN: 2662-8457. DOI: 10.1038/s43588-023-00434-1.

[167] Qing Hua Wang et al. "The Magnetic Genome of Two-Dimensional van der Waals Materials". In: *ACS Nano* 16.5 (May 2022), pp. 6960–7079. ISSN: 1936-0851. DOI: 10.1021/acsnano.1c09150.

[168] Cheng Gong and Xiang Zhang. "Two-dimensional magnetic crystals and emergent heterostructure devices". In: *Science* 363.6428 (Feb. 2019). ISSN: 0036-8075. DOI: 10.1126/science.aav4450.

[169] Ahmed A. Moosa and Mayyadah S. Abed. "Graphene preparation and graphite exfoliation". In: *Turkish Journal of chemistry* 45.3 (June 2021), pp. 493–519. ISSN: 13036130. DOI: 10.3906/kim-2101-19.

[170] Se Yun Kim et al. "Ultrasonic assisted exfoliation for efficient production of RuO2 monolayer nanosheets". In: *Inorganic Chemistry Frontiers* 8.20 (2021), pp. 4482–4487. ISSN: 2052-1553. DOI: 10.1039/D1QI00652E.

[171] David Nečas and Petr Klapetek. "Gwyddion: an open-source software for SPM data analysis". In: *Open Physics* 10.1 (Jan. 2012). ISSN: 2391-5471. DOI: 10.2478/s11534-011-0096-2.

[172] N. Masciocchi et al. "[Cu(imidazole)2(CO3)]H2O: an intermediate in the formation of the copper bis-imidazolate polymer (blue phase)". In: *Zeitschrift für Kristallographie - Crystalline Materials* 217.3 (Mar. 2002), pp. 131–134. ISSN: 2196-7105. DOI: 10.1524/zkri.217.3.131.20649.

[173] Graham A. Bowmaker et al. "Synthesis, spectroscopic and structural characterization of some novel adducts of copper(II) salts with unidentate nitrogen bases". In: *Inorganica Chimica Acta* 375.1 (Sept. 2011), pp. 31–40. ISSN: 00201693. DOI: 10.1016/j.ica.2011.04.005.

[174] Junya Kondoh. "Origin of the hump on the left shoulder of the X-ray diffraction peaks observed in Y2O3-fully and partially stabilized ZrO2". In: *Journal of Alloys and Compounds* 375.1-2 (July 2004), pp. 270–282. ISSN: 09258388. DOI: 10.1016/j.jallcom.2003.11.129.

[175] Y. Takano et al. "Magnetic properties and specific heat of MPS3 (M=Mn, Fe, Zn)". In: *Journal of Magnetism and Magnetic Materials* 272-276.SUPPL. 1 (May 2004), E593–E595. ISSN: 0304-8853. DOI: 10.1016/J.JMMM.2003.12.621.

[176] Jie Xing et al. "Synthesis, magnetization, and heat capacity of triangular lattice materials NaErSe2 and KErSe2". In: *Physical Review Materials* 3.11 (Nov. 2019), p. 114413. ISSN: 2475-9953. DOI: 10.1103/PhysRevMaterials.3.114413.

[177] Naveen Kumar Chogondahalli Muniraju et al. "Magnetocaloric Effect in a Frustrated Gd-Garnet with No Long-Range Magnetic Order". In: *Inorganic Chemistry* 59.20 (Oct. 2020), pp. 15144–15153. ISSN: 0020-1669. DOI: 10.1021/acs.inorgchem.0c02074.

[178] Burkhard Schmidt and Peter Thalmeier. "Frustrated two dimensional quantum magnets". In: *Physics Reports* 703 (Aug. 2017), pp. 1–59. ISSN: 03701573. DOI: 10.1016/j.physrep.2017.06.004. URL: https://linkinghub.elsevier.com/retrieve/pii/S0370157317302983.

[179] Tianshu Lan, Baofu Ding, and Bilu Liu. "Magneto-optic effect of two-dimensional materials and related applications". In: *Nano Select* 1.3 (Sept. 2020), pp. 298–310. ISSN: 2688-4011. DOI: 10.1002/nano.202000032.

[180] H. Zhang et al. "Topological magnon bands in a room-temperature kagome magnet". In: *Physical Review B* 101.10 (Mar. 2020), p. 100405. ISSN: 2469-9950. DOI: 10.1103/PhysRevB.101.100405.

[181] Bohayra Mortazavi et al. "Theoretical realization of two-dimensional M3(C6X6)2 (M = Co, Cr, Cu, Fe, Mn, Ni, Pd, Rh and X = O, S, Se) metal–organic frameworks". In: *Applied Materials Today* 15 (June 2019), pp. 405–415. ISSN: 23529407. DOI: 10.1016/j.apmt.2019.03.002.

[182] T. Takenaka et al. "Strongly correlated superconductivity in a copper-based metal-organic framework with a perfect kagome lattice". In: *Science Advances* 7.12 (Mar. 2021), eabf3996. ISSN: 2375-2548. DOI: 10.1126/SCIADV.ABF3996. URL: https://advances.sciencemag.org/content/7/12/eabf3996.

[183] Anna Widera et al. "Electron-Rich, Lewis Acidic Diborane Meets N-Heterocyclic Aromatics: Formation and Electron Transfer in Cyclophane Boranes". In: *Chemistry – A European Journal* 26.15 (Mar. 2020), pp. 3435–3440. ISSN: 0947-6539. DOI: 10.1002/chem.202000189.

[184] Prince Ravat et al. "Dimethylcethrene: A Chiroptical Diradicaloid Photoswitch". In: *Journal of the American Chemical Society* 140.34 (Aug. 2018), pp. 10839–10847. ISSN: 0002-7863. DOI: 10.1021/jacs.8b05465.

[185] Miklos Kertesz. "Pancake Bonding: An Unusual Pi-Stacking Interaction". In: *Chemistry – A European Journal* 25.2 (Jan. 2019), pp. 400–416. ISSN: 0947-6539. DOI: 10.1002/chem.201802385.

[186] D. M. Hatch H. T. Stokes and B. J. Campbell. "ISODISTORT, ISOTROPY Software Suite". In: (). URL: https://stokes.byu.edu/iso/isodistort.php.

[187] Shuichi Suzuki et al. "Aromaticity on the Pancake-Bonded Dimer of Neutral Phenalenyl Radical as Studied by MS and NMR Spectroscopies and NICS Analysis". In: *Journal of the American Chemical Society* 128.8 (Mar. 2006), pp. 2530–2531. ISSN: 0002-7863. DOI: 10.1021/ja058387z.

[188] J. J. Dannenberg. "An Introduction to Hydrogen Bonding By George A. Jeffrey (University of Pittsburgh). Oxford University Press: New York and Oxford. 1997. ix + 303 pp. $60.00. ISBN 0-19-509549-9." In: *Journal of the American Chemical Society* 120.22 (June 1998), pp. 5604–5604. ISSN: 0002-7863. DOI: 10.1021/ja9756331.

[189] Dileep Kumar Yadav et al. "Evidence of Long-Range and Short-Range Magnetic Ordering in the Honeycomb Na3Mn2SbO6 Oxide". In: *Inorganic Chemistry* 62.19 (May 2023), pp. 7403–7412. ISSN: 0020-1669. DOI: 10.1021/acs.inorgchem.3c00666.

[190] Shingo Tsubouchi, Tôru Kyômen, and Mitsuru Itoh. "Calorimetric study of La1Srx-CoO3δ (0 < x < 0.5): Evidence for long-range ferromagnetic ordering for x > 0.3". In: *Physical Review B* 67.9 (Mar. 2003), p. 094437. ISSN: 0163-1829. DOI: 10.1103/PhysRevB.67.094437.

[191] K. J. Tilli, A. Tiitta, and H. Pöyry. "Neutron powder diffraction study of the Debye–Waller factor in nickel using the reverse Fourier time-of-flight method". In: *Acta Crystallographica Section A* 36.2 (Mar. 1980), pp. 253–259. ISSN: 0567-7394. DOI: 10.1107/S0567739480000502.

[192] O. H. J. Mustonen et al. "Valence bond glass state in the 4d1 fcc antiferromagnet Ba2LuMoO6". In: *npj Quantum Materials* 7.1 (July 2022), p. 74. ISSN: 2397-4648. DOI: 10.1038/s41535-022-00480-4.

[193] Igor A. Zaliznyak and John M. Tranquada. "Neutron Scattering and Its Application to Strongly Correlated Systems". In: 2015, pp. 205–235. DOI: 10.1007/978-3-662-44133-67.

[194] Arnab Banerjee et al. "Excitations in the field-induced quantum spin liquid state of α-RuCl3". In: *npj Quantum Materials* 3.1 (Feb. 2018), p. 8. ISSN: 2397-4648. DOI: 10.1038/s41535-018-0079-2.

[195] Rui Chen et al. "Tunable room-temperature ferromagnetism in Co-doped two-dimensional van der Waals ZnO". In: *Nature Communications* 12.1 (June 2021), p. 3952. ISSN: 2041-1723. DOI: 10.1038/s41467-021-24247-w.

[196] Pranay Ninawe et al. “Robust Spin Liquidity in 2D Metal-Organic Framework Cu(HHTP)2 with S = 1/2 Kagome Lattice”. In: *Chemistry – A European Journal* 30.4 (Jan. 2024). ISSN: 0947-6539. DOI: 10.1002/chem.202303718.

[197] Bing Zhao et al. “A Room-Temperature Spin-Valve with van der Waals Ferromagnet Fe5GeTe 2 Graphene Heterostructure”. In: *Advanced Materials* 35.16 (Apr. 2023). ISSN: 0935-9648. DOI: 10.1002/adma.202209113.

[198] Bela Bauer et al. “Gapped and gapless spin liquid phases on the Kagome lattice from chiral three-spin interactions”. In: (Mar. 2013). URL: https://arxiv.org/abs/1303.6963v2.

[199] R. Chisnell et al. “Magnetic transitions in the topological magnon insulator Cu(1,3-bdc)”. In: *Physical Review B* 93.21 (June 2016), p. 214403. ISSN: 2469-9950. DOI: 10.1103/PhysRevB.93.214403.

Appendix A

Appendix

Table A.1: Summarised relaxation rates extracted from Lorentzian fits of μSR data collected at several temperature points.

Dilution fridge		**Cryostat**	
Temperature (K)	λ (μs^{-1})	Temperature (K)	λ (μs^{-1})
0.098	0.2009(23)	1.5843	0.1687(18)
0.114	0.2030(23)	1.9066	0.1650(18)
0.206	0.2062(22)	2.2762	0.1540(17)
0.300	0.2062(22)	2.7736	0.1575(16)
0.433	0.2000(22)	3.2818	0.1490(14)
0.526	0.1996(22)	3.7855	0.1525(14)
0.619	0.2008(22)	5.0508	0.1464(13)
0.712	0.1945(21)	6.0545	0.1648(13)
0.805	0.1939(21)	7.0601	0.1376(12)
0.900	0.2000(21)	8.0714	0.1419(12)
1.057	0.1972(21)	9.0833	0.1315(12)
1.299	0.2008(21)	10.1014	0.1280(12)
1.541	0.1957(20)	20.2018	0.1494(12)
2.025	0.1935(20)	30.2639	0.1139(12)
2.51	0.1845(20)	40.2997	0.0948(12)
3.06	0.1674(20)	50.303	0.1190(11)
3.55	0.1490(19)	100.049	0.0956(11)
4.05	0.1430(18)	148.476	0.0916(10)

Table A.2: Refined structure parameters for the $P\overline{3}$ model of MOF-*bipy* fit to all 5 banks, NPD data collected on WISH, at 15 K. Final refined lattice parameters were a = 15.8848(4)Å and c = 21.2240(3) Å, R_{WP} = 2.855 % and reduced χ^2 = 828.8.

Atom	Site	x	y	z	Occupancy	U_{iso}
Cu1	-1	0.5000	0.5000	0.5000	1	0.021(2)
Cu2	1	0.8326(9)	0.6492(7)	0.4951(5)	1	0.021(2)
Carbonate						
O1	1	0.6021(1)	0.6852(2)	0.5001(1)	1	0.026(9)
O2	1	0.7584(1)	0.7283(2)	0.5003(2)	1	0.025(2)
O3	1	0.6443(1)	0.5720(2)	0.4952(5)	1	0.028(5)
C1	1	0.6714(1)	0.6688(2)	0.5044(6)	1	0.027(1)
2,4'-bipyridine						
RB1	1	0.8708(4)	0.6846(4)	0.8970(4)	0.624	0.011(7)
RB2	1	0.8454(4)	0.6696(4)	0.6656(4)	0.376	0.001(1)
RB3	1	0.5489(4)	0.5141(4)	0.7607(4)	1	0.048(2)
RB4	1	0.8035(7)	0.6478(7)	0.2508(7)	1	0.070(2)
Perchlorates						
Cl1	1	0.9933(6)	0.9820(1)	0.9804(4)	0.1667	0.021(1)
O4	1	0.9482(6)	0.8853(7)	1.0075(5)	0.1667	0.055(1)
O5	1	0.9433(2)	1.031(2)	1.0053(2)	0.1667	0.036(1)
O6	1	0.9862(3)	0.9801(4)	0.9136(4)	0.1667	0.037(1)
O7	1	1.0948(1)	1.0332(1)	1.0013(3)	0.1667	0.026(1)
Cl2	1	0.9911(6)	1.0000	0.5064(5)	0.1667	0.017(2)
O8	1	0.9984(2)	0.9122(3)	0.5113(3)	0.1667	0.058(1)
O9	1	0.9463(3)	1.005(2)	0.5648(2)	0.1667	0.074(1)
O10	1	0.9374(2)	0.9980(2)	0.4499(2)	0.1667	0.089(1)
O11	1	1.0892(2)	1.0826(2)	0.4983(2)	0.1667	0.020(1)
Cl3	1	0.6756(2)	0.3496(3)	0.9839(3)	0.2000	0.0294(3)
O12	1	0.6869(5)	0.3492(5)	0.9151(5)	0.2000	0.028(1)
O13	1	0.7736(5)	0.4167(5)	1.0064(5)	0.2000	0.024(1)

O14	1	0.6364(4)	0.2491(4)	1.0059(4)	0.2000	0.006(1)
O15	1	0.6133(3)	0.3894(3)	0.9999(3)	0.2000	0.059(1)
Cl4	1	0.6647(3)	0.3216(4)	1.0198(3)	0.1333	0.029(4)
O16	1	0.7200(1)	0.4229(1)	0.9973(1)	0.1333	0.024(3)
O17	1	0.6793(2)	0.3234(2)	1.0874(2)	0.1333	0.009(1)
O18	1	0.6923(1)	0.2553(1)	0.9898(1)	0.1333	0.006(1)
O19	1	0.5607(3)	0.2816(4)	1.0054(4)	0.1333	0.046(1)
Cl5	1	0.6707(2)	0.3372(3)	0.4959(5)	0.3333	0.025(5)
O20	1	0.5832(3)	0.3403(3)	0.4982(2)	0.3333	0.030(1)
O21	1	0.7361(2)	0.4146(2)	0.5396(2)	0.3333	0.090(1)
O22	1	0.7015(2)	0.3639(2)	0.4309(2)	0.3333	0.080(1)
O23	1	0.6824(2)	0.2581(2)	0.5156(2)	0.3333	0.042(1)

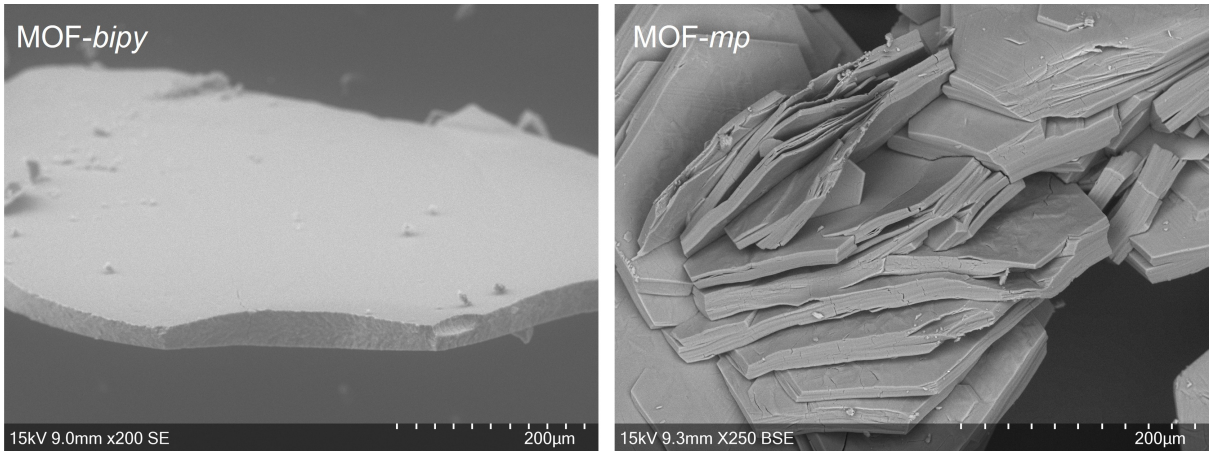


Figure A.1: Two SEM images collected for MOF-$bipy$ and MOF-mp at the same magnification. We can see here the difference in layering of these materials, with MOF-mp heavily intergrown and layered, these images are representative across several synthetic batches of these MOFs.

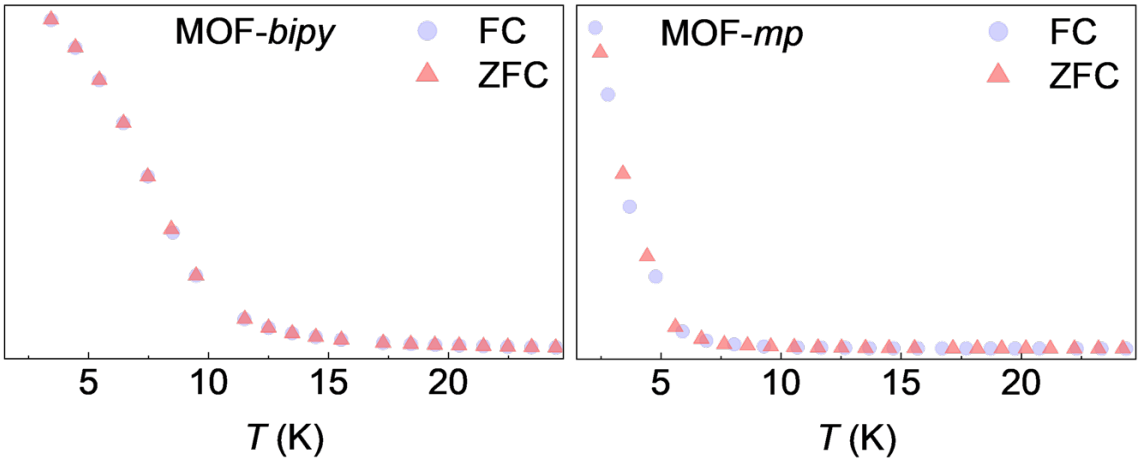


Figure A.2: Zero field and field cooled measurements for MOF-*bipy* and MOF-*mp* showing no bifurcation in either case ruling out spin-freezing. In both cases there appears to be an indication of a transition, with $T_C \approx 5.5$ K for MOF-*mp* and ≈ 11 K for MOF-*bipy*

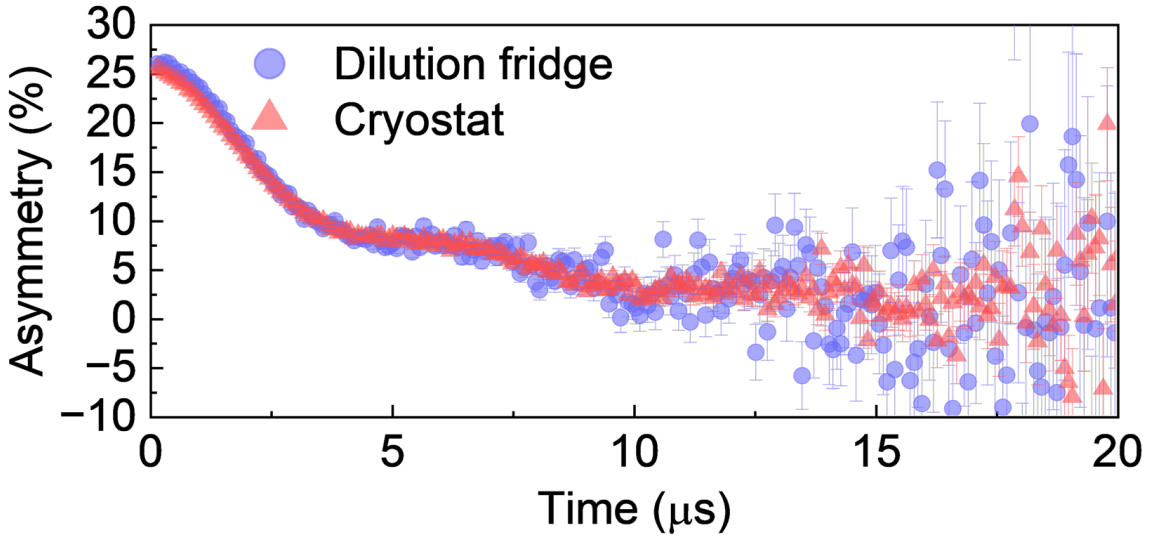


Figure A.3: MuSR data collected at 10 K in zero applied field showing that a small variation in the initial asymmetry is present between the two sample holders.

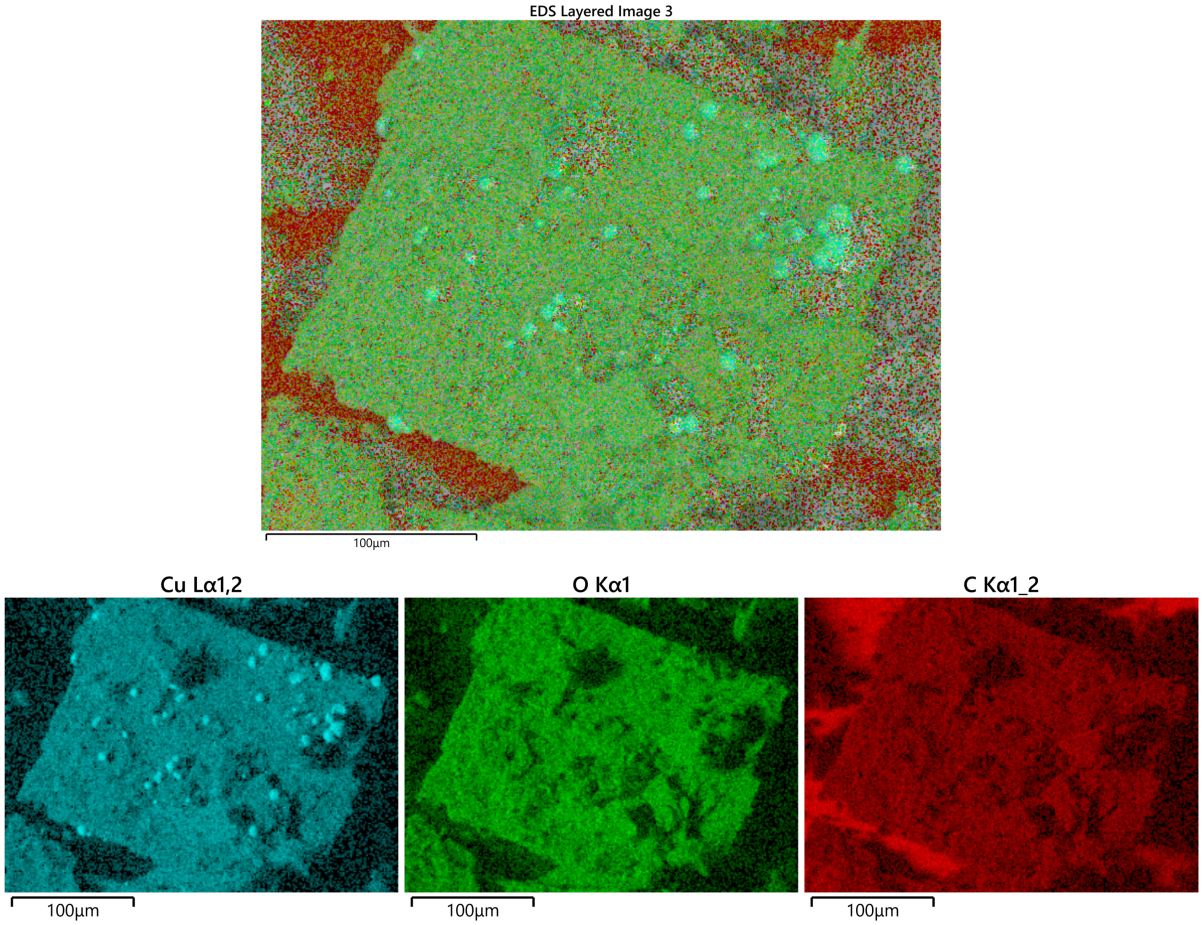


Figure A.4: Scanning electron microscopy images analysed using energy dispersive X-ray capabilities. Here we see that the material surface contains copper, suggesting supporting our conclusions that Cu-HHB nucleates on the surface of THQ crystals.

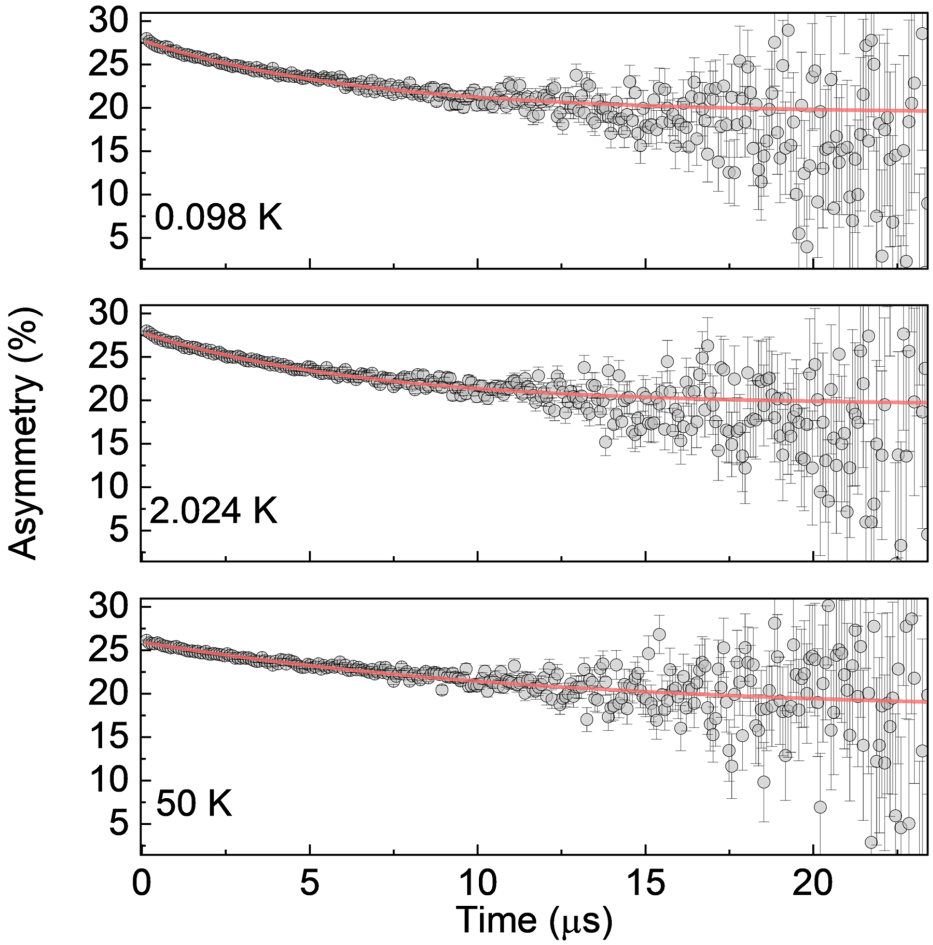


Figure A.5: MuSR data collected at three temperatures in 111 G applied LF, fit to a single Lorentzian function describing the relaxation observed. The calculated relaxation rates for 0.1, 2 and 50 K data were 0.2009(23), 0.1935(20) and 0.1190(11) cm^{-1}respectively showing a small decrease in relaxation rate between 0.1 and 2 K but a large decrease in relaxation rate upon increasing to higher temperature.